Ocean current patterns and variability around Curaçao for Ocean Thermal Energy Conversion

H.M.L. (Maria) Lems-de Jong

TU Delft

Bluerise

harnessing the ocean's power

Offshore and Dredging Engineering

Ocean current patterns and variability around Curaçao for ocean thermal energy conversion

To obtain the degree of Master of Science
at the Delft University of Technology,
to be defended publicly on Wednesday November 22, 2017 at 10:00 AM.

November 15, 2017

Author

H.M.L. (Maria) Lems-de Jong

4086511

Thesis committee

Prof. dr. J.D. Pietrzak

Dr. A.S. Candy

Ir. J.S. Hoving

Ir. B.J. Kleute

Faculty of Civil Engineering

Environmental Fluid Mechanics Section

Delft University of Technology

This study has been conducted using E.U. Copernicus Marine Service Information

"Though oceans roar, You are the Lord of all, the one who calms the wind and waves and makes my heart be still."

Psalm 46

Preface

This report is the result of 11 months of working, discovering the OTEC industry and exploring the oceanography of the Caribbean Sea. It concludes my time as a student and it is the proof that I have overcome this last obstacle named 'afstuderen'... It wasn't a cakewalk, but I was never on my own.

I would like to thank my committee member for the help that they have given me. Julie, thank you for your enthusiasm, for my work, as well as for your own. Thank you for making time for me when that was necessary, and thank you for the fruitful times when I visited you. Adam, I would like to thank you for the detailed feedback you have given me, and the smart suggestions you always made. Thanks also, for your help in preparing for the symposium. Jeroen, thanks for your relaxed attitude and detailed comments. And thank you, on behalf of all the offshore students, for the time you always make for us. Berend, you have an unrelenting enthusiasm, thanks for that. Thank you for providing the opportunity to graduate at Bluerise. Thanks to the Bluerise team for your enthusiasm and courage for what you want to achieve, and thanks for a place to work, people to chat with, ideas to share. Thanks very much for the trust you had in me, that you let me present my work at the 2017 OTEC symposium on La Reunion, France. Paul and Anne-Marie, thanks for being my travel partners (or parents ;)), it was a pleasure. It was great being a part of the successful Bluerise crowdfunding campaign. All the best of luck in the future with your ambitious plans. I hope I will keep hearing from you!

Some friends have read through parts of my report and commented on it. Some other friends were just being friends, and I would like to thank them for both! Thank you Marieke, Niek, Matthijs, Carine, Luuk, Marnix, Lisanne, Harold, Sytse, Gijs, Charlotte, Protogene. I am fortunate to know all of you. Lisanne and Carine, thank you for being my roommates and bearing with me along the way. I very much enjoyed my time with you at the 'Etalage'.

Papa, mama, thank you for all the support you have always given me. I am grateful for the way you have raised me and for the secure home you always provided.

Lennart, I love you. You believe in me and support me. Thank you for asking me to marry you. I feel very blessed to know you and be married to you. And thank you, God, for the ability to finish my studies, for giving me all these wonderfull people around me, for being in control always, and so much more.

Maria Lems-de Jong, 15 November 2017

Abstract

Large-scale changes in ocean conditions caused by installing and operating Ocean Thermal Energy Conversion (OTEC) have not been studied in depth. Conversely, the effect on an OTEC plant by oceanographic features are not researched in depth either. The aim of this research is to describe the natural patterns and variability of the ocean currents around Curaçao, an island in the Caribbean Sea and a potential OTEC deployment location. This research is carried out in order to assess possible implications for the OTEC industry. Ten years of data from the Mercator Ocean Model with a spatial resolution of $1/12^\circ$ and temporal resolution of one day was analyzed. The model is forced by wind data from ECMWF.

A strong current jet is found to dominate the flow from east to west in the Caribbean Sea. The jet is identified as the Caribbean Current and it is forced by currents in the north equatorial Atlantic Ocean and large-scale wind patterns. The Caribbean Low Level Jet, an intensification of the Trade Winds over the Caribbean Sea, is strongest in winter and weakest in fall. Consequently, the current jet is found to have a peak from December to March and a trough in October and November. The largest surface velocities of the order of 1 m/s are found along the coast of Venezuela, where wind-driven upwelling enhances surface flow to the west. Along the Venezuelan coast, subsurface currents to the east, in the opposite direction to the surface currents, are also found. The period from April to September is characterized by the meandering of the jet and the formation of large (diameter $>$ 200 km) anticyclonic eddies that cause large local surface velocities. These eddies contribute to the great variability observed in the Caribbean Sea. The origin of these eddies has not been clearly identified.

Due to upwelling, no OTEC system should be deployed more than 50 km south of Curaçao to avoid cold surface water decreasing the system's performance. Hydrodynamic forces due to the calculated expected maximum velocity of 1.8 m/s, induce stresses in the cold-water pipe that do not exceed the yield stress.

Context of research: Ocean Thermal Energy Conversion

The world's energy demand is rising and is predicted to continue to rise in the coming decades [Energy Information Administration (EIA), 2016]. At the same time, the ratification of the COP21 Paris Climate Agreement by 133 out of 195 countries sets in motion a trend towards limiting greenhouse gas emissions [United Nations Framework Convention on Climate Change (UNFCCC), 2016]. These two processes urge a slow but steady shift towards the use of less polluting energy sources. In 2011, 13% of the total world's primary energy supply was covered by renewable energy [World Energy Council (WEC), 2013]. Hydropower, wind and solar power are the most common and most developed renewable energy technologies. Challenges for reliable renewable energy supply are implementing renewable sources into existing infrastructure, the availability of resources (e.g. sunlight and wind) and, closely related to that, the storage of energy.

Ocean Thermal Energy Conversion (OTEC) uses the temperature difference between warm surface water and colder deep water as energy source for electricity generation, fresh water production and air conditioning. Cold deep water, typically 5°C, is pumped up from around one kilometer water depth to the power producing turbine at the water surface or on shore. Warmer surface water (around 25°C and 20 m water depth) is also pumped to the heat pumps and turbine. At lower latitudes, the availability of this energy resource, the temperature difference of around 20 degrees Celsius, remains large enough throughout the year for power generation. The OTEC capacity factor, the ratio of the actual to the maximum energy output over an amount of time, can therefore be much higher (around 80%) than for example for offshore wind energy farms (40% on average).

Because of this relatively small temperature difference, large volumes of water are required to generate reasonable amounts of energy. This volume flux is estimated to be in the order of 7.3 m^3/s per MW by Nihous [2006] and Grandelli et al. [2012]. In 2013, the energy demand of Curaçao was 100 MW baseload [Gardner et al., 2013]. This would come down to 730 m^3/s if the entire energy baseload would be produced by OTEC. To put this in perspective, the Rhine river has an average discharge of 2 330 m^3/s.

The working principle of OTEC was first proposed in 1881 by French physicist Jacques Arsene d'Arsonval and first proved in 1930 by George Claude [Claude, 1930]. He designed and operated an experimental 60 kW prototype plant in Belgium. Only in 1979 during the oil crisis a small 50 kW floating OTEC plant operated for a few months about two kilometers off the coast of Hawaii. Nowadays, only very few OTEC systems have been built. The plants that do exist are still relatively small (100 kW) and do not produce electricity on a commercial scale. As a comparison, the largest Dutch offshore wind farm has an installed capacity of 600 MW and provides 1.5 million people with

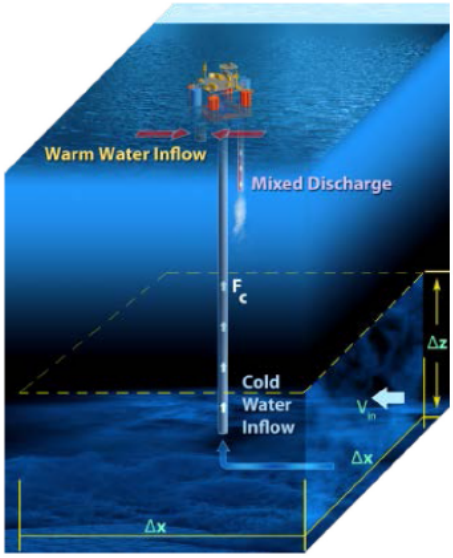

Figure 1: Overview of an offshore OTEC system with intake and discharge flows from Bluerise [2014].

electricity. Kleute and Vroom [2014] state that an installed power of 10 MW would suffice for an OTEC plant to become economically viable, with the current levelised cost of energy (LCOE) amounting to 0.19 euro cents per kWh, in particular for small tropical islands. The LCOE, as defined by Ernst & Young, is a representative cost unit that *"incorporates all the costs incurred during the life of a power station, including for example CAPEX, O&M (operations and maintenance), fuel and decommissioning costs, and divides the discounted sum of those costs by the discounted lifetime output from the power station, resulting in a lifetime average (levelised) cost per unit of electricity from the power station."* As a comparison, in 2015 offshore wind energy in Europe had a levelised cost of energy of 0.13 euro cents per kWh [Ernst & Young, 2015].

Especially for tropical islands, gaining electricity by OTEC is an interesting option. This is due to several factors. First of all, fuel and electricity equipment must all be imported and transported to the island. Consequently, electricity prices are relatively high on small islands. This, amongst other maybe more political reasons, gives a high incentive for becoming self-sustaining. Secondly, the resources for the transition towards renewable energy are plentiful at these locations, which are mostly warm, windy and sunny. Where the presence of wind and sun vary over the day, the presence of warm surface water and cold deep water is much more constant throughout the year. This gives OTEC the additional benefit of providing reliable power. Moreover, other forms of using cold seawater are especially beneficial for those islands, like fresh water production and air conditioning. Furthermore, Ocean Thermal Energy is a clean energy source with low greenhouse gas emission. It thus has a smaller contribution to climate change and the associated sea level rise. Rising sea levels is particularly disadvantageous for tropical islands.

Several companies are performing feasibility studies and gaining knowledge as a preparation for large-scale commercial power plants, land-based or floating offshore. The main challenge for these companies is the high investment risk, which is associated with the lack of experimental and operational data from running OTEC plants [Nihous, 2008].

Implications of installing and operating an offshore OTEC plant on the larger time scale are unknown. Some technical challenges are similar to other offshore installations, such as the mooring system and the floating platform. Other aspects, for example the installation and dynamics of the large diameter cold deep sea water pipe and the electricity cable to shore from water depths of more than 1000 m, are new. Also, limited experience has been gained about interaction between OTEC systems and the large-scale processes in the ocean. The redistribution of large water masses brings many challenges. Examples are the biological impact on the ecosystem and the physical influence on the ocean currents.

Bluerise is one of the several companies in the world investigating the potential for practical deployment of OTEC systems. It was founded in 2009 and has since then cooperated with Delft University of Technology and other knowledge and research institutes to gather expertise. This cooperation has led to the design and building of a small prototype OTEC plant, which is able to generate about 200 W. This prototype is currently used for analysis, optimization and model testing. Bluerise is currently developing plans to start a land-based OTEC facility on Curaçao and is exploring other possible areas suitable for hosting OTEC.

Contents

List of Tables

List of Figures

1 Introduction

1.1 Problem description for OTEC and motivation for research

OTEC (Ocean Thermal Energy Conversion) uses the potential energy from the natural temperature difference in the ocean. Surface waters are warmed by incoming solar radiation and air temperature. The deep water masses are significantly colder. This is because they originate at the north and south pole, where they lose their heat and sink. Furthermore, the deep ocean waters are well isolated from the warmer water and air at the surface by vast volumes of water between them.

To use the potential energy from this temperature difference, the warm and the cold water must be collected at an OTEC plant located at the ocean surface. The warm water is available at the surface. However, the cold water must be pumped from a depth of approximately a kilometer to the platform through a pipe. On the OTEC platform, the potential energy is harvested. In heat pumps, a working fluid is evaporated by the warm ocean water. The working fluid drives a turbine, which generates electricity. Subsequently, the working fluid is cooled by the cold ocean water and condenses again. After this process, the temperature difference between the warm and cold water has become much smaller. They are mixed and discharged back into the ocean at a depth of about 100 m, where the density of the surrounding water will be similar to the density of the discharged water. This is done to minimize the impact of the discharge water on the surrounding water. For OTEC to be economically viable, the temperature difference between warm and cold water before use, should be at least 20°C [Kleute and Vroom, 2014].

An offshore OTEC plant interacts with the ocean water surrounding it. The presence of an OTEC structure in water alters the flow of the water and the water exerts a force on the structure. An example of this interaction is the hydrodynamic force exerted on the OTEC structure and on the long cold-water pipe by the ocean currents.

Furthermore, an OTEC system utilizes the water that is present to harvest the potential energy stored in the water. In this way, it has a more direct influence on its natural marine environment, compared to other offshore structures. The intake and discharge of water masses in the order of 73 m^3/s as caused by a 10 MW OTEC system, could be regarded as a biological and physical disturbance for the natural state of the ocean Grandelli et al. [2012], Wilde [1979]. The uncertainty of the presence and degree of this disturbance, is undesirable. The consequence of this uncertainty is that it is unknown what precautions should be taken to minimize the impact on the marine environment.

The interaction between the ocean water and an offshore OTEC system has not been studied in depth. A first step in acquiring knowledge concerning this interaction, is determining the natural flow patterns of the ocean, without the interaction with an OTEC plant.

Knowledge of the natural flow patterns can be applied in several ways. First of all, for a successful implementation of an OTEC system, it is essential to be able to decide what is the optimal time period for the installation or decommissioning of an OTEC platform. Installation of an offshore OTEC platform, or part of it, will have a duration in the order of a week. A season with mostly low water velocities would be much more suitable for such an operation, especially since the pipe that transports the cold water is an essential, but also vulnerable part of the system.

In addition, being able to determine the current profile over depth over the year for the cold-water pipe is relevant to minimize the bending stresses in the material and to be able to estimate the influence of vortex induced vibrations. With this knowledge, mitigation measures can be taken to prevent the OTEC system from structural failure.

Furthermore, the determination of the direction and velocity of the surrounding waters at the inflow and outflow depths is critical. Firstly, for affirming that the discharged water will not mix with the inflow water. This would be a problem, because it causes the intake water to be colder. Thereby, it reduces the temperature difference of the ocean water in the OTEC system. Secondly, this will allow for assessment of environmental impact of the discharge flow. Nutrients in the deep waters are brought close to the surface, leading to potential algae blooms and phytoplankton growth. This requires more research. Appendix B summarizes some recent studies into the environmental impact of OTEC systems.

This study investigates natural flow patterns to explore the possibility of offshore OTEC near Curaçao, an island in the Caribbean Sea. The exact location of Curaçao can be seen in Figure 1.1. More specifications concerning the area can be found in Section 1.4. Existing knowledge of the natural flow patterns in the Caribbean Sea is presented in the next section.

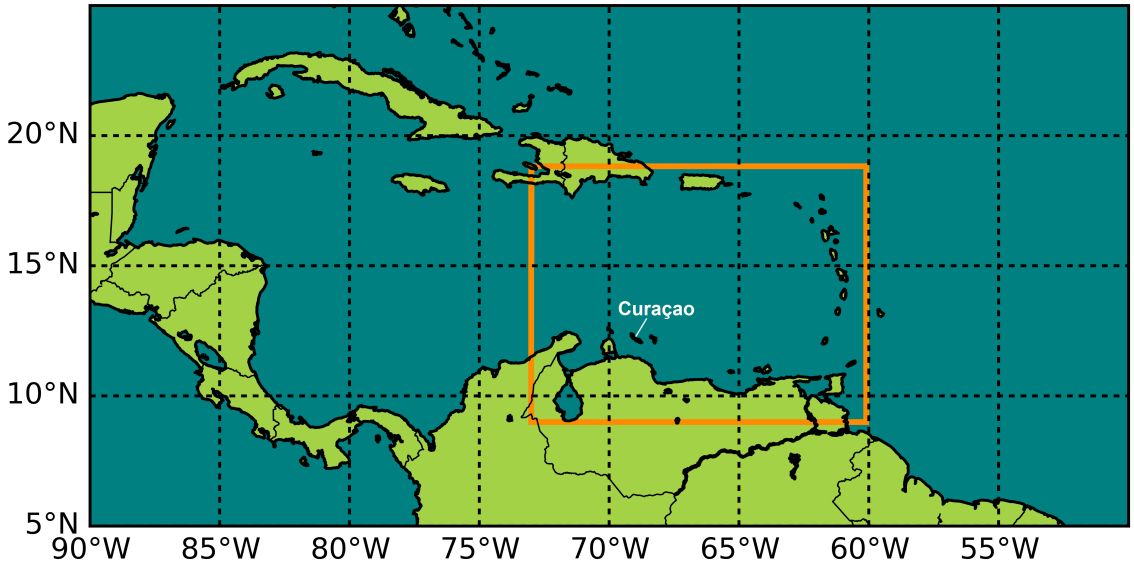

Figure 1.1: Caribbean Sea with South and Central America. Location of Curaçao is indicated. Region of interest for the project highlighted in orange.

1.2 Oceanography of the Caribbean Sea around Curaçao

Curaçao is situated along the north coast of Venezuela, South America, in the south of the Caribbean Sea, and lies between Aruba and Bonaire. In the Caribbean Sea, the general ocean circulation tends to be from the east of the basin to the west. This main flow driver is called the Caribbean Current. Maximum surface velocities are found in a southern jet along the Venezuela coast in the order of 0.7 m/s ([Fratantoni, 2001] and [Centurioni and Niiler, 2003]) with large observed variability. Evidence for subsurface countercurrents is found by Andrade et al. [2003]. The main forcing for the Caribbean Current is the Trade Winds [Wüst, 1963], that blow from east to west over the equatorial region. The Caribbean Low Level Jet, an intensification of the Trade Winds above the Caribbean Sea, shows a semiannual cycle with maxima in summer and winter and minima in spring and fall [Wang, 2007].

Along the south coast of the Caribbean Sea, upwelling is a frequent phenomenon ([Gordon, 1967], [Alvera-Azcárate et al., 2009a] and [Rueda-Roa and Müller-Karger, 2013]). Upwelling is the upward movement of cold water. This is believed to be wind-induced [Müller-Karger et al., 2004], since wind from east to west causes a northward Ekman transport in the northern hemisphere. Coastal surface temperature will be colder due to this coastal upwelling.

Eddies are believed to be a major source for intra-annual variability. They can give rise to high surface velocities and cause mixing of the water. Large anticyclonic eddies have been observed in the Caribbean Sea ([Murphy et al., 1999], [Andrade and Barton, 2000] and [Richardson, 2005]). These eddies are advected to the west by the Caribbean Current. The advection speed of around 15 cm/s implies that crossing the eastern basin of Caribbean Sea takes about two months. The generation of these eddies is a not yet

well understood process. Brazilian Current Rings and instabilities in the jet are believed to be main causes.

Two other phenomena are believed to have an influence in the Caribbean Sea. The region is known for its large hurricanes [Chang et al., 2016] and El Niño is a phenomenon with global effects [Giannini et al., 2000]. Influence of hurricanes and El Niño on the natural flow patterns in the Caribbean Sea are not well described. An extensive literature study can be found in Chapter 2.

In summary, large surface velocities, subsurface countercurrents, upwelling and generation of large eddies all influence the Caribbean Sea and in particular the vicinity of Curaçao. These phenomena are not yet well quantified, but can influence the OTEC performance. The interannual and intra-annual variability of the currents due to the mentioned processes, needs to be better understood, in order to guarantee safe and efficient OTEC operation. The high spatial and time resolution and availability of ten years of data in the Mercator Ocean model allow for assessing the role of these processes in depth.

1.3 Research objective

The aim of this project is to advance our understanding of the interaction between OTEC and large-scale processes in the ocean in order to assess possible implications for the OTEC industry. The first step in gaining this insight is to analyze and accurately describe the natural large-scale processes in the ocean at a location of interest for the OTEC business, or, as Wilde [1979] put it, *"the establishment of baseline oceanographic data at potential OTEC locations"*. Currents are essential among these large-scale processes. A second step is to assess implications of the large-scale ocean processes for OTEC.

Therefore, the objective of this project is formulated as: determining the natural oceanographic current characteristics around Curaçao and its interannual and intra-annual variability. This objective can be represented in the following research question:

What natural oceanographic patterns and what variability can be identified in the Caribbean Sea, specifically around Curaçao?

This question is rather general and various interesting aspects can be pursued. However, some processes are found to be of specific intetest in the Caribbean Sea, as was seen in Section 1.2. Therefore, the general research question can be divided into the following subquestions that will be answered:

- *What is the spatial and annual pattern of the surface currents around Curaçao and what is the variability?*
- *What is the spatial and annual pattern of the winds around Curaçao and how do they correlate to the surface currents?*
- *What is the spatial and annual pattern of the sea surface temperature around Curaçao and how does it relate to the surface currents?*
- *What is the influence of eddies on the surface currents and how are the Caribbean eddies generated?*

- *What is the current profile over depth around Curaçao and what is the variability?*
- *What is the spatial and annual pattern of the volume fluxes around Curaçao and what is the variability?*

A second research question can be defined, which focusses on the implications of the natural oceanographic patterns for OTEC:

How would these natural oceanographic patterns influence the design and operation of a 10 MW offshore OTEC plant near Curaçao?

This second research question is specified by the following subquestions:

- *What is the time period with the optimal ocean circumstances for installation, commissioning, maintenance or decommissioning of an offshore OTEC plant around Curaçao?*
- *What is the optimal location for a 10 MW offshore OTEC plant around Curaçao with regard to temperature differences and bathymetry?*
- *What is the maximum expected current velocity for the lifetime of an OTEC plant around Curaçao?*
- *What is the maximum expected hydrodynamic force on the cold-water pipe for the lifetime of an OTEC plant around Curaçao and what is the associated stress and deflection of the pipe?*
- *The knowledge of which processes will increase the predictability of the ocean currents and temperature distribution?*

1.4 Region of interest

Bluerise BV has a long-term business relationship with the airport on Curaçao. Plans for installing an onshore OTEC plant near the airport have proceeded over the last couple of years. Therefore, Curaçao might very well be the first location where a Bluerise OTEC plant will be built. Also, the circumstances for generating electricity with an offshore plant are promising. Large water depths near shore and high temperatures at the sea surface show the large potential of this location. Appendix B elaborates on this. Therefore, Curaçao and the Caribbean Sea are chosen as most interesting location to look into for this project.

The region of interest can be seen in Figure 1.1. It is a square of about 1300 km wide from east to west and 1100 km long from north to south (73°W to 60°W and 8°N to 19°N). This region is chosen because of the scale of oceanographic processes. This scale is mostly determined by the inflow jet to the east, through the Lesser Antilles, and the eddies in the Caribbean Sea which can become as big as 300 km in radius and can extend up to 3° in latitude. In order to understand the variability near Curaçao, on a smaller scale, the whole of the Caribbean Sea should be regarded.

1.5 Outline of the research

First, a literature study is carried out. A description of the most important findings can be found in Chapter 2. The literature review is a very important step in this research, since it points out processes and locations of interest for OTEC. In Chapter 3, the analyzed datasets and the methods for this analysis are described. Chapter 4 describes the general surface velocity and temperature pattern in the Caribbean Sea. In Chapter 5, we zoom in on Curaçao and quantify the patterns. Volume fluxes and subsurface currents are described in Chapter 6. Chapter 4 to 6 concern the results of the analysis, while Chapter 7 applies the identified patterns to OTEC. In this chapter, maximum expected currents and hydrodynamic forces on the OTEC plant are calculated. Discussion and conclusions of the results can be found in Chapter 8 and 9 respectively. Recommendations as a result of the research are summarized in Chapter 10.

During the course of this project, the research was presented at the 5th international OTEC symposium. The paper submitted for this conference can be found in Appendix A.

2

Literature on the oceanography of the Caribbean Sea

The most important aspects of the oceanography of the Caribbean Sea will be discussed in this chapter. First of all, the bathymetry of the Caribbean Sea influences the currents and depth of different water masses and will be discussed in Section 2.3 and 2.1. Secondly, the Caribbean Sea is a semi-enclosed sea with a general flow direction. This will be described in Section 2.3 and 2.4. And finally, some natural sources of annual and interannual variability are described in Section 2.5 to 2.11. This chapter ends with some remarks on the vicinity of Curaçao and assessment of the most important parameters in Sections 2.12 and 2.13.

2.1 Bathymetry

The Caribbean Sea consists of several basins, their depth ranging from 3000 m to a maximum of 7100 m in the Cayman Trench. These basins are divided by ridges which are less than 2000 m deep. See Figure 2.1 for an overview of the bathymetry of the Caribbean Sea. Curaçao and its neighboring islands are situated at the southern border of the Venezuela Basin at 69°W and 12°N.

The densest and deepest waters in these basins move or interact with other water masses only on a very large time scale with very low velocities [Gallegos and Maul, 1996]. Only the upper 1200 m of water column shows current velocities that are larger than 5 cm/s [Gordon, 1967].

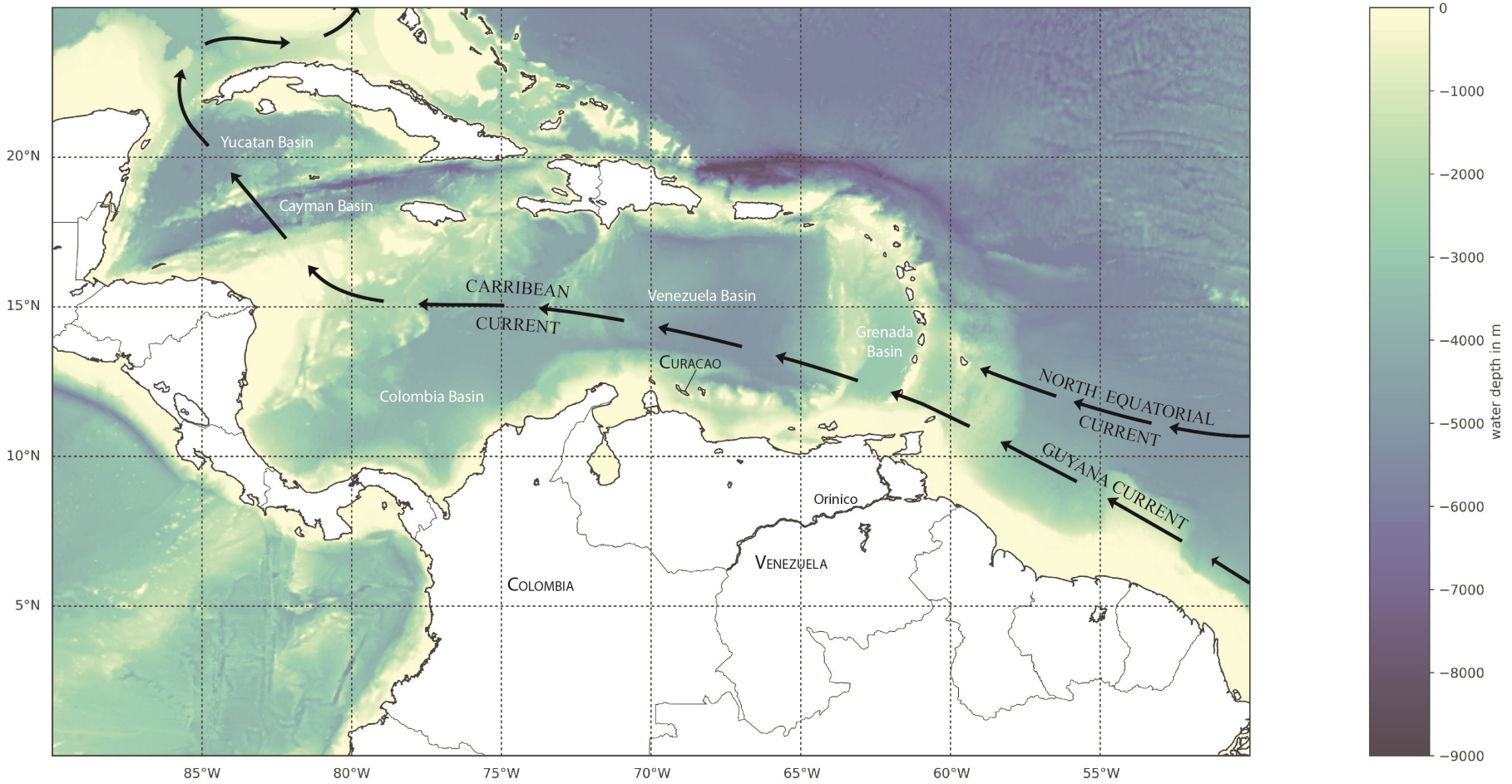

Figure 2.1: Bathymetry of the Caribbean Sea from GEBCO [2014]. Depth in meters. Drawn on top is the schematic Caribbean circulation, from pilot charts, adapted from Duncan et al. [1982]. Also indicated are the basin names and the location of Curaçao.

2.2 Water masses

The water in the Caribbean Sea can be divided into four water masses [Gallegos and Maul, 1996]. The top layer, from 0 to 50 m, is not considered as a separate water mass because it is mostly influenced by local air temperature, humidity and mixing by wind and waves. The Subtropical Underwater (SUW) consists of relatively warm and salty water (more than 20°C and 37 psu) and ranges from 50 to 250 m of water depth. This water mass is formed by Ekman convergence of the surface water (which is salty and warm) in the subtropical North Atlantic [Emery and Meincke, 1986]. The Western North Atlantic Central Water (WNACW) ranges from 250 to 750 m. This layer acts as a transition layer for the layers above and below. Therefore has a large range of temperature and salinity (7-20°C and 35-37 psu). Below this layer, from 750 to 950 m, is the Antarctic Intermediate Water (AAIW). It originates at the South Pole and is characterized by its low temperature and salinity (3°C and 34 psu). Deeper, the North Atlantic Deep Water (NADW) is found, from 950 to the sea floor (4°C and 35 psu). The NADW is formed by the Arctic Intermediate Water (AIW) from the North Pole, flowing over the Greenland-Scotland sill. The NADW accounts for more than 70% of the total volume of sea water in the Caribbean Sea.

2.3 Local oceanic currents

The Caribbean Current is the main flow driver in the Caribbean Sea and flows from the Lesser Antilles ridge in the southeast to the Yucatan Channel in the northwest and into the Gulf of Mexico, see Figure 2.1. The average transport in that direction is estimated to be 30 Sv by Gordon [1967], Gallegos and Maul [1996] and Gyory et al. [2014]. By means of surface drifters, two surface jets are observed, a northern one at 17°N and a southern one below 14°N [Centurioni and Niiler, 2003]. Maximum surface velocities are in the order of 0.7 m/s along the coast of Venezuela ([Fratantoni, 2001] and [Centurioni and Niiler, 2003]), within the southern jet. The North Atlantic Equatorial Current and the Guyana Current are the main drivers for water entering the Caribbean Sea ([Duncan et al., 1982] and [Johns et al., 2002]) and therefore strongly influence the properties of the water in the Caribbean Sea. The outflow of the Caribbean Sea in the northeast consists of the Loop Current into the Gulf of Mexico and the Florida Current, which will at a later stage become the Gulf Stream. The annual variability of the inflow has a range of about four Sverdrup with its maximum in the spring and summer and minimum in fall. The outflow displays similar variability, but slightly lags. Intraseasonal variations in volume transport (which are in the same order as the annual variation) are said to be caused by North Brazil Current rings that collide with the steep ridge of the Lesser Antilles.

2.3.1 Wind-driven transport

Wind plays a major part in inducing ocean currents. Due to the rotation of the earth and incoming solar radiation, Hadley cells arise. These cells can be explained as follows. At

the northern hemisphere, air at the equator warms up and rises, flows northward at great heights and is deflected towards the right by Coriolis. When it cools, sinks and flows southward, it is again deflected to the right, thus blowing to the west. This persistent feature around the equator is called the Trade Winds. Since the same phenomenon happens in the southern hemisphere, where Coriolis force causes the air to deflect to the left, a convergence zone around the equator is formed where the southern and northern Trade Winds converge. This zone is called the Intertropical Convergence Zone (ITCZ) and it is known for doldrums and heavy precipitation.

The main forcing for the Caribbean Current as well as for the North Atlantic Equatorial Current and the Guyana Current is the Trade Winds [Wüst, 1963]. However, Caribbean Current transport caused by wind alone does not add up to the observed 30 Sv.

From the Sverdrup equation, we know that wind stress curl plays an important role in driving wind-driven circulation:

$$\beta M_y = \frac{\delta \tau_{s,y}}{\delta x} - \frac{\delta \tau_{s,x}}{\delta y} \tag{2.1}$$

In the above equation, β is the beta plane approximation of the Coriolis force, $\delta f / \delta y'$ and M_y is the wind-driven transport in y-direction. The right-hand side of this equation is the curl of the wind stress. The Caribbean Sea is divided in half by a zero-mean wind stress curl line from east to west ([Hellerman and Rosenstein, 1983], [Johns et al., 2002] and [Josey et al., 2002]). Such a line theoretically separates ocean gyres and north-south net mass transport due to winds over these lines would be zero [Pietrzak, 2016]. This is not the case in the Caribbean Sea. Consequently, some other forcing mechanism must play a role.

2.3.2 Meridional Overturning Circulation

Meridional overturning circulation (MOC or thermohaline circulation) is mass transport in the ocean caused by density differences. Density is influenced by temperature, salinity, pressure, but also by internal mixing processes. Where wind-driven transport is limited to the upper few hundred meters of the ocean and acts locally, meridional overturning circulation causes movement of water masses over the entire depth and throughout all the oceans. It is sometimes referred to as 'the great conveyor belt'. However, there is non-linear interaction between the two forcing mechanisms. About 40% of the transport in the Caribbean Sea can be contributed to the meridional overturning circulation [Johns et al., 2002]. The wind-driven transport is concentrated in the northern jet of the Caribbean Current, while the MOC-driven current is concentrated in the southern jet.

2.3.3 Subsurface currents

At the southern border of the Caribbean Sea along the Panamanian, Colombian and Venezuelan coast, a mostly submerged eastward flow exists, as shown by Gordon [1967] and Andrade et al. [2003]. This eastward flow starts at the surface in the Panama-Colombia Gyre. At the Guajira Peninsula (the most northern part of Colombia) the

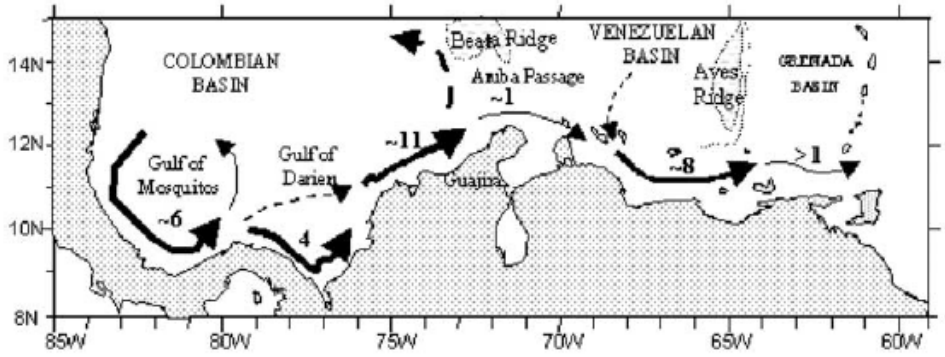

Figure 2.2: Schematic representation of the southern Caribbean Coastal Undercurrent as it was found in the different sections studied along the coast. The width of the arrows represents the current intensity at 200 m depth together with the averaged Undercurrent geostrophic transport in Sverdrup. Figure from Andrade et al. [2003].

eastward flow has sunken to a depth of about 200 m. It shows a maximum velocity of 0.4 m/s. This submerged countercurrent is suspected to continue all the way to the Antilles, but does vary in volume flow, see Figure 2.2. It is said to originate from the alongshore pressure gradient caused by wind in combination with the local upwelling (see Section 2.5).

2.4 Winds

A predominant meteorological feature in the Caribbean is the easterly (westward) winds. These winds are part of the equatorial Trade Winds. They are generated by the pressure gradient between the Azores High and the low-pressure band of the Inter Tropical Convergence Zone. The Azores High is a semi-permanent pressure system at about 30°N above the North Atlantic ocean. It is also known as the Bermuda High and the North Atlantic Subtropical High. This high atmospheric pressure system of around 1024 mbar is strongest in summer (June and July). Subsequently, it decreases in the fall, extends to the west towards North America in winter and retreats towards the east in spring.

This yearly movement and development induces the semiannual cycle of the Caribbean Low Level Jet (CLLJ) with peaks in February and July [Wang, 2007]. The CLLJ (or the Intra Americas Low Level Jet) is a maximum of easterly zonal winds at 925 hPa (between 100 and 1000 m above sea level) along 15°N. Its regional maximum is between 71°W and 76°W and 12°N and 16°N. It is suggested that the CLLJ is influenced by local topography; the presence of the mountain ridge in northern South America causes a north-south horizontal temperature gradient and intensifies the CLLJ, while it is weakened by the Greater Antilles to the north of the Venezuela Basin [Muñoz et al., 2007].

The Caribbean region is known for its devastating hurricanes. Section 2.9 elaborates on this subject.

2.5 Upwelling

Along the northern coast of South America, upwelling is a regular phenomenon. Two large upwelling systems have been studied in more detail. The first is west of the peninsula of Guajira near Santa Marta at the border between Colombia and Venezuela [Andrade and Barton, 2005]. The second is at the Venezuelan coast, in the Cariaco basin near Puerto La Cruz, Isla La Tortuga and Isla de Margarita [Müller-Karger et al., 2004]. Upwelling is induced by the Trade Winds blowing from east to west along the coast that generate an Ekman transport offshore. This causes the deeper and cooler waters to come to the surface. The variability of these upwelling systems is therefore strongly correlated to the variation in intensity of the Trade Winds. Thus, the upwelling is strongest in winter. The order of magnitude of the vertical velocity of the upwelling is estimated to be 6×10^{-6} m/s by Gordon [1967] and 4.4×10^{-5} m/s by Andrade and Barton [2005]. The maximum offshore Ekman transport is estimated to be between 9 m^2/s [Santos et al., 2016] and 11 m^2/s [Rueda-Roa and Müller-Karger, 2013]. The influence area of the upwelling areas is in the order of 10^3 km^2 but can become as big as 10^4 km^2 [Müller-Karger et al., 2004], partly due to filaments [Andrade and Barton, 2005]. These filaments are narrow arms of upwelled water, elongated by the general flow direction and eddies.

This upwelling has an effect on the sea surface salinity (higher salinity in regions with upwelling), but mostly on the sea surface temperature (lower temperature in regions with upwelling). In the Caribbean Sea, the Subtropical Underwater (SUW) and the Antarctic Intermediate Water (AAIW) are brought up to the euphotic zone by these upwelling systems [Müller-Karger et al., 1989]. Upwelling systems are normally known for their high biological productivity, because of the higher concentrations of nutrients in the euphotic zone. At the same time, upwelling causes the thermocline to rise. A decrease of surface or near-surface temperature can have a negative effect on an OTEC system. This is because it would lower the temperature difference that is the driver for the power generation.

In several upwelling systems, subsurface countercurrents are found [Smith, 1968]. This process is found in the Yucatan upwelling system and the Peruvian upwelling system. Also upwelling in the south of the Caribbean Sea has been linked to the subsurface countercurrent [Alvera-Azcárate et al., 2009a].

2.6 Eddies

Eddies are circular moving bodies of water in the horizontal plane with a vertical structure. They can range in size from a couple of centimeters to hundreds of kilometers. Eddies are an important phenomenon in the oceanography due to their ability to transport heat, salt and nutrients. They cause mixing and are important because of their kinetic energy. The generation of eddies is a complex process and is not yet well understood. Important parameters in this process are baroclinic instability and velocity shear.

Baroclinicity can be described as the misalignment of isobars (lines of constant pressure) and isopycnals (lines of constant density). It signifies a density gradient over a line of

constant pressure. Potential energy is associated with this situation. Baroclinic instability is the increasing amount of conversion of this potential energy into kinetic energy. Equilibrium is achieved through the Thermal Wind Balance. The horizontal density gradients $\delta\rho/\delta x$ and $\delta\rho/\delta y$ are balanced by vertical velocity shear $\delta u/\delta z$ and Coriolis f:

$$\frac{\delta u}{\delta z} = \frac{g}{f\rho_0}\frac{\delta \rho}{\delta y} \tag{2.2}$$

$$\frac{\delta v}{\delta z} = -\frac{g}{f\rho_0}\frac{\delta \rho}{\delta x} \tag{2.3}$$

Temperature differences can be the cause of density differences. Eddies often show a different temperature in the core compared to the surrounding circulating water. These cold-core and warm-core eddies rotate in opposite direction. In what direction they rotate is also determined by the Coriolis force. Consequently, it depends whether they are in the Northern Hemisphere or on the Southern Hemisphere. On the Northern Hemisphere, cold-core eddies rotate anticlockwise, thus cyclonic (in the same direction as the earth rotates when viewed from above), whereas warm-core eddies rotate clockwise, thus anticyclonic.

In the Caribbean Sea, large anticyclonic and some cyclonic eddies have been observed by sea level anomaly ([Murphy et al., 1999] and [Andrade and Barton, 2000]) and by surface drifters [Richardson, 2005]. They propagate in the direction of the Caribbean Current. The cyclonic eddies were located near the coast, not within the main jets of the Caribbean Current. Therefore, they traveled at lower speeds (1.3 cm/s) than the anticyclonic eddies (13.4 cm/s), that were often found in the jets. A minimum of four anticyclones per year is said to form in the Caribbean Sea [Richardson, 2005]. This comes down to an estimate of twelve anticyclonic eddies per year with a minimum diameter of 200 km. Surface drifter data implied that more anticyclones were formed during summer and fall than during winter and spring [Richardson, 2005]. Eddy Kinetic Energy was calculated to be highest between June and October [Andrade and Barton, 2000].

The anticyclonic eddies are said to originate from potential vorticity advected from the Brazilian Current Rings [Murphy et al., 1999] or from instability in the meandering jet through the Caribbean Sea ([Jouanno et al., 2012], [Richardson, 2005], [Alvera-Azcárate et al., 2009b] and [Andrade and Barton, 2000]. A link was found between low frequency mean kinetic energy and mean eddy kinetic energy. This would imply that more intense surface currents provide energy for the eddies, while the Brazilian Current Rings provide perturbations that trigger the instability. These eddies can intensify greatly along the way. The advection speed of the eddies is estimated to be 20-30 cm/s according to Andrade and Barton [2000], 13 cm/s according to Richardson [2005], or 15 cm/s according to Murphy et al. [1999]. Consequently, crossing the Venezuela Basin takes about two months. The diameter of these eddies can range from the order of tens of kilometers up to several hundreds of kilometers.

2.7 El Niño

El Niño is a periodic event that has global effects on weather and oceans. It is also called El Niño Southern Oscillation (ENSO). About once every seven years, the usually per-

sistent Trade Winds that blow around the equator from east to west reduce in strength. The warmer equatorial surface waters of the Pacific Ocean, that are transported to the west by these winds, spread out to the east. This is called an ENSO event. The opposite happens, when the Trade Winds transport the warm surface water to the east, and the normal situation restores. This is called a La Niña. The consequences of an El Niño and La Niña vary per region. They can be more precipitation (parts of Africa, Asia and South America) or more drought (north Australia, Indonesia, Philippines and north Brazil), higher temperatures (south Asia, west coast of Canada, south Australia and parts of South America) or lower temperatures (southern U.S.), more or less upwelling (west coast of South America) and indirect effects on the availability of drinking water, food production and mud avalanches.

The influence of an El Niño can also be observed in the Caribbean Sea. It can be the cause of dry summers and wet winters [Giannini et al., 2000]. This could have an influence on the sea surface salinity due to precipitation and evaporation. Also, South American river discharges reduce, due to El Niño [Hu et al., 2004]. An ENSO event can also alter the wind pattern. It is even said to be the biggest influencing factor on the variability of the Caribbean Low Level Jet [Maldonado et al., 2016]. An ENSO event causes sea level pressure anomalies in the Azores High, which effect the CLLJ. How an EL Niño affects the CLLJ, varies per season. In the winter, the CLLJ is weaker than usual, whereas in the summer the CLLJ is stronger than usual. The reason for this is that ENSO induces negative (positive) sea level pressure anomalies in the Azores High during winter (summer) [Wang, 2007]. Intensification of the CLLJ during the summer is also described by Hidalgo et al. [2015] and Whyte et al. [2008].

Whether an El Niño event takes place, can be identified from different indices, see Pietrzak [2016]. The ONI (Oceanic Niño Index) value is determined using sea surface temperature anomalies at 5°S,170°W to 5°N,120°W. From the ONI, four ENSO events during the period of 2007 until 2016 can be identified of type 'moderate', 'strong' or 'very strong' [NOAA Climate Prediction Center, 2017]. In the winter from 2007-2008 and in the winter from 2010-2011, moderate La Niña events took place. In the winter from 2009-2010, a moderate El Niño took place. In the winter from 2015-2016, a very strong El Niño event occurred. It is even said to be one of the strongest ever measured. An overview of the past ONI values can be found in Figure 2.3 and a summary in Table 2.1.

Other low frequency events that could influence the Caribbean Sea are the North Atlantic Oscillation (NAO), the Pacific Decadal Oscillation (PDO) and the Pacific/North American Pattern (PNA). The effects of these events on winds are estimated to be lower than the ENSO events [Maldonado et al., 2016].

2.8 River run off

Together, the Amazon and the Orinoco river represent 20% of the annual global river discharge. Both of these rivers are located upstream of the Caribbean Sea at the coast of South America, at a distance of 2700 km and 1000 km alongshore from Curaçao relatively, see Figure 2.1. The Amazon river has an average discharge of 200 x 10^3 m^3/s and the

Table 2.1: ENSO events in the years 2007 until 2016. In brackets is the maximum three monthly mean ONI value for the event.

Period	Event	Strength (ONI value)
Winter 2007-2008	La Niña	moderate (-1.4)
Winter 2009-2010	El Niño	moderate (1.3)
Winter 2010-2011	La Niña	moderate (-1.4)
Winter 2015-2016	El Niño	very strong (2.3)

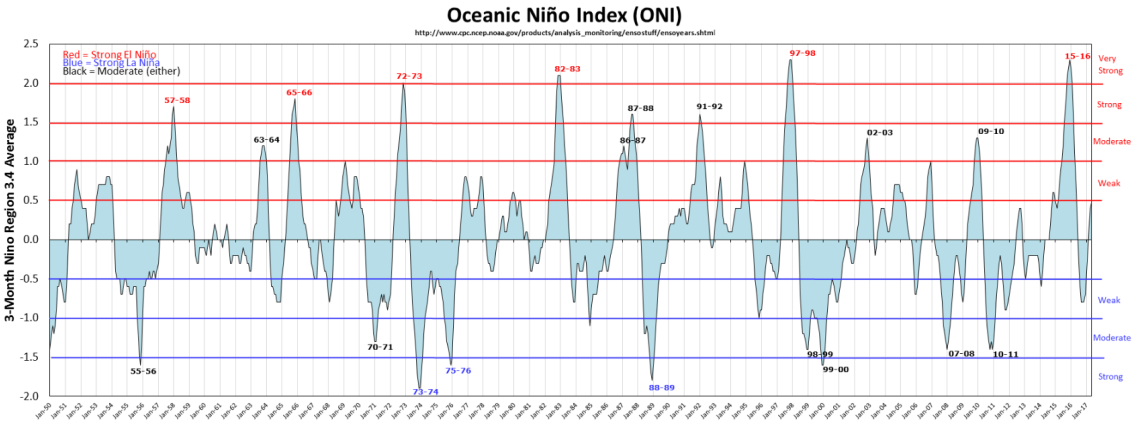

Figure 2.3: Overview of the ONI values from 1950 up to 2016. Three months average values are used. From NOAA Climate Prediction Center [2017]

Orinoco river 35 x 10^3 m^3/s [Degens et al., 1991]. The Magdalena river runs through Colombia and also ends in the Caribbean Sea. Its discharge, however, is a lot smaller compared to the Amazon and Orinoco rivers (8 x 10^3 m^3/s). It is located downstream of Curaçao, to the west of the ABC islands. For comparison, the Rhine river discharge is 2.3 x 10^3 m^3/s.

Amazon river discharge peaks in June and July, the Orinoco discharge peaks around August. Both of these plumes are said to influence the south-east Caribbean Sea heavily ([Hu et al., 2004] and [Müller-Karger et al., 1989]). Interaction of the plumes with the North Brazil Rings, effects the inflow volume into the Caribbean Sea. Due to the river plumes, concentrations of chlorophyll, colored dissolved organic matter (CDOM) and phytoplankton growing on the nutrients in the river water will be higher than usual [Hu et al., 2004]. Also, the sea surface salinity will be lower because of the fresh water from the rivers [Froelich Jr. et al., 1978].

Closer to the island of Curaçao is the Maracaibo lake and the Gulf of Venezuela. Their proximity to the ABC islands makes them, and their properties, relevant to this research. The Catatumbo river and the Escalante river end in the lake. These discharges also influence the local water properties. Primary productivity near the Gulf of Venezuela was observed to be in the range of 96-650 mg C /(m^2 d) due to high concentrations of chlorophyll and nutrients [Müller-Karger et al., 1989]. This is in the same order as in the Orinoco Delta.

Table 2.2: Hurricanes above the Venezuela basin in the years 2007 until 2016. Strength of a hurricane is determined by sustained wind speeds and type of damage as caused by the hurricane. Category 5 indicates strongest hurricanes with highest wind speeds and most severe damage.

Year	Date	Name	Strength above Venezuela Basin
2007	Aug 17 - Aug 19	Dean	Category 2-5
2007	Sep 1 - Sep 3	Felix	Category 1-5
2007	Oct 26 - Oct 29	Noel	Tropical storm
2008	Aug 25 - Aug 26	Gustav	Tropical storm
2008	Oct 13 - Oct 16	Omar	Category 1-4
2009	Sep 2 - Sep 4	Erika	Tropical storm
2010	Sep 7 - Sep 8	Gaston	Tropical depression
2010	Oct 30 - Nov 3	Tomas	Tropical storm - category 2
2011	Aug 2 - Aug 4	Emily	Tropical storm - category 1
2012	Aug 3 - Aug 5	Ernesto	Tropical storm
2012	Aug 12 - Aug 13	Helene	Tropical depression
2012	Aug 23 - Aug 25	Isaac	Tropical storm
2012	Oct 12 - Oct 14	Rafael	Tropical storm
2013	Jul 9 - Jul 10	Chantal	Tropical storm
2013	Sep 4 - Sep 5	Gabrielle	Tropical depression
2014	Aug 2	Bertha	Tropical storm
2015	Aug 27 - Aug 28	Erika	Tropical storm
2016	Sep 28 - Oct 2	Matthew	Category 1-5

2.9 Hurricanes

The Caribbean Sea and the southern part of North America are known for large hurricanes that pass over the region. Hurricanes emerge where the humidity is high, winds are light and sea surface temperature is high, slightly north and south of the equator. A hurricane begins as a small thunderstorm, caused by the convergence of surface winds. This can occur in the Inter Tropical Convergence Zone or due to tropical disturbance, called the easterly wave. Pressure drops in the region surrounding the storm when water in the air condenses, releases its heat and causes the atmospheric gases to expand. The air rises, cools down and condenses more. This process intensifies, causing the pressure to drop even more and wind speeds to increase. The Atlantic hurricane season runs from June until November, when the sea surface temperature is high enough to sustain the condensation of water. In Table 2.2, the hurricanes or tropical storms that entered the Caribbean region in the years 2007 until 2016 are displayed [National Oceanic and Atmospheric Administration (NOAA), 2017].

2.10 Precipitation and climate change

Precipitation effects the ocean because of its ability to lower the temperature or salinity of the water. The annual mean rainfall over the Caribbean Sea is 1 618 mm/y. However, along the Venezuelan coast and in the Netherlands Antilles it is less than 600 mm/y

on average [Giannini et al., 2000]. Annual precipitation is more than twice as high in summer and fall (August to October) compared to winter and spring (February to May) [Wüst, 1963].

The effects of climate change on the Caribbean Sea environment, as for any location, are hard to predict. However, as described by Peterson et al. [2002], the probability of parameters such as precipitation, hurricane events and temperature reaching an extreme maximum or minimum value has become larger over the last 50 years.

2.11 Tides

In the Caribbean Sea, tidal amplitudes are generally small. In the Venezuela Basin, the tidal signal is mainly diurnal, although in the western and eastern part of the basin the signal is mixed, but still primarily diurnal (see Figure 3 from Kjerfve [1981]). The mean tidal range is around 10 cm, but becomes as high as 40 cm in the Grenada Passage in the southeast. There, at the southern passages, tidal currents can be as large as the long-term mean currents (typical values are 0.1 to 0.3 m/s). In general, the tidal currents can be masked entirely by oceanographic conditions [Kjerfve, 1981].

2.12 Curaçao

Curaçao is an island located about eighty kilometer north of the northern coast of Venezuela at 12.1°N, 69.0°W, see Figure 2.1. A hundred kilometer to the west of Curaçao is the peninsula Paraguaná that encloses the Gulf of Venezuela. Curaçao lays between Bonaire and Aruba, which are approximately 50 km to the east and 110 km to the north-east respectively. Together they form the so-called 'ABC islands'. All three islands are part of the Kingdom of the Netherlands. The islands, together with some other islands and shoals more to the east like Gran Roque, Isla La Orchilla and Isla La Blanquilla, form a ridge of islands. Together, these islands more or less separate the great water depth of the Venezuela Basin (more than 6000 m) from a channel in between the ridge and the Venezuelan coast (about 2000 m water depth).

In Figure 2.4, the bathymetry around Curaçao can be seen. It is expected that all four water masses as described at the beginning of this chapter, will be present in the channel between Curaçao and the mainland, and around the island. The current velocities, which might be magnified by the local bathymetry, can induce mixing of different layers due to turbulence. The processes described above cover the entire Caribbean Sea. However, when analyzing currents on a smaller scale, other effects begin to play a more significant role. For example, topographic steering and Von Karman-like vortices that are caused by small islands as described by Bowman et al. [1996]. These vortices are eddies with a magnitude in the order of the island size and cause perturbations for a distance of about eight times the islands diameter.

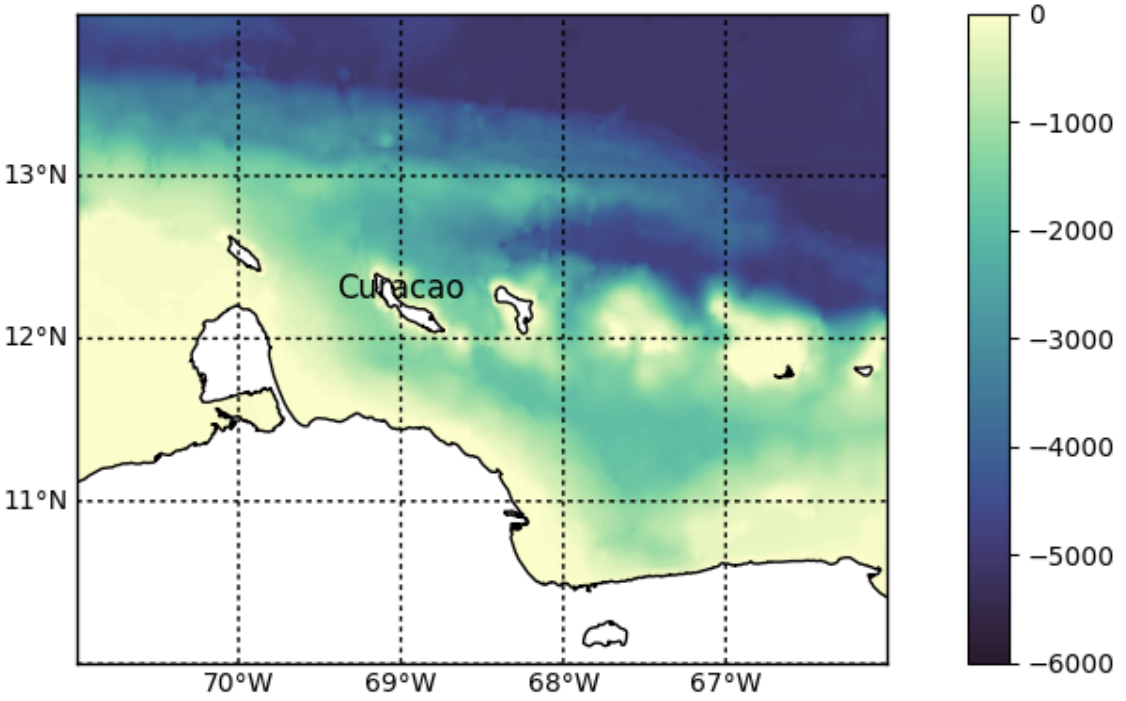

Figure 2.4: Bathymetry around the island of Curaçao. Depth in meters.

2.13 Assessment of most important parameters influencing the currents

From this chapter, it can be concluded that the Caribbean Sea is dominated by a generally westward surface current and volume flux, mainly above 1200 m of water depth. Regional winds are quite persistent and in the same direction as the currents. Large variability in the flux can be contributed to the existence of large eddies. In the south of the Caribbean Sea, along the coast of Colombia and Venezuela, subsurface currents towards the east are found. For that same region, coastal upwelling of colder water to the surface is described by several authors. The most important parameters that drive the ocean currents are [Pietrzak, 2016]:

- Sea surface height
- Density and therefore temperature and salinity
- Wind stress
- Friction
- Turbulence
- Coriolis

The seawater density is not available in the data but can be calculated from the linear equation of state for seawater, where sea water density ρ depends on sea water temperature T and sea water salinity S [Knauss and Garfield, 2017]:

$$\rho = \rho_0(1 - \alpha_T(T - T_0)) + \beta_S(S - S_0) \tag{2.4}$$

where ρ_0 is the reference density of 1.027 kg m^{-3}, T_0 and S_0 are the reference temperature and salinity, with the values 2°C and 35 psu respectively, α_T is the thermal expansion

coefficient and β_S is the saline contraction coefficient, where $\alpha_T = 2 * 10^{-4}$ °C^{-1} and $\beta_S = 7.5 * 10^{-4}$ psu^{-1}.

3 Methodology

Data from different datasets are analyzed. A description and specifications of the models that provided these datasets, amongst others the Mercator Ocean model, can be found in Section 3.1. Sources for wind data and bathymetry data that are used can be found in Section 3.1.2 and 3.1.3. Parameters that are analyzed include water velocity and direction, water temperature, wind velocity and direction, sea surface height and bathymetry. What methods were used for the analysis, are described in Section 3.2. Lastly, the focus of this research is described in Section 3.3.

3.1 Model

3.1.1 Mercator Ocean model

Mercator Ocean, an ocean research center situated in France, has been developing a model. This model has been included in the European Commission Earth Observation program Copernicus Marine Environment Monitoring Service (CMEMS) in 2014. It is used for forecasting and analysis of the physical and biochemical state of the ocean on a global scale. For this project the global ocean physical analysis and forecast model that is updated daily is used (GLOBAL_ANALYSIS_FORECAST_PHY_001_024) [CMEMS, 2015]. It includes the global ocean in a 1/12° resolution and 50 depth levels from 0 to 5000 m water depth (unevenly spaced). Around the region of interest, this yields a horizontal resolution of slightly less than ten kilometers.

The model output includes the parameters: sea surface height above the geoid, mixed layer thickness, current velocities in x (eastward) and y (northward) direction, potential temperature and salinity. The last three parameters are available in three dimensions. The geoid is defined as the sea level for purely gravitational and centrifugal forces of only the earth for a non-dynamic ocean. The mixed layer thickness is the upper layer of ocean water where temperature and salinity, and thereby density, do not (or very little) change

over depth because of mixing due to wind and waves. For this dataset, the mixed layer thickness is defined as the depth at which density difference from the surface reaches 0.02 kg/m^3. Also ice parameters are available from the model output, but these were left out completely during this project given that it focusses on the Caribbean Sea. Tides are not included in the sea surface height data nor in the current velocities. Data are available from December 27th, 2006 until the present day, including a ten days forecast that is updated daily.

For obtaining the data, Mercator Ocean uses the ocean model NEMO version 3.1 [Madec and the NEMO team, 2008]. The wind forcing in the model is taken from the European Centre for Medium-Range Weather Forecasts (ECMWF) [Anderson, 2015]. For more detailed explanation about these models, see Appendix C.

Quality Information Documents have been produced and published by CMEMS for the different products. For the product used in this project, one year of hindcast data, 2015, has been compared to satellite and in-situ measurements to validate the Mercator Ocean model. The summarized results can be found in Table 3.1. This information is critical when assessing the reliability of the conclusions of this research.

The use of Mercator Ocean model is preferred for this project, for several reasons. The first reason is the high horizontal resolution in which the data is available. The currents on a relatively small scale are observed. Consequently, high resolution is required to be able for the data to contain and include the bathymetric details. A second reason is the timespan of ten years of the dataset. This timespan is large enough to be able to analyse interannual variation and yearly processes according to Thomson and Emery [2014]. Also the ocean model NEMO is a widely used model, that has been extensively validated ([Storkey et al., 2010], [Tonani et al., 2015], [Dombrowsky et al., 2009], [DrÃĭvillon et al., 2008], [Dee et al., 2014]).

3.1.2 Wind data

The European Centre for Medium-Range Weather Forecasts (ECMWF) - ERA Interim dataset ([ECMWF, 1975], [Dee et al., 2011] and [Anderson, 2015]) was used for wind data for the same ten years. This is also the dataset that is used by the Mercator Ocean model as input forcing. Long term monthly means from the National Centers for Environmental Prediction - National Centers for Atmospheric Research (NCEP-NCAR) reanalysis field on a 2.5° grid [Kalnay et al., 1996] were also used. This dataset provided means of a relatively long period, namely forty years.

3.1.3 Bathymetry data

Bathymetry data was used from the General Bathymetric Chart of the Oceans ([GEBCO, 2014] and [Weatherall et al., 2015]). The GEBCO_2014Grid dataset was used. This is a global bathymetry and topography dataset. It has a spatial resolution of 30 arc-seconds. It combines measurement data from ship depth soundings, interpolation between measurement points and gravity data derived from satellites.

Table 3.1: Deviation of parameter values in the Mercator data as calculated by the hindcast model from values measured in different ways for the year 2015 for the Tropical Atlantic Ocean. Misfit is defined as (measurement - model). The temperature over depth showed a mostly warm bias in the model. Root mean square of the misfits of the velocity is not available. From: Lellouche et al. [2016].

Parameter (depth)	**Mean misfit**	**RMS misfit**	**Measurement method**
Temperature (0-5 m)	-0.1 K	0.45 K	satellite
Temperature (0-5 m)	-0.05 K	0.40 K	in-situ profiler
Temperature (5-100 m)	-0.19 K	1.10 K	in-situ profiler
Temperature (100-300 m)	-0.11 K	0.73 K	in-situ profiler
Temperature (300-800 m)	-0.06 K	0.51 K	in-situ profiler
Temperature (800-2000 m)	0.01 K	0.12 K	in-situ profiler
Temperature (2000-5000 m)	-0.02 K	0.11 K	in-situ profiler
Temperature (0-5000 m)	-0.03 K	0.43 K	in-situ profiler
Salinity (0-5 m)	0.029 psu	0.229 psu	in-situ profiler
Salinity (5-100 m)	0.015 psu	0.170 psu	in-situ profiler
Salinity (100-300 m)	-0.012 psu	0.114 psu	in-situ profiler
Salinity (300-800 m)	-0.004 psu	0.051 psu	in-situ profiler
Salinity (800-2000 m)	0.002 psu	0.023 psu	in-situ profiler
Salinity (2000-5000 m)	0.0 psu	0.021 psu	in-situ profiler
Salinity (0-5000 m)	0.0 psu	0.061 psu	in-situ profiler
Sea surface height	0.49 cm	3.41 cm	satellite altimetry
Sea surface height	0.83 correlation	4.6 cm	tide gauges
Velocity (15 m)	0.10 m/s	-	in-situ of drifting buoys
Velocity direction (15 m)	5°	-	in-situ of drifting buoys

3.2 Method

3.2.1 Data analysis

The analysis is done by visualization of the data. Different formats are used for this. 2D surface plots of the entire region of interest for important parameters, such as velocities, temperature, sea surface height and salinity are made. This is done for the surface, but also at other selected depths. The surface plots that show daily values of the surface parameters are made into movies. Consequently, they are shown in chronological order, to gain insight in the variation over time and space.

Vertical sections and vertical profiles with temperature and velocity are plotted to gain insight in the distribution of these parameters over depth. A vertical profile is a profile over depth of the value of a certain parameter at a certain depth. A vertical section shows the value of a certain parameter over a transect (a horizontal line) and over depth. Consequently, it shows a vertical surface. Graphs that show a parameter, for example velocity magnitude, on the y-axis and time on the x-axis are made to indicate variation over time.

So called rose plots and stick plots are made to visualize velocity magnitude and direction in one figure. Rose plots show velocity direction, magnitude and frequency of occurence on a radial axis. Stick plots show velocity magnitude and direction over a certain transect or over time. In order to determine volume fluxes, the daily velocities are integrated over depth. These daily volume fluxes are plotted over time in order to highlight interannual and intra-annual variability.

3.2.2 Observation of large eddies

Eddy identification and observation is performed based on the surface plot movies of sea surface height and velocities. These plots have been analyzed by eye. Only eddies larger than 200 km in diameter that were generated below 15°N and existed for at least twenty days were taken into account. The parameters that are analyzed are: generation date, dissipation date or date that the eddy left the region of interest at 73°W, generation location and direction of rotation. The region of interest was specified in Figure 1.1. It was decided not to use an eddy tracker. Only the large scale eddies are assumed to have a big enough influence to affect an OTEC system. In addition, large scale eddies are easily detected by eye. Apart from that, eddy trackers can give incorrect output. Consequently, (visual) investigation is desirable anyway.

3.2.3 Pearson correlation analysis

For the data analysis, first an area large enough to cover the large scale oceanography is analyzed, see Figure 1.1. In addition, a smaller area around the island of Curaçao is also investigated. To understand and explain the visualized data, Pearson correlation coefficients were calculated to identify whether a correlation exists between two parameters. Pearson correlation coefficients are a measure for linear correlation between two

variables [Pearson, 1895]. It is a way of quantifying a forcing relation between different variables over a certain timespan, as has been done in Knudsen et al. [2014] and Mauas et al. [2008]. The Pearson correlation coefficient R is defined as:

$$R = \frac{cov(X,Y)}{\sigma_X \sigma_Y} \tag{3.1}$$

The covariance of dataset X and Y with size N, $cov(X,Y)$ can be calculated by:

$$\sum_{i=1}^{N}(x_i - \bar{x})(y_i - \bar{y}) \tag{3.2}$$

The standard deviation σ_Z of dataset Z with size N can be calculated by:

$$\sigma_Z = \sqrt{\frac{\sum_{i=1}^{N}(x_i - \bar{x})^2}{N-1}} \tag{3.3}$$

In the above equations, subscript i indicates the ith number in the dataset. The bar above a variable indicates its mean.

3.2.4 Force and bending stress calculations

Calculation of expected maxima and their return period is performed by statistical analysis of the data and the use of probability density functions. Force, moment and deflection estimation of the cold-water pipe based on the current profile is performed by calculation of hydrodynamic forces and the use of Euler beam theory. The drag equations are used to calculate the hydrodynamic forces on the system, with C being the drag coefficient, ρ the density in kg/m^3, A the area in m^2, v the velocity in m/s, which gives the force F in N.

$$F = \frac{1}{2} C \rho A v^2 \tag{3.4}$$

The example case of a 10MW offshore OTEC plant near Curaçao is used, with pipe material being HDPE, pipe diameters between 4.5 and 7 m and maximum pipe length of 870 m.

3.3 Focus of research

Physical ocean properties include more than just the current velocities. Parameters as temperature, salinity, sea surface height and mixed layer thickness are available in the data that are analysed. For the OTEC industry, temperature difference between the warm and cold water used, is one of the most important parameters, since that is directly related to the performance of a plant. In Appendix B, a Bluerise tool is described that assesses possible OTEC locations. The criteria for possible locations are average temperature difference between warm surface water and cold deep water, and bathymetry. Although that tool could be optimized, see the appendix, the main focus for this project will be the ocean currents and variability, since that is a largely unexplored research area.

Waves can exert large forces on offshore structures. However, waves, wave forces and wave generation mechanisms are not a part of this study. Waves are not included in the Mercator dataset that is used for this project. They were therefore not taken into account. This also applies to tidal waves; they are not included in the Mercator dataset and were not taken into account. Tidal currents were also not taken into account in this study.

The focus of this study is on the large scale parameters, and on the inter- and intra-annual variability of these parameters.

4

Description of the velocity patterns in the Caribbean Sea

In this chapter, first a general description of the current patterns over the year is given. Additionally, a general analysis of the yearly patterns of sea surface temperature is presented. This is an important part of this research, due to its relevance to OTEC, and because of the interaction observed between temperature and velocities. This is followed by a description of the generation and the presence of large eddies in the Venezuela Basin.

4.1 Seasonal variability of the sea surface currents

Surface velocity plots for the region of interest as described in Section 1.4 are analyzed for the years 2007 until 2016. Even though a yearly pattern can be found, there is quite a large seasonal (intra-annual) and interannual variability, which is also mentioned in Section 2.3 and by Johns et al. [2002]. Strong current velocities are found in the southern half of the Venezuela Basin below, 15°N, a fast-current jet originating at the Grenada Passage in the southeast of the Caribbean Sea at 62°W, 12°N. This southern jet is described by Fratantoni [2001] and Centurioni and Niiler [2003]. The path and intensity of this jet has been observed to vary over the year, related to wind speed and direction.

The jet is directed west, along the Venezuelan coast, with high velocities of on average 0.6 m/s from mid-December through to the end of March. Generally, westward winds are strongest in this period of the year. These westward winds drive the volume transport to the west, due to the negative wind stress curl, as depicted in Figure 4.1a. In these months, coastal upwelling along the Venezuelan coast is most evident, see Section 4.3 for evidence of this and more details on temperature distribution over the year.

Starting in April, the southern fast-current jet turns to the northwest and starts meandering through the Venezuela Basin. This was observed in the daily surface plots. Figure 4.1d shows slightly lower velocities in the southern jet and a wider 'jet', compared to Figure 4.1b. Jet velocities decrease to an average of 0.5 m/s. This transition time has proven to be the most prone to the generation of large anticyclonic eddies. Section 4.4 discusses the large eddies in the Venezuela Basin in more detail.

In autumn, from October to halfway in December, the overall velocities throughout the entire Venezuela Basin are smaller, and the jet is less distinct with an average velocity of 0.4 m/s, see Figure 4.1f. A large variability in flow direction is seen, along with a large number of small eddies, that rotate in both directions and exist for short periods of time (a couple of days). In this period, eastward flowing currents are sometimes found along the Venezuelan coast. Wind speeds are lowest in this period.

The path of the jet follows the line of strong sea surface height gradient. Along the coast of Venezuela, a negative sea surface height area can be found most of the year. On the other hand, a positive sea surface height is found in the rest of the basin. A relaxation of this sea surface height gradient occurs from October to December, and coincides with the decrease of the overall and jet sea surface velocities.

The northern jet at 17°N, as described by Centurioni and Niiler [2003] and Richardson [2005], could not be observed in the daily surface plots. However, when considering the mean surface plots in Figure 4.1, a slight accelaration of the current can be seen at 17.5°N. Particularly from 70°W and further west, this is visible.

Precipitation and river run-off influence the salinity of the sea water. No precipitation data was analyzed. The reason for this is that river run off is found to be of significantly larger influence on the sea surface salinity. Surface salinity plots showed biggest variations due to river run-off from the Orinoco and Amazon river transported into the Caribbean Sea by the Guiana Current. These influences were greatest in the west of the Caribbean Sea. The large fresh-water ligaments extend up to 70 °W and are advected by the southern jet of the Caribbean Current. An overview of the analysis of the different surface parameters in the Mercator dataset is given in Appendix D. It was used as a means of coming to an understanding of the seasonal variability in the region of interest.

4.2 Seasonal variability of the wind speed

The seasonal variability of the wind speed can be seen in Figure 4.2. This plot shows the long term mean of the wind speed over the southern part of the Venezuela Basin. The data shows a semiannual signal, with a maximum in February and a minimum in October. A local minimum is found in May and a local maximum in June. The colored areas indicate the three periods described above. The first period is from December to March, when highest surface current velocities are found. This coincides with the peak in wind speed. The second period includes the two local peaks, where wind and current speeds are in between the two extremes. The last period, from September to November, shows lowest wind speed, and lowest current speed. This semiannual cycle of the Caribbean Low Level Jet was also described in Section 2.4 and by Wang [2007]. The

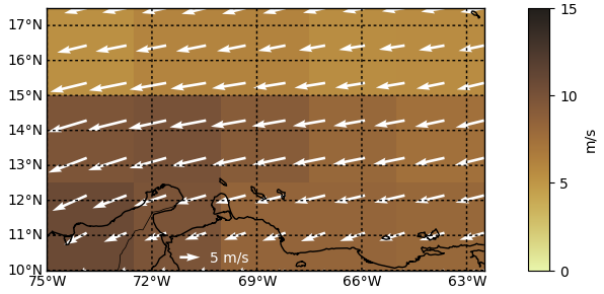

(a) Long term mean winds from December to March.

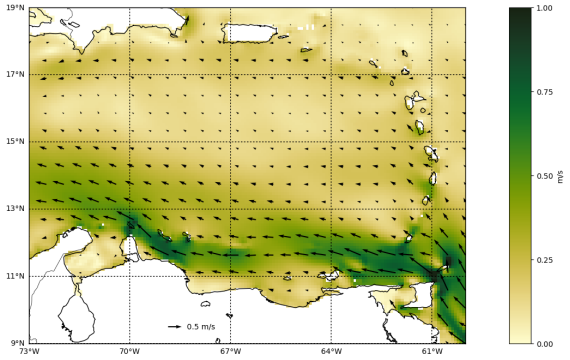

(b) Long term mean velocities from December to March.

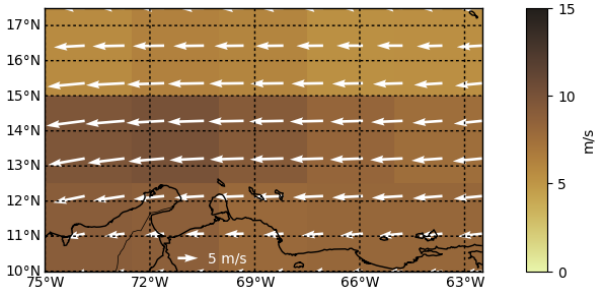

(c) Long term mean winds from April to August.

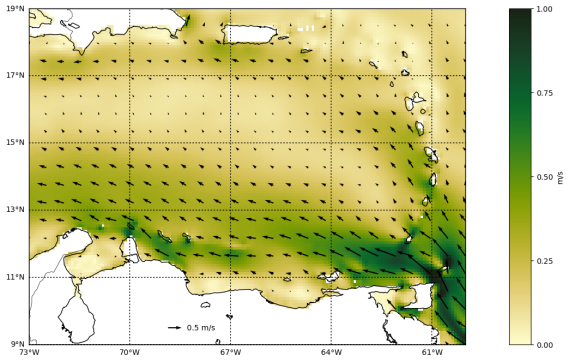

(d) Long term mean velocities from April to August.

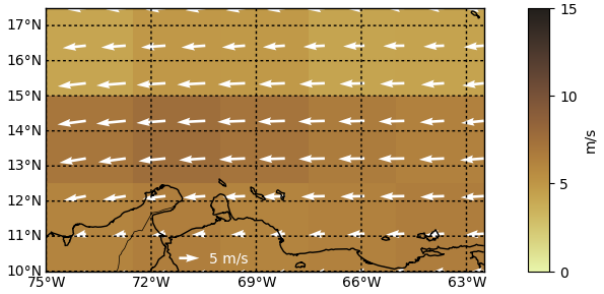

(e) Long term mean winds from September to November.

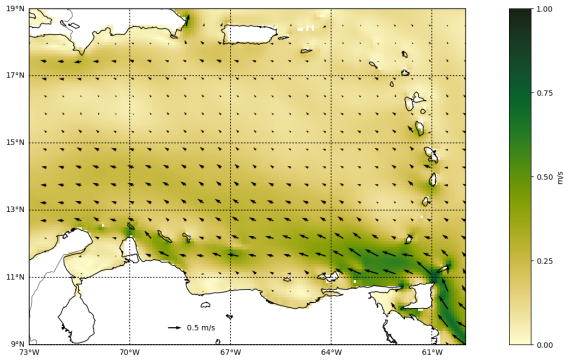

(f) Long term mean velocities from September to November

Figure 4.1: The mean over the ten years of data of winds and currents over the Caribbean Sea for three different periods. Wind data from the ERA Interim dataset [Kalnay et al., 1996].

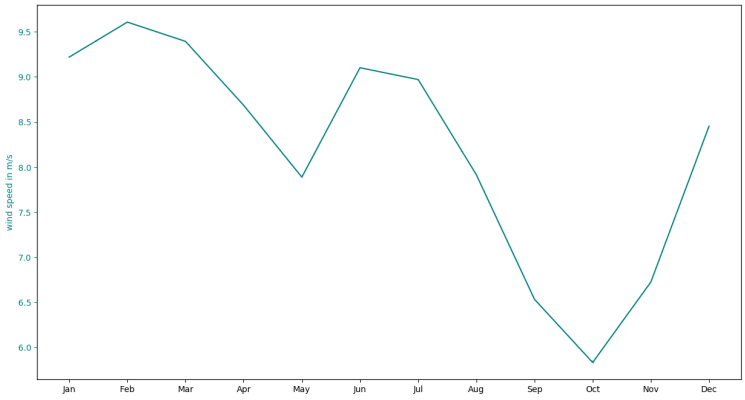

Figure 4.2: The long term mean of the wind speed along the coast of Venezuela over forty years. The colored areas indicate the three periods described in Section 4.1. Data from Kalnay et al. [1996].

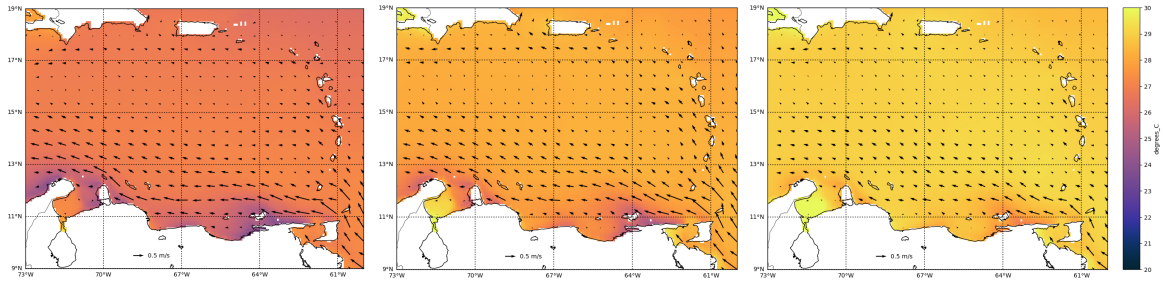

(a) December to March. *(b)* April to August. *(c)* September to November.

Figure 4.3: The mean over the ten years of data of sea surface temperature and currents of the Caribbean Sea for three different periods.

long term mean direction of the wind speed is between 250 and 270°, with 0° pointing northwards and positive to the east. This can be seen in Figure J.21. This figure shows the long term mean of the wind and current direction.

4.3 Seasonal variability of the sea surface temperature

Temperature and current velocities are interrelated, since water with a certain temperature is advected due to the currents. Additionally, a horizontal temperature difference enhances a vertical shear. Coastal upwelling along the entire Venezuelan coast is most intense in December to March, because of the winds, as concluded by Andrade and Barton [2005] and indicated in Section 2.5. The fast-current jet follows the cold-water front that arises because of the upwelling, see Figure 4.3a. The path of the jet is diverted towards the west and magnified by this cold-water front that causes vertical velocity shear due to the Thermal Wind Balance, see Equation 4.3 and 4.4. Consequently, the jet is intensified by the coastal upwelling. In Figure 4.4, it can be seen that in winter. the horizontal temperature difference is highest, as the line dividing cold deviation and warm deviation is sharpest in that period.

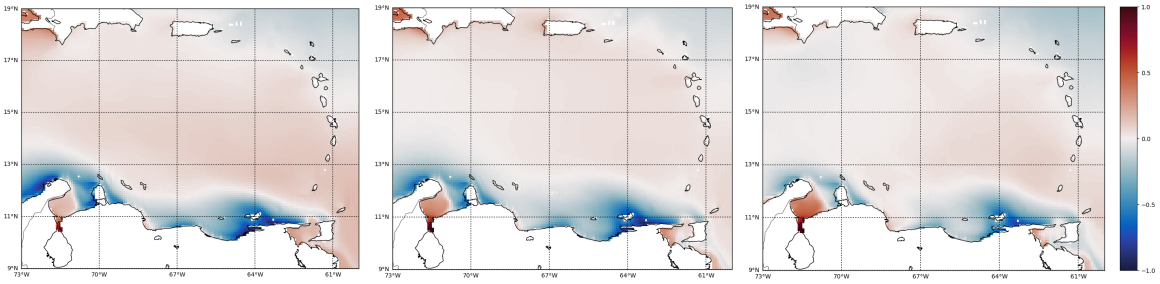

(a) Dec to March. **26.6°C** (3.2°C) *(b)* April to August. **28.1°C** (3.6°C) *(c)* Sept to Nov. **29.0°C** (2.6°C)

Figure 4.4: Unified temperature deviation from the long term mean. The long term mean is indicated in bold with the value of the maximum deviation in brackets.

From April to August, this upwelling is less intense, which allows the current to be diverted more towards the northwest. The upwelling region at 63°W, 11°N is still prominent and gives rise to large baroclinic instability. It corresponds to the location where most large anticyclonic eddies start to form, see Section 4.4. September, October and November are the months in which the sea surface temperature is highest and most uniform. This is also seen in Figure 4.4c. This, together with generally low wind speeds, explains the relatively calm sea surface in Figure 4.1f.

The intensification of the jet can be explained qualitatively by the Thermal Wind Balance and the Geostrophic Balance. The Geostrophic Balance is:

$$fv = \frac{1}{\rho}\frac{\partial p}{\partial x} \tag{4.1}$$

$$fu = -\frac{1}{\rho}\frac{\partial p}{\partial y} \tag{4.2}$$

In the above equations, f is the Coriolis parameter in rad/s, u and v are water velocities, in x and y-direction respectively, and ρ is water density in kg/m^3. The Coriolis parameter f depends on the Earth's rotation speed Ω, and latitude ϕ by $2\Omega \sin \phi$.

The Geostrophic Balance balances a horizontal pressure gradient $\partial p/\partial x$ by the Coriolis effect. The Ekman transport is directed to the north, due to the westward direction of the wind. In other words, surface water is transported offshore. Therefore, the sea surface height has a north-south slope, with a higher sea surface height found further offshore. This can be seen in Figure D.5a, a surface plot of the sea surface height in the Venezuela Basin. A slope in the sea surface corresponds to a hydrostatic pressure difference. This pressure gradient causes water to flow from the higher pressure in the north, towards the lower pressure in the south. This flow is directed to the right, in this case to the west, by Coriolis effect. Thereby, the westward jet of the Caribbean Current is intensified.

This intensification by the Geostrophic Balance is is most frequent in winter months, since it is related to the sea surface height slope. Figure D.6 and Figure D.9 show the sea surface height variations over time and over the ten years of data. It can be seen that the sea surface height near the coast is lowest around January and highest around October. The sea surface height away from the coast does not show this variation and is generally higher. Consequently, the sea surface height slope is steepest in the winter.

The Thermal Wind Balance is:

$$\frac{\partial u}{\partial z} = \frac{g}{f\rho_0}\frac{\partial \rho}{\partial y} \tag{4.3}$$

$$\frac{\partial v}{\partial z} = -\frac{g}{f\rho_0}\frac{\partial \rho}{\partial x} \tag{4.4}$$

The Thermal Wind Balance follows from the Geostrophic Balance and the Hydrostatic Balance. The Hydrostatic Balance or Hydrostatic Equilibrium relates pressure p to the product of density ρ, gravitational constant g and height h. The Thermal Wind Balance implies that a horizontal density gradient $\partial\rho/\partial y$ causes a vertical geostrophic velocity gradient $\partial u/\partial z$. Density is dependent on temperature. A temperature rise causes the water to extend, thereby causing a decreasing density. A horizontal temperature gradient, as caused by upwelling, induces a vertical velocity gradient. The other parameters in Equations 4.3 and 4.4 are the constants: gravitation acceleration g in m/s^2 and Boussinesq approximated density ρ_0 in m^3/s. The Boussinesq approximation assumes that density, in accelaration terms, is constant.

Equation 4.3 shows a relation between flow in eastward direction u and a north-south density difference $\partial\rho/\partial y$. Upwelling induces a north-south density difference, due to the north-south temperature difference. Consequently, the flow in westward direction at the surface is intensified by this balance.

Appendix E elaborates on the Geostrophic Balance and the Thermal Wind Balance. A qualitative and quantitative analysis of the two balances is performed for one day with clear upwelling and a clear north-south sea surface height slope. The quantitative analysis yields a westward velocity of 0.5 m/s due to the north-south pressure difference. The westward velocity due to upwelling is 0.2 m/s. No interaction between these two processes is studies.

In summary, the wind has two types of impact on the water. Firstly, friction causes motion of the water in an offshore direction. This causes a north-south sea level difference, with a lower sea surface height to the south. Figure D.5a shows the surface plot of sea surface height in the Venezuela Basin. This drives a geostrophic current to the west. Secondly, colder water being upwelled to the surface, generates a density difference, which drives a jet following the cold-water front.

4.4 Existence and generation of eddies in the Venezuela Basin

Eddies are a large source of variability of sea surface currents and temperatures in the Caribbean Sea. Figure 4.5 shows the possible size and impact of these eddies in the Venezuela Basin. They can be several hunderd of kilometers in diameter and the cause advection of water masses and large velocities. Large, anticyclonic and persistent eddies have been observed and analyzed in the years 2007 to 2016. Results and method of this analysis can be found in Appendix F. From the analysis, it was calculated that the average advection of the large anticyclonic eddies through the Venezuela Basin was 0.12

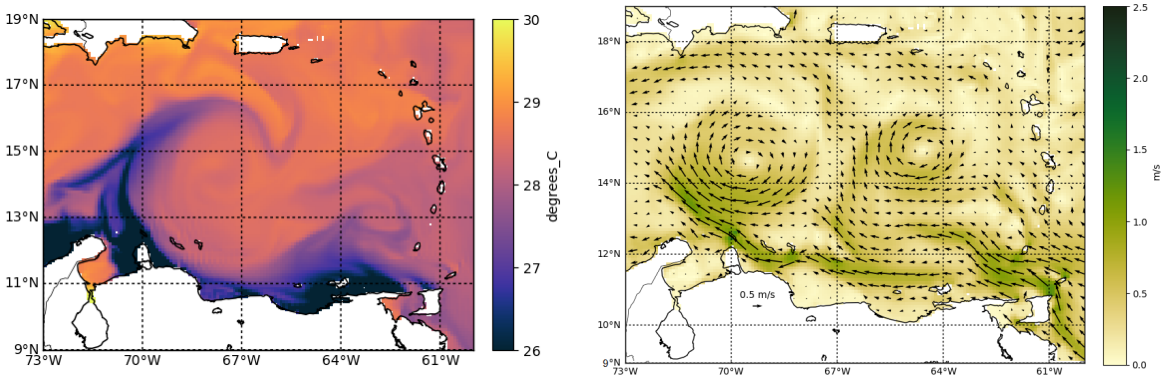

(a) Sea surface temperature on July 13th, 2007, when a large cold-water ligament extended up to 17°N.

(b) Sea surface currents on July 10th, 2016, when current velocity was up to 1.5 m/s.

Figure 4.5: Snapshots of sea surface temperature and velocity to show the consequences of eddies.

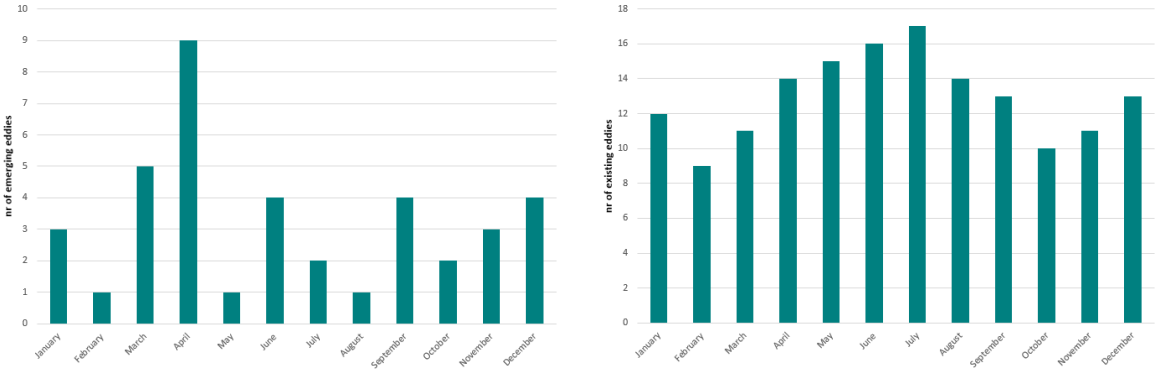

(a) Number of eddies that emerged per month.

(b) Number of eddies that existed per month.

Figure 4.6: Eddies analyzed to have emerged or existed per month for the period between January 2007 and December 2016. 4.6b matched with the results of Jouanno et al. [2012].

m/s during this period. Additionally, an average of five large anticyclonic eddies per year were identified.

In April, a peak in eddy generation can be seen in Figure 4.6a. This figure shows the number of emerging eddies per month, for the years 2007 to 2016. The peak in April corresponds to a period with diminishing wind and current speeds, while a horizontal temperature gradient still exists due to upwelling. Since only large eddies (diameter > 200 km) were detected, the generation and favorable conditions for the generations of these eddies may be some time earlier than depicted in Figure 4.6a.

Figure 4.6b shows the amount of eddies that existed each month for the ten years of data. Consequently, if an eddy existed from April to August, one existing eddy is added to April, May, June, July and August. A semiannual cycle in eddy population can be seen in this figure, with peaks in January and July. This corresponds to the semiannual cycle in wind and current speed.

Jouanno et al. [2012] relates the mean kinetic energy (MKE) to the eddy kinetic energy (EKE) where a peak in EKE follows a peak in MKE. The seasonal variation of the currents in its semiannual cycle results in a semiannual cycle in EKE, with a peak

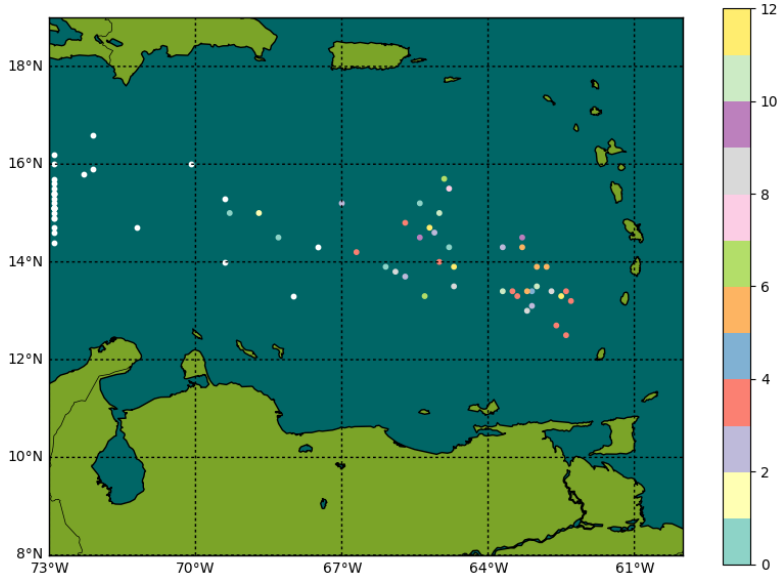

Figure 4.7: Emergence and dissipation location of the centers of the eddies observed. Origin location is in pastel colors ranging from January (lightblue) to December (yellow). Dissipation location is in white. Dissipation at 73° W indicates that the eddy left the region of interest at that position so could no longer be tracked. The method for the eddy observation can be found in Appendix F.

between May and August. This data corresponds to the data in Figures 4.6a and 4.6b. This semiannual cycle in EKE was related to semiannual cycle in the CLLJ (the wind jet). Furthermore, Jouanno et al. [2012] suggests that, Caribbean eddy activity variation appears to be related to local processes along the South American coast, while NBC rings act as pertubations and thus as triggers.

The interaction between coastal upwelling and eddies seems two-way. Firstly, the large eddies can transport the filaments of cold water up to 17°N as seen in Figure 4.5a. Secondly, where the temperature gradient is strongest, the vertical shear will be strongest and a horizontal shear arises. High velocities enter the Caribbean Sea through the Grenada Passage. Due to the presence of this horizontal shear, instabilities in the flow will occur, that give rise to eddy generation. The upwelling system at 63°W, 11°N is very prominent, especially in winter. Figure 4.7 shows the location of the emergence of the eddies observed. Most eddies emerge close to the high-velocity inflow through the Grenada Passsage and also close to the upwelling system at 63°W, 11°N. The average trajectory of the eddies clearly coincides with the general direction of the current in the Venezuela Basin. No eddies emerged at the 64°W line in all ten years.

The depth extent of some eddies is shown in Figure 4.8. The figure shows a vertical section of eastward velocities, and the corresponding surface plots of surface velocities, where the location of the vertical section is also indicated. A sharp increase in velocities due to the presence of these eddies, does not extend below 100 m of water depth.

The annual eddy cycle can be summarized as follows. In winter, high wind speeds give rise to high current velocities in the Venezuela Basin and upwelling along the coast. From Figure 4.4a, it can be seen that the horizontal temperature gradient along the coast is strongest in boreal winter. The direction of flow is forced by the wind and follows the cold-water front formed by upwelling. These circumstances correspond to high

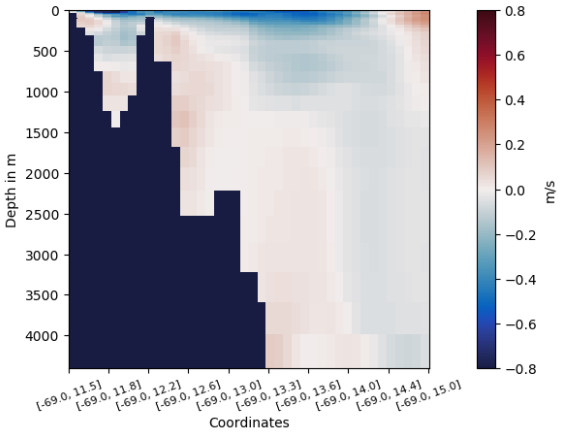

(a) Vertical section of July 22nd, 2012.

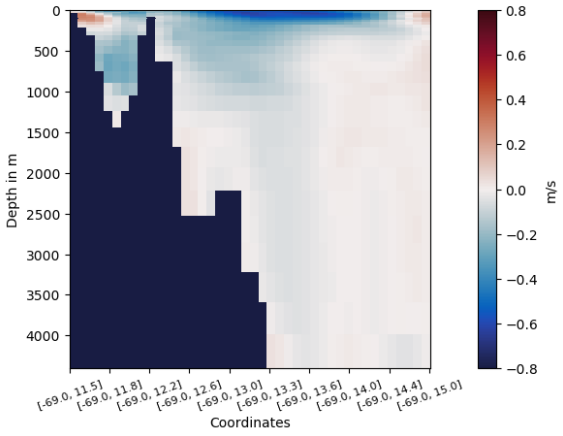

(b) Vertical section of August 8th, 2014.

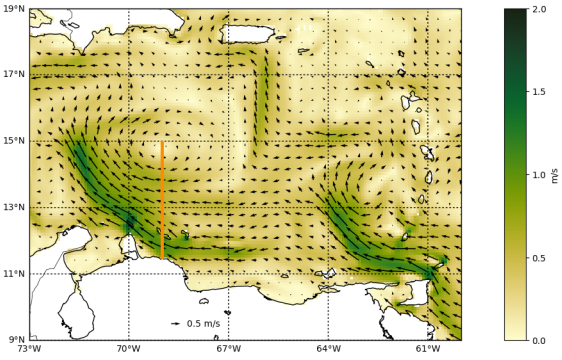

(c) Surface plot of July 22nd, 2012.

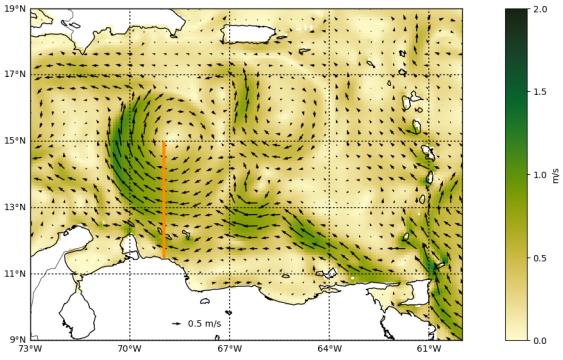

(d) Surface plot of August 8th, 2014.

Figure 4.8: Vertical sections (4.8a and 4.8b) and according surface plots (4.8c and 4.8c) of days when an eddy was present at 69° W to show the depth extent of the eddies. The location of the vertical sections is indicated by the orange line in the surface plots.

baroclinic instability and provide favorable circumstances for eddies to form. However, this analysis does not provide a conclusion as to whether the eddies are formed locally or are continuations of the NBC rings or are the result of a combination of those two things.

In April, wind speed diminishes. As a result, current velocities become lower and upwelling decreases. The fast-current jet turns towards the northwest and starts meandering. Eddies are known to originate from meandering flows, as happens in the Gulf Stream [Kang and Curchitser, 2013], since this is an indication of flow instability. The large anticyclonic eddies are generated by instabilities in the mean flow. These instabilities arise from the high velocities caused by the cold-water front, that is formed by upwelling. Since the wind has a semiannual cycle, a similar series of events happen around August, when wind speed decreases. This peak is, however, smaller and less visible in eddy generation in Figure 4.6a. However, it is visible in the peak in existing eddies in January in Figure 4.6b.

An overview of the results of the performed eddy identification and observation is given in Appendix F.

4.5 Application to OTEC

The relevance for OTEC operation of above described processes, lies in the water velocities, temperature distribution and advection of water masses. This is also mentioned in Section 1.1. Surface temperature advection can have an influence on the system's performance. The reason for this is that the performance of an OTEC system depends on the temperature difference between water at the warm water inlet (roughly at the surface) and water at the cold water inlet (roughly at a kilometer deep). In particular on the south side of the island, lower performance due to upwelled advected water is a risk. Location assessment of an OTEC plant around Curaçao should take the upwelling and current velocities into account.

Flowing water exerts a drag and friction force on structures, that are in its path. The magnitude of the force is determined mostly by the speed of the flowing water and shape of the structure. The direction of the velocities, together with the shape and movement of the structure, determine the direction of the force.

By identifying periods with generally higher or lower velocities, an advice can be given as to when to install the OTEC system. Lowest current velocities are seen in September to November, and highest in December to March. Highest variability is seen in the period in between. Low current velocities are desirable for an installation process, because it will simplify the procedure. However, the period with lowest current velocities coincides with the hurricane season. Hurricanes, however, are predictable up to a week in advance, and are therefore unlikely to form a big risk. Other than that, most hurricanes pass north of Curaçao.

4.6 Summary

In this chapter, the intra- and interannual variation of sea surface temperature and velocity is assessed. It is found that wind velocities are largest in the boreal winter months, from mid-December to March. They go in westward direction, parallel to the north coast of Venezuela, in the south of the Venezuela Basin. This causes the westward currents in that area to be largest in this period as well. Also coastal upwelling is most pronounced in these months. The presence of upwelling intensifies surface currents in westward direction in the south of the Basin, due to the Geostrophic Balance and the Thermal Wind Balance. The combination of the strong jet and the horizontal temperature difference allow for instabilities to arise and large anticyclonic eddies to emerge. These eddies can advect water for hundreds of kilometers and are the cause of large local and temporal surface velocities.

5

Surface velocity patterns around Curaçao

The previous chapter, Chapter 4, mainly discussed the general current pattern in the entire Venezuela Basin. This chapter zooms in on the vicinity of Curaçao to be able to quantify the current velocities that are found in that region. Firstly, definitions of different regions are given. Then, the seasonal variability of the sea surface currents is discussed. Thirdly, it is demonstrated that the surface currents are highly correlated to the wind. Lastly, the local influences of eddies on the surface currents is presented.

5.1 Definition of the regions on a transact over Curaçao

Curaçao is situated 50 km from the mainland of Venezuela. High current velocities are observed to the south of the island, see Figure 4.1b. The current velocities around the island are influenced by the bathymetry of the region shown in Figure 2.4. Since the current velocity in the Caribbean Sea is mostly from east to west, a transect is drawn from southwest to northeast of the island, see Figure 5.1a. In this way, the channel formed between Curaçao and the mainland is fully covered by the transect. A distance of the same length on the other side of the island is covered. This transect is chosen because in this way the main direction of the flow is perpendicular to the transect. Also, economically viable OTEC locations will not be outside of the radius of the currently chosen transect (this radius is 100 km). Consequently, possibly suitable OTEC locations are within the scope of the region.

Different regions, within which the flow behaves in a similar way, can be identified from stick plots as in Figure 5.1b. Local bathymetry is the main cause for the existence of these regions. The first region is the more or less sheltered region in the most southwestern part of the transect and the most left part of the stick plot. From the local bathymetry (the brown line in Figure 5.1b), it can be seen that in this part of the transect is shallow

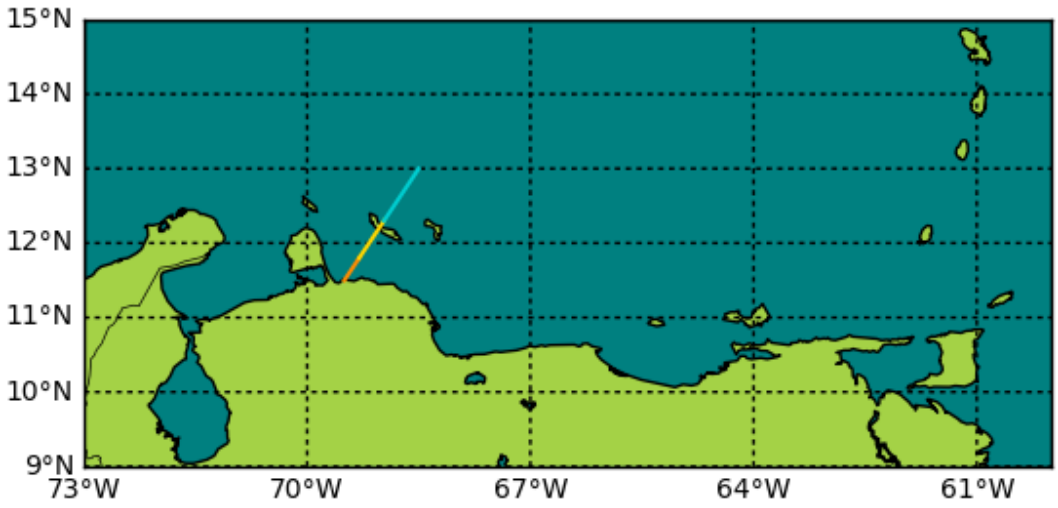

(a) The transect starts at [69.5° W, 11.5° N] in the southwest and ends at [68.5° W, 13.0° N] in the northeast.

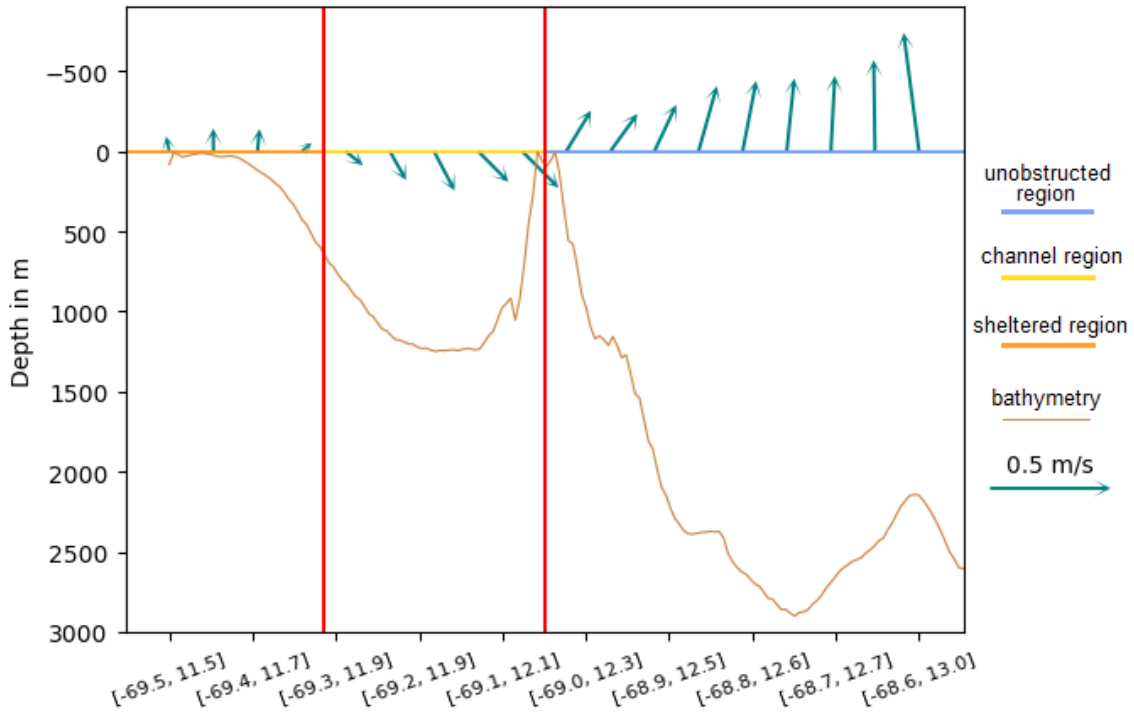

(b) Stick plot of the transect as indicated in figure above. This plot shows the surface current velocities on December 2nd 2011. This date is chosen to show the variability of the currents over the different regions of the transect. Also indicated by the brown line in the figure is the water depth in meters.

Figure 5.1: Transect over which the velocities around Curaçao are analysed. It is divided into three regions as indicated by the colors and explained in Section 5.1. From left to right; sheltered (orange), channel (yellow) and unobstructed (blue) region.

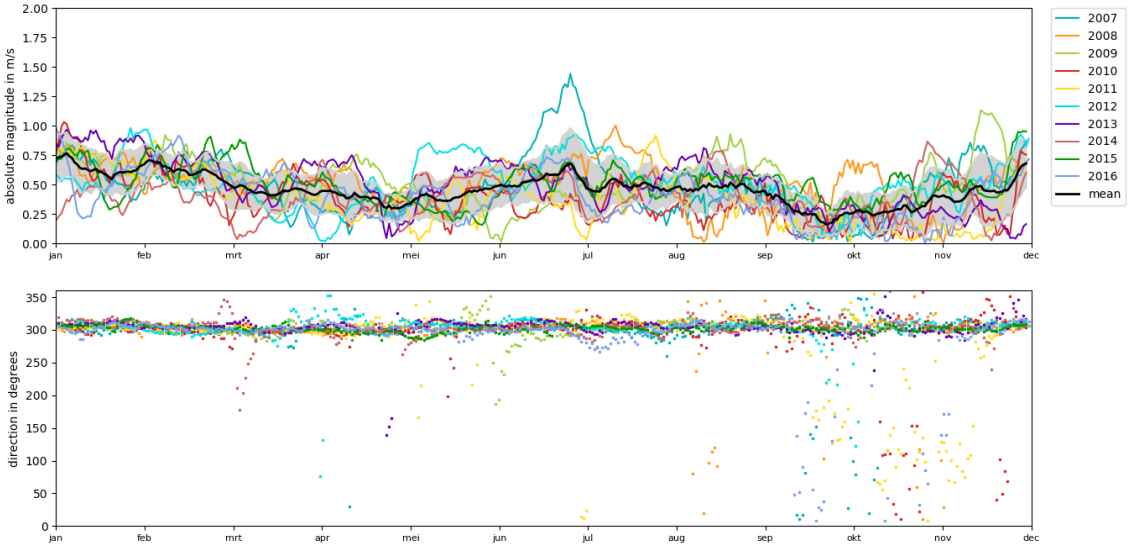

Figure 5.2: Velocity magnitude (upper pannel) and direction (lower pannel) averaged over the line from the coast of Venezuela to the island of Curaçao (channel region and sheltered region together) for the years 2007 until 2016. Appendix G includes plots the years apart for overview. This can be found in Figures G.1 to G.10. The mean of the magnitude is plotted in black and the standard deviation is plotted in the grey areas. The direction is plotted in degrees, with 0 degrees defined as north and positive towards the east.

(max 600 m). Moreover, the local ocean is sheltered in between two land masses that stick out into the sea and restrict the flow from entering this region. This part of the transect is called the **sheltered region**.

The second region is the deep part of the channel southwest of Curaçao where the surface current velocities are very high. This part of the region is called the **channel region** and has a maximum water depth of around 1000 m.

The last region is the part of the transect that is northeast of the island. It is regarded as one region, since the bathymetric features or land causing forcing of the flow are much less pronounced. This part of the transect is called the **unobstructed region**. The maximum water depth is almost 3000 m.

5.2 Seasonal variability of sea surface currents around Curaçao

The velocities, magnitude as well as direction, in the channel region between Curaçao and the mainland are plotted in Figure 5.2. The magnitude varies up to a maximum in 2007 of almost 2.0 m/s. The mean of the magnitude (the bold black line) appears to have a semiannual cycle, with a minimum around April/May and an even smaller minimum around October. The maxima are found in December/January (global maximum) and June/July (local maximum). This coincides with the peaks in wind speed. However, highest variability and highest standard deviation is found from May to September. The standard deviation is calculated as described in Equation 3.3.

There is a general direction of the current through the channel. It is about 300°, where 0° is defined northwards and positive is to the east. This corresponds to a general west-northwest direction. Very distinct are the backflow events that occur almost every year, especially in late autumn and early winter, from October to December. These backflow events coincide with very low velocities, generally below 0.2 m/s. The reversal of the current extends for short periods of time, one to forty days per event. This can be seen in Appendix H. This appendix shows an overview of identified backflow events in the channel in the years 2007-2016.

From halfway September until the end of December reversal of the current is very frequent. This period coincides with the time period of the lowest wind speed. In contrast, in January and February no reversal in all ten years is observed. A reversing current coincides with small magnitudes of the current. The period from March until September is more variable. Every year from 2007 until 2016 has one event of reversing currents in the channel in that period with the exception of 2015 and 2011, which had respectively none and two events. The timing of those events is evenly spread out over this period with a small intensification around May/June.

Magnitudes on the opposite site of Curaçao in the unobstructed region are lower as their mean lays around 0.3 m/s, but also display maxima in July/August and December/January. The direction is less uniform, but still generally west to northwest. The period prone to reversal of the current is slightly shifted, from August to November. Again, reversal seems to correnspond to low velocities. Figure 5.3 shows the surface velocities in the unobstructed region.

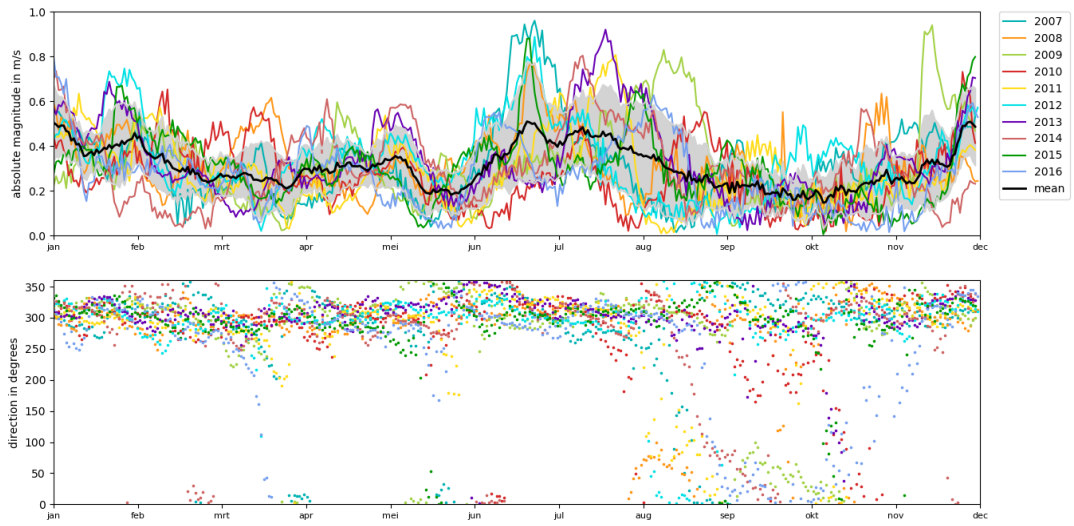

Figure 5.3: Velocity magnitude (upper pannel) and direction (lower pannel) averaged over the transect line, the unobstructed region, for the years 2007 until 2016. The mean of the magnitude is plotted in black. Figures G.11 to G.20 show plots of surface velocity in the unobstructed region per year. The direction is plotted in degrees, with 0 degrees defined as north and positive towards the east.

For both regions, a semiannual cycle can be identified. This is in accordance with the general velocity pattern that was found in Section 4.1 and what has been found in literature for wind [Wang, 2007] and mean kinetic energy [Jouanno et al., 2012].

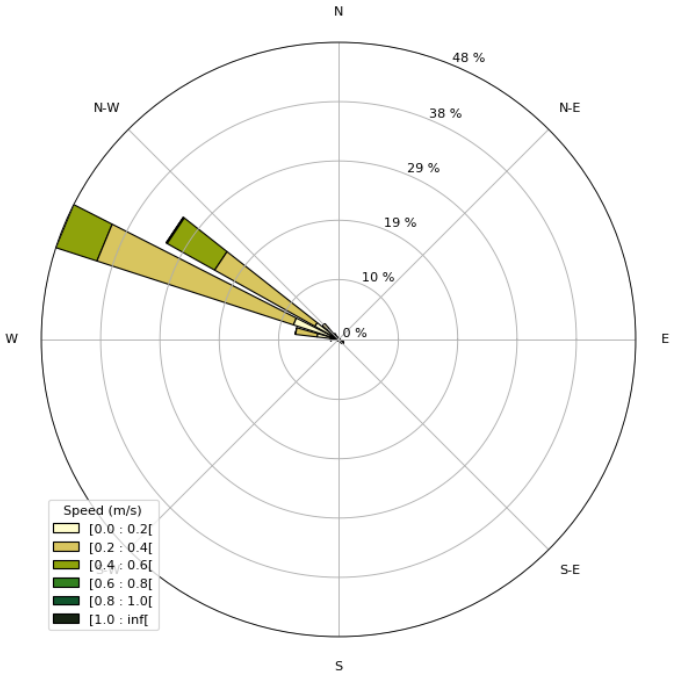

Figure 5.4: Rose plot of surface current velocity in the sheltered region for all data. Sheltered region is defined as [69.5° W, 11.5° N] to [69.43° W, 11.6° N]. Corresponding bar graph can be found in Figure J.3.

5.2.1 Sea surface currents displayed in rose plots

Another intuitive way of displaying current velocities, directions and occurrence is in a so called rose plot, see Figures 5.4 to 5.8. All rose plots include the data from 2007 until 2016. On the radial axis, occurrence of current speed and direction in percentages is displayed. The polar axis indicates the direction in which the current in flowing. The indication N stands for north, and is defined as 0°. Positive is to the east, so E equals 90°and so on. The circle is divided into 32 bins, so each bin is 11.25°. The colors in the bars indicate the velocity magnitude range in m/s and the length of the colored bars indicate percentage of occurence. The velocities are averaged over part of the transect; the sheltered, channel or unobstructed part.

From the rose plots, it can be concluded that surface velocities are highest and most unidirectional in the channel region, see Figure 5.5. The average velocity in the channel region is 0.51 m/s. The direction is generally northwest, 85.2% of the data is in a 33.75° N-W bin, from 287° to 321°. The current in the unobstructed region in Figure 5.6 is less unidirectional, only 46.9% of the data is in northwestern direction. Also velocities are lower, on average 0.31 m/s. The sheltered region has an even lower average velocity, 0.28 m/s, and the water is directed to the west-northwest. Also the velocities in the sheltered region are unidirectional since 86.9% is within a 33.75° bin.

Corresponding bar graphs of all displayed rose plots can be found in Appendix J. These bar graphs show the current direction on the x-axis and the occurence in percentage on the y-axis, represented in a non-radial manner. This allows for better representation of the directions that have low percentages.

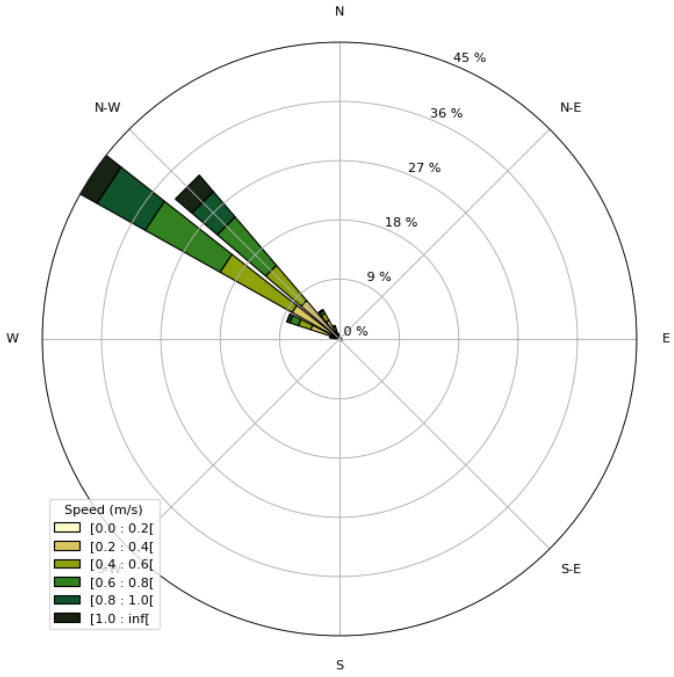

Figure 5.5: Rose plot of surface current velocity in the channel region for all data. Channel region is defined as [69.43° W, 11.6° N] to [69.03° W, 12.2° N]. Corresponding bar graph can be found in Figure J.4.

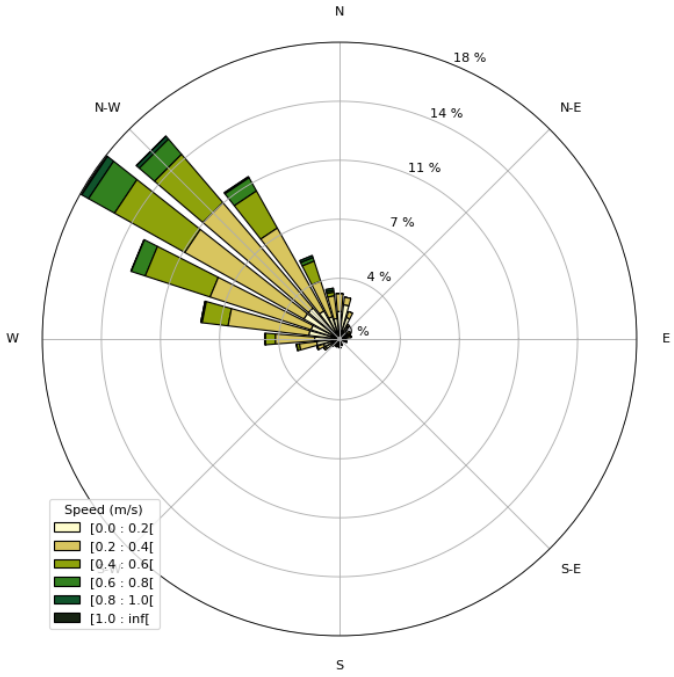

Figure 5.6: Rose plot of surface current velocity in the unobstructed region for all data. Unobstructed region is defined as [69.03° W, 12.2° N] to [68.5° W, 13.0° N]. Corresponding bar graph can be found in Figure J.5.

5.2.2 Seasonal variability of sea surface currents displayed in rose plots

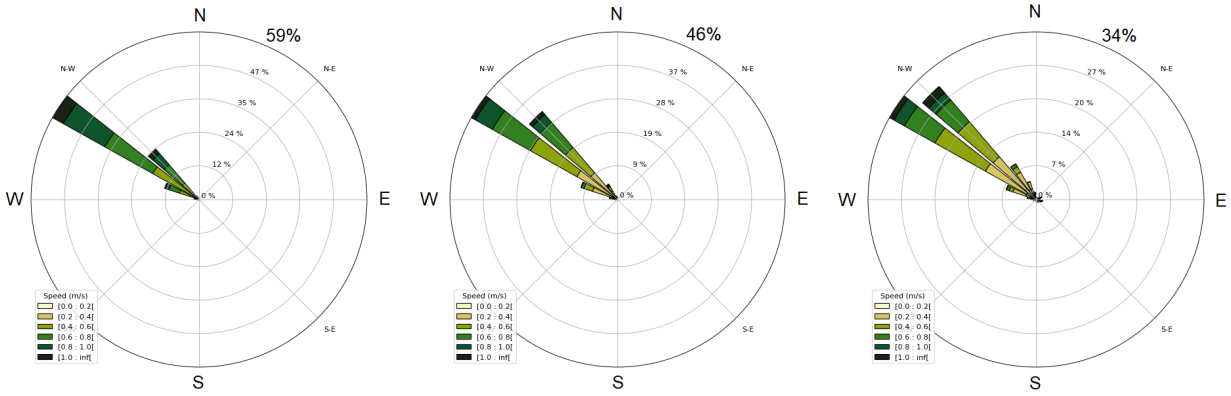

(a) January to March. *(b)* April to August. *(c)* September to December.

Figure 5.7: Rose plots of surface current velocity in the channel region for all three periods. Channel region is southwest of Curaçao. Corresponding bar graphs can be found in Figure J.6.

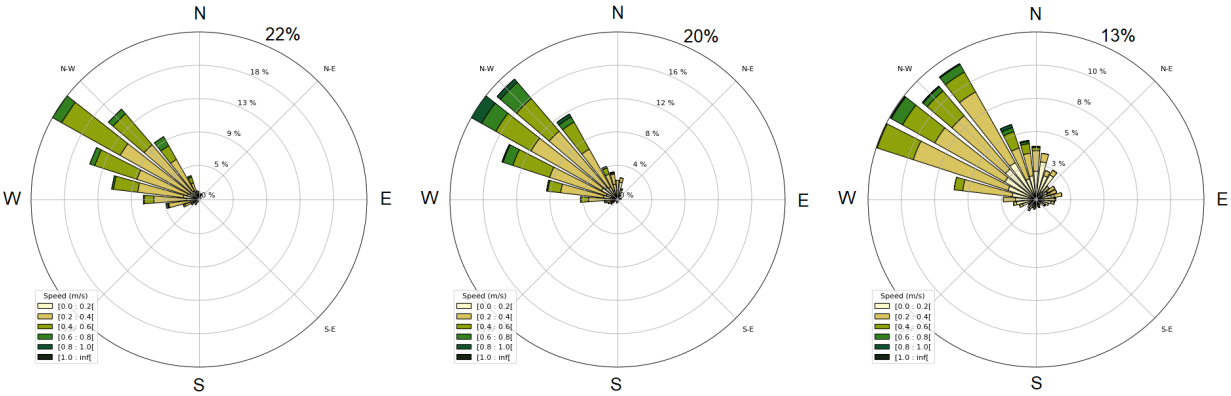

(a) January to March. *(b)* April to August. *(c)* September to December.

Figure 5.8: Rose plots of surface current velocity in the unobstructed region for all three periods. Unobstructed region is northeast of Curaçao. Corresponding bar graphs can be found in Figure J.7.

Periods of similar situations in direction and magnitude of the current can be identified and plotted. These periods are chosen in accordance with the periods described in Section 4.1 and based on visual inspection of the velocities plotted over time in the channel region, Figure 5.2. A similar pattern is found with high extremes in the winter months December, January and February, low extremes in September, October and November and medium velocities in the months in between. Subsequently, the three periods that are identified are: 1) December to March are defined as the first period with relatively high velocities and few backflow events, 2) April to August with lower velocities and incidental backflow events and 3) September to November with very low speeds and regular reversal of the current.

For the surface velocities, above assumptions about the three periods and three regions give the following results in the Figures 5.7 to 5.8. From the rose plots can be concluded

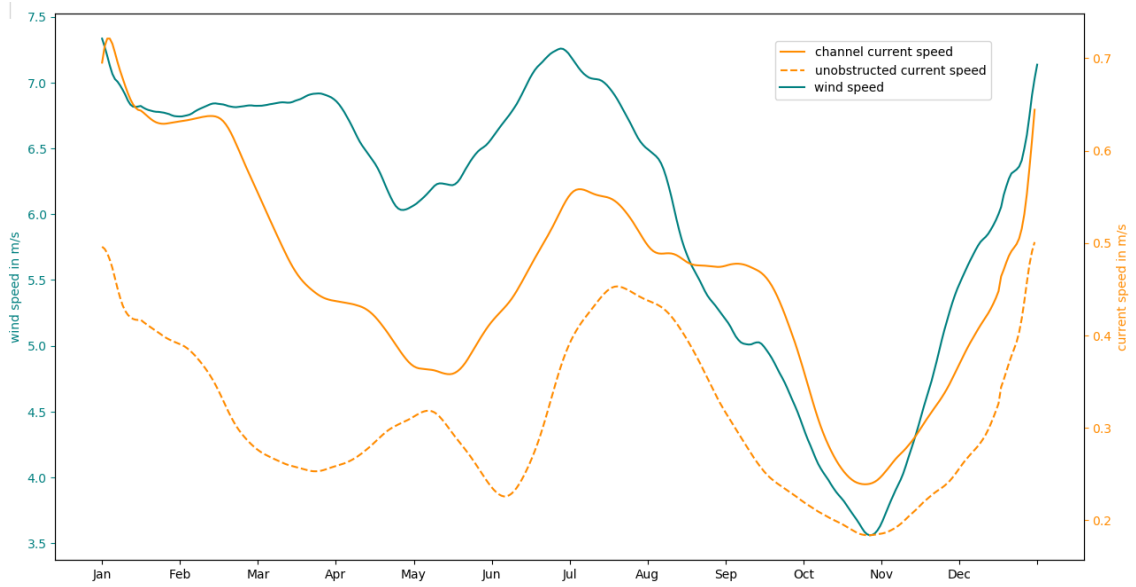

Figure 5.9: Annual cycle of long term mean of wind speed and surface current speed values. Wind speed is in blue and values are on the y-axis to the left. Surface current speeds are in orange and values are on the y-axis to the right. The dotted orange line is for the unobstructed region, the uninterrupted orange line is for the channel region. The uninterrupted orange line in this plot is identical to the black line in Figure 5.2, except that it is a 30 day rolling average to smooth the line. Wind data from the European Centre for Medium-Range Weather Forecasting [ECMWF, 1975].

that in the channel the direction of the current is very persistent throughout the year. 94.8% for the first period, 88.6% for the second period and 70.5% for the third period. The average velocities are 0.67, 0.51 and 0.40 m/s respectively.

In the unobstructed region, the direction becomes more variable throughout the year. During the first period, 53.3% of the data is in northwest direction, between 285° and 320° with an average velocity of 0.33 m/s. During the second period, in the months April to August, current velocities are slightly higher and more unidirectional compared to the other two periods. 53.7% of the data is contained is that same direction bin while velocities are averaged to 0.34 m/s. Only 36.3% is in that same bin in the third period and averaged velocities decrease to 0.25 m/s.

The rose plots for the sheltered region can be found in Appendix J, Figure J.8. Averaged velocities over time are very low, only 0.28 m/s throughout the year, with slightly higher velocities in the second period. The direction is to the west-northwest, from 275° to 300° and is very consistent over the year.

These rose plots are in good accordance with the long term mean surface plots in Figures 4.1b, 4.1d and 4.1f in the previous chapter.

For the identified backflow events in Appendix H, this accounts for only 6% of the days. Other than that, the backflow velocities are very low, on average 0.1 m/s.

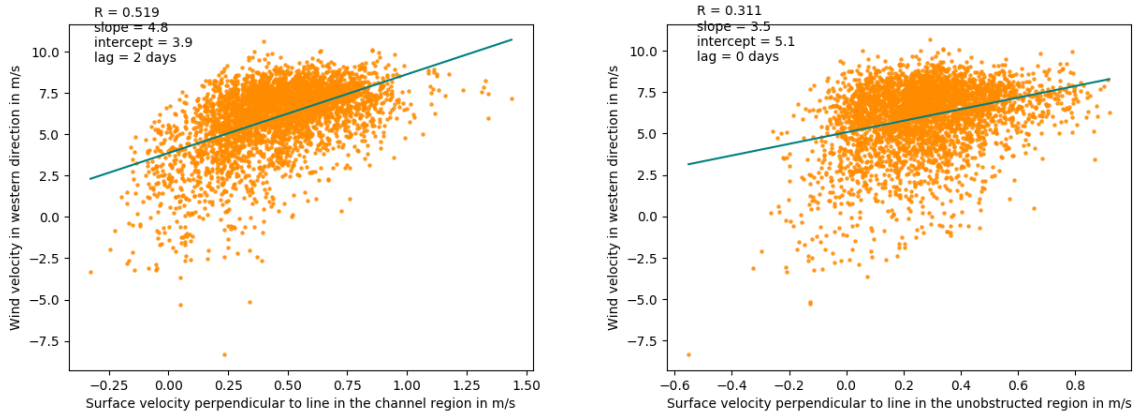

(a) Channel region. *(b) Unobstructed region.*

Figure 5.10: Correlation between the surface currents perpendicular to the transect for two different regions and the wind in western direction. Correlation coefficient is higher in the channel region where Pearson correlation coefficient R is 0.519, compared to R is 0.311 for the unobstructed region. R set out to lag can be found in Figure J.10. Wind data from the European Centre for Medium-Range Weather Forecasting [ECMWF, 1975].

5.3 Correlation of sea surface currents to wind

Wind forcing is one of the most influential factors for surface currents. This can be substantiated by Figure 5.9, where the long term mean of wind and sea surface current values are plotted. From the figure, it can be seen that a semiannual sign can be identified in the wind speed with a local minimum in April/May and an absolute minimum in October/November. This same semiannual sign can be seen in the current speeds in the channel region (the uninterrupted orange line). The dotted orange line, indicating the surface current speed in the unobstructed region, does not display a clear identical signal, although a semiannual pattern can still be identified with maxima in December/January and July/August.

The period of September to December, when wind speed are lowest, can explaine the identified pattern in Section D.1.3, where the abrupt increase of the negative SSH band is described. An interruption appeared in May and from halfway September to halfway December 2016, when the long term wind speeds are lower. Also, as written in Section D.1.4, the deviating velocity pattern in October and November 2016 with lower velocities is probably caused by the lower wind speeds. Furthermore, the identified backflow events in Appendix H occur mostly at the end of the year, when long term wind speeds are lower.

Pearson correlation is a measure for linear correlation between two variables. It can be used to quantify a relation between two variables. The method of determining the Pearson correlation coefficient is decribed in Section 3.2.3. It is known that wind forces currents and from Figure 5.9, this is seen in the data around Curaçao. Therefore, Pearson correlation is applied to quantify the correlation between wind and current speed.

In Figure 5.10 the correlation between wind speed and current speed is plotted. It appears that the correlation is stronger in the channel region (0.519) compared to the

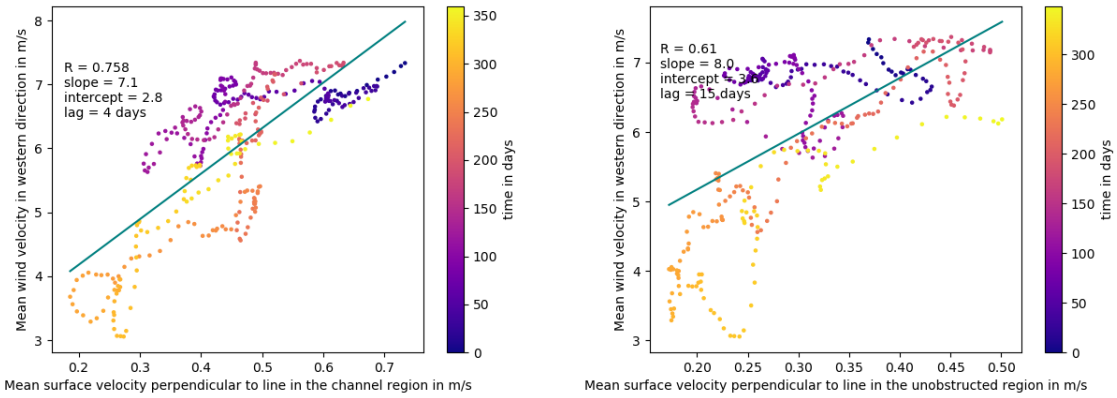

(a) Channel region. *(b) Unobstructed region.*

Figure 5.11: Correlation between the average year surface currents perpendicular to the transect for two different regions and the mean wind in western direction. Correlation coefficient is higher in the channel region where Pearson correlation coefficient R is 0.758, compared to R is 0.61 for the unobstructed region. The colors of the dots indicate the day in the year, with day 0 being 1rst January. R set out to lag can be found in Figure J.11. Wind data from the European Centre for Medium-Range Weather Forecasting [ECMWF, 1975].

unobstructed region (0.311). This could be due to the fact that in the channel region speeds are magnified by the bathymetry. If the wind blows along the coast, all the water to the east of Curaçao is directed through the channel. Other than that, the cold water front due to upwelling runs through the channel, see Figure 4.4a. In the previous chapter, it was observed that a fast current jet follows the cold water front. This would intensify the correlation of the surface currents to the wind. These assumptions are supported by the fact that the slope of the correlating line is steeper for the channel region (a slope of 4.8 versus 3.5 for the unobstructed region, as from Figure 5.10). This means that higher wind speeds induce higher current speeds in the unobstructed region, but even higher current speeds in the channel region and with a greater certainty.

When the means of the wind and current velocities are correlated, correlation coefficients jump up to 0.758 and 0.610 respectively for channel and unobstructed region, see Figure 5.11. Averaging out part of the intra-annual variations increases the correlation.

When calculating the Pearson correlation coefficient, the lag between the two parameters to be correlated that gave the optimal correlation coefficient (highest absolute value) was determined. This lag is also displayed in the graphs, in the upper left corner, together with the parameters for the trend line. These parameters are the slope $\delta y/\delta x$ and the interception with the y-axis, $y(x = 0)$. In Appendix J, figures that set out the Pearson correlation coefficient R on the y-axis to the lag in days on the x-axis are shown. It can be seen that when correlating wind to surface current speeds, optimal lags are around 0, which indicates no lag, or very small but positive. This indicated that current speeds follow wind speeds with no lag or a lag of only a couple of days. The difference in R with no lag is very small.

The Pearson correlation coefficient between the surface velocities at both sides of the island was also calculated. It is 0.498 when looking at all ten years of data. This is quite

low when realizing that these two regions are only seperated by a small island of 10 km wide. When correlating the means, R becomes 0.734. Again, averaging out the intra-annual variations helps increase the correlation. The optimal lag is calculated to be three days with the channel region in advance. A possible explanation for this could be that both sides are correlated to the wind, but the channel region has a stronger correlation. Thus, wind influence is stronger in the channel region, and also gives rise to higher velocities, what can be the cause for the lag. The water downwind transported towards the island, reaches the channel region first, because the velocities there are higher.

5.4 Eddy and hurricane influences on the sea surface currents

For the forcing mechanism behind the intra-annual variability, eddies are assumed to be the main driver. All eddies larger than 200 km in diameter emerging in the south of the Venezuela Basin are analyzed for the ten years of data. In Appendix F, an overview of this eddy identification can be seen. To calculate the influence of eddies on the surface currents, three different means are compared. These means are obtained by averaging over time. The first mean is the overall mean of the surface current at a certain location. The second mean is the mean of the surface currents at a certain location, of only the days when an eddy was present at 69°W. The third mean is the mean of the remainder of the days in the ten year, so when no eddy was present.

An effect of the large anticyclonic eddies identified is found. The overall mean of the surface velocities is highly influenced by the presence of eddies. The overall mean of the surface velocities is 0.51 m/s and 0.31 m/s for channel and unobstructed respectively. For the channel region this becomes 0.57 m/s when an eddy is present compared to 0.41 m/s when no eddy is present. For the unobstructed region, these values are 0.44 m/s and 0.21 m/s respectively.

Also, peak velocities in both regions are found from June to August, see Figure 5.2 and 5.3. Figure 4.6b shows a peak in present eddies in July. Peak velocities in both regions are often caused by passing eddies. This is confirmed by analyzing the sea surface velocity plots for each day.

Some hurricanes passed over the Caribbean Sea in the analyzed timespan. They can be found in Table 2.2, along with when they existed and how strong they were. Their influence on surface currents was merely local and temporary, only when the hurricane was present. The strong winds induce strong surface currents, but as soon as the hurricane has passed, the normal situation is restored within a day or two. Consequently, the influence of hurricanes on the surface currents near Curaçao has been very limited in the years of data analyzed. Only when a hurricane would hit Curaçao directly, currents become much higher. As stated in the scope of this reseach, waves have not been analyzed. It is expected however that the vicinity of Curaçao will be influences by swell waves generated by the hurricane, because waves are known to travel from the location of a storm in all directions for thousands of kilometers.

5.5 Application to OTEC

Surface velocities around Curaçao are on average 0.5 m/s. However, velocities as large as 1.7 m/s are seen when eddies are present. Mean velocities increase by 40% due to the presence of eddies. Higher velocities are an indication for higher variability and cause advection of warm and cold water masses. In addition, higher velocities induce higher forces. Overall larger and more uniform curernt velocities are seen to the south of Curaçao. Predictability of current velocities is increased when the forcing mechanism of the current velocity is well understood. It was seen that wind and eddies are important factors that influence the surface velocities around Curaçao. Especially in the channel region, wind is very well correlated to surface velocities.

5.6 Summary

In this chapter, surface currents around Curaçao are analyzed. Three regions are defined on a transect across Curaçao perpendicular to the general flow direction. The sheltered region is a shallow area sheltered by Venezuelan land masses. Consequently, current velocities there are low throughout the year. The channel region is the deep part of the channel between the mainland of Venezuela and Curaçao where velocities of almost 2 m/s are found. Average velocity is 0.51 m/s, the highest found around Curaçao. The flow is very unidirectional, with a northwest direction. Average velocities are highest in January and February, but from May to September daily velocities are the most variable, and have the highest peaks. The unobstructed region is the part of the transect northeast of Curaçao and extends about 100 km into the Caribbean Sea. Average velocity is 0.31 m/s, lower than in the channel region. The flow is also more variable in direction, although still generally to the northwest. Peak velocities are found from May to September.

The pattern and variability of the surface currents is highly influenced by wind speeds over the Caribbean Sea. Reasonable correlation coefficients between surface currents perpendicular to the transect and wind speeds to the west are found for the channel region as well as the unobstructed region, 0.519 and 0.311 respectively. However, when obtaining a yearly average by averaging over the ten years in the dataset, 2007 to 2016, correlation coefficients go up to 0.758 and 0.610 respectively. By averaging over the different years, a large part of the variability is filtered out. In summary, wind is the main driver for the general background flow, while other processes that influence the currents as well, and cause the intra-annual variability, are not taken into account in the correlation.

Intra-annual variability can for a large part be explained by the presence of large anticyclonic eddies. These eddies are seen to have a large influence on the velocity. The presence of eddies observed caused a temporal increase of 40% to 110% in average velocity for the channel and the unobstructed region respectively, compared the average when no eddy was present.

6

Volume flux patterns around Curaçao

In this chapter, focus is on currents beneath the surface and volume fluxes. The first section analyzes the volume fluxes and their seasonal variability around Curaçao. In the second section, subsurface countercurrents that were identified are described and interannual variability within the ten years is analyzed. Then, volume flux through the Grenada Passage is correlated to volume fluxes near Curaçao. Lastly, the influence of eddies on volume flux is assessed.

Although highest velocities are usually found at the surface, a large part of the total mass transport happens further down. This is relevant for OTEC, since the OTEC systems extend to deep water depths of 1000 m below the surface. Furthermore, literature suggests the existence of a subsurface countercurrent which can cause the advection of outflow water to the east.

6.1 Volume fluxes over the transect

For the analysis, different region definitions were used than in the previous chapter when analyzing velocities. The sheltered region and the channel region are taken together as one region, because together they form a passage between Curaçao and the mainland. This will be refered to the **totalchannel** or just the channel and sheltered region taken together. The extending of the unobstructed region is explained in Section 6.5.

In Figures 6.1 and 6.2, the daily volume fluxes for the two sections on the transect are shown. First thing that stands out when looking at the total volume fluxes for the totalchannel region and the unobstructed region for the years 2007 to 2016 in these figures is the great variability. For the totalchannel region, a similar semiannual cycle can be found in the mean, the thick black line, that was seen when analyzing the mean current velocities and wind speeds from Figure 5.9, with minima in May and October and maxima in January and July. The overall mean transported volume through the

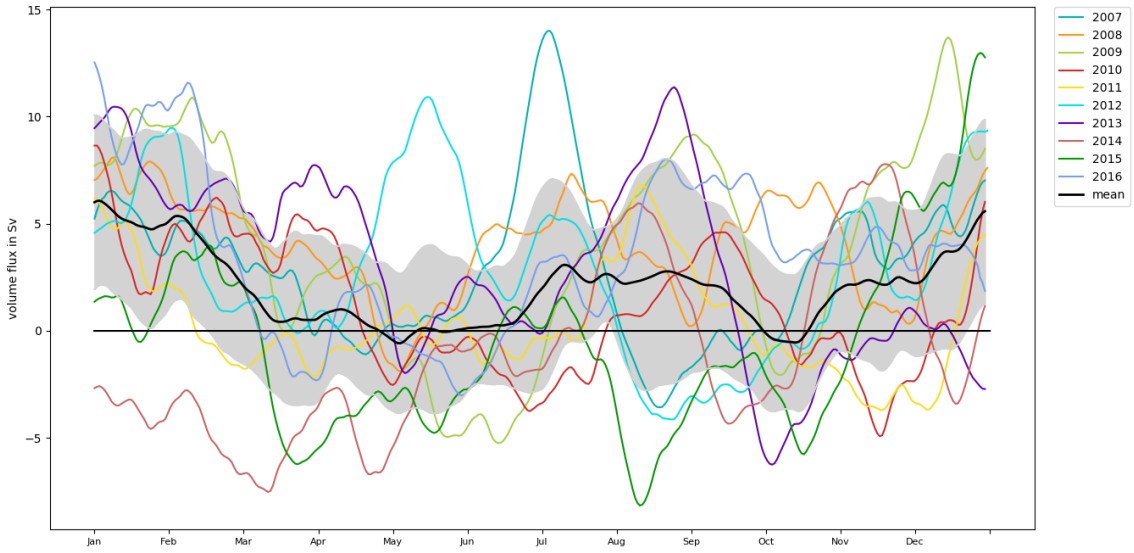

Figure 6.1: Volume flux for the years 2007 to 2016 over the transect line in the channel and sheltered region. The mean is plotted in black and the grey areas indicate the magnitude of the standard deviation. A rolling average of eight days was used to smooth the lines. Plots per year can be found in Figures I.1 to I.10.

totalchannel is 1.99 Sv. The standard deviation is calculated to be 3.69 Sv, which is large when compared to the mean. Large positive peaks are identified in 2007, 2009, 2012, 2013 and 2015 in the months May July, August and December. 2014 and 2015 show large negative peaks in March and August.

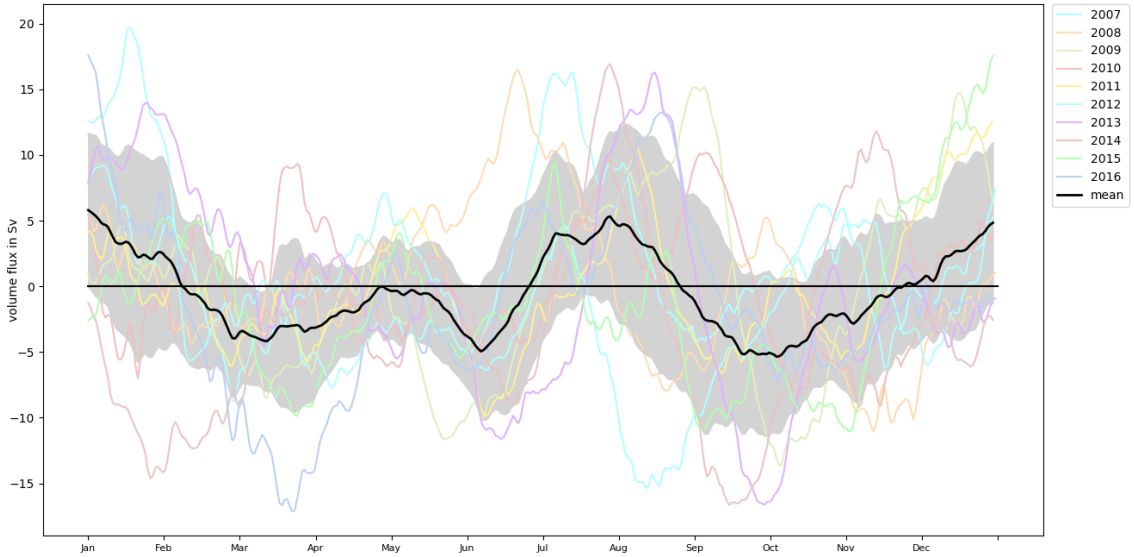

Figure 6.2: Volume flux for the years 2007 to 2016 over the transect line in the unobstructed region. The mean is plotted in black and the grey areas indicate the magnitude of the standard deviation. Plots per year can be found in Figures I.11 to I.20.

Figure 6.2 shows the volume transport over the transect in the unobstructed region. It is positive in the winter (December and January) and in the summer (July and August). That is also when peaks in mean volume transport occur in the totalchannel region. The

mean volume transport over all the ten years is -0.48 Sv. The fact that this is negative seems to indicate that below the surface large volumes of water must flow in opposite direction (towards the east), since backflow at the surface was concluded to be rare in Section 5.2. It happens only on 2% of the days. The standard deviation over the ten years is 5.50 Sv, which again indicates very large variability.

The total daily volume fluxes were correlated to the wind in western direction. Correlation coefficients are low for both regions, lower than 0.1. This indicates that wind influence on the volume fluxes is not so pronounced. This raises the question of what does influence the subsurface flows. The remainder of this chapter explores the volume fluxes to find an answer to this question.

6.2 Subsurface currents around Curaçao

Since the variability in volume fluxes is quite large, interesting to look at next is the distribution of the volume flux over depth. A depth of generally eastward (negative) flow at both sides of the island can be distinguished from Figures 6.3a and 6.3b. This depth is from 100 to 250 m in the channel region and from 300 to 1600 m in the unobstructed region. According to Section 2.2, these depths correspond to the Subtropical Underwater and the Western North Atlantic Central Water respectively.

Figure 6.3c shows a snapshot of the flow over depth for both regions for one day. This subsurface countercurrent in eastward direction (red) can be identified at both sides of the island. The subsurface countercurrents seem to be located at the south side of both regions. In the totalchannel region, the subsurface current flows along the Venezuelan coast. In the unobstructed region, the subsurface current flows along the coast of Curaçao. When observing other days than the one in Figure 6.3c, however, great variability over depth is seen. The existance and persistence of the undercurrents is backed by the rose plots in Figure 6.4. Around 61% of the flow at 150 m water depth is in negative direction over the line in the totalchannel region, in southeastern direction. About 39% is in positive direction. In the unonbstructed region, 77% is in negative direction. Similar rose plots on other water depths are shown in Appendix J, Figure J.13 to J.16.

As described in Section 2.3 and by Andrade et al. [2003], the subsurface countercurrent may be the effect of an alongshore pressure gradient caused by wind or may be induced by local upwelling. In Appendix E, a detailed explanation is given considering the Thermal Wind Balance and the relation to upwelling and the subsurface countercurrent. There it is argued that the subsurface countercurrent is too deep to be related to upwelling. The next section will discuss the strength of the subsurface countercurrent for the different years and the two different regions, see Figure 6.5.

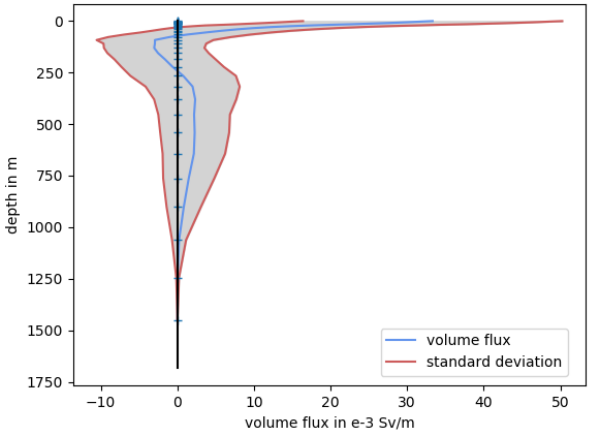

(a) Channel and sheltered region.

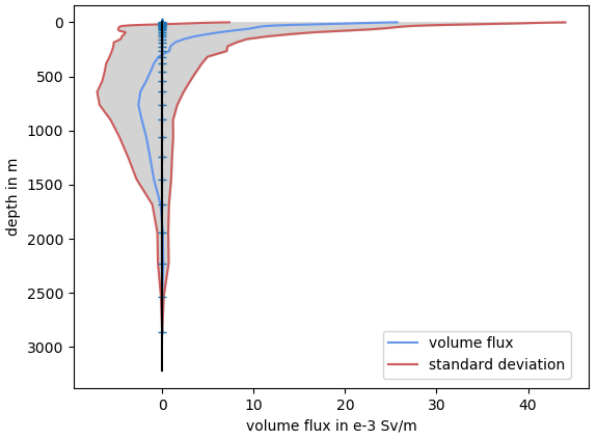

(b) Unobstructed region.

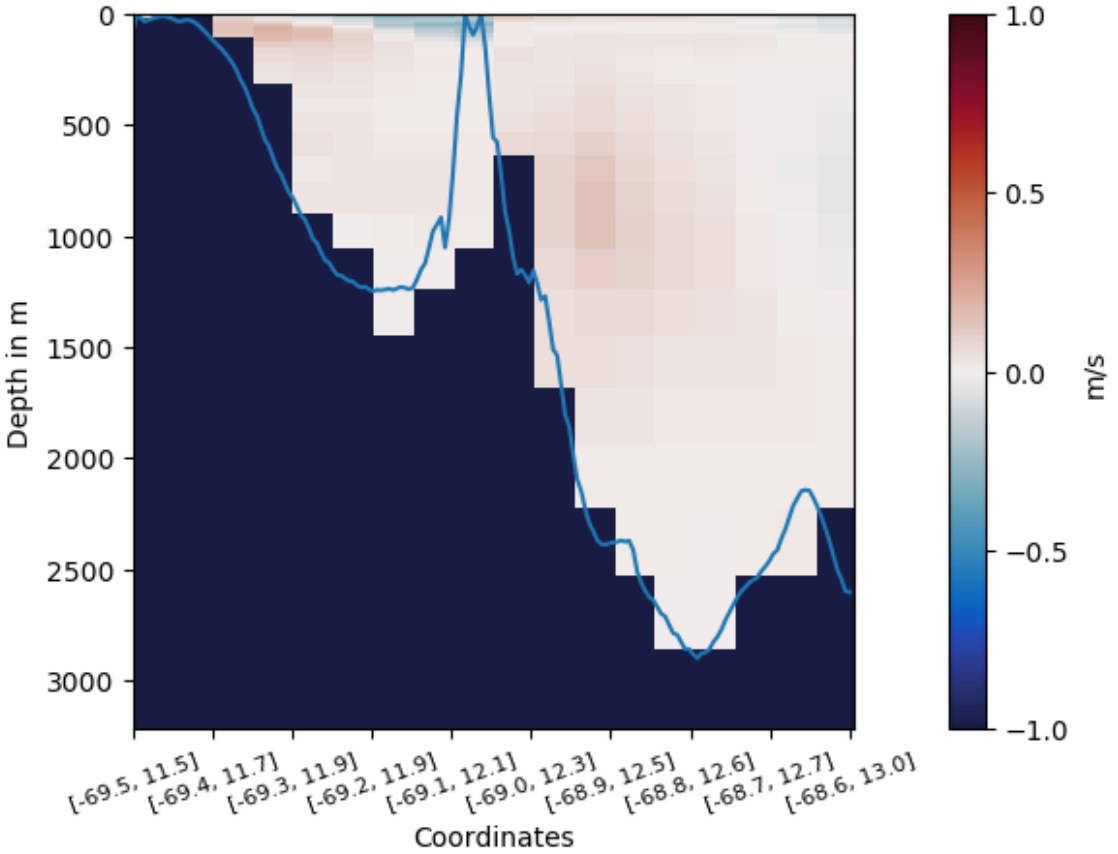

(c) Example plot of a vertical section over the same transect as indicated in Figure 5.1a. Positive flow is in this figure to the southeast. The blue line is a plot of the bathymetry from GEBCO [2014]. The data is from July 4th 2011.

Figure 6.3: Volume profiles over depth for two locations averaged over the years 2007 to 2016 in 6.3a and 6.3b. The volume flux is shown per meter over depth. A depth of generally negative flow, to the east, can be distinguished in both plots. This depth is from 100 to 250 m in the channel region and from 300 to 1600 m in the unobstructed region. The standard deviation is plotted in grey and is relatively large compared to the actual values. This represents the great variability over the depth, as was also noticed in Figures 6.1 and 6.2. Figure 6.3c also shows the subsurface countercurrents on both sides of the island.

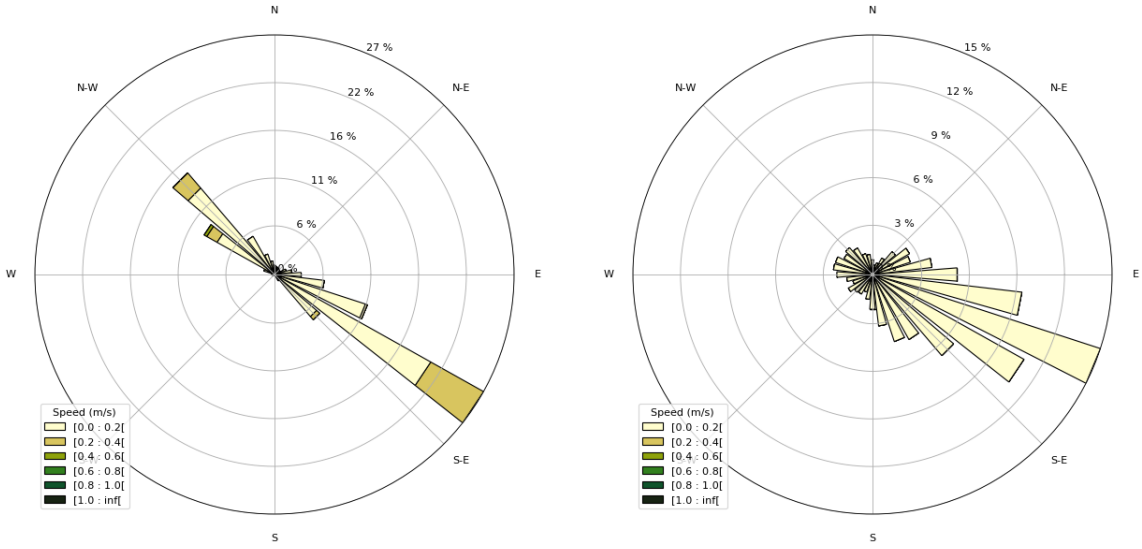

(a) Totalchannel region at 150 m depth. *(b) Unobstructed region at 800 m depth.*

Figure 6.4: A subsurface countercurrent can be observed at 150 m in the totalchannel region and at 800 m in the unobstructed region. The subsurface countercurrent in the unobstructed region is practically always present (76.5%), while in the totalchannel region it is less persistent (61.2%). Corresponding bar graphs can be found in Figure J.12.

6.3 Interannual variability of the volume fluxes and subsurface currents

The interannual variation of the currents between the different years is conjectured to be due to: 1) eddies that occur at semi-random times in the year and have substantial influence; 2) wind that varies over different years and; 3) ENSO. Eddies cause large velocities at relatively short moments in time. This can cause peaks in volume flux a well. Wind is a well-known factor for volume transport and ENSO has global impact, amongst others on the wind over the Caribbean Sea.

In Figure 6.5, the average volume flow per year through the two different regions is plotted. The net of the mean volume transport (indicated by the green line in Figure 6.5) through the totalchannel region, is 1.99 Sv and the standard deviation is 3.69 Sv. The peak volume transport in this region is 14 Sv. The total volume transport, the negative and the positive added up, is 4.93 Sv. For the unobstructed region, the net volume flux is negative, to the east, -0.49 Sv with a standard deviation of 5.50 Sv. The total mean transport, however, is 4.23 Sv.

Total volume flux through both regions is of comparable size. However, the total area of the totalchannel is much smaller compared to the unobstructed region, which is much deeper. The areas are respectively 63.0 km^2 and 230.9 km^2. It can be concluded that velocities in the totalchannel region (specifically the deep part of the region, the channel region, defined in the previous chapter) are bigger than in the unobstructed region.

According to Andrade et al. [2003], the volume flux due to the subsurface countercurrents

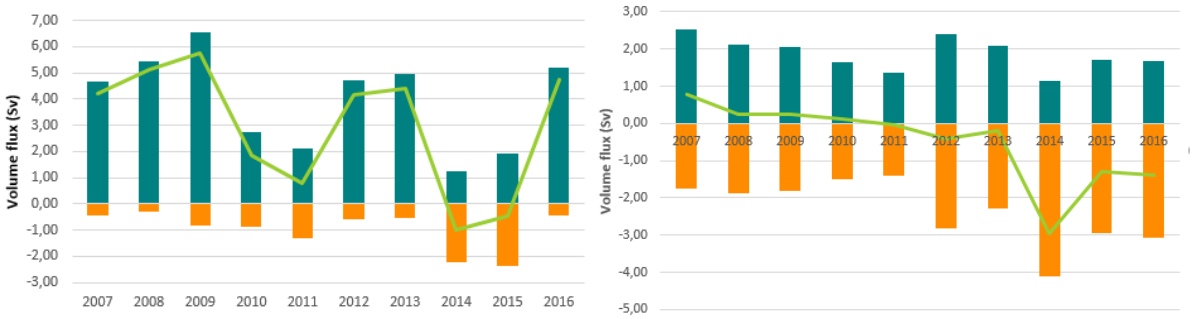

(a) Channel and sheltered region. *(b) Unobstructed region.*

Figure 6.5: The average volume flow through the two different regions per year. Displayed are the averages over time of daily volume fluxes. At some days, the volume flux was negative. The averages over time of the positive and the negative volume fluxes are shown. The green line is both bars added up and gives the net mean volume flux for each year.

near Curaçao should be between 1 and 8 Sv. From Figure 6.5, it can be seen that the negative volume flux, to the east, is between 2 and 6 Sv when both regions are added up. Consequently, these two findings are in good agreement.

The volume flow in the channel region appears to show a four-annual cycle within the ten years analysed. The unobstructed region seems to show a steady decline with an extreme negative peak in 2014. The reasons for this behaviour are yet unknown.

ENSO is one of the biggest global causes for interannual variability. See Section 2.7 for an explanation of ENSO and ONI. When the yearly ONI values are correlated to the different volume fluxes from Figure 6.5 however, no strong correlation was found. Pearson correlation coefficients were lower than 0.01 although they became higher when only the mean negative volume flow was correlated; -0.38 and -0.07 for the totalchannel and the unobstructed region respectively.

From these numbers only, it can not be concluded that ENSO is a large influencing factor.

6.4 Volume flux through the Grenada Passage

It is assumed that the volume flux through the upstream passages between the Windward and the Leeward Islands, at the eastern border of the Caribbean Sea, influence the volume flux through the transect at both sides of the island of Curaçao. The volume flux through the Grenada Passage is analysed in the Mercator dataset. It is the most southern passage with the biggest volume transport compared to the other southern passages [Wilson and Johns, 1997]. Most of the Caribbean inflow is through the southern passages of the Lesser Antilles ([Kinder et al., 1985] and [Johns et al., 2002]). It also displayed the biggest surface velocities in Figures 4.1b, 4.1d and 4.1f compared to the other passages.

The volume flux, as displayed in Figure 6.6, through the Grenada Passage is positive, into the Caribbean Sea, on average 8.89 Sv, with only a couple of periods between 2007 and 2016 where the flow was negative. Large variability over the years and between the

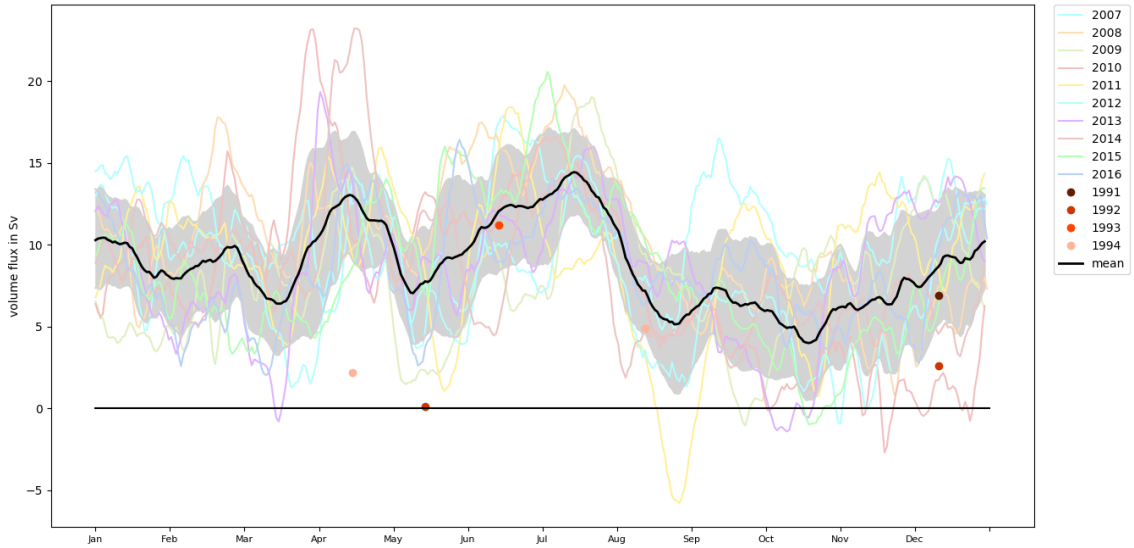

Figure 6.6: Volume flux for the years 2007 to 2016 through the Grenada Passage. The mean is plotted in black and the grey areas indicate the magnitude of the standard deviation. The dots indicate measurement data from Wilson and Johns [1997]. Figures I.21 to I.30 show the plots for every year.

years is displayed in the figure. This indicates that possible seasonal variability could be obscured by processes with shorter time scales but larger amplitudes [Wilson and Johns, 1997]. The average volume flux seems to be slightly higher compared to measurements performed in the beginning of the '90's [Wilson and Johns, 1997]. These measurement values are also shown in the plot by the colored dots. The average volume flux through the Grenada Passage was estimated to be 4.7 Sv (compared to 6 Sv from Stalcup and Metcalf [1972] and Mazeika et al. [1980]). The distribution of the volume flux over depth, as shown in Figure 6.7, shows positive volume flux over depth. No subsurface countercurrent is seen in the Mercator data, although it was found by Wilson and Johns [1997]. They found a countercurrent from 100 to 300 m depth, with a maximum at 200 m. It is possible, however, that the subsurface countercurrent is partly masked by a positive current. Figure 6.7 shows this mechanism.

A possible explanation for the masking of the subsurface current is that it has decreased between 1994 and 2007 or that the general positive flow has increased. Both of these explanations would also explain the generally higher volume fluxes from 2007 to 2016 compared to 1991 to 1994. In Figure 6.8 a slowly declining trend can be seen. This could indicate a multiple-year cycle in volume flux through the Grenada Passage. However, the ten years of data available are not enough to substantiate this.

6.4.1 Correlation of volume flux around Curaçao to volume flux through the Grenada Passage

No correlation is found between the daily values of the volume flux through the Grenada Passage and the volume flux through the totalchannel region, since R is only 0.084. This Pearson correlation coefficient R was calculated for an optimal lag of twelve days. The lag was taken into account, because the 800 km between the Grenada Passage and

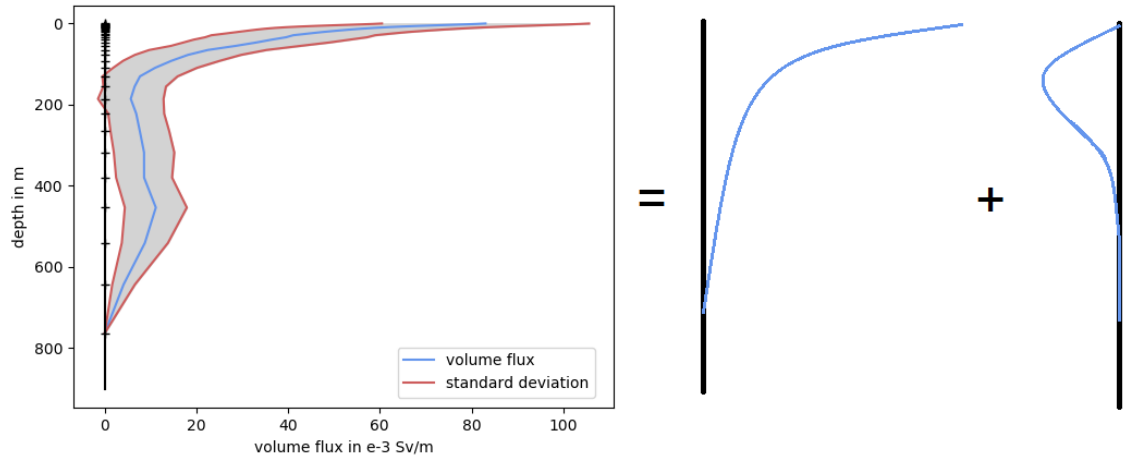

Figure 6.7: Volume profile over depth for the Grenada Passage averaged over the years 2007 to 2016. To the right, a possible mechanism that explains the shape of the mean volume flux profile is shown. This mechanism shows the presence of a subsurface countercurrent with a maximum velocity at 200 m depth, as was found by Wilson and Johns [1997]. The volume flux is divided by depth meters.

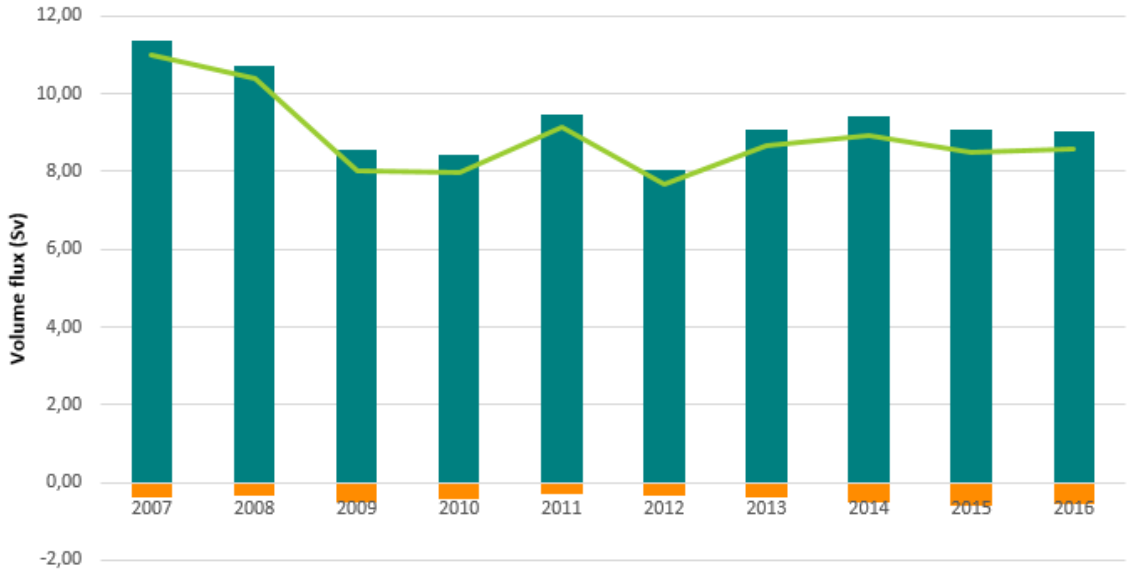

Figure 6.8: Volume flux per year through the Grenada Passage. Displayed are the averages over time of daily volume fluxes. At some days, the volume flux was negative. The averages over time of the positive and the negative volume fluxes are shown. The green line is both bars added up and gives the net mean volume flux for each year.

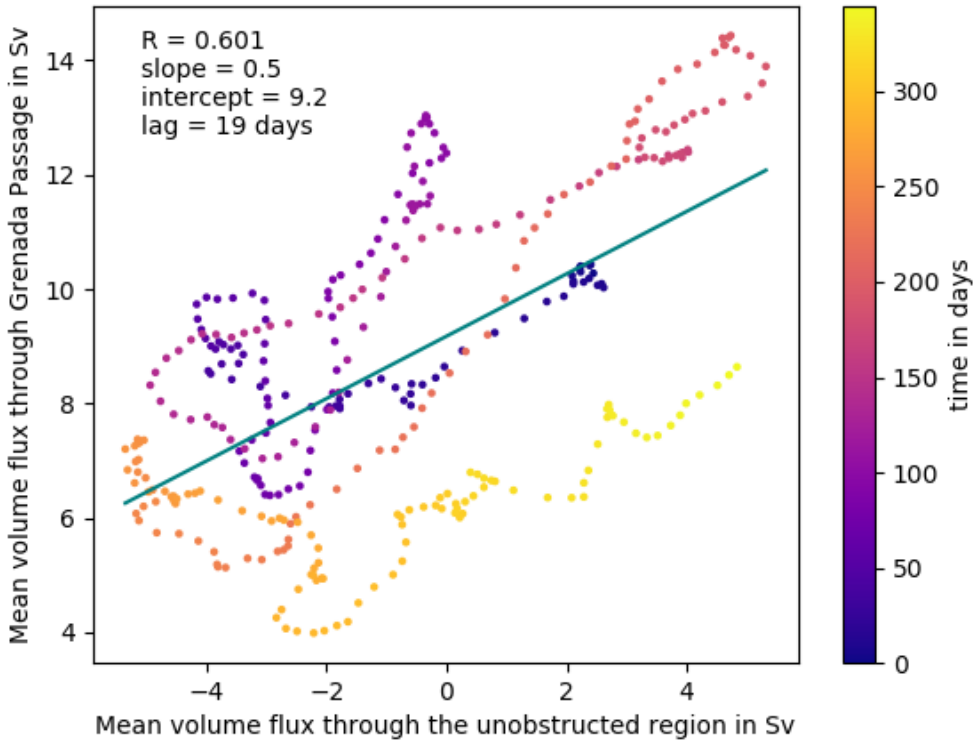

Figure 6.9: Correlation between the yearly mean volume flux through the unobstructed region and the Grenada Passage. R is 0.601. It shows that R is significantly higher compared to the total volume flux correlation coefficient, which was only 0.334.

Curaçao must be traveled by the water. The optimal lag is defined as the lag that gives the highest correlation coefficient.

When correlating yearly means, a very high correlation coefficient is found (0.948). However, this is calculated for an optimal lag of -162 days, which means that a peak in volume flux through the total channel is followed by a peak in volume flux through the Grenada Passage with a lag of 162 days. This high correlation coefficient can be explained by the semiannual cycle that can be viewed in both yearly means. When shifting the means 162 days, one of the two peaks from the semiannual cycle overlaps with the other. Plus, it means that only 365-162=203 days are still correlated. Consequently, this high value of correlation should be regarded as nonsense.

The correlation coefficient of the daily values is much stronger for the unobstructed region; 0.334. An optimal lag was calculated for this correlation. The optimal lag is calculated to be around thirteen days. This would come down to an average speed of 0.8 m/s, which is quite reasonable at the southern border of the Caribbean Sea for the surface velocities. A remarkable result is that the correlation between the mean of the total volume fluxes through the Grenada Passage and the unobstructed region is significantly higher; 0.601. The plot can be seen in Figure 6.9. This could mean that the volume flux through the unobstructed region is strongly correlated to the volume

flux through the Grenada Passage, when all intra-annual variability is not taken into account.

6.5 The extended unobstructed region

The unobstructed region was defined in the previous chapter to be able to compare the surface currents at the two sides of the island. However, when analyzing volume fluxes and interannual variability, one might argue that the unobstructed part of the transect is too small to capture the large scale processes such as eddies in the analysis. Therefore another section on the north side of Curaçao was defined and analyzed as well. This section is chosen to extend from Curaçao, at 69°W, 12°N to 69°W, 15°N. This section was chosen because it is roughly perpendicular to the main flow and because it includes the southern jet described in Fratantoni [2001] and Centurioni and Niiler [2003] and seen in Figures 4.1b, 4.1d and 4.1f. This southern jet is most influential for the vicinity of Curaçao in contrast to the more northern jet.

6.5.1 Volume flux through the extended unobstructed region and correlations

The volume flux over this transect is shown in Figure 6.10. The mean volume flux over the ten years and over this section is 13.75 Sv with a standard devation of 15.02 Sv. Even for this larger section of 1,122.7 km^2 with on average much larger volume fluxes, the volume flux at times was negative. In Figure 6.11 the yearly volume fluxes are shown and in Figure 6.12 the volume flux profile over depth is shown. In Appendix J, Figure J.17a and J.17b, show the rose plots for the extended unobstructed region at the surface and at 700 m water depth respectively.

When relating the volume fluxes through the Grenada Passage to the volume flux through the extended unobstructed region, correlation coefficients become slightly different; 0.264 for the volume flux per day (optimal lag of 22 days) and 0.719 for the yearly mean volume flux (with an optimal lag of 18 days). These lags correspond to an average velocity of 0.5 m/s from the Grenada Passage to the 69°W. This is a slightly lower correlation when compared to the old unobstructed region, but it is still present.

The yearly averages of the volume flux through the extended unobstructed region is correlated to ONI values with very low correlation coefficients. ONI is defined in Section 2.7. The value was lower than 0.01.

6.6 Eddy influences on the volume fluxes

For the forcing mechanism behind the intra-annual variability, eddies are likely to be the main driver. Large anticyclonic eddies identified in Appendix F influence the volume fluxes. The average volume flux when an eddy was present at 69°W is much higher compared to the overall mean. The analysis shows that the overall mean for the totalchannel

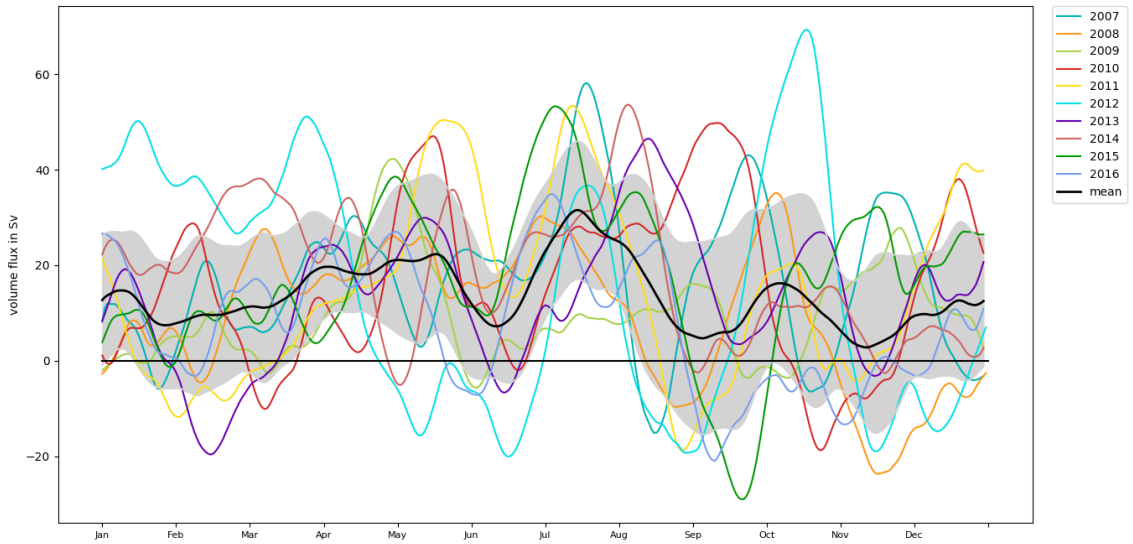

Figure 6.10: Volume flux for the years 2007 to 2016 over the transect line in the extended unobstructed region. The mean is plotted in black and the grey areas indicate the magnitude of the standard deviation. A rolling average of eight days was used to smooth the lines. Plots per year can be found in the appendix, in Figures I.31 to I.40.

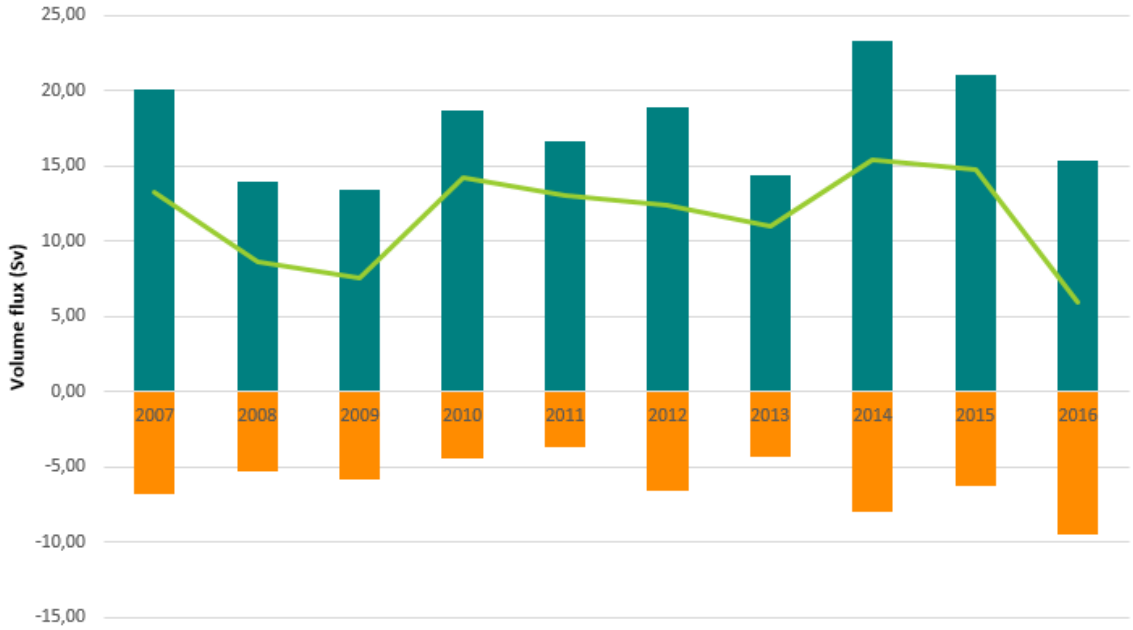

Figure 6.11: The average volume flow through the extended unobstructed region per year. Displayed are the averages over time of daily volume fluxes. At some days, the volume flux was negative. The averages over time of the positive and the negative volume fluxes are shown. The green line is both bars added up and gives the net mean volume flux for each year.

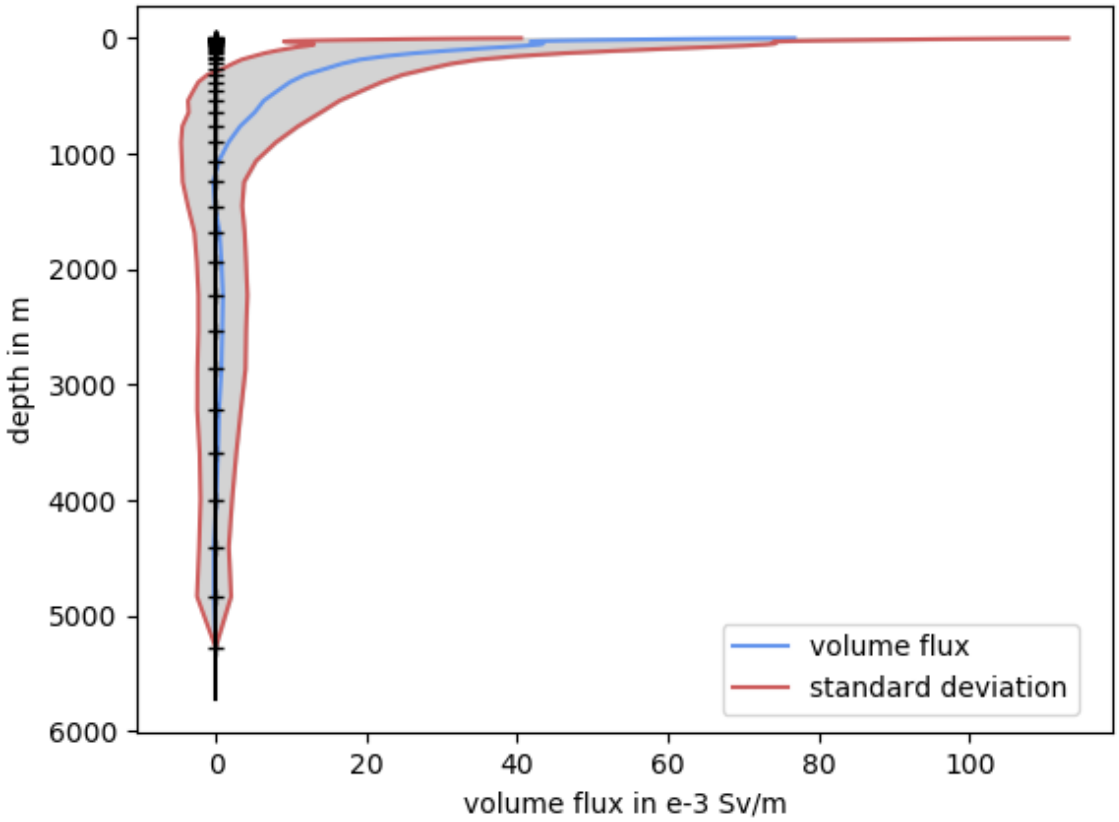

Figure 6.12: Volume profiles over depth for two locations averaged over the years 2007 to 2016. The volume flux is per depth meter.

region is 1.99 Sv. However, the mean when an eddy was present is 2.87 Sv and when no eddy was present is 1.51 Sv. 32% of the days an eddy was present at 69°W.

For the extended unobstructed region, the overall average is 13.74 Sv. The average of the days when an eddy was present is 22.76 Sv. Conversely, when no eddy was present, it is 10.04 Sv.

6.7 Application to OTEC

Current velocities over depth are important for operating an OTEC system, because the cold water pipe extends to water depths up to 1000 m. Forces due to water flowing past the pipe, will exert large moments on the connection between the pipe and the floater.

The direction and speed of the subsurface currents will determine where the intake water comes from and where the discharge water is going to. Subsurface speeds and directions are very important input parameters for prediction of the diffusion and advection of the discharge plume. This will determine the risk for algae blooms and alteration of the local ocean environment. A subsurface countercurrent as seen on the south side of the island, may advect the discharge water upstream of the intake. If the current would reverse again, it would bring the discharge water back to the plant. Understanding of the subsurface currents is therefore very important.

Volume fluxes around Curaçao are influenced by the volume flux through the Grenada Passage. Volume fluxes past the island also give an indication of the maximum scale of OTEC before it starts interacting with the global ocean circulation.

6.8 Summary

Following from Section 2.3.3, there was a reason to believe a subsurface countercurrent could be found along the coast of Venezuela in the south of the Caribbean Sea. From the data, it appeared that there is indeed such a subsurface current. Not the entire Venezuelan coast was analyzed when looking for this subsurface current. On the northern and southern side of the island of Curaçao, transects were made and volume fluxes were analyzed. It appeared that on the south side of Curaçao, a subsurface countercurrent at a depth of around 200 m existed for about 50% of the time. It existed on the south side of the channel between Curçao and the mainland, close to the coast of Venezuela. On the north side of the island, a subsurface countercurrent existed about 800 m deep. It is very persistent and was found in 80% of the data. It is also located on the south side of the transect, against the coast of the island.

It can be concluded that the variability in volume fluxes, interannual, intra-annual and between the two regions, is very big compared to the net mean. The totalchannel shows a semiannual cycle with a net mean over the ten years of 1.99 Sv and a mean standard deviation of 3.69 Sv. This flows through an area of 63 km^2 and does not show correlation to wind speed or volume flux through the Grenada Passage. The unobstructed region also shows a semiannual cycle with a net mean of -0.48 Sv and a mean standard deviation

of 5.50 Sv. The area of this region is 230 km^2 and does not correlate to wind, but does to the volume flux through the Grenada Passage. The extended unobstructed region volume flux is 13.75 Sv with a mean standard deviation of 15.02 Sv. Its area is 1,123 km^2 and it also correlates well to the Grenada Passage volume flux.

The eddies also have a big influence on the volume fluxes and the variability thereof. A respective increase in average volume flux of 90% and 127% is seen for the totalchannel and the extended unobstructed region, when comparing the mean with no eddy present to the mean with an eddy present.

In summary, large variability, in the order of twice the net mean, is observed in volume fluxes around Curaçao. This behaviour is only partialy explained. Volume flux through the Grenada Passage correlates well to the volume flux to the north of the island (R=0.334 for daily values, R=0.601 for the ten-year averaged year). Volume flux to the south of Curaçao appears not to be correlated to the volume flux through the Grenada Passage. The presence of eddies increases the volume fluxes on both sides of the island significantly. The average volume flux rises from 1.51 Sv to 2.87 Sv in the totalchannel region. In the extended unobstructed region, the average volume flux rises from 10.04 Sv to 22.76 Sv.

7

Application to OTEC of previously identified processes

In the previous chapters, Chapter 4 to 6, data from the Mercator dataset were analyzed and visualized. Processes such as upwelling and eddies in the Caribbean Sea were identified and described. Sections 4.5, 5.5 and 6.7 summarize the most important findings. In this chapter, the applicability for OTEC of the Mercator data and the identified processes is highlighted. It is used for assessing a suitable location to place a plant in the vicinity of Curaçao regarding the water temperature and the influence of upwelling on the water temperature. This is done in Section 7.1.

With the Mercator data available, it is possible to calculated the maximum expected current velocity at this chosen location for the lifetime of an OTEC plant. This is done to be able to calculate the maximum expected hydrodynamic forces on the plant, and specifically on the 1000 m long cold-water pipe. The results can be found in Section 7.2 and 7.3. In addition, some remarks are made on the complex problems of vortex induced vibrations and modeling of the discharge of the used water.

7.1 Location assessment for an OTEC plant around Curaçao based on water temperature

For choosing the optimal location for an OTEC plant, two of the most important physical parameters are bathymetry and water temperature difference between the water from the warm-water inlet near the surface and water from the cold-water inlet at a kilometer depth [Bluerise, 2017]. Both of these parameters have been analyzed in the previous chapters and will be further explored in the next sections. A location for installing an offshore OTEC plant will be choosen based on these findings. This location will then be used for determining input parameters for the extreme velocity and force calculations.

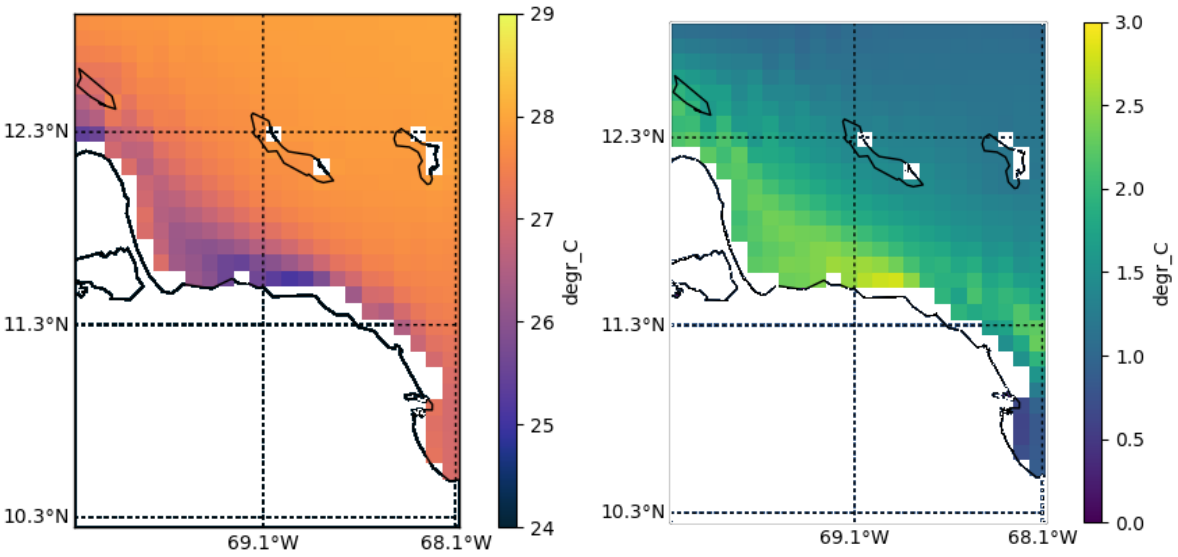

(a) Mean water temperature.

(b) Average deviation from the mean.

Figure 7.1: Water temperature around Curaçao at 15 m water depth, the depth of the warm-water inlet. Figure 7.1a shows the mean water temperature of all data from 2007 to 2016. Figure 7.1b shows the average deviation from the mean of the water temperature. Colors indicate the temperature or deviation in °C respectively, values can be seen on the right in the colorbar. White areas are land.

7.1.1 Location assessment regarding bathymetry

Bathymetry is the topography of the seabed. In Chapter 2, in Figure 2.4, the bathymetry around Curaçao is shown. The slope of the seabed is steeper at the south side of the island compared to the north side. A steeper slope is preferred, because the deeper water with low temperatures will be closer to shore. The plant can be placed closer to shore, reducing costs of installation, maintenance and decommissioning operations and of electricity cables, connecting the OTEC system to the main grid. Consequently, when considering bathymetry, the south side of the island is preferred for placing an OTEC system.

7.1.2 Location assessment regarding warm-water intake

The location of the intake of warm water should be chosen such that the cold water, upwelled to the surface by the westward winds and transported by the westward currents, does not reduce the system performance, or only to a limited extent. Upwelling in combination with currents cause risks for the system performance because it lowers the temperature of the water at the warm-water inlet, decreasing the temperature difference while a threshold of at least 20°C is required for the system to be economically viable. Some locations are therefore more suitable than others.

In Figure 7.1a, the mean water temperature of the water at 15 m deep, the depth of the warm-water inlet, for the area around Curaçao is shown. The colors indicate the temperature in °C and the dark areas indicate the absence of sea water and mean that

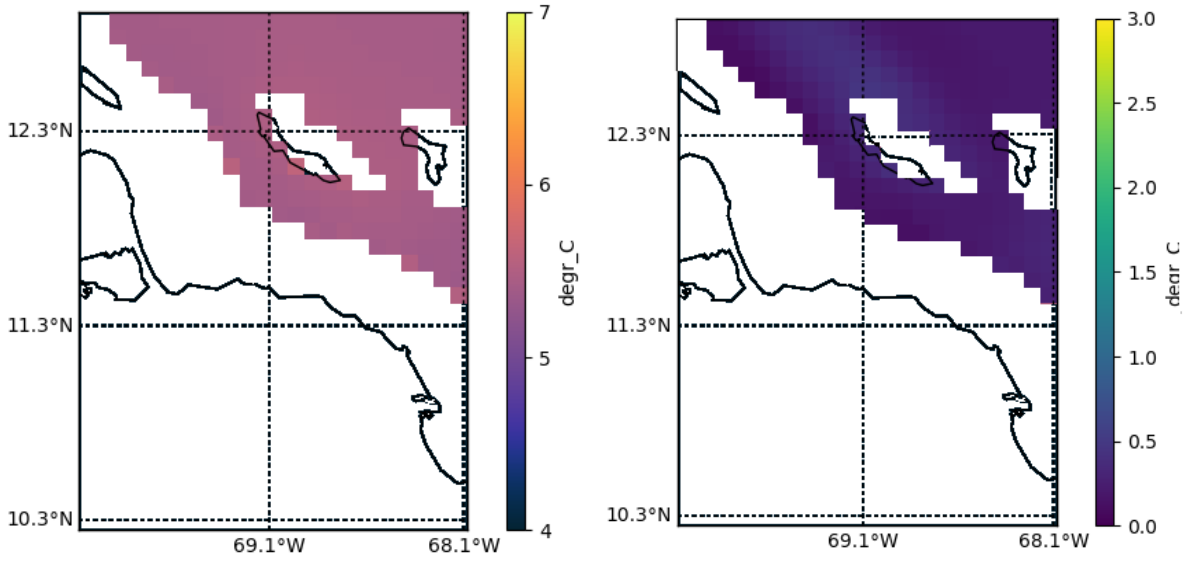

(a) Mean water temperature.

(b) Average deviation from the mean.

Figure 7.2: Water temperature around Curaçao at 900 m water depth, the depth of the cold-water inlet. Figure 7.2a shows the mean water temperature of all data from 2007 to 2016. Figure 7.2b shows the average deviation from the mean of the water temperature. Colors indicate the temperature or deviation in °C respectively, values can be seen on the right in the colorbar. White areas indicate land.

there is land at that loaction. In Figure 7.1b, the average deviation of the mean water temperature in °C is shown. The average deviation from the mean is a measure of the variability of the temperature. From the figures, it can be seen that the surface temperature around Curaçao is around 28°C and quite consistent, showing an average deviation from the mean of around 1.5°C in Figure 7.1b. The variation of the temperature over the year is known from Chapter 4. Surface temperature varies between 26°C in winter and 29°C in summer. Slightly lower mean temperatures and slightly more variability of the temperature are seen to the south of Curaçao.

Only the area close to the Venezuela coast, the so called sheltered region from previous chapters, is subjected to upwelling and the surface temperature is generally lower there, with on average 24°C in winter. This colder water is advected to the north west and away from Curaçao by the strong surface currents. Since these currents are persistently strong, the region close to the south coast of the island will not experience decrease in sea surface temperature due to upwelling. The cold surface water from the upwelling systems upstream of Curaçao, more to the east, do not influence the surface temperatures near Curaçao on the long term. From Figure 7.1b, it can be seen that the upwelling system at the coast is most subjected to temperature variation throughout the year, with the average deviation from the mean approaching 3 °C. No cold water is usually advected along the north coast of Curaçao as can be seen from Figure 7.1.

It is therefore recommended not to place an OTEC system more than 50 km to the south or southwest from Curaçao. This will not be a problem, since such a distance to shore is too large to make for a economically viable plant.

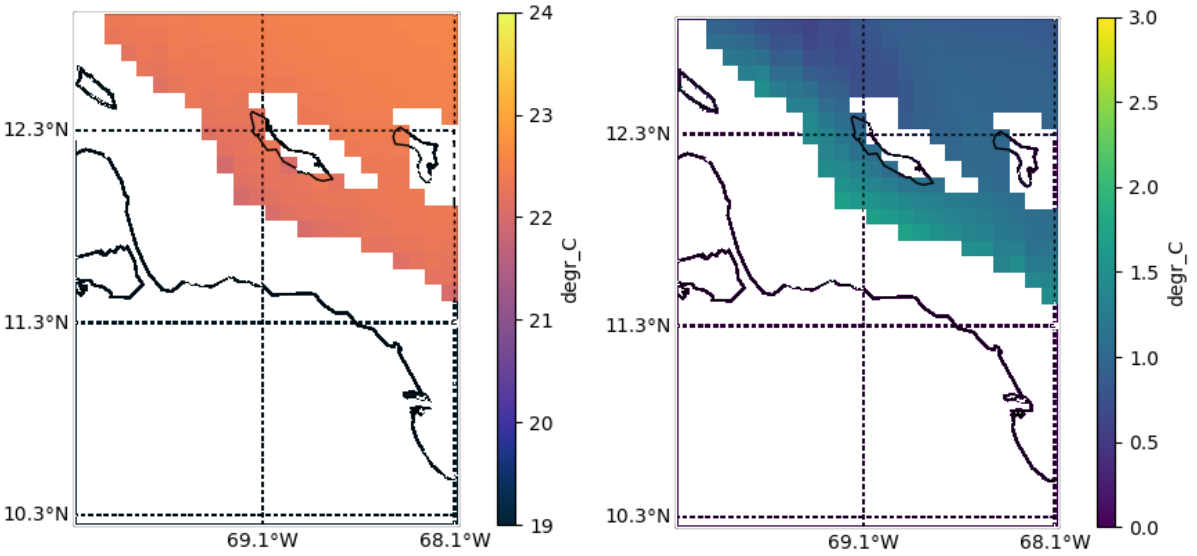

(a) Mean temperature difference.

(b) Average deviation from the mean difference.

Figure 7.3: Difference between mean water temperature at 15 m water depth and 900 m water depth, the depths of the two inlets, around Curaçao. Figure 7.3a shows the difference of the two means of all data from 2007 to 2016. Figure 7.3b shows the average deviation from the difference of the means. Colors indicate the temperature difference or deviation in °C respectively, values can be seen on the right in the colorbar. White areas indicate land.

7.1.3 Location assessment regarding cold-water intake

In Figure 7.2, similar plots are shown as Figure 7.1, but for the depth of the cold-water inlet, at 900 m. The rough estimate for the length of this pipe has been 1000 m. However, as proven by Veijer [2017], the temperature difference between surface water and water at 900 m is already large enough for OTEC to be economically viable. Again, mean water temperature and average deviation from the mean around Curaçao are shown. The dark areas are bigger, this is due to the fact that at this water depth, a bigger part of the map is land, where water depth does not extend up to 900 m. It can be seen that the deep water temperature experiences much less variability, spatial as well as temporal. The average deep water temperature is between 5 and 6°C. The average deviation from the mean is less than 0.5°C.

Neither upwelling, nor temperature advection caused by large water velocities or influence from incoming sunlight and air temperature are present at this depth. This explains the much smaller variations.

7.1.4 Location assessment regarding temperature difference

What is most important for the OTEC industry, is the temperature difference between the water at 15 m depth and 900 m depth. Therefore, Figure 7.3 was plotted. It shows the difference between the mean water temperature at the depths of the two inlets and again the average deviation. The average temperature difference is about 22°C and the average deviation is between 0.5 and 2°C, with bigger deviation towards the south. The

temperature difference to the south of Curaçao is slightly lower compared to the north. This is, however, less than 0.5°C. Since the surface water temperature is more variable, the variation seen in Figure 7.3b can mostly be attributed to the variation at the surface. This underlines the conclusions from section 7.1.2, that an OTEC plant should not be placed more than 50 km south of Curaçao. The temperature difference plotted over all ten years can be found in Appendix J, in Figure J.19 and J.20.

7.1.5 Chosen location for the OTEC plant

With regard to temperature difference, it can be concluded that more than 50 km south of Curaçao no suitable OTEC locations will be found. The difference between locations north and south of the island with respect to temperature difference is not big enough to make a decision. Therefore, also bathymetry was taken into account. The location chosen is south of Curaçao, at 12.1°N and 69.0°W. The advantage of the location to the south is that the deep water is very close to the coast, which is beneficial as well for onshore as for offshore systems, due to transportation and installation of pipes and cables to and from the platform. In contrast, to the north of the island the slope of the bathymetry is much less steep and deeper waters are further away from the coast. This location is further investigated in the next sections.

7.2 Maximum expected current velocity

Currents exert forces on structures in water. When calculating the maximum force due to currents on a structure, as will be done in section 7.3, first the maximum current needs to be known. Since an OTEC plant is expected to have a lifetime of 30 years Kleute and Vroom [2014] and only 10 years of current data is available, a maximum expected current must be calculated by use of probability density functions. First, it is shown that the current speed distribution can be approximated by a Weibull distribution. Then the annual extreme values are approximated by a Gumbel distribution. By extrapolating the cumulative distribution function, the expected maximum velocity can be calculated. The method used here is described in Palutikof et al. [1999], where different methods are reviewed for assessing extreme wind speeds. This method can also be applied to other environmental extremes Gringorten [1963].

7.2.1 Weibull distribution of current velocities

First, an overview was made of occurence of absolute current velocities in bins of 0.05 m/s. This fitted a Weibull distribution, a general distribution that is often used for environmental parameters, such as wind speed, wave height and current speed Ott [1995]. The Weibull distribution is defined as:

$$f(x) = \frac{k}{\lambda}\left(\frac{x}{\lambda}\right)^{k-1} exp(-(x/\lambda)^k) \tag{7.1}$$

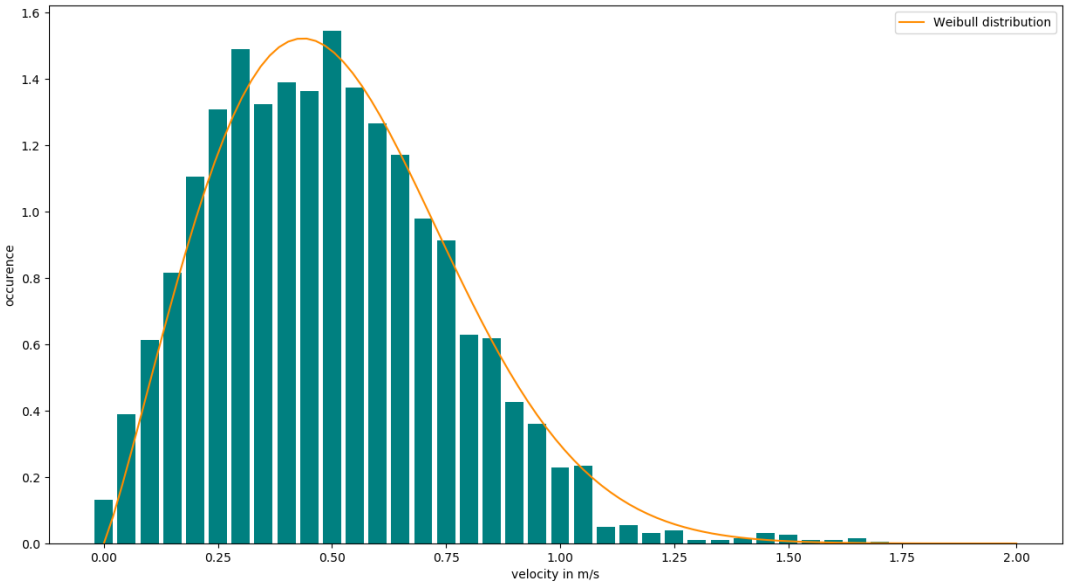

Figure 7.4: Distribution of current velocities at the chosen location for the 10 years of data, with a Weibull probability density function plotted in orange. $k = 2.09$ and $\lambda = 0.59$.

where k is a shape parameter and λ is a scale parameter of the distribution. In Figure 7.4, the occurance of absolute surface velocities at the chosen location of section 7.1.5 is shown. The Weibull distribution is plotted on top, to show the good fit.

7.2.2 Gumbel distribution of annual maxima of current velocities

After this first step, the yearly maxima were taken and a new distribution was plotted for these maxima. Within extreme value theory, there are three types of probability density distributions that can be used. Type I is the Gumbel distribution, type II is the Fréchet distribution and type III is the Weibull distribution. The Generalized Extreme Value (GEV) distribution combines these three types into one generalized distribution. If the Weibull distribution is used for extreme values, it relates to extreme minima. The Fréchet distribution includes a lower limit for the extreme values. Since the current study concerns maxima without a lower limit, the Gumbel distribution was used. It showed good agreement with the GEV. The probability density function of the Gumbel distribution is:

$$f(x) = \frac{1}{\sigma} exp(-\frac{x-\mu}{\sigma} - exp(-\frac{x-\mu}{\sigma})) \tag{7.2}$$

where μ is a location parameter and σ is a scale parameter that should be positive.

7.2.3 Extrapolation in order to determine the expected maximum current velocity

Figure 7.6 shows a Gumbel Plot. This plot resembles a linearized cumulative distribution function with the axis reversed and shows the annual maximum velocity on the y-axis

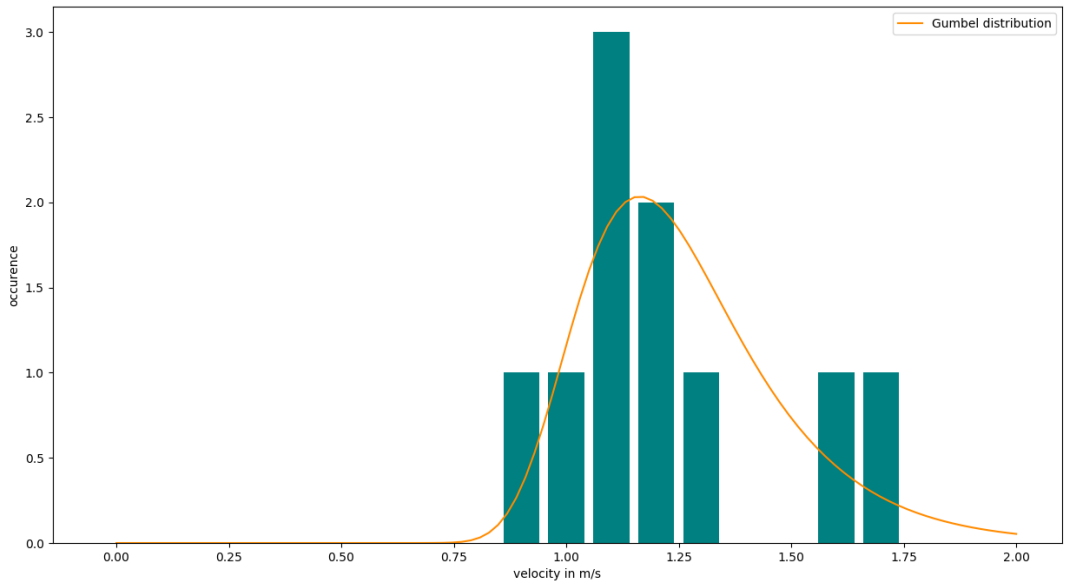

Figure 7.5: Distribution of annual velocity maxima, with a Gumbel distribution plotted on top of it. The Gumbel distribution parameters are: $\mu = 1.16$, $\sigma = 0.18$.The maxima that were found have the following values in the following years: 1,74 m/s (2007), 1.19 m/s (2008), 1.61 m/s (2009), 1.13 m/s (2010), 1.02 m/s (2011), 1.17 m/s (2012), 1.31 m/s (2013), 0.95 m/s (2014). 1.28 m/s (2015), 1.28 m/s (2016).

and the reduced variate on the x-axis. The reduced variate x_{Gumbel} is defined as:

$$x_{Gumbel} = -ln(-ln(F(x))) \tag{7.3}$$

where $F(x)$ is the probability that an annual maximum speed is less than x. It can be calculated by sorting the annual maxima from low to high x_m and then:

$$F(x_m) = \frac{m - 0.448}{N + 0.104} \tag{7.4}$$

with N being the total number of annual maxima, ten in this case [Gringorten, 1963]. The reduced variate relates to the return period T of the annual maximum by:

$$T = \frac{1}{1 - F(x)} \tag{7.5}$$

By extrapolating the least-squares approximation for the current maxima, values with a higher return period than the current values can be found. An OTEC plant is assumed to have a lifetime of 30 years [Kleute and Vroom, 2014]. The maximum expected surface current velocity in 30 years is 1.84 m/s. This can also be seen in Figure 7.6.

However, in the past ten years, no hurricane has passed over Curaçao. Therefore, the effects of a nearby hurricane are not included in the above method. Maximum current velocities will be higher when a hurricane passes.

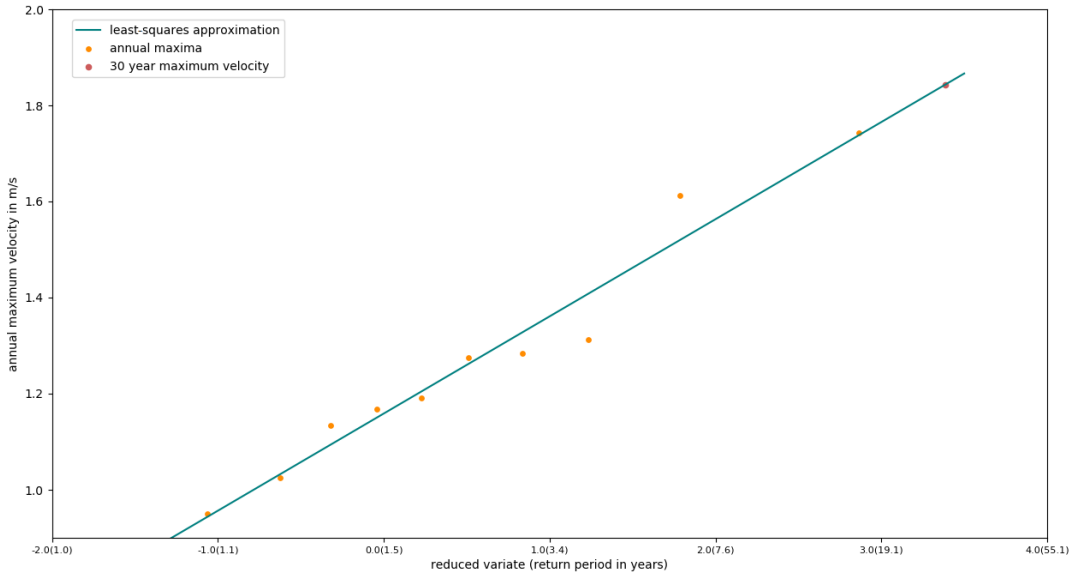

Figure 7.6: A Gumbel Plot, showing the ten annual maxima on the y-axis and the Gumbel reduced variate with the return period inbrackets on the x-axis. A least-squares approximation is drawn. Extrapolation renders a maximum surface velocity with a 30 year return period, which can be found in red. The value of the maximum is 1.84 m/s.

7.3 Hydrodynamic forces on a 10 MW offshore OTEC plant at the given location

7.3.1 Modeling the OTEC plant

The current is generally assumed to be a quasistatic phenomenon because the variation of the current is very slow. Furthermore, it is assumed that the floating part of the offshore OTEC plant is a similar vessel as the ship *PROTEFS* that has been transformed into an FPSO (a Floating Production, Storage and Offloading vessel) as designed by Guerrero [2017]. Details of the ship *PROTEFS* can be found in Appendix L. This is a ship hull that weathervanes due to winds and currents around its turret. These currents and winds are generally from the same direction, from the east. However, there can be a difference of about maximum 30° between the two, as seen in Figure J.21. In this figure, the long term mean of the annual wind direction and the annual surface current direction are shown. However, the direction of the FPSO will mostly depend on the current direction, and forces on the FPSO are biggest when wind and current are acting on the vessel from the same direction. Therefore, only a difference between wind and current of 0° will be used.

The diameters and lengths of the pipes used for the calculation, as in Table 7.1 are from Kleute and Vroom [2014]. Other parameters that are used are also given in Table 7.1. For calculation of density, see equation 2.4.

For calculating the force per meter, the drag equations were used. The areas A and S, frontal area and wetted area respectively, are divided by depth, so their units are m^2/m.

$$F_{form} = \frac{1}{2} C_d \rho A v^2 \tag{7.6}$$

Table 7.1: Parameters used for calculating the hydrodynamic forces on a 10 MW OTEC plant.

Parameter	**Symbol**	**Value**	**Units**
Length of FPSO	L	217.0	m
Width of FPSO	W	32.2	m
Depth of FPSO	T	12.5	m
Outer diameter of CWP	D_{cwp}	4.5	m
Outer diameter of WWP	D_{wwp}	4.5	m
Outer diameter of DP	D_{dp}	6.9	m
Length of CWP	L_{cwp}	900-T	m
Length of WWP	L_{wwp}	0	m
Length of DP	L_{dp}	100-T	m
Water viscosity	ν	1.3 * 10^{-6}	m^2/s at 10°C
Angle between FPSO and current	ϕ	0	°

*Table 7.2: Parameters changing over the three depth parts; 1) only FPSO, 2) CWP and DP, 3) only CWP. * is the ITTC-1957 line, standard from the International Towing Tank Conference. ** from the boundary layer theory from Blasius for laminar flows.*

Parameter	**Symbol**	**Value**	**Units**
Drag coefficient	C_{d1}	0.12	-
	C_{d2}	0.3 - 12 (depending on Re)	-
	C_{d3}	0.3 - 12 (depending on Re)	-
Friction coefficient	C_{s1}	$0.075/(\log Re - 2)^{2}$*	-
	C_{s2}	" or $1.328/\sqrt{Re}$ **	-
	C_{s3}	"	-
Frontal area	A_1	$0.8W$	m^2/m
	A_2	$D_{cwp} + D_{dp}$	m^2/m
	A_3	D_{cwp}	m^2/m
Wetted surface	S_1	$1.1L$	m^2/m
	S_2	$(D_{cwp} + D_{dp})\pi$	m^2/m
	S_3	$D_{cwp}\pi$	m^2/m

$$F_{skin} = \frac{1}{2} C_s \rho S v^2 \tag{7.7}$$

The depth is divided into three parts, between which all parameters except for current speed are assumed constant. The first part covers the depth of the FPSO, down to 32.2 m below the sea surface. The second part is the cold-water pipe (CWP) and the discharge pipe (DP). The length of the warm-water pipe (WWP) is not taken into account, because the FPSO itself extends deep enough to be always submerged, because taking in the water from even deeper would decrease the temperature difference needed for economically viable OTEC, and mostly because forces on the WWP will be small. The discharge pipe is assumed to be 100 m long. Consequently, the second part of the depth is 67.8 m deep and extends to 100 m deep. The last part includes only the CWP and extends to 900 m. An overview of these depths can be found in Figure 7.7. In equation 7.6 and 7.8, the parameters that change depending on the depth are C_d, C_s, A and S.

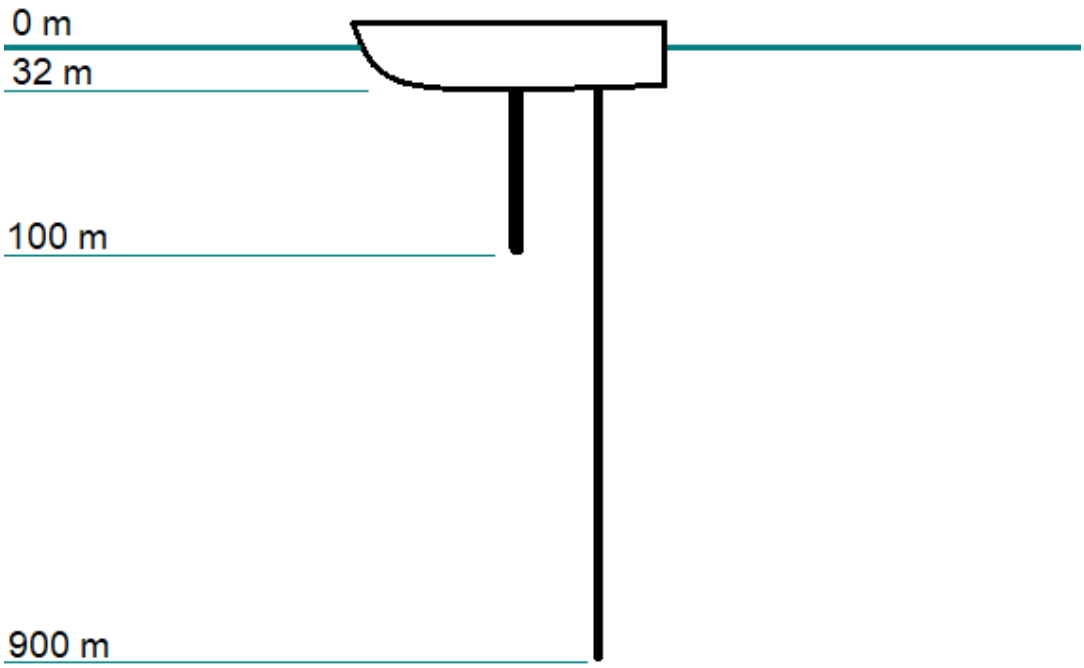

Figure 7.7: An overview of the OTEC system and the three parts in which system parameters are assumed to be constant. Not on scale.

The friction and drag coefficients C_d and C_s depend on the Reynolds number.

$$Re = \frac{VD}{\nu} \tag{7.8}$$

in which D is a relevant length parameter and V a relevant velocity parameter. In case of the FPSO, $D = L$. In case of pipes, $D = D_{pipe}$. For a hull, the friction coefficient C_{s1} can be calculated by the ITTC-57 formula [International Towing Tank Conference (ITTC), 1957], which depends on the Reynolds number. It is given in Table 7.2. The form coefficient of a ship that has a hydrodynamic shape, C_{d1}, is around 0.12. The friction coefficient of a pipe $C_{s2,3}$ can be calculated by Blasius formula if the flow is laminar or by the ITTC if the flow is turbulent. It thus depends very much on the Reynolds number. Different drag coefficients for pipes $C_{d,pipe}$ are given in table 4.3 in Journée and Massie [2001]. An overview of these parameters or how thay can be calculated is given in Table 7.2.

7.3.2 Horizontal forces due to current

The profile of the maximum surface current found in the ten years (on 10 July 2007 due to a major eddy), is multiplied by a factor to obtain the maximum expected surface current velocity profile. This profile can be seen in Figure 7.8a. The result of above calculation, the force profile on the pipes due to currents, can be seen in Figure 7.8b.

From the forces on the pipe, the shear, moment, curvature and deflection along the pipe can be calculated by beam theory. The pipes will be modelled as beams, subjected to a

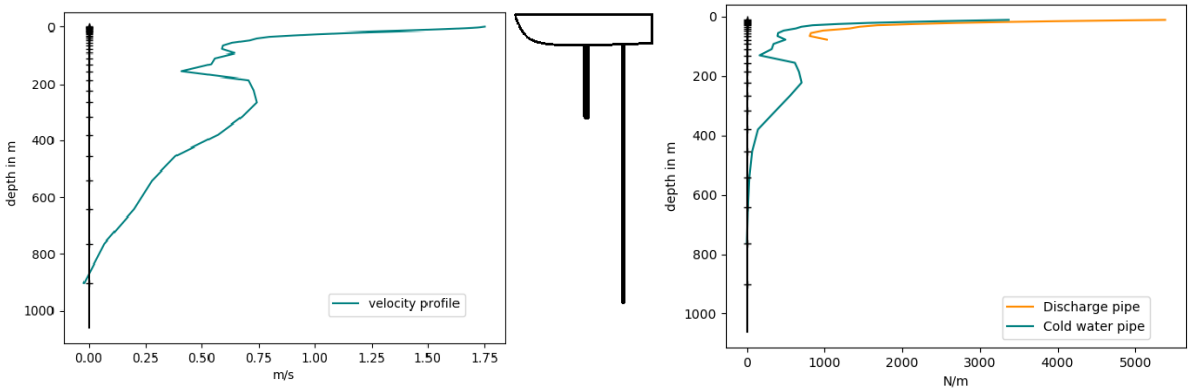

(a) Maximum expected current profile for the pipes.

(b) Profile of the force per meter.

Figure 7.8: Current profile in Figure 7.8a, used to calculate the force profile on the discharge pipe (orange) and the cold-water pipe (blue) in Figure 7.8b. A schematic offshore OTEC system is shown for reference, this is not on scale.

Table 7.3: Parameters for the pipes. Assumed is that the pipes are made of high density polyethylene (HDPE). Wall thickness is calculated using the a Standard Dimension Ratio of 17 Veijer [2017].

Parameter	**Symbol**	**Value**	**Units**
Youngs modulus	E	900	MPa
Moment of inertia	I	$\frac{\pi}{2}(r^4 - (r-t)^4)$	m^4
Pipe radius	r	$D_{pipe}/2$	m
Wall thickness (DP)	t_{dp}	0.43	m
Wall thickness (CWP and WWP)	t_{cwp}	0.27	m
Yield stress	σ_y	26	MPa

distributed load, clamped at the connection point to the FPSO and free at the bottom. This theory is explained in chapter 6 and 12 in Hibbeler [2008] and shown by the formulas below. Euler beam theory is used.

$$\frac{dV}{dx} = -w(x) \tag{7.9}$$

$$\frac{dM}{dx} = V \tag{7.10}$$

$$\frac{d^2v}{dx^2} = \frac{M(x)}{EI} \tag{7.11}$$

In the above formulas, $w(x)$ is the intensity of the distributed load along the beam in N/m, where x is along the length of the pipe or beam, V is the shear in N, M is the moment in Nm, v is the deflection in m, E is the Youngs modulus and I is the moment of inertia. The value of the integration constants can be determined by applying the boundary conditions. At the clamped side, these boundary conditions are $v(x=0) = \theta(x=0) = 0$, where θ is the curvature $\frac{dv}{dx}$. In othe words, the curvature and the deflection are zero at the connection to the FPSO.

The results for these calculations can be found in Figures 7.9. The total horizontal force on the OTEC system due to the maximum expected currents is 495 kN. The total horizontal force on the FPSO is 63 kN, while the total horizontal force on the discharge

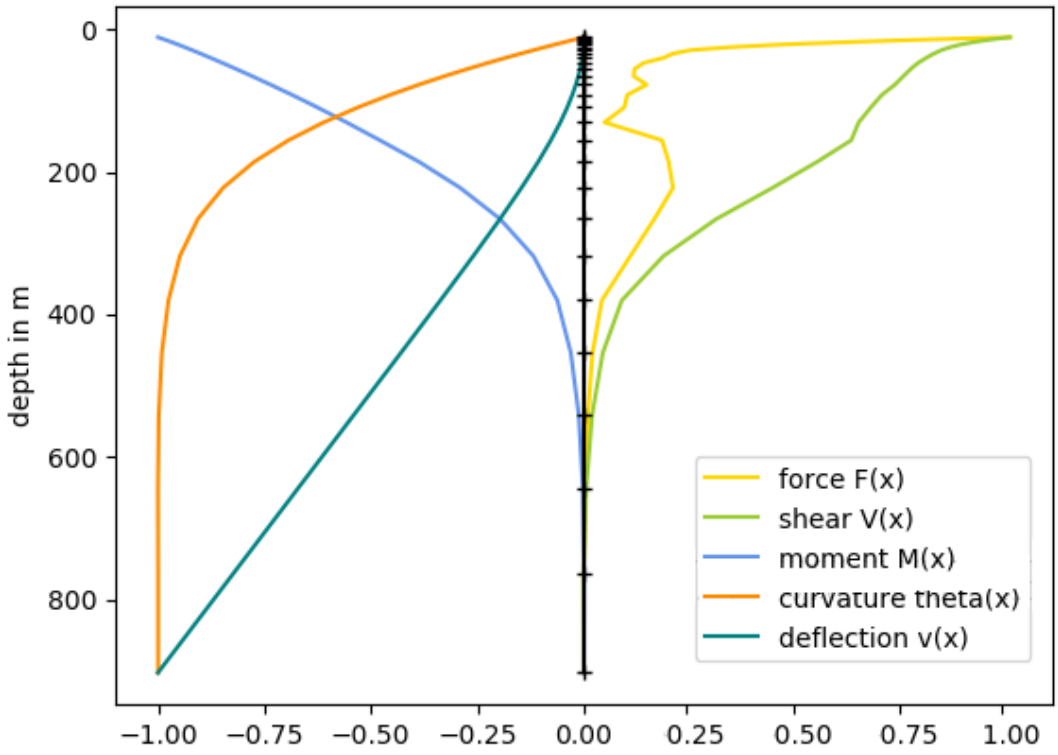

Figure 7.9: Profile of the force, shear, moment, curvature and deflection along the cold-water pipe. The values are normalized in order to visualize them in one plot.

pipe and the cold-water pipe is 152 kN and 277 kN respectively. The force on the FPSO looks small in comparison to the other two. However, the shape of a ship hull is designed such that friction forces will be low, and the considered pipes are fairly huge, in length as well as in diameter.

7.3.3 Deflection and stresses in the cold-water pipe

In Figure 7.10 the deflection of the cold-water pipe over the length due to the maximum expected current is shown. It can be seen that the maximum deflection is at the lowest point of the pipe. This is as expected because the pipe has no restrictions there. The maximum deflection is about 370 m along with the current. A similar calculation was performed for average current velocities. The pipe deflection for that situation was around 80 m. The maximum moment can be found at the top, near the floater. A stiff (clamped) connection was assumed. The maximum moment can be used to calculate the maximum stress in the pipe.

The maximum bending stress σ_{max} is calculated by:

$$\sigma_{max} = \frac{M_{max} y_z}{I} \tag{7.12}$$

y_z is the distance from the neutral axis. To find the maximum stress, y should also be maximum. The maximum bending stress in the pipe due to the deflection caused by currents, 6.68 MPa, stays well below the yield stress of the material, 26 MPa.

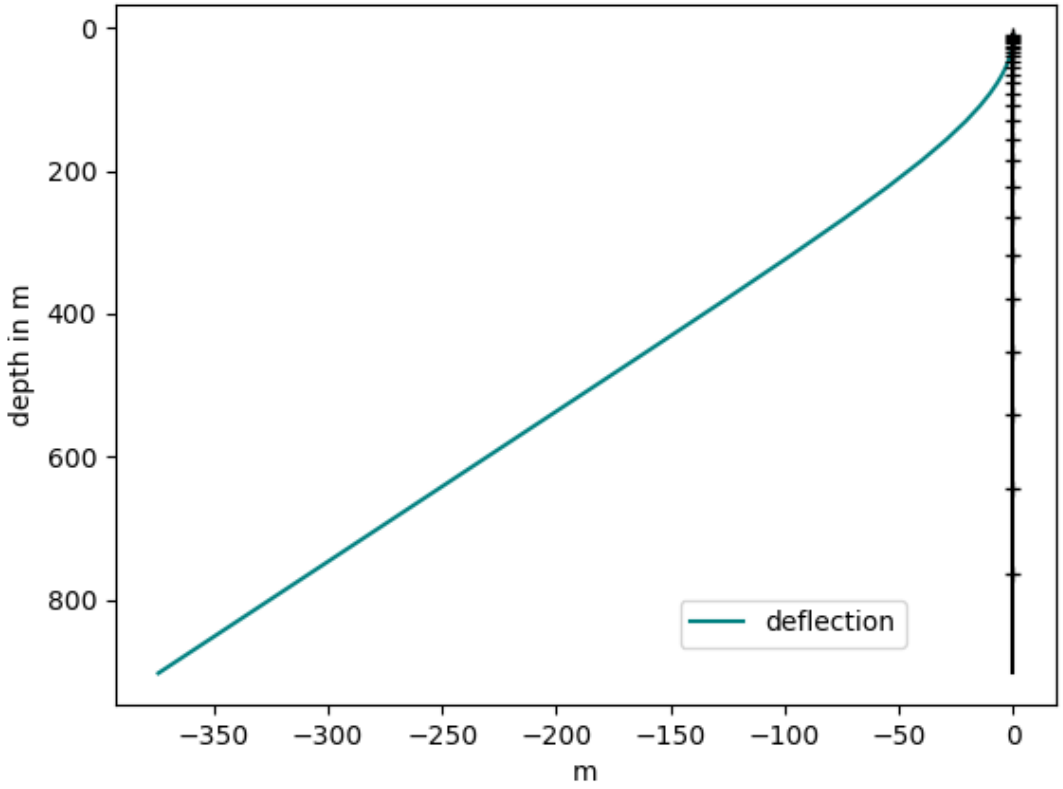

Figure 7.10: Deflection of the cold-water pipe.

7.3.4 Discussion of used parameters and results

To come to the conclusions in the above sections, the problem was highly simplified. First of all, the overall maximum velocity profile was assumed to be similar to another annual maximum. Secondly, the parameters were assumed to be constant over certain depths and gravity was not taken into account. No interaction was assumed between the two pipes, by one being in the other's wake. Furthermore, the values of some of the used parameters were assumed, or adapted from literature. In particular, the pipe coefficients $C_{s,pipe}$ and $C_{d,pipe}$ cause an uncertainty, because these values have a rather large range, from 0.3 to 12, and because they relate directly to the applied force. Moreover, the cold-water pipe was modeled as a clamped-free Euler beam, while in reality the pipe deflection is restrained at the tip by a weight or mooring system.

No waves or wave forces were taken into account in the above calculation. Waves are known to be able to exert high dynamic forces on structures in the ocean. However, waves are not included in the dataset analyzed. Moreover, waves are considered a smaller scale phenomenon compared to the parameters that have been analyzed. Since it was not included in the analysis and the pattern identification, it was left out of the force calculations as well.

Therefore, these calculation must mostly be regarded as an example case of how the Mercator data can be applied when designing an offshore OTEC plant. Consequently, the results of the calculation are not immediately applicable, but can be seen as a rough estimation of the order of the forces.

The general form of the deflection is as one would expect for a clamped-free beam. The total deflection at the tip is relatively large. This can however be explained firstly by the use of HDPE instead of steel. HDPE has a much lower Youngs Modulus, thus being more elastic and allowing for higher deflections. Secondly, the maximum expected current in the total lifetime of the OTEC plant were applied, with at a depth of 400 m still a velocity of 0.5 m/s. This large deep current exerts a force and a large moment on the pipe, due to the long arm. This causes large deflection.

Since the FPSO will weathervane due to currents, the pipes could be placed strategically behind each other in order to decrease the forces on the pipes. The maximum deflection of both pipes should be taken into account to prevent collision. Since the currents would mainly be coming from the foreship of the FPSO, the pipes could be given a more hydrodynamic shape, to lower forces. Making the connection to the FPSO flexible, will reduce the moment and therefore bending stresses in the pipe. The total tip deflection, however, could become bigger. The application of a weight or mooring system at the tip will highly reduce the deflection. However, an added force in vertical direction (e.g. a weight) will add to the stresses in the pipe. These stresses were calculated to be 1/4 of the yield stress without weight. The effect of this added vertical force should be considered carefully in the design to prevent exceeding of the yield stress.

7.3.5 Forces due to Vortex Induced Vibrations (VIV)

Vortex induced vibrations are caused by vortex shedding in the wake of the pipe. This phenomenon is known in the offshore industry to occur for pipes, mooring lines and risers, slender structures where the current is perpendicular to the axis of the structure. Whether VIV occurs depends on the frequency of the vortex shedding. Vortex shedding occurs depending on the current velocity and the size and shape of the structure in the water. It can form a risk when the vortex shedding frequency f_v is close to a natural frequency of the structure in the water ω_n. Then resonance will occur which can cause fatal damage due to fatigue to the structure.

$$f_v = \frac{StV}{D} \tag{7.13}$$

where St is the Strouhal number and depends on the Reynolds number Re. V and D are again relevant velocity and length parameters. Natural frequencies of the pipes can be calculated by:

$$\sqrt{\omega_n} = \frac{n\pi}{L\sqrt[4]{\frac{\rho A}{EI}}} \tag{7.14}$$

where ω_n is the n^{th} frequency of the pipe, L is the length, ρ is the density, A is the area of the section of the pipe and E and I are the Youngs modulus and the moment of inertia. In this case, the pipes are modelled as Euler-Bernoulli beams. However, this natural frequency will change when water flows through the pipe and it is fully submerged in water.

This complex problem will not be further explored in this study. However, since it is a well known phenomenon that could have catastrophic consequences, it is mentioned nonetheless. Mitigation measures to prevent VIV are also known. This mostly involves structural elements on the outside of the pipe to disrupt the flow around the pipe.

7.4 Depletion of cold or warm water due to long term and large scale OTEC

Another question when regarding the impact of the OTEC industry on the environment, is the availability of the temperature difference. In other words, whether the cold or warm water supply will ever finish and whether the intake of this cold and warm water will influence the properties of the water downstream. The volume fluxes at both sides of the island (the two regions defined with a transect of 100 km long, as in Chapter 6) is compared to the volume flux as used by a 100 MW OTEC system. 100 MW would be enough to provide the baseload for Curaçao and ten times the amount that was regarded in this study. The volume of water used for such OTEC scale is less than 0.2% of the volume flux at one side of the island. It can be concluded that large scale influence is small.

7.5 Discharge water outlet

In section 7.1.2 and 7.1.3, location assessment was performed based on the intake of the OTEC system. It was also seen that taking this amount of water out of the ocean will not have a large effect on the ocean, considering the scale of OTEC that is proposed at the moment. However, when the temperature difference is 'harvested', the surface and deep water will be mixed and discharged back into the ocean.

To prevent the discharge water from changing the local environment, the length of the discharge pipe is chosen such that the discharged water has a neutral buoyancy. This means it has a similar density to the surrounding waters and therefore does not rise or sink. The length will therefore be of the order of 100 m. In Chapter 6, the currents at depth were analyzed. It was seen that to the south of the island, a subsurface countercurrent existed between 100 and 250 m. This would mean that around the depth of the discharge water outlet, the average volume flux is 0 Sv/m (with a large standard deviation of around 8 Sv/m).

This could pose a risk for disruption of the local environment. Grandelli et al. [2012] investigated the biochemical influence of an OTEC plant offshore of Hawaii. The study showed small local downstream changes in the picoplankton level. Since this should be modeled on a much smaller scale than has been the focus of the current study, it will not be further researched.

7.6 Summary

The mean water temperature at the surface south of Curaç, close to the Venezuela mainland, is significantly colder and shows more variation than water more to the north. This is due to locally upwelled cold water to the surface. It can be concluded that an OTEC plant should not be placed 50 km south of Curacçao to maintain a constant performance output.

A suitable OTEC location is chosen. The maximum expected current velocity in the lifetime of an OTEC plant at that location is calculated. Extrapolation of a Gumbel distribution is performed. This gives a maximum surface current velocity of 1.83 m/s. This maximum velocity is used for calculating the hydrodynamic horizontal forces on the OTEC plant. The cold-water pipe is modeled as a clamped-free beam. This gives a deflection of 370 m at the tip of the cold water pipe and a bending stress of 6.7 MPa.

8 Discussion

In this chapter, the results are put in context and compared to previous studies. Generally, there is good agreement with different studies. Furthermore, this chapter discusses the contribution of the current research to what had already been investigated. Also, some limitations to the research are discussed. The results from Chapter 7 are of a different kind. Therefore, a separate section is devoted to their discussion, Section 8.5.

8.1 Comparison of identified patterns to literature

The results of the present research are generally in good correspondence with the reviewed literature in Chapter 2. This indicates that the data from the Mercator Ocean model is a reasonable representation of the processes in the ocean.

The general current direction from east to west and the maximum current velocities of one meter per second in the south of the Caribbean Sea as described by Fratantoni [2001] and Centurioni and Niiler [2003] were also found in the present study. This present study has elaborated on this and shown that velocities of approaching two meters per second can also occur south of Curaçao. Furthermore, it has shown that the wind speed, as well as the current speed, show a semiannual cycle. This cycle in wind speed was also described by Wang [2007].

The surface current jet at 17°N as described by Centurioni and Niiler [2003] has been identified. However, it was much less distinct and fast, compared to the southern jet. When observing the daily surface plots, this jet was hard to distinguish from the surrounding currents. However, when analyzing the mean surface plots, the northern jet was visible.

The phenomenon of upwelling in the Caribbean Sea has been extensively reported. The current study confirms its presence, its relation to wind and peak in winter. However,

the relation to the subsurface countercurrent as referred to by Alvera-Azcárate et al. [2009a] was not found in the vicinity of Curaçao.

The presence and advection of eddies are an important factor in the variability of the surface currents in the Caribbean Sea. Very large anticyclonic eddies have been observed and analyzed. The advection speed found in this research supported the findings of Richardson [2005]. Only the very large, longer existing and southern eddies were considered in this study. Therefore, no founded estimate of the total number of eddies per year forming in the Caribbean Sea can be given. The average amount of large eddies per year found in this study is five, while the estimate of other studies range from 4 to 12 [Richardson, 2005].

Richardson [2005] concluded from surface drifter data that more anticyclones are formed in summer and fall than during winter and spring. This contradicts the findings of the current study, where a peak in eddy generation has been observed in March and April. However, Richardson [2005] based his assumption on the number of looping days of the drifters per months. This had a peak in October and November. However, this number does not necessarily coincide with generation period of the eddies, but more with eddy population. Largest eddy population found in the current study was in the summer months. The difference in conclusions between these two studies can also be explained by the difference in observation technique. The number of anticyclonic eddies was 10 for the study of Richardson [2005], compared to 40 in the current study. Besides, in the current study, criteria considering eddy diameter and generation location were applied when observing the eddies. No such thing was done in the other study. The trajectories of most anticyclonic eddies observed in the study from Richardson [2005] coincides with the general trajectory found in the current study.

Different theories exist concerning eddy generation in the Caribbean Sea. One of the theories is that rotating water enters the Caribbean Sea and, once within, forms 'new' eddies. Since the region of interest for this study did not include a large enough part of the Atlantic Ocean, that hypothesis cannot be supported or rejected. However, the analysis performed in this study strongly suggests a link between the formation of eddies and the persistent and strong upwelling region near the Grenada Passage entrance into the Caribbean Sea. Conditions for eddy generation are favorable there, with high velocities, strong horizontal shear and strong horizontal density gradients, inducing instabilities that give rise to eddy generation. The assumption that frontogenesis plays a major role in the formation of large eddies in the Caribbean Sea, is investigated by C. Pérez and R. Calil [2017].

The presence and size of subsurface countercurrents along the southern border of the Caribbean Sea have been suggested by Andrade et al. [2003]. The results of his study are in good agreement with what has been concluded about the subsurface currents by the present study. However, the present study has also indicated the large variability and the difference in depth of the subsurface currents between the two sides of Curaçao.

The ocean waters in the southern jet of the Caribbean Current are believed to be coming from the South Atlantic ([Johns et al., 2002], [Richardson, 2005]). High correlation coefficients between the volume flux through the Grenada Passage, the most southern passage on the eastern border of the Caribbean Sea, and volume flux around Curaçao

were found. This indicates that water in the southern jet of the Caribbean Current enters the Caribbean Sea from the southeast. The water flowing northwards along the Brazilian coast towards the southeast of the Caribbean Sea comes from the South Atlantic. Consequently, these two findings support each other.

A link of volume flux in the Caribbean Sea to El Niño was not found, although it was expected. What could change this result, is taking a bigger transect up to the Dominican Republic in the north and thereby taking into account the entire volume flux through the Caribbean Sea. By doing this, two physical boundaries (of land, in the north and in the south) will prohibit the volume flux to show values that are not representative of the whole. Another possibility is to correlate wind speed, surface current or upwelling to El Niño.

8.2 Addition to existing knowledge

The current research is an addition to studies performed for the oceanography of the Caribbean Sea. Partly, because of the method used for identification of oceanographic processes. Models can be used to calculate simplified situations for a large area, while measurements can be used to validate the model results to reality. However, measurements, in particular for large areas, can be very expensive. The method used in this research combines these two in a way. The Mercator Ocean model models reality and includes complex mechanisms, but is assimilated continuously with measurement data from different sources.

In addition, the current research contributes to the common knowledge of the Caribbean Sea, because it has pointed out some of the dominant oceanographic features in the eastern Caribbean Sea. The fast-current jet in the south and its interaction with the wind, upwelling and eddies have been described. Furthermore, quantification, support and application of previously found phenomena has been achieved.

Furthermore, this study has focussed on Curaçao and it's vicinity, in addition to regarding the Caribbean Sea or the Venezuela Basin as a whole. An oceanographic study had not been done on this small scale for this region. Usually, large scale studies are preferred because of the scale of the processes, for example, eddies that influence the entire Venezuela Basin. However, to be able to find a useful application for OTEC, smaller scale research is required and has been performed in the current research. From the perspective of OTEC, no research on this large oceanographic scale has been done before.

The implication of the current comprehensive analysis of the ocean parameters in the vicinity of Curaçao is that the OTEC industry is able to make better-founded choices regarding possible OTEC plant locations, resilience against environmental parameters and the dimensions of the different pipes.

8.3 Limitations

The performed research also knows some limitations. A comprehensive explanation of all processes described and their interaction has not been given. Large variability in volume fluxes and velocities has not always been explained or understood. Nor has the eddy generation mechanism been completely sorted. In fact, only a suggestion of what may be important parameters has been given. Subsurface currents have only been observed and analyzed around Curaçao, not along the rest of the Venezuela and Colombia coast, where they have also been observed by others. Moreover, a thesis project knows a limited duration. Consequently, not all questions that arose when analyzing the Mercator data have been addressed with the amount of time and attention that they might deserve. This would have improved the predictability of the processes and thereby increasing the applicability and reliability for the OTEC industry.

This project has regarded the physical properties of the ocean water. Therefore, it did not treat the interaction with the marine biology, e.g. nutrients being brought to the surface by the OTEC process. The biology is typically limited by and very much depends on the physical environment. The understanding of the physical aspects of the region of interest will provide a good background for a biological study, that could be a follow-up project for the current one.

8.4 Error ranges in the Mercator dataset

As discussed in Chapter 3, the analyzed dataset is merely the output from a model. As also discussed in that chapter, validation has been performed for the output of this model. Values for mean misfits of different parameters in the dataset compared to measured data can be found in table 3.1. These misfits are small enough for the major conclusions of this research to remain valid. This validation, however, was done by the same organization that also developed the model. It is therefore questionable whether that would provide unbiased validation.

The analyzed dataset has also induced limitations for the research. For example, the number of parameters available, the resolution in which they were available, and the timespan over which they were available, have put restraints on what could be done. For example, it was not possible to zoom in more than has been done without losing a sense of the bigger picture, and smaller scale processes that might be relevant for OTEC, like coastal processes, could not be analyzed.

8.5 Relevance to OTEC

The Mercator Ocean model is a very suitable tool for assessing a possible OTEC location based on the large-scale ocean temperature variations. The model data are consistent with the literature and span a reasonable period of time (ten years). Consequently, the temperature differences and variations around Curaçao are quite well understood.

The maximum expected current velocity was calculated using an extrapolation technique. However, extrapolation of data of the past ten years is only applicable when ocean and weather conditions remain constant over the extrapolated time. This is an assumption that has been done. For example, climate change and increasing hurricane strength might change these conditions over time. These effects are not taken into account when calculating the maximum expected currents.

As stated in Section 7.3.4, when calculating forces on the OTEC system, a highly simplified model was used. This exemplary application of the Mercator data shows the order of magnitude of the hydrodynamic forces on the cold-water pipe. The data can function as input for more detailed structural calculations used for the detailed design of an OTEC plant.

The variability of the currents, particularly over depth, is still a largely unexplored area and therefore less understood. In addition, modeling the exact interaction between the OTEC inflow, outflow and natural currents is quite a complex problem and needs further attention.

9 Conclusions

The aim of this research is to determine the natural current velocity pattern in the oceans around Curaçao. The conclusion of the research can therefore not be a simple answer. It is a general description of this pattern. Now and then, a more specific and detailed description is given, when there was tried to gain insight into the forcing mechanism and underlying processes. Another aim is to apply the obtained knowledge to the design and operation of a 10 MW offshore OTEC system.

This chapter discusses the results of this research, as presented in Chapter 2 to 7. The subquestions posed in Chapter 1 are repeated and answered.

9.1 Natural surface current velocity pattern

The research questions have been answered by the results described in Chapter 2 to 7. However, I do not pretend that this answer is complete in a way that every aspect of it has been addressed and fully understood. It includes only to a limited extent driving mechanisms of the flow. This yields many interesting topics for further research. Yet, a big first and comprehensive step has been taken and many aspects of the currents around Curaçao can now be considered as known or are more clear then they were before this research.

What is the spatial and annual pattern of the surface currents around Curaçao and what is the variability?

In the Venezuela Basin, largest velocities are found in the south, in a jet from the Grenada Passage along the Venezuala coast to the northwest. The intensity of this jet shows a semiannual cycle, with a global maximum in boreal winter months, December, January and February, and a global minimum in boreal fall, September, October and November. A local minimum is found in May and a local maximum is found in July. Interannual variability is big, with an average standard deviation of 0.2 m/s. with the

biggest variability between May and September. In that period, the standard deviation is up to 0.4 m/s. This is likely to be caused by eddies. To the south of Curaçao, surface currents are generally higher than to the north of the island. To the south, the mean velocity is 0.5 m/s, and the current direction is more unidirectional, with 83% of the time in a 34° bin to the northwest. To the north, the mean velocity is 0.3 m/s and only 47% is in that same 34° bin.

What is the spatial and annual pattern of the winds around Curaçao and how do they correlate to the surface currents?

Wind direction is from east to west over the Caribbean Sea. Highest wind speeds are found to the south of the Caribbean Sea. Wind speed shows a semiannual cycle, similar to the surface currents. Pearson correlation coefficients between wind speed and surface current speed show reasonably high values, with wind being the forcing factor. The correlation is higher for the surface currents to the south of Curaçao, where R is 0.52, than to the north. The Pearson correlation factor R for the north of Curaçao is 0.33. Correlation coefficients increase when taking the average of all ten years, instead of all ten years. Respectively, R is 0.76 and 0.61 for the south and the north side of the island. By doing this, peaks in surface currents caused by processes unrelated to the wind, for example, eddies, are filtered out by averaging them with other years when no peak occured at that specific time in the year.

What is the spatial and annual pattern of the sea surface temperature around Curaçao and how does it relate to the surface currents?

The two most important factors influencing the sea surface temperature, are incoming solar radiation and upwelling. Incoming solar radiation causes the sea surface temperature to be lowest in March and highest in September. Coastal upwelling at the north coast of Venezuela causes the sea surface temperature to decrease. Since upwelling is induced by wind and highest wind speeds are found in winter[Wang, 2007], upwelling is most pronounced in winter. The east-to-west surface current jet follows the cold-water front and is intensified along it. This can be explained by the Geostrophic Balance and the Thermal Wind Balance. Figure 9.1 and 9.2 show the working principle of these two balances in the Caribbean Sea and their influence on the westward current. The cold-water front leads the jet along the south of Curaçao. This explains why correlation coefficients for wind and surface currents are higher for the waters south of Curaçao. Higher wind speeds cause more upwelling and a stronger cold-water front and therefore intensification of the currents along the south of Curaçao.

What is the influence of eddies on the surface currents and how are the Caribbean eddies generated?

Eddies are a major source of large local and temporal water velocities. The average surface velocities and volume fluxes around Curaçao due to eddies double, compared to when no eddy is present. On average five large anticyclonic eddies per year are identified with an advection speed of 12 cm/s. The month of April is found to be most prone to eddy generation, but the eddy population shows a semiannual cycle over the year with peaks in January and July.

The generation of Caribbean eddies is a subject with much discussion and theories exist-

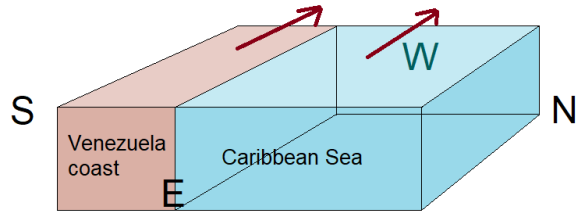

(a) Wind along the coast.

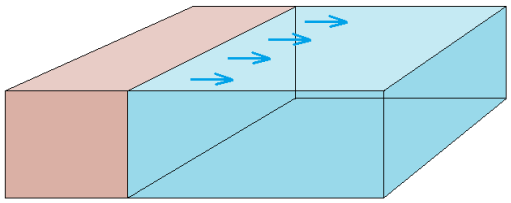

(b) Ekman transport offshore.

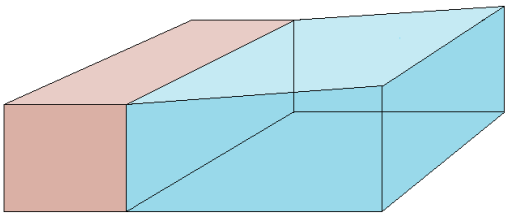

(c) North-south pressure gradient.

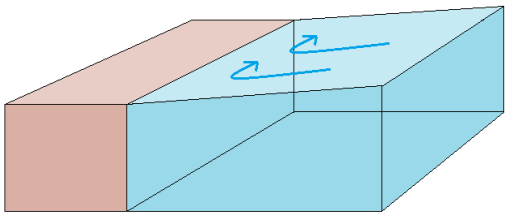

(d) Geostrophic Balance.

Figure 9.1: Schematic overview of the working principle of the Geostrophic Balance along the coast of Venezuela. The figures show the coast of Venezuela to the left and the Caribbean Sea to the right. North is to the right, as depicted in Figure 9.1a. Figure 9.1a shows the Caribbean Low Level Jet blowing from east to west along the coast of Venezuela. Figure 9.1b shows the resulting Ekman transport offshore. This leads to in increase in sea surface height offshore, resulting in a north-south pressure gradient, as in Figure 9.1c. A westward flow is the result of the pressure gradient balanced by Coriolis and a geostrophic current. This is shown in Figure 9.1d.

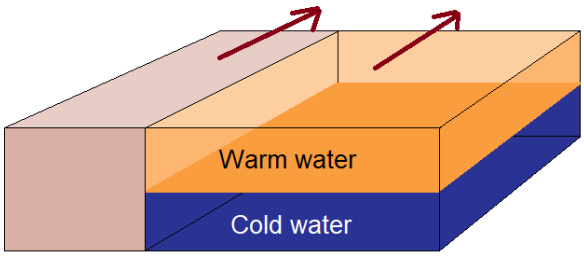

(a) Wind along the coast.

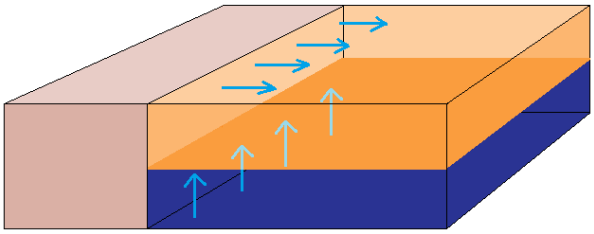

(b) Coastal upwelling.

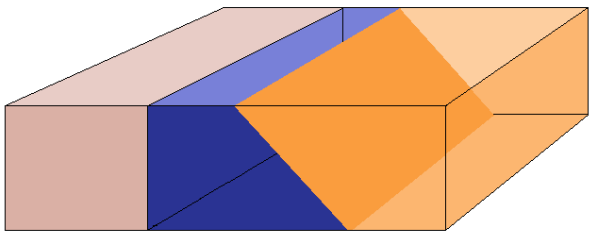

(c) Baroclinic instability.

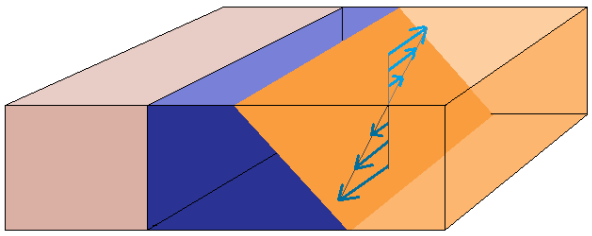

(d) Thermal Wind Balance.

Figure 9.2: Schematic overview of the working principle of the Thermal Wind Balance along the coast of Venezuela. A similar situation is shown as in Figure 9.1. Cold water in purple is upwelled in Figure 9.2b, by the wind in Figure 9.2a. Figure 9.2c shows a situation with baroclinic instability due to a horizontal temperature difference. Figure 9.2d shows the balancing of this instable situation with a vertical velocity shear, with westward velocity at the surface.

ing alongside each other. The current study suggests interaction between high velocities entering the Caribbean Sea through the Grenada Passage and the cold-water front due to strong upwelling near that entrance along the Venezuelan coast. This suggestion is based on generation location and period. These two processes cause instability of the flow that can be triggered into becoming meanders and eddies.

What is the current profile over depth around Curaçao and what is the variability?

On both sides of the island of Curaçao, subsurface currents are found that are in opposite direction compared to the surface currents. At the south side, this subsurface countercurrent is between 100 and 250 m water depth, while on the north side it is between 300 and 1600 m water depth. The speeds of these countercurrents are much lower than speeds at the surface, less than 0.13 m/s at the south side and even less than 0.07 m/s at the north side. The variability of these subsurface currents is very large, even such that the countercurrents are not always present. The persistence of the subsurface current is bigger on the north side of the island. The intensity of these subsurface countercurrents is larger at the southern side of each transect, so against the coast of Venezuela at the south side of Curaçao and against the coast of Curaçao at the north side of the island.

What is the spatial and annual pattern of the volume fluxes around Curaçao and what is the variability?

Volume fluxes in the Caribbean Sea show large variability. This variability includes interannual, intra-annual variability and variability between the north and south side of the island. At the south side of the island, a similar semiannual cycle is seen as described in Section 9.1. The mean volume flux is 2.0 Sv with a mean standard deviation over the ten years of 3.7 Sv. For a transect defined on the north side of the island, extending 100 km into the Venezuela Basin, the mean volume flux is -0.5 Sv with a mean standard deviation of 5.5 Sv. Especially the volume flux north of Curaçao correlates well to the volume flux through the Grenada Passage, when a lag between the two locations of about twenty days is applied. This correlation can be explained by the path of the water flowing into the Caribbean Sea, that is direction to the northwest and passes Curaçao on the north.

9.2 Application to OTEC

What is the time period with the optimal ocean circumstances for installation, commissioning, maintenance or decommissioning of an offshore OTEC plant around Curaçao?

Lowest current velocities are found in September to November, while highest velocities are seen in December to March. Highest variability is seen in the period in between. Low current velocities are desirable for accessing the OTEC plant, because it will simplify the procedure of for example maintenance. The period with lowest current velocities coincides with the hurricane season, which is from June until November. Hurricanes, however, are predictable up to a week in advance, and are therefore unlikely to form a big risk. Other than that, most hurricanes pass north of Curaçao.

What is the optimal location for a 10 MW offshore OTEC plant around Curaçao with regard to temperature differences and bathymetry?

The vicinity of Curaçao is affected by upwelling. The colder water that is brought to the surface by this process will decrease the OTEC performance if it is taken into the system. When temperature differences around Curaçao at the depths of the two inlets, the warm-water inlet at 15 m and the cold-water inlet at 900 m, are analyzed, it is concluded that no OTEC system should be situated near the coast of Venezuela. Closer than 50 km to the island of Curaçao, the temperature difference between the surface and deep water is large and persistent enough for an OTEC system to be placed. The temperature difference is on average 22°C and the average deviation is about 1°C. At the north side of the island, no influence of upwelled water is detected.

Within a radius of 50 km around Curaçao, the temperature difference between the north and south side is small. Since temperature difference is therefore not a major factor in choosing a location, a location is chosen based on bathymetry. The coastline is steeper at the south side of the island, providing the possibility of placing the OTEC system closer to shore, reducing installation and maintenance costs.

What is the maximum expected current velocity for the lifetime of an OTEC plant around Curaçao?

At this chosen location, maximum expected current velocity for the lifetime of an OTEC system of 30 years is calculated. The ten years of data is used as input and by defining a Gumbel distribution and extrapolating the linearized cumulative distribution function, the maximum expected velocity is calculated. For the chosen location to the south of Curaçao, this was 1.8 m/s.

What is the maximum expected hydrodynamic force on the cold-water pipe for the lifetime of an OTEC plant around Curaçao and what is the associated stress and deflection of the pipe?

By applying Euler beam theory, the distributed force due to currents, moment, curvature and deflection of the cold-water pipe are calculated. The pipe is modeled having a diameter of 4.5 m, a wall thickness of 0.3 m and a length of 870 m, made from High Density PolyEthylene (HDPE) and rigidly attached to a floating hull. The total deflection is 370 m along with the current. The maximum bending stress is 6.7 MPa, well below the yield stress of 26 MPa.

The knowledge of which processes will increase the predictability of the ocean currents and temperature distribution?

From above description of the surface currents, volume fluxes, and correlation coefficients, it can be concluded that there is a significant difference between the north and the south side of Curaçao. The waters south of Curaçao are mostly influenced by wind, while the waters north of Curaçao are mostly influenced by volume fluxes upstream, through the Grenada Passage. Both sides of the island experience great influence from passing eddies.

Identified and verified seasonal patterns can be used to predict mean ocean currents. Generally, high currents are expected at the end of December, January and February

and low currents are expected in September, October and November. Furthermore, high wind velocity will induce higher current velocity, especially to the south of Curaçao, and high volume fluxes through the Grenada Passage generally lead to high volume fluxes to the north of Curaçao. High wind velocities will also increase the amount of cold upwelled water along the coast of Venezuela. This cold water will be advected by the currents.

Also, maximum expected currents for the lifetime of an OTEC system can be calculated, following the method used in Chapter 7. However, this is only a statistical value and it is not known when this maximum will occur. The ten days forecast of the Mercator dataset model can be used for predicting ocean currents up to ten days in advance.

10 Recommendations

10.1 Recommendations concerning the oceanographic research of the Caribbean Sea

10.1.1 Mercator Ocean model

Only ten years of data is yet available in the Mercator dataset. Also, the resolution was not sufficiently high to include coastal currents, coastal processes, and other bathymetric features of the currents. This has led to limitations of the research. A dataset or model with more than ten years of data available and a higher local resolution could be used to improve and add on the current research. Furthermore, an independent validation of the model could be performed by means of measurements or comparison to other model outputs.

10.1.2 Topics for further study

One of the questions that need answering before building an actual OTEC plant is regarding the environmental impact of OTEC systems on the large scale oceanographic features. In particular, the consequences of discharging large volumes of mixed ocean water back into the ocean are yet unclear. For selecting the optimal depth of the outlet, knowledge of location, depth, strength and persistence of subsurface countercurrents directing the discharge water is vital. In this research, baseline oceanographic data has been provided which could be a good starting point for a follow-up project regarding the environmental impact. The discovery of the subsurface currents, in particular, provides an interesting subject to pursue. The subsurface currents create situations of very low velocities, velocities in opposite direction to velocities lower or higher in the water column, and velocities alternating between positive and negative, carrying along the discharge

plume back and forth. 2D or 3D modeling of the discharge plume and its advection and diffusion would be very valuable for the OTEC industry. In cooperation with Deltares, application of Delft3D could be a way to approach this problem.

To understand the variability, origin, destination and forcing of the subsurface currents, the entire coastline of South America could be examined at different depths, with the use of Mercator data. Andrade et al. [2003] also suggested an interaction of the subsurface currents with deep ocean circulation in the different basins in the Caribbean Sea. For the current research, the subsurface currents were only addressed in the vicinity of Curaçao.

Concerning eddy generation in the Venezuela Basin, much research has been performed and is being performed. Some of the questions that arose during this project, for which finding an answer would be a research in itself, are: What are the favorable conditions for eddies to be generated in the Venezuela Basin, when and where are these conditions present, what is the influence of the local bathymetry on the eddy formation and propagation, what would be the effect of lower or higher mean velocities in the Grenada Passage on eddy generation, what would be the effect of more or less upwelling at the Grenada Passage on eddy generation, what is the influence of interaction between the NBC rings and conditions within the Caribbean Sea on eddy formation?

Another interesting question concerns the influence of ENSO on the Caribbean Sea climate and oceanography. In this project, no clear relation was found between ENSO and volume fluxes. In addition, the correlation to other parameters was briefly explored, for example, upwelling, with no result. Since ENSO is a phenomenon with global impact, and impact on the wind pattern in the Caribbean region is observed by Wang [2007], one would expect a relation. This requires further research. The influence of ENSO on the wind pattern could be taken as a starting point for this research.

10.2 Recommendations for the application of OTEC near Curaçao

When considering locations for placing an OTEC plant around Curaçao, the area 50 km south of the island should be considered unfit. This is due to the generally colder and more variable surface water due to upwelling. An intake height of warm water at 15 m water depth and an intake height of cold water of 900 m water depth renders a sufficient temperature difference at other locations around Curaçao.

Proposed pipe length and diameter are strong enough to resist the hydrodynamic forces.

If it would be desirable to predict the currents, measurement systems for detecting wind speed, volume flux through the Grenada Passage, eddy identification and hurricane predictions could be used, because they are the biggest influencing factors for the current.

Hurricanes can be of devastating power and can cause enormous damage to everything in their path. In the ten years analyzed, no hurricanes passed over Curaçao. However, if that would happen, wind speeds, current speeds and wave heights will be much bigger than without a hurricane. Especially wind speed and waves might cause great damage to an OTEC system. It was seen that surface current velocities will be high, but only

at the surface and not for a long period. A hurricane effect assessment should be done before placing an OTEC system anywhere in the Caribbean Sea.

10.2.1 Generalizing the research method for assessing other locations

Curaçao is not the only island in the Caribbean Sea, and the Caribbean Sea not the only area, where OTEC could be economically viable. It would be useful to perform a similar study to other possible suitable OTEC locations before installing a plant there, to avoid unpleasant surprises concerning current speed and direction and water temperature.

Mercator data is globally available, so can be used when assessing other locations. However, from the current study, it appeared that literature research as a first step and to verify the model is very good. Surface velocities and surface temperature on the large scale are very good first indicators of the suitability of the location. How large that large scale is, depends on the local ocean processes, features and bathymetry. Other than that, one is too soon inclined to zoom in on the possible OTEC location. However, this reduces the overview and possibility of understanding the local processes and the option of relating them to bigger processes. It is therefore required be careful before zooming in.

References

A. Alvera-Azcárate, A. Barth, and R. H. Weisberg. A nested model of the Cariaco Basin (Venezuela): description of the basin's interior hydrography and interactions with the open ocean. *Ocean Dynamics*, 59:97–120, 2009a. doi: 10.1007/s10236-008-0169-y.

A. Alvera-Azcárate, A. Barth, and R. H. Weisberg. The surface circulation of the Caribbean Sea and the Gulf of Mexico as inferred from satellite altimetry. *Journal of Physical Oceanography*, 39(3):640–657, 2009b. doi: 10.1175/2008JPO3765.1.

E. Anderson. User guide to ECMWF forecast products. 2015. https://www.ecmwf.int/sites/default/files/elibrary/2015/16559-user-guide-ecmwf-forecast-products.pdf.

C. A. Andrade and E. D. Barton. Eddy development and motion in the Caribbean Sea. *Journal of Geophysical Research: Oceans*, 105(C11):26191–26201, 2000. ISSN 2156-2202. doi: 10.1029/2000JC000300.

C. A. Andrade and E. D. Barton. The Guajira upwelling system. *Continental Shelf Research*, 25(9):1003–1022, 2005. ISSN 0278-4343. doi: http://dx.doi.org/10.1016/j.csr.2004.12.012.

C. A. Andrade, E. D. Barton, and C. N. K. Mooers. Evidence for an eastward flow along the Central and South American Caribbean Coast. *Journal of Geophysical Research: Oceans*, 108(C6), 2003. ISSN 2156-2202. doi: 10.1029/2002JC001549. 3185.

Bluerise. Overview of OTEC system, 2014. http://www.bluerise.com.

Bluerise. My Ocean Potential online tool, 2017. http://my.oceanpotential.com.

M. J. Bowman, D. E. Dietrich, and C. A. Lin. Observations and modeling of mesoscale ocean circulation near a small island. *Coastal and Estuarine Studies 51: Small Islands - Marine Science and Sustainable Development*, 1996.

J. G. C. Pérez and P. H. R. Calil. Regional turbulence patterns driven by meso- and submesoscale processes in the caribbean sea. *Ocean Dynamics*, 67(9):1217–1230, Sep 2017. doi: 10.1007/s10236-017-1079-7.

L. R. Centurioni and P. P. Niiler. On the surface currents of the Caribbean Sea. *Geophysical Research Letters*, 30(6):1279, 2003. ISSN 1944-8007. doi: 10.1029/2002GL016231.

Y.-C. Chang, R.-S. Tseng, P. C. Chu, J.-M. Chen, and L. R. Centurioni. Observed strong currents under global tropical cyclones. *Journal of Marine Systems*, 159(Supplement C):33 – 40, 2016. ISSN 0924-7963. doi: https://doi.org/10.1016/j.jmarsys.2016.03.001.

G. Claude. Power from the Tropical Seas. *Mechanical Engineering*, 52(12):1039–1044, 1930.

CMEMS. E.U. Copernicus Marine Environment Monitoring Service, 2015. http://marine.copernicus.eu/services-portfolio/access-to-products/.

D. P. Dee, S. M. Uppala, A. J. Simmons, P. Berrisford, P. Poli, S. Kobayashi, U. Andrae, M. A. Balmaseda, G. Balsamo, P. Bauer, P. Bechtold, A. C. M. Beljaars, L. van de Berg, J. Bidlot, N. Bormann, C. Delsol, R. Dragani, M. Fuentes, A. J. Geer, L. Haimberger, S. B. Healy, H. Hersbach, E. V. HÃşlm, L. Isaksen, P. KÃěllberg, M. KÃűhler, M. Matricardi, A. P. McNally, B. M. Monge-Sanz, J.-J. Morcrette, B.-K. Park, C. Peubey, P. de Rosnay, C. Tavolato, J.-N. ThÃľpaut, and F. Vitart. The ERA-Interim reanalysis: configuration and performance of the data assimilation system. *Quarterly Journal of the Royal Meteorological Society*, 137(656):553–597, 2011. ISSN 1477-870X. doi: 10.1002/qj.828.

D. P. Dee, M. Balmaseda, G. Balsamo, R. Engelen, A. J. Simmons, and J.-N. ThÃľpaut. Toward a consistent reanalysis of the climate system. *Bulletin of the American Meteorological Society*, 95(8):1235–1248, 2014. doi: 10.1175/BAMS-D-13-00043.1.

E. T. Degens, S. Kempe, and J. E. Richey. Scope 42: Biogeochemistry of major world rivers. *United Kingdom: Wiley*, 1991.

E. Dombrowsky, L. Bertino, G. B. Brassington, E. P. Chassignet, F. Davidson, H. E. Hurlburt, M. Kamachi, T. Lee, M. J. Martin, S. Mai, and M. Tonani. GODAE systems in operation. *Oceanography*, 22(3):80–95, 2009.

M. DrÃľvillon, R. BourdallÃľ-Badie, C. Derval, J. M. Lellouche, E. RÃľmy, B. Tranchant, M. Benkiran, E. Greiner, S. Guinehut, N. Verbrugge, G. Garric, C. E. Testut, M. Laborie, L. Nouel, P. Bahurel, C. Bricaud, L. Crosnier, E. Dombrowsky, E. Durand, N. Ferry, F. Hernandez, O. L. Galloudec, F. Messal, and L. Parent. The GODAE/Mercator-Ocean global ocean forecasting system: results, applications and prospects. *Journal of Operational Oceanography*, 1(1):51–57, 2008. doi: 10.1080/1755876X.2008.11020095.

C. P. Duncan, S. G. Schladow, and W. G. Williams. Surface currents near the Greater and Lesser Antilles. *International Hydrographic Review*, 59(2):67–78, 1982.

ECMWF. European Centre for Medium-Range Weather Forecasting - ERA-Interim reanalysis dataset, 1975. http://apps.ecmwf.int/datasets/data/interim-full-daily/levtype=sfc/.

W. J. Emery and J. Meincke. Global water masses: summary and review. *Oceanologica Acta*, 9(4):383–391, 1986.

Energy Information Administration (EIA). U.S. Energy Information Administration: International Energy Outlook 2016, 2016. http://www.eia.gov/outlooks/ieo/ Accessed on December 2016.

Ernst & Young. Offshore wind in europe, 2015. https://www.ewea.org/fileadmin/files/library/publications/reports/EY-Offshore-Wind-in-Europe.pdf.

D. M. Fratantoni. North Atlantic surface circulation during the 1990's observed with

satellite-tracked drifters. *Journal of Geophysical Research: Oceans*, 106(C10):22067–22093, 2001. ISSN 2156-2202. doi: 10.1029/2000JC000730.

P. N. Froelich Jr., D. K. Atwood, and G. S. Giese. Influence of Amazon River discharge on surface salinity and dissolved silicate concentration in the Caribbean Sea. *Deep Sea Research*, 25(8):735–744, 1978. ISSN 0146-6291. doi: http://dx.doi.org/10.1016/0146-6291(78)90627-6.

A. Gallegos and G. A. Maul. *Descriptive Physical Oceanography of the Caribbean Sea*, pages 36–55. American Geophysical Union, 1996. ISBN 9781118665237. doi: 10.1029/CE051p0036.

D. O. N. Gardner, D. Alleyne, and C. Gomes. An assessment of fiscal and regulatory barriers to deployment of energy efficiency and renewable energy technologies in Curaçao, 2013. United Nations Economic Commission for Latin America and the Caribbean.

GEBCO. General Bathymetric Chart of the Oceans: GEBCO_2014 Grid. British Oceanographic Data Centre, 2014. http://www.gebco.net/data_and_products/gridded_bathymetry_data/.

A. Giannini, Y. Kushnir, and M. A. Cane. Interannual Variability of Caribbean Rainfall, ENSO, and the Atlantic Ocean. *Journal of Climate*, 13(2):297–311, 2000. doi: 10.1175/1520-0442(2000)013<0297:IVOCRE>2.0.CO;2.

A. L. Gordon. Circulation of the Caribbean Sea. *Journal of Geophysical Research*, 72 (24):6207–6223, 1967. ISSN 2156-2202. doi: 10.1029/JZ072i024p06207.

P. Grandelli, G. Rocheleau, J. Hamrick, M. Church, and B. Powell. Modeling the Physical and Biochemical Influence of Ocean Thermal Energy Conversion Plant Discharges into their Adjacent Waters. Technical report, Makai Ocean Engineering, 2012.

I. I. Gringorten. A plotting rule for extreme probability paper. *Journal of Geophysical Research*, 68(3):813–814, 1963.

T. Guerrero. Design of a OTEC FPSO. *A Delft University of Technology & Bluerise Thesis*, 2017.

J. Gyory, A. J. Mariano, and E. H. Ryan. Surface Currents in the Caribbean: The Caribbean Current, 2014. http://oceancurrents.rsmas.miami.edu/caribbean/caribbean.html.

S. Hellerman and M. Rosenstein. Normal monthly wind stress over the world ocean with error estimates. *Journal of Physical Oceanography*, 13(7):1093–1104, 1983.

R. C. Hibbeler. *Mechanics of Materials*. Prentice Hall, 7th si edition, 2008. ISBN 13 978-981-06-7994-1.

B. Hickey. The relationship between fluctuations in sea level, wind stress and sea surface temperature in the equatorial pacific. *Journal of Physical Oceanography*, 5(3):460–475, 1975. doi: 10.1175/1520-0485(1975)005<0460:TRBFIS>2.0.CO;2.

H. G. Hidalgo, A. M. Durán-Quesada, J. A. Amador, and E. J. Alfaro. The Caribbean Low-Level Jet, the Inter Tropical Convergence Zone and precipitation patterns in the

Intra-Americas Sea: A proposed dynamical mechanism. *Geografiska Annaler, series A: Physical Geography*, 97:41–59, 2015. doi: 10.1111/geoa.12085.

C. Hu, E. T. Montgomery, R. W. Schmitt, and F. E. Muller-Karger. The dispersal of the Amazon and Orinoco River water in the tropical Atlantic and Caribbean Sea: Observation from space and S-PALACE floats. *Deep Sea Research Part II: Topical Studies in Oceanography*, 51(10):1151–1171, 2004. ISSN 0967-0645. doi: http://dx.doi.org/10.1016/j.dsr2.2004.04.001. Views of Ocean Processes from the Sea-viewing Wide Field-of-view Sensor (SeaWiFS) Mission: Volume 2.

International Towing Tank Conference (ITTC). ITTC - Recommended Procedures and Guidelines, 1957.

W. E. Johns, T. L. Townsend, D. M. Fratantoni, and W. D. Wilson. On the Atlantic inflow to the Caribbean Sea. *Deep Sea Research Part I: Oceanographic Research Papers*, 49(2):211–243, 2002. ISSN 0967-0637. doi: http://dx.doi.org/10.1016/S0967-0637(01)00041-3.

S. A. Josey, E. C. Kent, and P. K. Taylor. Wind stress forcing of the ocean in the SOC climatology: Comparisons with the NCEP/NCAR, ECMWF, UWM/COADS, and Hellerman and Rosenstein datasets. *Journal of Physical Oceanography*, 32(7):1993–2019, 2002. doi: 10.1175/1520-0485(2002)032<1993:WSFOTO>2.0.CO;2.

J. Jouanno, J. Sheinbaum, B. Barnier, J. M. Molines, and J. Candela. Seasonal and interannual modulation of the eddy kinetic energy in the Caribbean Sea. *Journal of Physical Oceanography*, 42(11):2041–2055, 2012. doi: 10.1175/JPO-D-12-048.1.

J. M. J. Journée and W. W. Massie. *Offshore Hydromechanics*. Delft University of Technology, 1 edition, 2001.

E. Kalnay, M. Kanamitsu, R. Kistler, W. Collins, D. Deaven, L. Gandin, M. Iredell, S. Saha, G. White, J. Woollen, Y. Zhu, A. Leetmaa, R. Reynolds, M. Chelliah, W. Ebisuzaki, W. Higgins, J. Janowiak, K. C. Mo, C. Ropelewski, J. Wang, R. Jenne, and D. Joseph. The NCEP/NCAR 40-year reanalysis project. *Bulletin of American Meteorological Society*, 77:437–470, 1996.

D. Kang and E. N. Curchitser. Gulf Stream eddy characteristics in a high-resolution ocean model. *Journal of Geophysical Research: Oceans*, 118:4474–4487, 2013. doi: 10.1002/JGRC.20318.

T. H. Kinder, G. W. Heburn, and A. W. Green. Some aspects of the Caribbean circulation. *Marine Geology*, 68:25–52, 1985.

B. Kjerfve. Tides of the Caribbean Sea. *Journal of Geophysical Research*, 86(C5):4243–4247, 1981.

B. Kleute and M. Vroom. Feasibility 10MW offshore ocean thermal energy conversion. Technical Report March, Bluerise, 2014.

J. A. Knauss and N. Garfield. *Introduction to Physical Oceanography*. Waveland Press, 3rd edition, 2017. ISBN 978-1-4786-3250-41.

M. F. Knudsen, B. H. Jacobsen, M.-S. Seidenkrantz, and J. Olsen. Evidence for external

forcing of the Atlantic Multidecadal Oschillation since termination of the Little Ice Age. *Nature Communications*, 25(5):3323, 2014. doi: 10.1038/ncomms4323.

N.-J. Kuo, Q. Zheng, and C.-R. Ho. Satellite Observation of Upwelling along the Western Coast of the South China Sea. *Remote Sensing of Environment*, 74(3):463–470, 2000. ISSN 0034-4257. doi: https://doi.org/10.1016/S0034-4257(00)00138-3.

J. M. Lellouche, O. Legalloudec, C. Regnier, B. Levier, E. Greiner, M. Drevillon, and Y. Drillet. Quality information document for global sea physical analysis and forecasting product. 2016. Copernicus Marine Environment Monitoing Service.

J. Lingwood and T. Knaggs. *Significant Ships of 2004*. Royal Institution of Naval Architects (RINA), 2004. ISBN 978-1905040063.

G. Madec and the NEMO team. NEMO ocean engine. *Note du Pôle de modélisation*, (27), 2008. Institut Pierre-Simon Laplace (IPSL), France, ISSN No 1288-1619.

T. Maldonado, A. Rutgersson, J. Amador, E. Alfaro, and B. Claremar. Variability of the Caribbean Low-Level Jet during boreal winter: large scale forcings. *International Journal of Climatology*, 36(4):1954–1969, 3 2016. ISSN 1097-0088. doi: 10.1002/joc.4472.

P. J. D. Mauas, E. Flamenco, and A. P. Buccino. Solar forcing of the stream flow of a continental scale South American river. *Physical Review Letters*, 101(16):168501, 2008.

P. A. Mazeika, D. A. Burns, and T. H. Kinder. Measured flow in St. Vincent and Grenada Passages. *Naval Ocean Research and Development Activity Tech. Note 62*, page 56, 1980.

F. E. Müller-Karger, C. R. McClain, T. R. Fisher, W. E. Esaias, and R. Varela. Pigment distribution in the Caribbean sea: Observations from space. *Progress in Oceanography*, 23(1):23–64, 1989. ISSN 0079-6611. doi: http://dx.doi.org/10.1016/0079-6611(89)90024-4.

F. E. Müller-Karger, R. Varela, R. Thunell, Y. Astor, H. Zhang, R. Luerssen, and C. Hu. Processes of coastal upwelling and carbon flux in the Cariaco Basin. *Deep Sea Research Part II: Topical Studies in Oceanography*, 51(10):927–943, 2004. ISSN 0967-0645. doi: http://dx.doi.org/10.1016/j.dsr2.2003.10.010. Views of Ocean Processes from the Sea-viewing Wide Field-of-view Sensor (SeaWiFS) Mission: Volume 2.

E. Muñoz, A. J. Busalacchi, S. Nigam, and A. Ruiz-Barradas. Winter and summer structure of the Caribbean Low-Level Jet. *Journal of Climate*, 21:1260–1276, 2007.

S. J. Murphy, H. E. Hurlburt, and J. J. O'Brien. The connectivity of eddy variability in the Caribbean Sea, the Gulf of Mexico, and the Atlantic Ocean. *Journal of Geophysical Research: Oceans*, 104(C1):1431–1453, 1999. ISSN 2156-2202. doi: 10.1029/1998JC900010.

National Oceanic and Atmospheric Administration (NOAA). Ocean Thermal Energy Conversion: Assessing Potential Physical, Chemical and Biological Impacts and Risks, 2010.

National Oceanic and Atmospheric Administration (NOAA). World Ocean Atlas 2013, 2013. https://www.nodc.noaa.gov/OC5/WOA09/pr_woa09.html.

National Oceanic and Atmospheric Administration (NOAA). Historical hurricane tracks, 2017. https://coast.noaa.gov/hurricanes/?redirect=301ocm.

G. C. Nihous. A preliminary assessment of Ocean Thermal Energy Conversion resources. *Journal of Energy Resources Technology*, pages 10–17, 2006. doi: 10.1115/1.2424965.

G. C. Nihous. *Ocean Thermal Energy Conversion (OTEC) and Derivative Technologies: Status of Development and Prospects*, pages 31–37. The Executive Committee of Ocean Energy Systems: Ocean Energy Systems Implementing Agreement, 2008.

NOAA Climate Prediction Center. Historical El Niño / La Niña episodes (1950-present), 2017. http://www.cpc.noaa.gov/products/analysis_monitoring/ensostuff/ensoyears.shtml.

W. R. Ott. *Environmental Statistics and Data Analysis*. CRC Press LLC, 1995. ISBN 0-87371-848-8.

J. P. Palutikof, B. B. Brabson, D. H. Lister, and S. T. Adcock. A review of methods to calculate extreme wind speeds. *Meteorological Applications*, 6:119–132, 1999.

K. Pearson. Notes on regression and inheritance in the case of two parents. *Proceedings of the Royal Society of London*, 58:240–242, 1895.

T. C. Peterson, M. A. Taylor, R. Demeritte, D. L. Duncombe, S. Burton, F. Thompson, A. Porter, M. Mercedes, E. Villegas, R. Semexant Fils, A. Klein Tank, A. Martis, R. Warner, A. Joyette, W. Mills, L. Alexander, and B. Gleason. Recent changes in climate extremes in the Caribbean region. *Journal of Geophysical Research: Atmospheres*, 107(D21):ACL 16–1–ACL 16–9, 2002. ISSN 2156-2202. doi: 10.1029/2002JD002251.

J. D. Pietrzak. *An Introduction to Oceanography for Civil and Offshore Engineers*. Delft University of Technology, 2016.

P. Richardson. Caribbean Current and eddies as observed by surface drifters. *Deep Sea Research Part II: Topical Studies in Oceanography*, 52:429–463, 2005. ISSN 0967-0645. doi: http://dx.doi.org/10.1016/j.dsr2.2004.11.001. Direct observations of oceanic flow: A tribute to Walter Zenk.

D. T. Rueda-Roa and F. E. Müller-Karger. The southern Caribbean upwelling system: Sea surface temperature, wind forcing and chlorophyll concentration patterns. *Deep Sea Research Part I: Oceanographic Research Papers*, 78:102–114, 2013. ISSN 0967-0637. doi: http://dx.doi.org/10.1016/j.dsr.2013.04.008.

F. Santos, M. Gómez-Gesteira, R. Varela, M. Ruiz-Ochoa, and J. M. Días. Influence of upwelling on SST trends in La Guajira system. *Journal of Geophysical Research: Oceans*, 121(4):2469–2480, 2016. ISSN 2169-9291. doi: 10.1002/2015JC011420.

R. L. Smith. Upwelling. *Oceanographic and Marine Biology - An Annual Review*, 6: 11–46, 1968.

M. C. Stalcup and W. G. Metcalf. Current measurements in the passages of the Lesser Antilles. *Journal of Geostrophic Research*, 77(6):1032–1049, 1972.

D. Storkey, E. W. Blockley, R. Furner, C. GuiavarcâĂŹh, D. Lea, M. J. Martin, R. M. Barciela, A. Hines, P. Hyder, and J. R. Siddorn. Forecasting the ocean state using NEMO: The new FOAM system. *Journal of Operational Oceanography*, 3(1):3–15, 2010. doi: 10.1080/1755876X.2010.11020109.

R. E. Thomson and W. J. Emery. *Data Analysis Methods in Physical Oceanography*. Elsevier, 3 edition, 2014. ISBN 978-0-12-387782-6.

M. Tonani, M. Balmaseda, L. Bertino, E. Blockley, G. Brassington, F. Davidson, Y. Drillet, P. Hogan, T. Kuragano, T. Lee, A. Mehra, F. Paranathara, C. A. Tanajura, and H. Wang. Status and future of global and regional ocean prediction systems. *Journal of Operational Oceanography*, 8(sup2):s201–s220, 2015. doi: 10.1080/1755876X.2015.1049892.

United Nations Framework Convention on Climate Change (UNFCCC). Paris agreement, 2016. http://unfccc.int/paris_agreement/items/9485.php Accessed on December 2016.

H. M. Veijer. Synergies in an Ocean Thermal Energy system - integration and optimization of OTEC, SWAC and Ecopark. *A Delft University of Technology & Bluerise Thesis*, 2017.

C. Wang. Variability of the Caribbean Low-Level Jet and its relations to climate. *Climate Dynamics*, 29:411–422, 2007. doi: 10.1007/s00382-007-0243-z.

P. Weatherall, K. M. Marks, M. Jakobsson, T. Schmitt, S. Tani, J. E. Arndt, M. Rovere, D. Chayed, V. Ferrini, and R. Wigley. A new digital bathymetric model of the world's oceans. *Earth and Space Science*, 2:331–345, 2015. doi: 10.1002/2015SEA000107.

F. S. Whyte, M. A. Taylor, T. S. Stephenson, and J. D. Campbell. Features of the Caribbean low level jet. *International Journal of Climatology*, 28:119–128, 2008. doi: 10.1002/joc.1510.

P. Wilde. Environmental monitoring and assessment program at potential OTEC sites. *6th Annual Ocean Thermal Energy Conversion Conference*, 1979.

W. D. Wilson and W. E. Johns. Velocity structure and transport in the Windward Islands Passages. *Deep Sea Research Part I: Oceanographic Research Papers*, 44(3):487–520, 1997. ISSN 0967-0637. doi: http://dx.doi.org/10.1016/S0967-0637(96)00113-6.

World Energy Council (WEC). World energy resources, 2013. https://www.worldenergy.org/wp-content/uploads/2013/09/Complete_WER_2013_Survey.pdf.

G. Wüst. On the stratification and the circulation in the cold water sphere of the Antillean-Caribbean basins. *Deep Sea Research and Oceanographic Abstracts*, 10 (3):165–187, 1963. ISSN 0011-7471. doi: http://dx.doi.org/10.1016/0011-7471(63)90354-1.

A

Appendix: Paper submitted to the 5th OTEC symposium

The following paper has been submitted to and accepted by the 5th international OTEC symposium, that took place from 7 to 9 November 2017 in Saint-Pierre, Réunion. A presentation regarding the results of the current research was given at the symposium by the author.

Figure A.1: OTEC symposium logo.

Ocean Current Patterns and Variability around Curaçao: An Analysis for Ocean Thermal Energy Conversion

H.M.L. Lems-de Jong[a]*, A.S. Candy[b], J.S. Hoving[a], B.J. Kleute[c] and J.D. Pietrzak[b]

[a]Offshore and Dredging Engineering Section, Delft University of Technology,
Mekelpark, Delft, The Netherlands
[b]Environmental Fluid Mechanics Section, Delft University of Technology
Mekelpark, Delft, The Netherlands
[c]Bluerise BV,
Molengraaffsingel, Delft, The Netherlands
**Corresponding Author: H.M.L.deJong@student.tudelft.nl*

ABSTRACT

Large-scale changes in ocean conditions caused by installing and operating Ocean Thermal Energy Conversion (OTEC) are not well quantified. Conversely, the effect on an OTEC plant by oceanographic features are neither researched in depth. The aim of this research is to describe the natural patterns and variability of the ocean currents around Curaçao, an island in the Caribbean Sea and a potential OTEC location, to be able to assess possible risks and opportunities for the OTEC industry. Ten years of data from the Mercator Ocean Model with a spatial resolution of 1/12˚ and temporal resolution of one day was analyzed. In the Caribbean Sea, global ocean gyres and wind patterns force the water from the Lesser Antilles in the east towards the Yucatan Channel in the west in a fast-current jet, with a peak from December to March and a trough in October and November, related to wind stress. Largest surface velocities in the order of 1 m/s are found along the coast of Venezuela, where upwelling enhances surface flow to the west. Along that coast, subsurface currents to the east are also found. The period from April to September is characterized by meandering of the jet and the formation of large (diameter > 200 km) anticyclonic eddies that cause large local surface velocities and contribute to the great variability in the Caribbean Sea. Due to upwelling, no OTEC system should be deployed more than 50 km south of Curaçao to avoid cold surface water decreasing the system's performance. Hydrodynamic forces and moments on the cold-water pipe due to the calculated expected maximum velocity of 1.8 m/s do not cause exceeding of the yield stress.

Keywords: OTEC, physical oceanography, natural flow patterns, variability, upwelling, eddies, subsurface counter current, Caribbean Sea, Curaçao

1 INTRODUCTION

The present transition towards the use of more sustainable energy resources opens up possibilities for Ocean Thermal Energy Conversion (OTEC). This harnesses the potential energy in the temperature difference between the warm surface ocean waters and the persistently colder deep ocean waters. Tropical islands, in particular, can benefit from this technique due to the high level of incoming solar radiation warming the ocean surface. Additionally, this reduces the reliance on and need to import energy resources, lowering the relatively high local electricity prices and increasing the independence of island communities.

1.1 Problem definition and research objective

Offshore structures interact with the water surrounding them. However, compared to oil platforms, there is a more direct interaction for OTEC platforms, as they use large volumes of ocean water, extracting them from the ocean and discharging them back into the ocean at another depth. It is a challenge to install and operate an OTEC plant offshore, and more so when there is the potential for large-scale changes in ocean conditions. The effect on an OTEC plant by oceanographic features – that vary over large temporal and spatial scales, and conversely the effect of the plant's feedback on the ocean are not well quantified. The aim of this research is to determine the natural patterns and variability of ocean currents around Curaçao, an island in the Caribbean Sea and a potential OTEC deployment site. This is key to be able to assess possible risks and opportunities for the OTEC industry. Furthermore, the results of this research can serve as input for further studies on the interaction between OTEC plants and ocean processes.

1.2 Method

Oceanographic data from 2007 until 2016, with a spatial resolution of 1/12˚ and temporal resolution of one day from the Mercator Ocean model physical dataset [1] has been analyzed. The Mercator Ocean model uses NEMO for data assimilation [2]. For bathymetry data, GEBCO [3] was used and wind data is from ECMWF [4]. Findings were compared to measurements and results from numerical models as found in literature [5-11] in order to verify the conclusions and to place them in context. Starting point of this analysis is a 10MW

offshore OTEC plant, with the warm-water inlet at 15 m water depth and the cold-water inlet at 900 m water depth. The discharge pipe is at 100 m water depth. The minimum temperature difference between the cold and the warm water should be around 20˚C for OTEC to be economically viable.

1.3 Outline

In the following section, the description of the surface current pattern that was found in the Caribbean Sea and in the vicinity of Curaçao is given. This pattern is correlated to the wind pattern. Subsequently, currents below the surface, flowing in the opposite direction at the north and the south side of Curaçao, are identified. Then, some applications of the oceanographic parameters to OTEC are described. A location assessment based on temperature difference between surface and deep water is performed. Lastly, the deflection and bending stress in the cold-water pipe are calculated to assess the risk of damage to the pipe due to subsurface currents.

2 SURFACE CURRENT PATTERN

2.1 Surface current pattern in the Caribbean Sea

In the Caribbean Sea, global ocean gyres and wind patterns force the water from the Lesser Antilles in the east towards the Yucatan Channel in the west in a fast-current jet, identified as the Caribbean Current. An overview can be seen in Fig. 1, which shows mean surface currents in the east of the Caribbean Sea. This jet has a velocity peak in boreal winter, from December to March when the winds are strongest, and a trough in fall, October and November when the winds are weakest. This is in accordance with [12]. Largest surface current velocities of the order of 1 m/s are found in the south of the Venezuela Basin [6,7] where coastal upwelling enhances the surface flow to the west due to the Thermal Wind Balance [13]:

$$\frac{\partial u}{\partial z} = \frac{g}{f\rho_0}\frac{\partial \rho}{\partial y} \tag{1}$$

$$\frac{\partial v}{\partial z} = \frac{g}{f\rho_0}\frac{\partial \rho}{\partial x} \tag{2}$$

Here, u and v are water velocities in x and y direction respectively (in m/s), g is the gravitational constant (in m/s^2), f is the Coriolis parameter (in rad/s) and ρ is the water density (in kg/m^3). In eqs. (1) and (2) horizontal density gradients are balanced by vertical shear. A horizontal density difference arises due to the horizontal temperature difference that is caused by upwelling. A vertical shear along the cold-water front balances this horizontal density difference, thus increasing the surface velocities to the west.

The period from April to September is characterized by meandering of the jet [14] and the presence of large (diameter > 200 km) anticyclonic eddies [15] which cause large local surface velocities and contribute to the great variability in the Caribbean Sea.

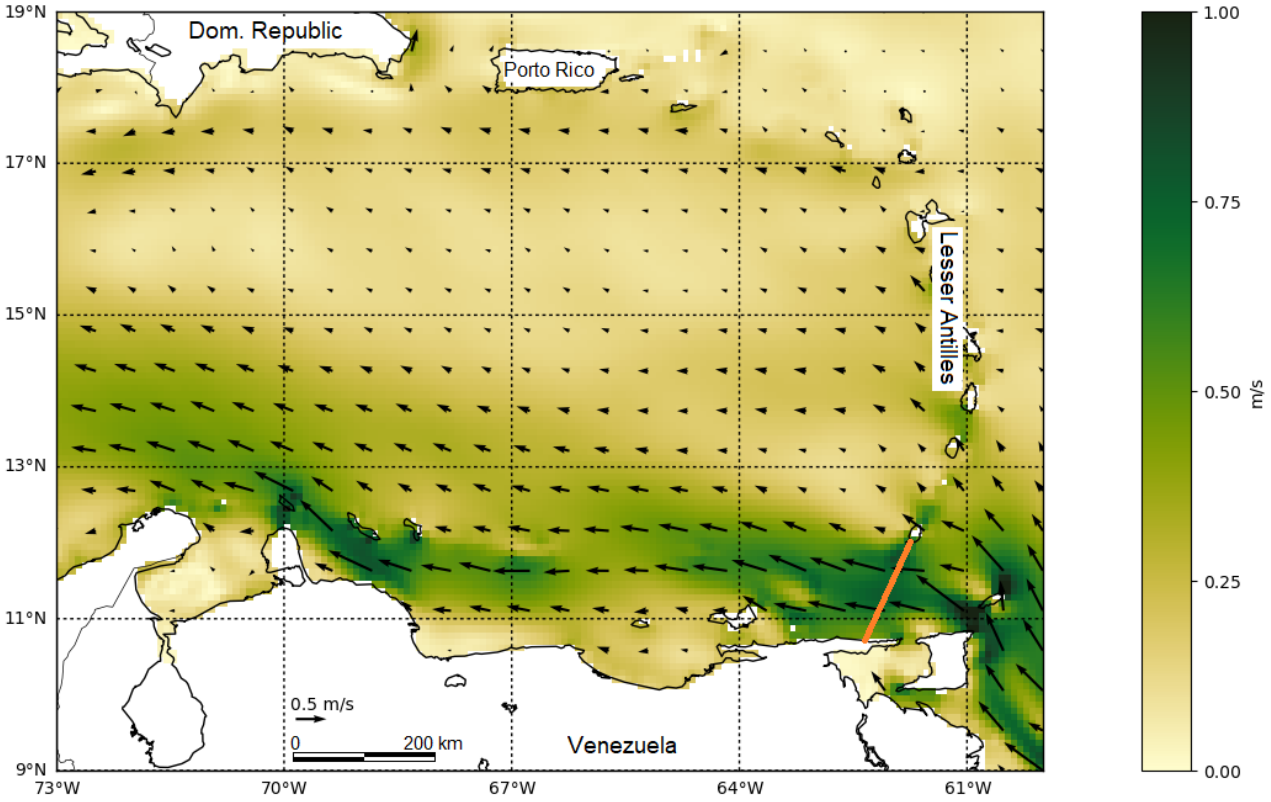

Fig. 1 The eastern part of the Caribbean Sea, known as the Venezuela Basin, with Venezuela in the south, the Lesser Antilles in the east and the Dominican Republic and Puerto Rico to the north. The mean of surface currents from the year 2007 to 2016 is shown. The orange line indicates the Grenada Passage. Arrows indicate ocean current surface velocity and direction, scaled linearly to velocity magnitude. Color indicates surface current velocity.

2.2 Surface current pattern in the vicinity of Curaçao

Closer to Curaçao, within a radius of 100 km around the island, surface currents flow from east to west with an average speed of 0.5 m/s to the south and 0.3 m/s to the north of the island. However, in the ten years analyzed, surface velocities of up to almost 2 m/s were also identified. The observed semiannual cycle in current velocities has a global peak in January and a global trough in November. A local trough and local peak are found in May and July respectively. A similar semiannual cycle has been seen in wind speeds over the Caribbean [12] and kinetic energy of the surface water [9].

Pearson correlation coefficients are a measure for linear correlation between two variables [16]. High Pearson correlation coefficients (around 0.7) are found between wind speed and surface currents which indicate a strong relation to wind speed, although these are higher to the south of the island. So, the surface currents to the south of Curaçao are stronger related to wind. Eddies are found to be a major cause for intra-annual variability, giving rise to an increase in average surface currents of at least 40%.

3 SUBSURFACE CURRENTS

Subsurface countercurrents were identified around Curaçao. The depth of these countercurrents centered around 200 m in the waters south of Curaçao and 800 m to the north. Volume fluxes north of the island were correlated to the volume fluxes through the Grenada Passage, upstream of the island as indicated in Fig. 1, with correlation coefficients up to 0.7. This indicates that flows north of the island are heavily influenced by inflow through the Grenada Passage to the Caribbean Sea from the Atlantic Ocean. Also, volume fluxes are largely influenced by the presence of eddies. Average volume fluxes increased at least 90% due to the presence of eddies.

4 SURFACE TEMPERATURE AND DIFFERENCE

To the south of Curaçao, near the Venezuela coast, the water is influenced by upwelling and displays colder and more variable surface temperatures, see Fig. 2. This figure shows mean temperature of the waters around Curaçao at a depth of 15 m, where the inlet of the warm water is. The temperature close to the Venezuela coast is 25˚C with an average variation of 3˚C compared to a temperature of 28˚C with an average deviation of 1˚C in waters to the north. The water at 900 m shows an average temperature of 6˚C with an average

deviation of 1˚C. The Venezuelan coastal waters are unfit for OTEC deployment, because the temperature difference between the surface and the deep water is too small.

5 HYDRODYNAMIC FORCES ON THE COLD-WATER PIPE

Currents induce forces and moments on the OTEC system and the pipes. The expected maximum current for the lifetime of an OTEC plant, 30 years, is calculated at a suitable location to the south of the island. The expected maximum surface velocity is 1.8 m/s. The cold-water pipe is modelled as an Euler-beam with a length of 900 m, a diameter of 4.5 m, a wall thickness of 0.4 m that is made of High Density PolyEhylene (HDPE). When subjected to the expected maximum current profile, the pipe deflection is 370 m at the tip with a maximum bending stress of 6.7 MPa at the connection point to the platform, which is well below the yield stress of the pipe material.

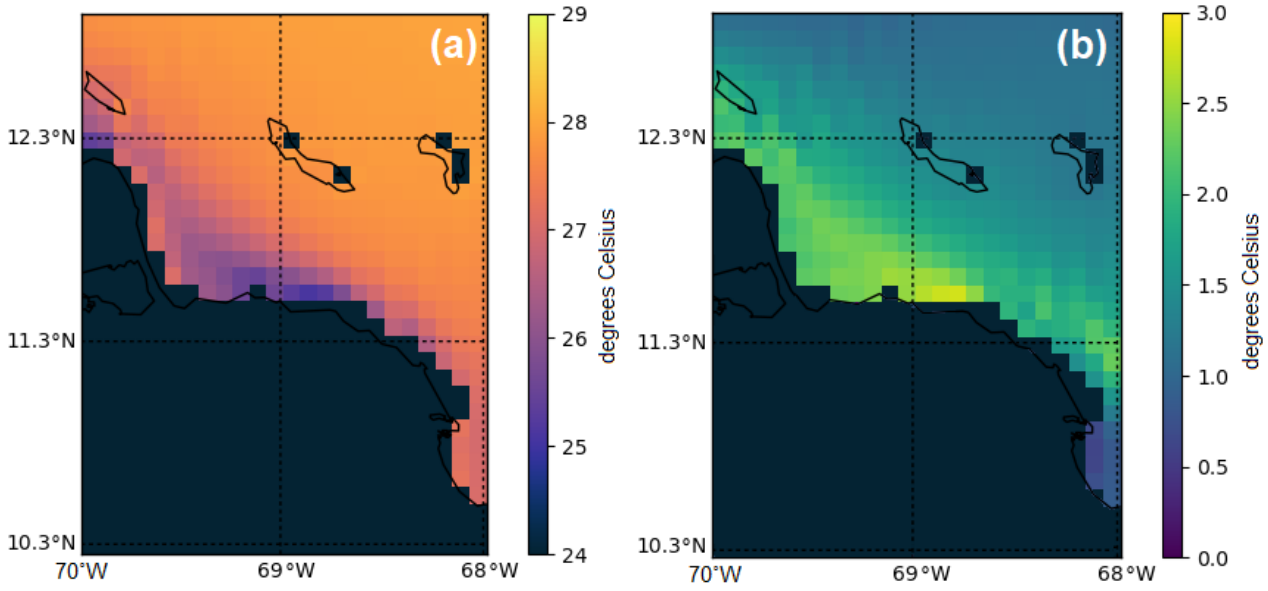

Fig. 2 A surface view centred on Curaçao, with Bonaire to the east and the mainland of Venezuela in the south. The dark areas indicate land. The mean of the water temperature at 15 m water depth, the inlet depth of the warm water used in the OTEC process is shown in (a) and average deviation from the mean in (b).

NOMENCLATURE

f	Coriolis parameter, rad/s
g	gravity constant, m/s2
u	current velocity in x direction, m/s
v	current velocity in y direction, m/s

Greek symbols

ρ	density, kg/m3

Subscripts and superscripts

0	Boussinesq approximation

REFERENCES

[1] Copernicus Marine Environment Monitoring Service (CMEMS), Operational 1/12º global ocean physics and analysis data set. Product: GLOBAL_ANALYSIS_PHY_FORECAST_001_024 – Available at: http://marine.copernicus.eu/services-portfolio/access-to-products/ . [accessed 2017]

[2] Madec G., and the NEMO team. NEMO ocean engine. Note du Pole de modélisation. Institut Pierre-Simon Laplace (IPSL), France; 2008.

[3] General Bathymetric Chart of the Oceans (GEBCO), British Oceanographic Data Centre. Product: GEBCO_2014 Grid. Available at: http://www.gebco.net/data_and_products/gridded_bathymetry_data/. [accessed 2017]

[4] European Centre for Medium-Range Weather Forecasting (ECMWF). Product: ERA interim. Available at: http://apps.ecmwf.int/datasets/data/interim_full_daily/levtype-sfc/. [accessed 2017]

[5] Johns W.E., Townsend T.L., Fratantoni D.M., Wilson W.D., On the Atlantic inflow to the Caribbean Sea. Deep Sea Research part I 2002;49(2):211-243.

[6] Fratantoni D.M., North Atlantic surface circulation during the 1990's observed with satellite-tracked drifters. Journal of Geophysical Research: Oceans 2001;106(C10):22067-22093.

[7] Centurioni L.R., Niiler P.P., On the surface currents of the Caribbean Sea. Geophysical Research Letters 2003;30(6):1279.
[8] Andrade C.A., Barton E.D., The Guajira upwelling system. Continental Shelf Research 2005;25(9):1003-1022.
[9] Jouanno J., Sheinbaum J., Barnier B., Molines J.M., Candela J., Seasonal and interannual modulation of the eddy kinetic energy in the Caribbean Sea. Journal of Physical Oceanography 2012;42(11):2041-2055.
[10] Andrade C.A., Barton E.D., Mooers C.N.K., Evidence for an eastward flow along the Central and South American Caribbean Coast. Journal of Geophysical Research: Oceans 2003;108(C6):2156-2202.
[11] Wilson W.D., Johns W.E., Velocity structure and transport in the Windward Islands Passages. Deep Sea Research Part I 1997;44(3):487-520.
[12] Maldonado T., Rutgersson A., Amador J., Alfaro E., Claremar B., Variability of the Caribbean Low-Level Jet during boreal winter: large scale forcings. International Journal of Climatology 2016;36(4):1954-1969.
[13] Pietrzak J.D., An introduction to oceanography for civil and offshore engineers. Delft, The Netherlands: Delft University of Technology; 2016.
[14] Alvera-Azcárate A., Barth A., Weisberg R.H., The surface circulation of the Caribbean Sea and the Gulf of Mexico as inferred from satellite altimetry. Journal of Physical Oceanography 2009;39(3):640-657.
[15] Andrade C.A., Barton E.D., Eddy development and motion in the Caribbean Sea. Journal of Geophysical Research 2000;105(C11):26191-26201.
[16] Pearson K., Notes on regression and inheritance in the case of two parents. Proceedings of the Royal Society of London 1895;58:240-242.

B

Appendix: Review of studies to date into environmental impact of OTEC systems

B.1 Studies to date

Already in 1979, a report was written for the 6th Annual Ocean Thermal Energy Conversion Conference discussing a strategy for the evaluation of the effects of an OTEC plant on the environment. Ocean water mixing was at that moment considered an issue and it was stated that more research was required. According to the author, this research consists of the development of a computer model to predict the impact of OTEC operations on oceanographic characteristics; the establishment of baseline oceanographic data at potential OTEC locations; the characterization of changes in the oceanographic characteristics resulting from OTEC operations and the determination of the impacts of oceanographic changes in the marine ecosystem Wilde [1979].

That until today still not all of this research has been done can be derived from multiple studies into OTEC, like National Oceanic and Atmospheric Administration (NOAA) [2010] and Kleute and Vroom [2014]. What still needs to be investigated can be split up in 1) the effect of intake of large volumes of warm and cold water and 2) the effect of discharge of large volumes of mixed water at a certain depth on oceanographic characteristics. For the discharge water, the main concern includes the redistribution of nutrient-rich water (mostly nitrates) from the deep into the upper layers of ocean water potentially leading to for example algae blooms and phytoplankton growth. This could cause disruption of the local ecosystem.

A study into environmental impact of OTEC systems has been performed by Makai Ocean Engineering in 2012 Grandelli et al. [2012]. This was done for several proposed 100 MW plants near the Southwest coast of O'ahu, Hawaii. The results of this study showed that the perturbations caused by the discharge of the OTEC plants were small enough to remain within the natural variability of the system. This was mainly due to the

depth of the discharge; nutrients can only cause disturbance of the ecosystem if enough light penetrates to the depth of the nutrients to cause algae or phytoplankton to grow. In Hawaii, this water depth is 60 m National Oceanic and Atmospheric Administration (NOAA) [2010] while the discharges were modeled at 60 m or below. It was observed however that larger perturbations were found twenty to thirty kilometers downstream of the OTEC plant, when the plume nutrients disperse into the euphotic zone. Also, the study recommends more sampling in time and space due to a greater than anticipated ocean variability.

B.2 My Ocean Potential tool

The OTEC power generating potential can be estimated with a tool developed by Bluerise and validated by Deltares called 'My Ocean Potential' Bluerise [2017]. It assesses regions around the world specified by the user and generates suitable locations for hosting onshore or offshore OTEC plants. The criteria in this tool for a suitable location are water depth, temperature difference and proximity to shore. My Ocean Potential uses monthly means of sea surface temperature and temperature profiles from World Ocean Atlas 2013 (WOA13) National Oceanic and Atmospheric Administration (NOAA) [2013]. A screen shot of the tool can be seen in Figure B.1

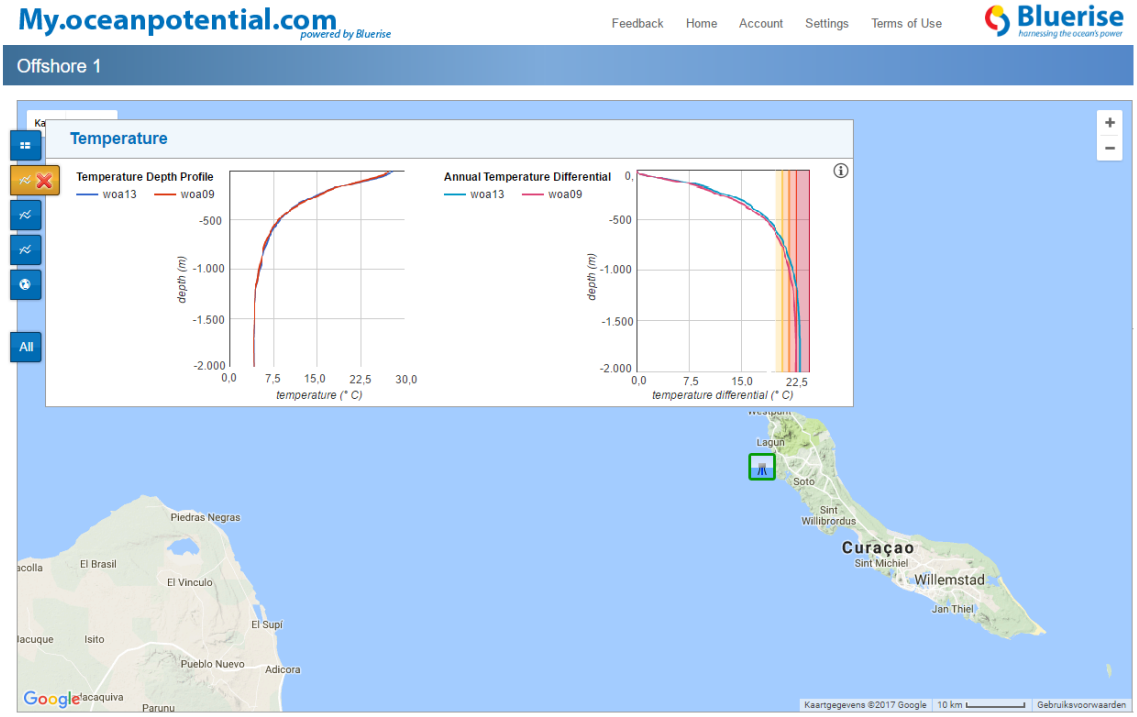

Figure B.1: Screen shot from the Ocean Potential tool. The tool assesses a region specified by the user and generates suitable locations for hosting onshore or offshore OTEC plants. One promising offshore location is indicated by the icon near the coast of Curaçao, with key site figures of that location in the top left corner Bluerise [2017].

The spatial resolution of the ocean water temperature data from WOA is 1/4°. This gives the tool a resolution in the order of 25 km. As a comparison, the length of the island of

Curaçao is 60 km. Temperature over depth is the only parameter taken into account and for that parameter only one set of monthly means is displayed. It is critical for Bluerise to have more accurate temperature data (higher resolution and more possibilities to review means). Also, other parameters, like currents and density that will have an effect on the direction of the discharge flow, will give a better insight in what the consequences might be of building an OTEC plant at a certain location.

C

Appendix: Details about the climate models used

C.1 NEMO

Ocean water is subjected to the physics as described in the Navier-Stokes equations, together with the non-linear equation of state that relates temperature and salinity to density. The following assumptions are made in the NEMO ocean model:

- Spherical earth approximation
- Thin shell approximation
- Turbulence closure hypothesis
- Boussinesq hypothesis
- Hydrostatic hypothesis
- Incompressibility hypothesis

Observations from satellites and in-situ systems are incorporated into the model. This is called data assimilation. Data assimilation is performed by SAM2V1-3DVAR and uses a method based on reduced-order Kalman filter based on the Singular Evolutive Extended Kalman filter (SEEK) formulation with a 3D-Var bias correction. The atmospheric parameters that force the ocean model are from ECMWF. With use of Python, the data in netCDF format was processed. The following packages were used: cmocean, datetime, math, mathdef, matplotlib, mpl_toolkits.basemap, netCDF4, numpy, sys, time and windrose.

C.2 ECMWF

The Europian Centre for Medium-Range Weather Forecasting (ECMWF) ([ECMWF, 1975], [Dee et al., 2011] and [Anderson, 2015]) was used for atmospheric data. This dataset is a global atmospheric reanalysis. Wind data was used from 2007 to 2016.

C.3 System sheet of Mercator Ocean model

SYSTEM SHEET

SYSTEM FOR GLOBAL OCEAN PHYSICAL ANALYSIS AND FORECAST AT 1/12°

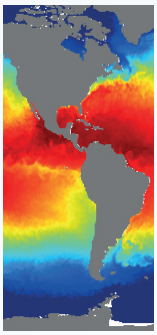

Geographical coverage : Global Ocean (180°W-180°E; 77°S-90°N)
Physics or Biogeochemistry : Physics
Grid and Resolutions : ORCA12 [1/12°; 50 levels]
Grid size : 4322x3059x50 (partial steps)
Code et Version : Nemo3.1
Data assimilation : Yes
Sea Ice Modeling : LIM2 EVP Sea Ice Model
Tides : No
Bathymetry : ETOPO1 for deep ocean and GEBCO on coast and continental shelf
Free run configuration name : ORCA12_LIM_T321
Time step : 360 s
Update : Daily

Reference : PSY4V2R2

Forcing and Data Assimilation

Data assimilation :	Yes
Data assimilation scheme:	SAM2v1 (Kalman filter with SEEK formulation) and bias correction (3D-Var) with Incremental Analysis Update
Data assimilated :	Sea Surface Temperature (Reynolds AVHRR-AMSR 1/4°); Sea Surface Height (Jason2, Cryosat, Saral); InSitu temperature and salinity vertical profiles from Coriolis Center with Extra Quality Control; Hybrid MSSH
Atmospheric forcings	3 Hourly ECMWF operational forcings; Bulk CORE Formulation;
Runoff :	Dai and Trenberth (2002) Monthly Climatology (Cf Bourdalle-Badie and Treguier, 2006); Addition of runoffs from iceberg melting;
Open Boundary Conditions :	No

Initial Conditions and Relaxation

Initial conditions :	T and S Levitus (2009) for the Ocean; Ifremer/CERSAT data for sea ice concentration and GLORYS2V1 for sea ice thickness
Surface relaxation :	No
Water column (3D) relaxation :	No
Convection :	By intensification of vertical mixing (diffusion term)

Parameterisation

Surface physics parametrisation :	Free Surface (explicit + filtering)
Bottom friction :	Non linear (constant bottom drag)
Lateral friction :	Partial slip (shlat = 0.5)
Vertical mixing :	TKE 1.5 closure scheme; New parameterisation of vertical mixing
Advection :	TVD 2nd order centered scheme and energy/enstrophy conservation scheme
Tracer diffusion :	Isopycnal laplacian
Momentum diffusion :	Horizontal bilaplacian
Horizontal diffusion coefficient for tracers and momentum :	aht0 = 80 m2/s ahm0 = -1.0 e11 m2/s
Vertical diffusion coefficient for tracers and momentum :	avt0 = 1.0 e-5 m2/s avm0 = 1.0 e-4 m2/s

Mercator Ocean - Latest update : May 2015

Figure C.1: System sheet of the global ocean physical analysis and forecast sytem

D

Appendix: Analysis of ocean parameters from Mercator data in the Caribbean Sea

The relevant parameters in the Mercator dataset are temperature, salinity, sea surface height and current velocities. These parameters are first analyzed for the latest year in the dataset, 2016. Subsequently the earlier years in the dataset, up to 2007, are analysed as well, so some interannual variability is shown.

D.1 Sea surface parameters for the year 2016

First, the year 2016 was analysed. The parameters analysed were sea surface salinity, sea surface temperature, sea surface height and sea surface velocities, consisting of eastward velocity $u(t, x, y, z)$ and northward velocity $v(t, x, y, z)$. For the region of interest, the surface values per day were plotted to get an overview of the annual spatial variability of the parameters. After that, a mean was plotted over the year to show the variability.

D.1.1 Sea surface salinity

The sea surface salinity is mostly influenced by fresh water river run off and precipitation. It follows that the lowest salinity values are found near the coast. For the region of interest, this is at 72°W, 11°N where lake Maracaibo connects to the Gulf of Venezuela, and at 62°W, 10°N where the Orinoco river runs into the open ocean, as can be seen in Figure D.1. In August and September, a larger area also away from the coast experiences lower salinity values, see Figure D.1b. The ligaments can be related to the river run off, since one can clearly distinguish their origin location. Surface water that is not part of one of the fresher filaments is also fresher in summer. Since precipitation on average has its peak in the same period of the year, the lower salinity is attributed to precipitation.

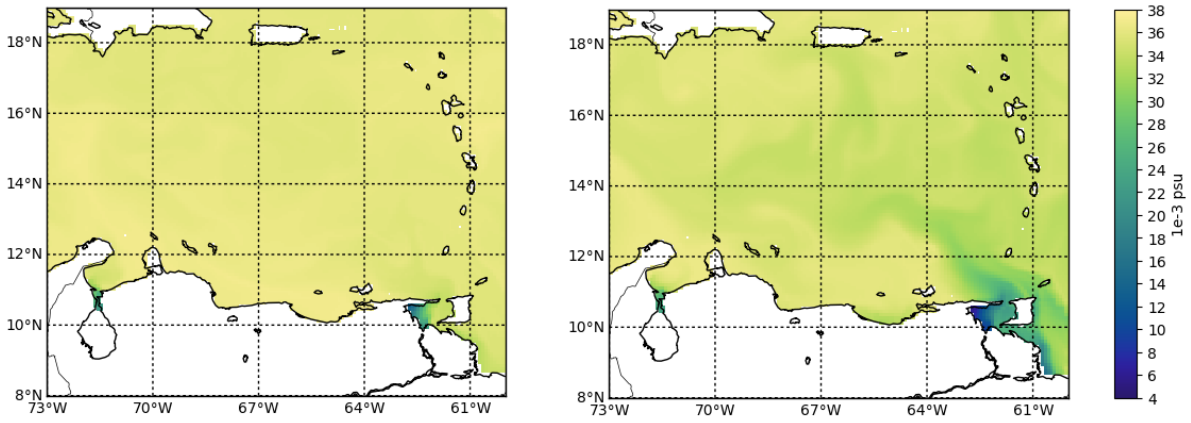

(a) Sea surface salinity on February 1st, 2016.

(b) Sea surface salinity on September 20th, 2016.

Figure D.1: Sea surface salinity on two different dates in 2016 to show the variability over time and over space.

On average, the sea surface salinity of the Caribbean Sea in the region of interest is 36 x 10^{-3} psu. A temporal variation can clearly be distinguished, see Figure D.2. The lower salinity values in September as shown in Figure D.2 can be related to peaks in river run off from the Orinoco and the Amazon river in July and August Hu et al. [2004], as stated in Section 2.8.

D.1.2 Sea surface temperature

Again, the inflow of the Maracaibo lake can be distinguished clearly in Figure D.3. The surface water at that location is very warm, almost 32°C in summer and still around 28°C in winter. The lake has an average depth of 40 m, so it warms up more and faster than the surrounding ocean water. Another very outstanding feature that can be seen, especially in Figure D.3a, is the colder water ligaments that extend from the border of Venezuela into the Caribbean Sea. From literature, as described in Section 2.5, it was found that upwelling caused by the westward Trade Winds is a process of frequent occurance in that area. From Figure D.3a it can be seen that almost the entire Venezuelan coast is prone to upwelling. However, where the coastline is very much east-to-west, or slightly tilted to east-to-westsouthwest, the upwelling is strongest. This is related to the wind direction. The upwelling is found to be strongest in winter, from January to March, which corresponds to the literature described in Section 2.5. It can also be seen in Figure D.4, where the temperature difference between surface water near the coast and away from the coast becomes in winter as big as 3°. The effect of upwelling however, the colder water at the surface, can be found year round.

The sea surface temperature is predominantly determined by solar radiation and air temperature, which is also determined by solar radiation. Solar radiation is most intense in summer, and that causes the surface water temperature to rise from about 27°C in January to 30°C in September/October, see Figures D.3b and D.4.

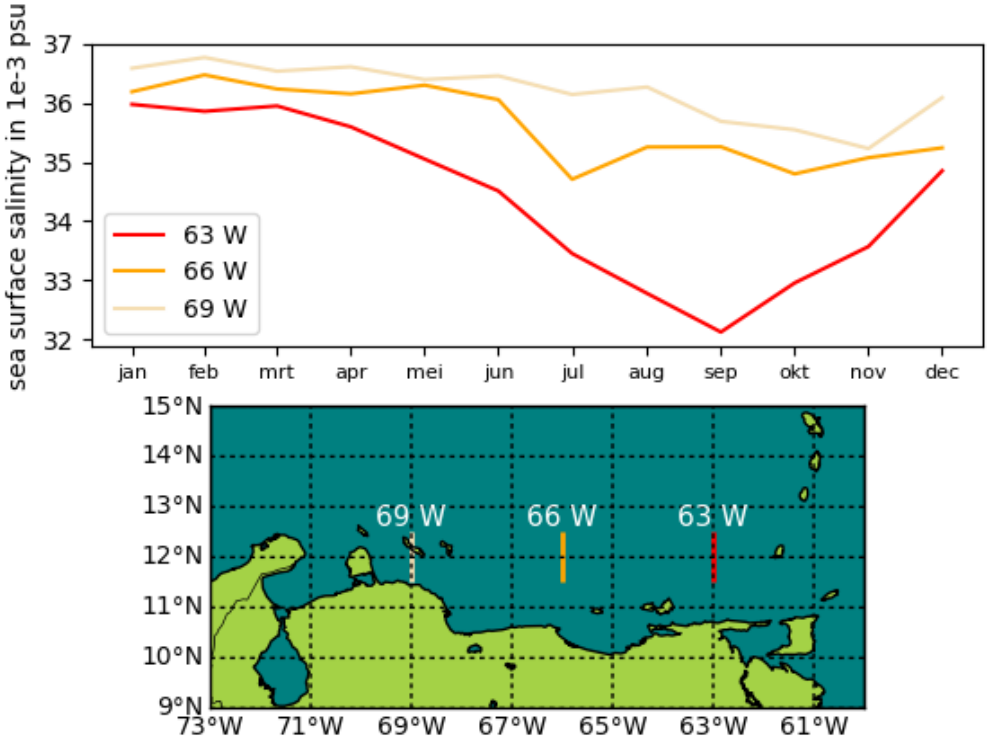

Figure D.2: Monthly averaged sea surface salinity variation over the year 2016 for three locations that are indicated in the map below.

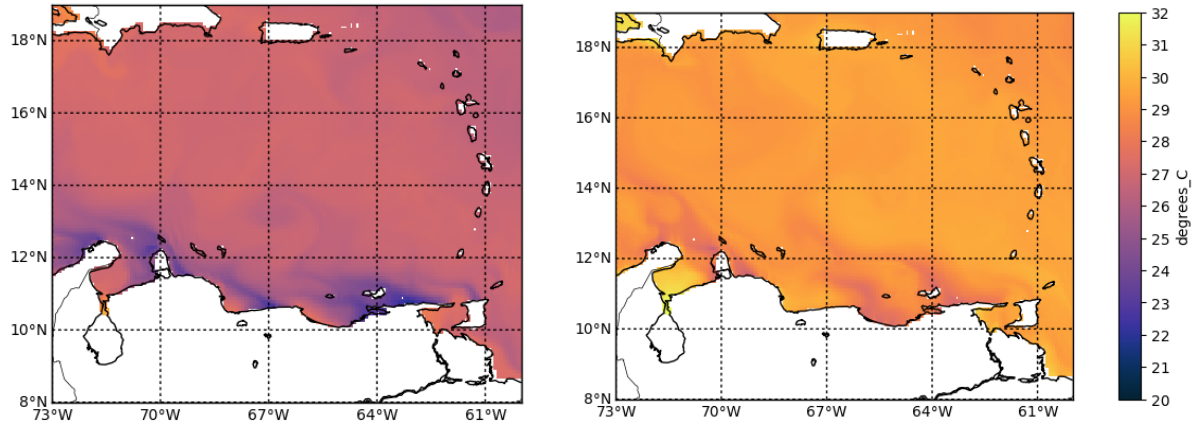

(a) Sea surface temperature on February 18th, 2016.

(b) Sea surface temperature on September 9th, 2016.

Figure D.3: Sea surface temperature on two different dates in 2016 to show the variability over time and over space.

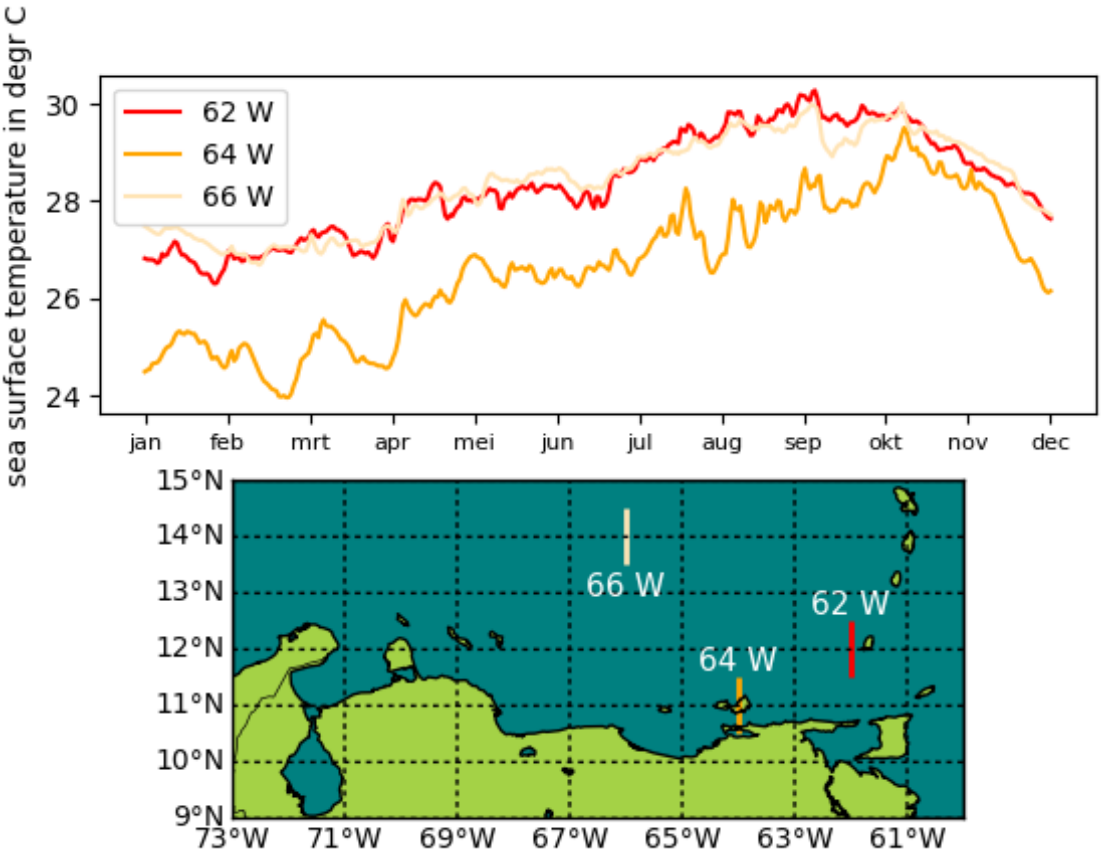

Figure D.4: Daily sea surface temperatures over the year 2016. The temperatures are averaged over the lines indicated in the map below. A clear temperature difference of around 2° between locations near the coast (at 64° W) and away from the coast (at 62 and 66° W) can be seen.

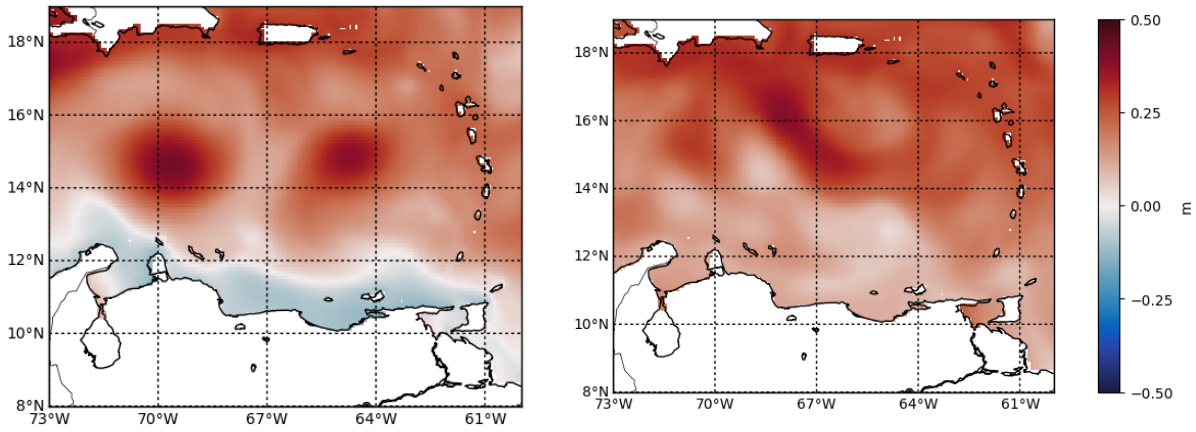

(a) Sea surface height on July 10th, 2016.

(b) Sea surface height on October 27th, 2016.

Figure D.5: Sea surface height on two different dates in 2016 to show the variability over time and over space.

D.1.3 Sea surface height

As can be seen from Figure D.5a, at the south of the region of interest, along the coast of Venezuela, a band of negative sea surface height exist, the width of which varies over time and space. To the north, a generally positive sea surface height can be seen.

The negative SSH band is very persistent. A change in this situation begins at April 26th, 2016 at the western part of the band and extends to the east and causes the band to vanish entirely on May 6th, 2016. It returns again on May 23rd, 2016. This might be related to the stength of the wind, the local air pressure or the temperature of the water. Some big eddies come rolling by at that time, see the dark red areas in Figure D.5a. Also after hurricane Matthew, from September 23rd 2016 to December 11th 2016, the negative SSH band disappears as the sea surface height equalizes as in Figure D.5b.

From Figure D.6 it can be seen that the temperal variation very much depends on the location. The forcing mechanism that determines the sea surface height is different for the two locations. At the southern border, upwelling plays a major role. The generally westward wind forces the water away from the coast. This has two consequences. First is that deeper and colder water is forced to the surface and secondly the sea surface height is lowered. These two phenomena as a consequence of upwelling are also described in in Kuo et al. [2000] and Hickey [1975]. An explanation for the coincidence of these two processes could be the steric height effect, as indicated by Alvera-Azcárate et al. [2009b]. This effect relates the expanding of the ocean water, so rise of the sea level, to water temperature increase. These two processes both depend heavily on the intensity of the wind speed and direction. If the wind speed and direction would vary in the same way along the entire coast, then the sea surface height at different locations along the coast varies in the same way. The mean of the sea surface height does differ for the different locations along the coast. More to the east is a higher surface height, or a less negative sea surface height. In the middle of the Caribbean Sea, at 14°N, it can be seen that the SSH of one location is related to the other locations with a lag. The sea surface height

variations seem to travel from east to west, so along with the general direction of the current. The variations are caused by eddies, as can be seen in Figure D.7a.

D.1.4 Sea surface velocity patterns

As described in Section 2.3, the flow is predominantly from southeast to northwest. In Figure D.7, a fast jet current around the corner of Venezuela, through the Grenada Passage at 62°W in the southeast, entering the Caribbean Sea can be seen. Current velocities as high as 2.2 m/s are observed in the Grenada Passage. A fast-current jet is present throughout the year.

In the winter, last half of December to March, large sea surface velocities are found at the southern border of the Venezuala Basin. A fast-current jet flows from the Grenada Passage at 62°W in the southeast of the Caribbean Sea along the coast of Venezuela to the west, as also described by Centurioni and Niiler [2003]. This phenomenon is presumably caused by upwelling and local winds. Wind-driven transport is to the west as follows from the wind stress curl is negative when going north, see Figures 4.1a to 4.1f. Upwelling causes a westward flow, as follows from the thermal wind relation, see equation 4.3 and 4.4.

Local winds are the main driver for the upwelling (Müller-Karger et al. [1989] and Andrade and Barton [2005]). Thus the wind has two ways of magnifying westward currents in the winter. To the north, a more variable flow is found. More meandering and lower velocities are seen.

From April to June, the fast-current jet turns towards the northwest, is less distinct and overall velocities are lower.

Three big anticyclonic eddies between 13°N and 17°N are identified in 2016. In the channel between Curaçao and the mainland relatively high velocities of around 1.5 m/s can be seen. These high velocities seem to be caused by channeling of the velocities at the eastside of the island.

In April and May large eddies were identified. October and November show a deviating velocity pattern compared to other months, with lower velocities overall and a less distinguished jet in northwestern direction.

D.2 Sea surface parameters for the years 2007 until 2016

After analysing one year in the dataset, 2016, it became clear that it was not possible to draw conclusions about the variation of the parameters over the year, because of some non-annual processes like hurricane Matthew and El Niño that occured in 2016. For that reason, years 2007 until 2015 were also analysed to get an idea of the persistence of the processes observed in 2016. Since sea surface salinity did not vary so much over the year and did not seem to interact with the flow, it was left out of the following analysis. A detailed description of the sea surface velocities is found in Section 4.1.

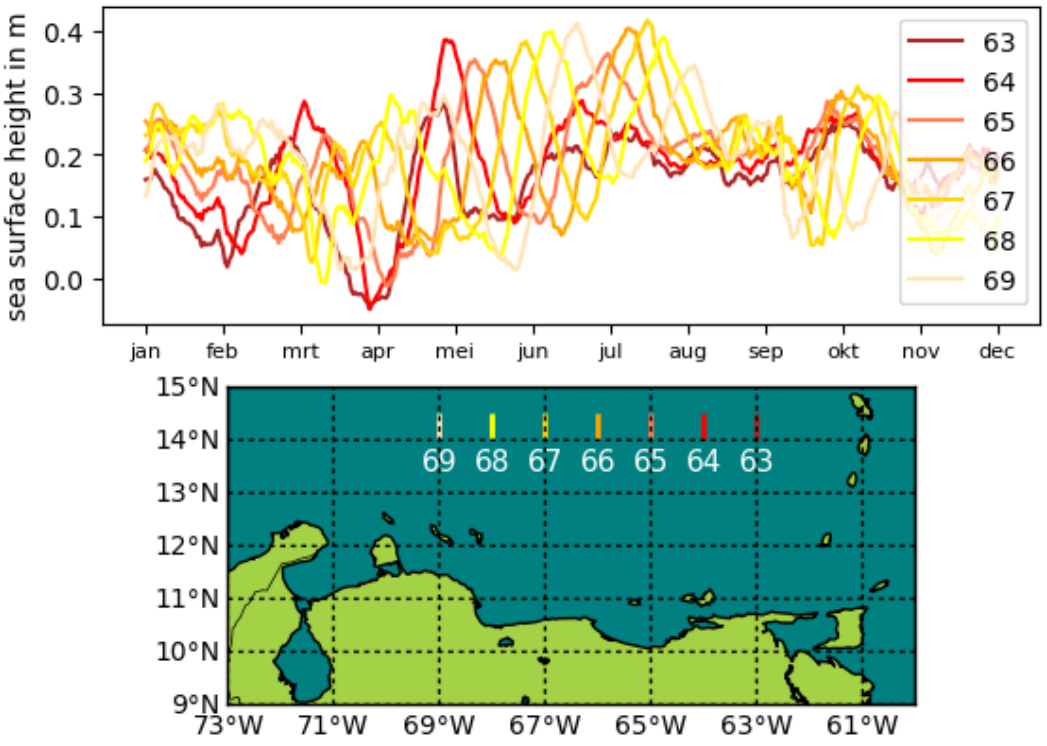

(a) Sea surface height at 14°N.

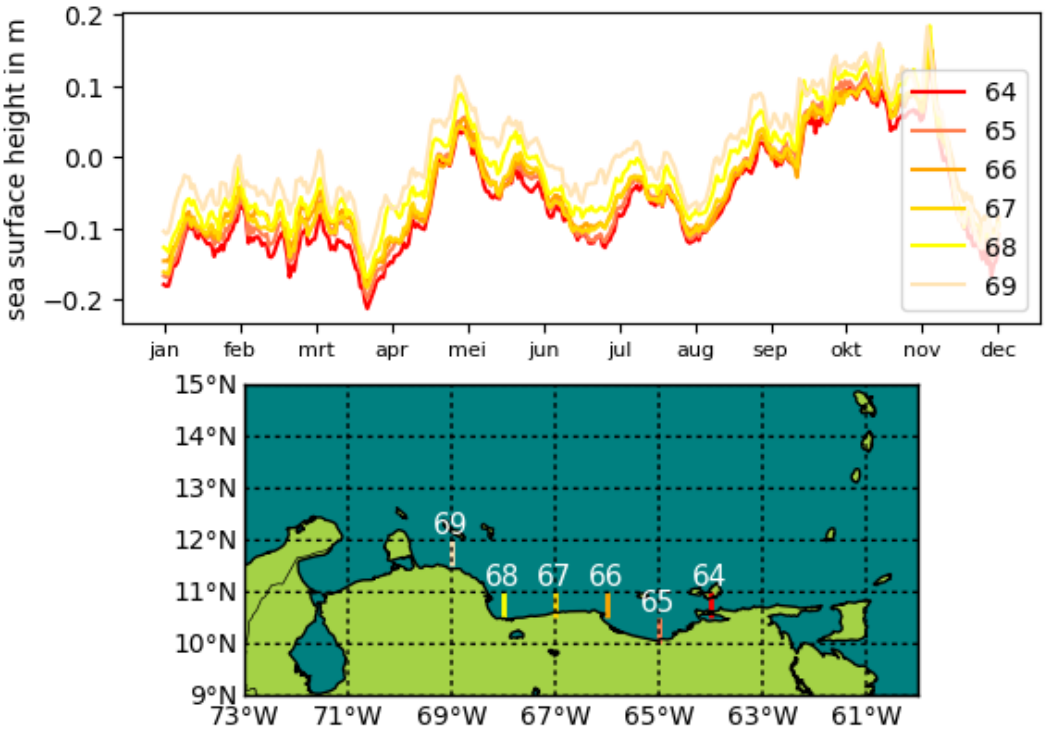

(b) Sea surface height near the coast of Venezuela.

Figure D.6: Daily sea surface height values over the year 2016. The different locations (indicated on the map below) experience very different SSH values over the year.

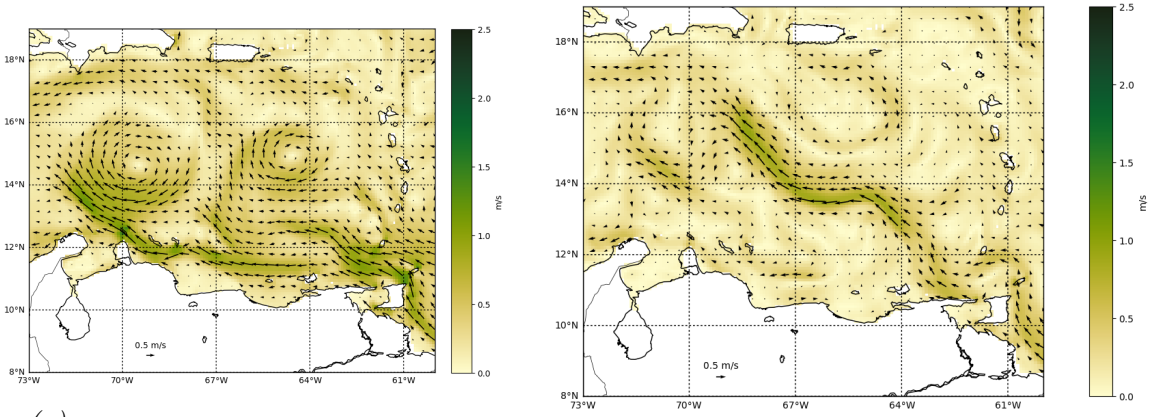

(a) Sea surface velocities on July 10th, 2016.

(b) Sea surface velocites on October 27th, 2016.

Figure D.7: Sea surface velocities on two different dates in 2016 to show the variability over time and over space. D.7b is right after hurricane Matthew.

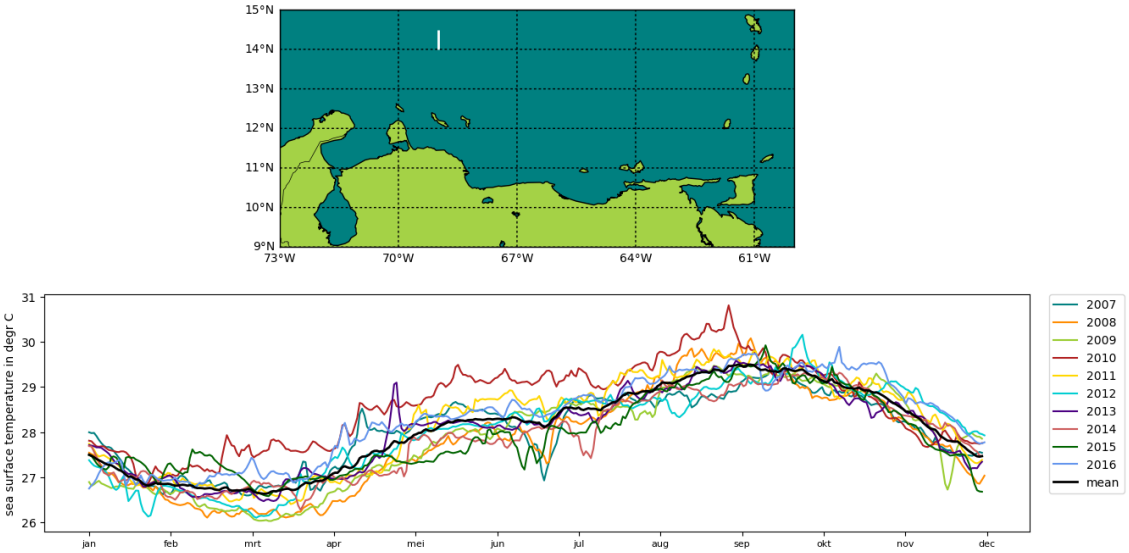

Figure D.8: Daily sea surface temperature values of the years 2007 until 2016. The mean is plotted in black.

D.2.1 Sea surface temperature

In Figure D.8 the daily sea surface temperature values for the years 2007 until 2016, together with their mean, are plotted. The months February and March are the coldest while August and September are the warmest months. 2010 appears to be a relatively warm year, especially for the months April until September. From these ten years it cannot be concluded that 2016 was an exceptional year.

D.2.2 Sea surface height

The influence of hurricane Matthew is not as clear as was expected. In Figure D.9b, it can be seen that the mean of the sea surface height near the coast becomes less negative in the autumn months, so what stood out in 2016 and was related to hurricane Matthew,

seems to be a yearly process. The year 2016 is relatively positive however compared to other years. Also the standard deviations for these two locations are plotted and shown in Figure D.10. The standard deviation is significantly bigger at 14°N. This is mostly due to the passing eddies in the period June to October.

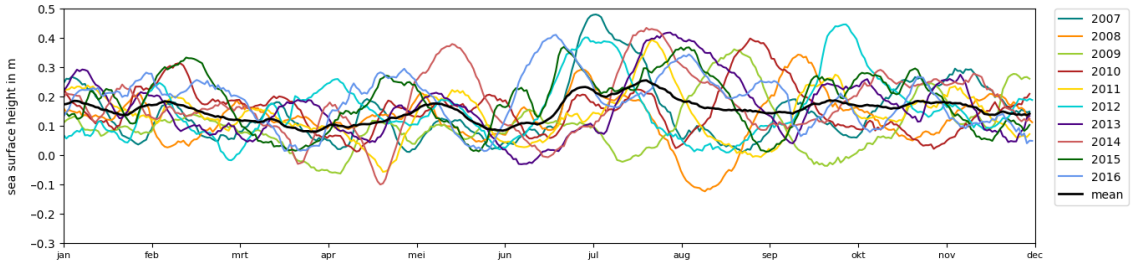

(a) Daily sea surface height values of the years 2007 until 2016 at 69°W, 14°N. The mean is plotted in black.

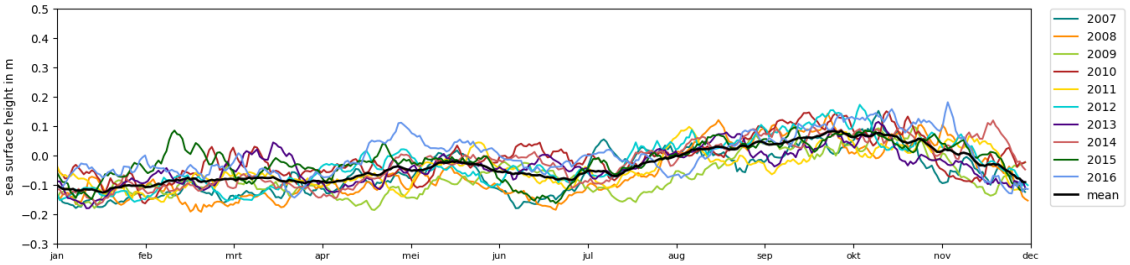

(b) Daily sea surface height values of the years 2007 until 2016 at 69°W, 11.5°N. The mean is plotted in black.

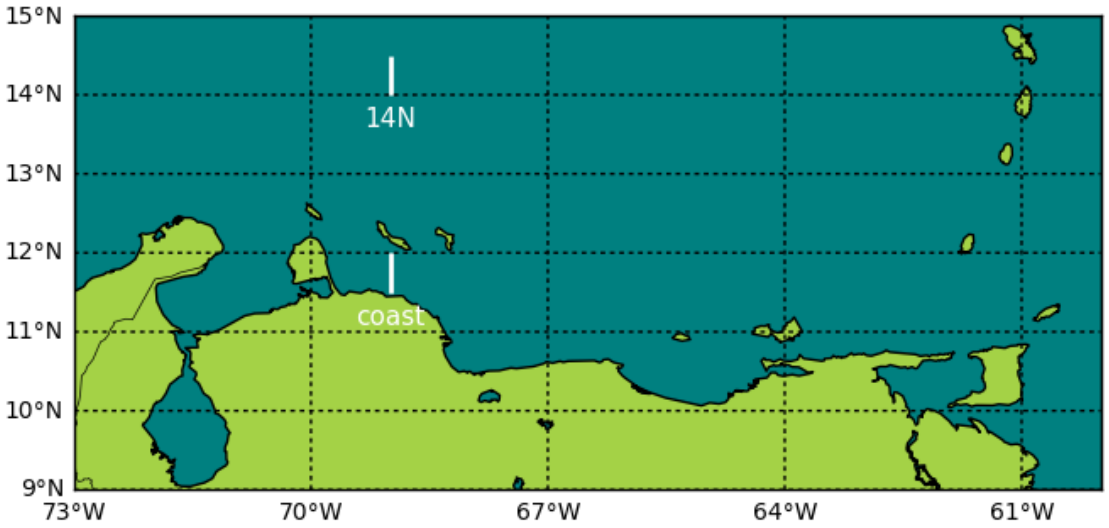

(c) Locations of the two above plots.

Figure D.9: Daily sea surface height values for the years 2007 until 2016.

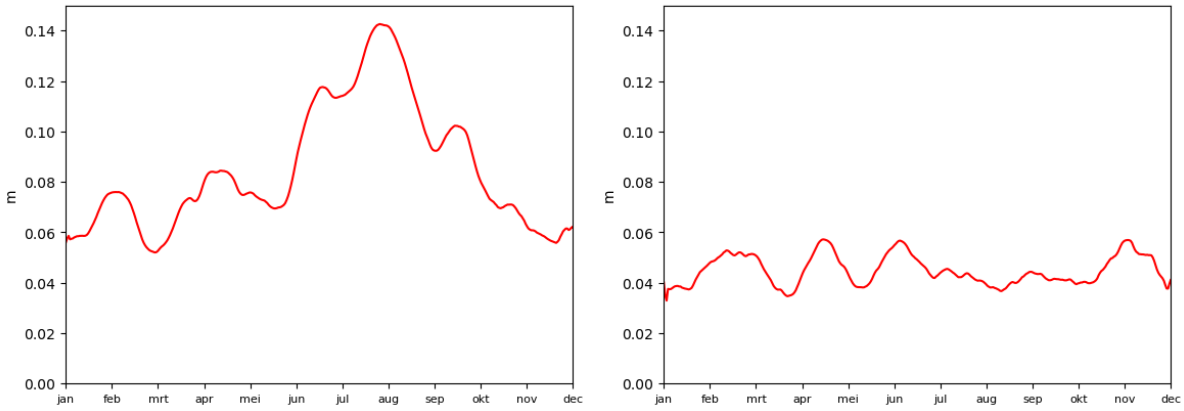

(a) Standard deviation over time of SSH at 14°N, 63°W. *(b)* Standard deviation over time of SSH at 11°N, 63°W.

Figure D.10: Standard deviation of the mean sea surface height at two different locations. It can be seen that the standard deviation for the more northern location is significantly higher than for the standard deviation near the coast.

E

Appendix: Elaboration on the Geostrophic and Thermal Wind Balance for the upwelling system along the coast of Venezuela

This appendix elaborates on the Geostrophic Balance and the Thermal Wind Balance and focusses on the upwelling region in the south of the Venezuela Basin. First, a qualitative analysis is performed for both of these balances to understand the mechanism of the relation. Subsequently, a quantitative analysis is performed to investigate the influence of the upwelling in the south of the Venezuela Basin on the strength of the southern jet of the Caribbean Current. This is done using the situation of one day in the ten years of data analyzed, 9 January 2016 along the 63°W line. This time and location are chosen because of the clear presence of upwelling. The interaction between these two different processes is not investigated in this analysis. A highly simplified overview of the Venezuela coast and the Caribbean Sea is shown in figure E.1.

Figure E.1: Schematic overview of situation in the Venezuela Basin. y is to the north, x is to the east.

E.1 The Geostrophic Balance

Referred is to Equation 4.1 and 4.2 for the Geostrophic Balance:

$$fv = \frac{1}{\rho}\frac{\partial p}{\partial x} \tag{4.1}$$

$$fu = -\frac{1}{\rho}\frac{\partial p}{\partial y} \tag{4.2}$$

In these equations, $\partial p/\partial x$ is a horizontal pressure gradient, f is the Coriolis parameter, u and v are water velocities in x and y-direction respectively and ρ is water density.

E.1.1 Qualitative analysis

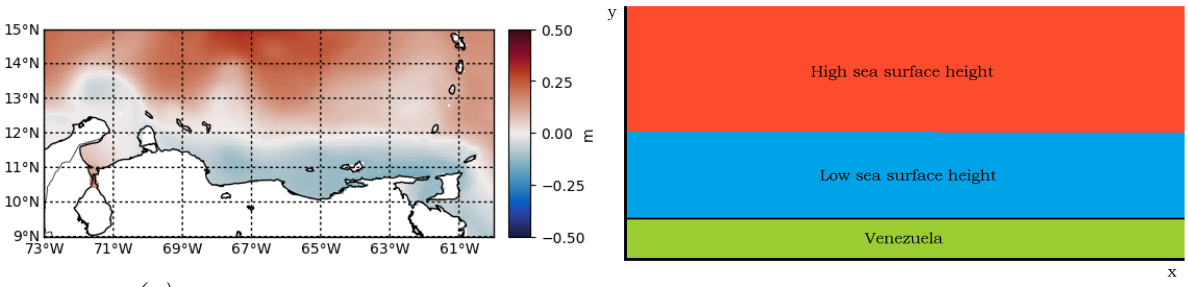

(a) Situation on 9 January 2016.

(b) Schematic overview.

Figure E.2: Sea surface height along the coast of Venezuela. The actual situation of 9 January 2016 in E.2a is schematized in E.2b. High sea surface height is found to the north and low sea surface height to the south.

1) The wind blows from east to west. The Ekman transport due to the wind along the coast is directed to the right by Coriolis, thus in offshore direction.

2) Therefore, the sea surface height has a north-south slope, with higher sea surface height found further offshore, as in Figure E.2. For $\partial y > 0$, $\partial h > 0$.

3) This causes a positive pressure gradient; $\partial p/\partial y > 0$

4) Since $f > 0$ and $\rho > 0$, $u < 0$. u is positive in positive x-direction, so the water will flow to the west.

In summary, the water flows from the higher pressure in the north to the lower pressure in the south. This flow is directed to the right, in this case to the west, by Coriolis effect. Thereby, the westward jet is intensified by the north-south pressure gradient.

E.1.2 Quantitative analysis

On 9 January 2016 at 63°W, the sea surface height showed a shape as in Figure E.3. The hydrostatic pressure difference ∂p between two points can be calculated by $\rho g(h_1 - h_2)$. The sea surface heights h_1 and h_2 are taken at point 1 at 63°W, 12°N and point 2 at

63°W, 11°N. From Figure E.3, h_1 is 0.04 m and h_2 is -0.12 m. The average ρ is 1022 kg/m^3 and g is 9.81 m/s^2. The distance between point 1 and point 2 is 110 919 m.

The Coriolis parameter f can be calculated by $2\Omega \sin\phi$. Ω is the rotational speed of the earth, $7.29 * 10^{-5}$ rad/s. ϕ is the latitude of the location of interest, on average 11.5° in this case. f is $2.91 * 10^{-5}$ s^{-1}.

Filling this into Equation 4.2, gives:

$$u * 2.91 * 10^{-5} = -\frac{1}{1022} \frac{1022 * 9.81(0.04 - -0.12)}{110919} \tag{E.1}$$

This gives a u of -0.49 m/s, consequently in westward direction.

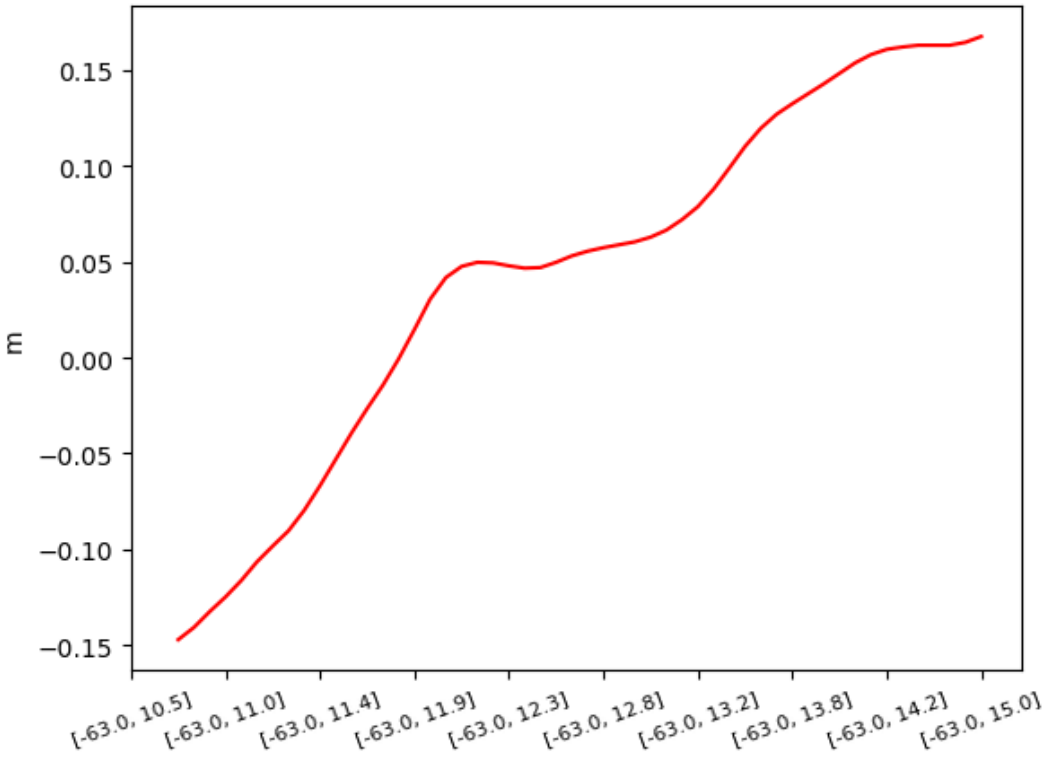

Figure E.3: Sea surface height along 63° W on 9 January 2016 in meter.

E.2 The Thermal Wind Balance

Referred is to Equation 4.3 and 4.4 for the Thermal Wind Balance:

$$\frac{\partial u}{\partial z} = \frac{g}{f\rho_0} \frac{\partial \rho}{\partial y} \tag{4.3}$$

$$\frac{\partial v}{\partial z} = -\frac{g}{f\rho_0} \frac{\partial \rho}{\partial x} \tag{4.4}$$

In these equations, the used variables have identical meaning to the variables in Equations 4.1 and 4.2.

E.2.1 Qualitative analysis

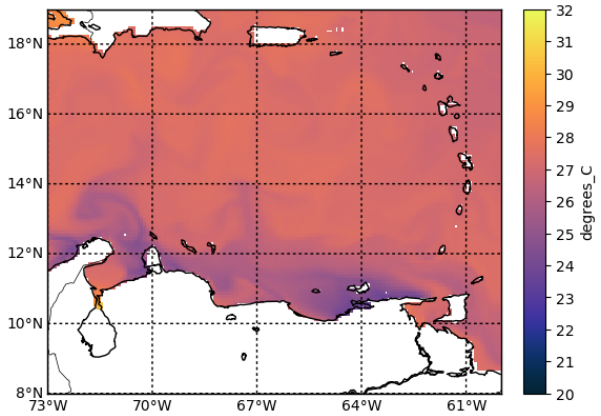

(a) Situation on 9 January 2016.

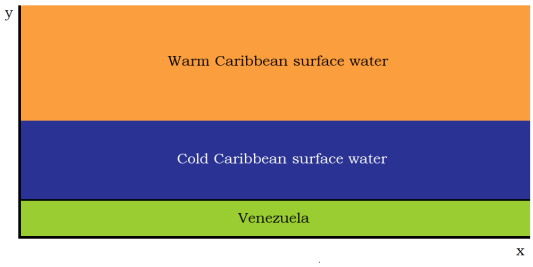

(b) Schematic overview.

Figure E.4: Sea surface temperature along the coast of Venezuela. The actual situation of 9 January 2016 in E.4a is schematized in E.4b. Coastal upwelling induces cold deep water to come to the surface. Consequently, a positive horizontal temperature gradient in y direction exists.

1) In Figure E.4, when increasing y, the sea surface temperature T also increases, so for $\partial y > 0$ then $\partial T > 0$.

2) When $\partial T > 0$ then $\partial \rho < 0$ according to Equation 2.4.

3) So $\partial \rho / \partial y < 0$.

4) This means $\partial u / \partial z < 0$.

5) When z is positive in upward direction, u decreases upwards. This means u is enhanced in negative x direction, so to the west at the surface, decreasing over depth.

E.2.2 Quantitative analysis

The Boussinesq approximated density ρ_0 is 1000 kg/m^3. $\partial \rho$ is calculated by $\rho_1 - \rho_2$. Density ρ can be calculated by the equation of state, Equation 2.4, $\rho = \rho_0(1 - \alpha_T(T - T_0)) + \beta_S(S - S_0)$. Salinity S_1 and S_2 at point 1 and 2, as described before, were both taken as 36 psu, see Figure D.1a. This figure shows the sea surface salinity in the beginning of 2016. Temperatures T_1 and T_2 are 26° C and 22° C. ρ_1 is 1022.07 kg/m^3 and ρ_2 is 1022.89 kg/m^3.

Vertical shear $\partial u / \partial z$ can be estimated by $(u_1 - u_2)/(z_1 - z_2)$, where subscripts 1 and 2 indicate different depth levels. Subscript 1 is chosen to be surface level. The depth of subscript 2 can be assumed from a velocity over depth section. In Figure E.5, the vertical section of the eastward water velocity on 9 January 2016 is shown. Between 11 and 12°N, at z = -80 m, u = 0 m/s on average. Thus, z_1 = 0 m, z_2 = -80 m and u_2 = 0 m/s. Only u_1 is unknown now. Equation 4.3 becomes:

$$\frac{u_1 - 0}{0 - -80} = \frac{9.81}{2.91 * 10^{-5} * 1000} \frac{1022.07 - 1022.89}{110919} \tag{E.2}$$

u_1 becomes -0.20 m/s.

To know to the extend of the vertical shear gradient, one needs to know the temperature distribution over depth. This is shown in Figure E.6. The temperature gradient close to the coast extends to about 125 m depth. This means that the subsurface countercurrent at about 200 m water depth can not be contributed to upwelling.

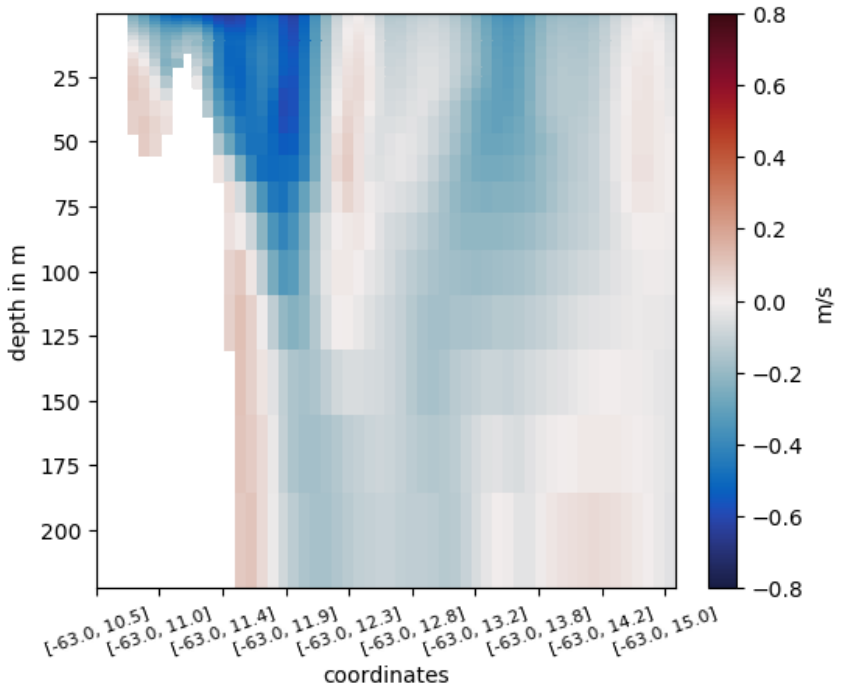

Figure E.5: Vertical section at 63° W from 10.5° N to 15.0° N showing the horizontal and vertical eastward velocity distribution on January 9th, 2016.

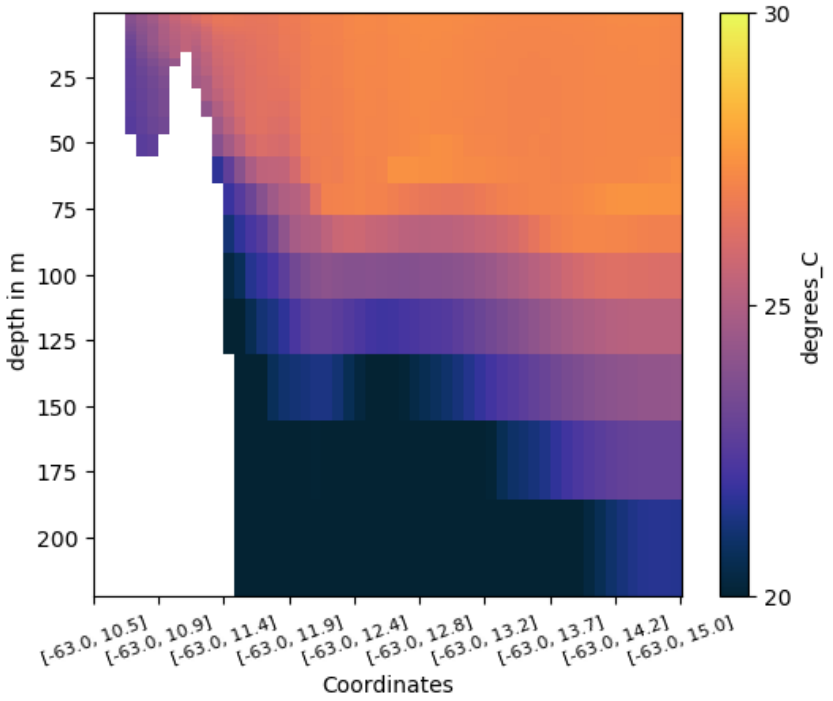

Figure E.6: Vertical section at 63° W from 10.5° N to 15.0° N showing the horizontal and vertical temperature distribution on January 9th, 2016, a regular day when upwelling occured.

F

Appendix: Identified eddies in the Venezuela Basin

Visual identification of eddies in the surface plots of the velocities was performed to analyse the behaviour of eddies. Only large anticyclonic eddies, of at least 200 km in diameter, that originated in the southern half of the Caribbean Sea, so below 15°N, and lasted for at least twenty days were taken into account. It was chosen not to use an eddy tracker mechanism, because only the large scale eddies have a big enough influence to affect an OTEC system and large scale eddies are easily detected by eye. Apart from that, eddy tracker mechanisms can give incorrect output, so (visual) investigation is desirable anyway.

Identification of the eddies was done by observation of surface current velocity plots. Currents were defined as eddies when a 360° rotating body of water was observed. The location and date of this emerged eddy was noted. When the rotation was no longer 360° or the eddy had been advected out of the region of interest, the location and date was noted again. Thirtynine anticyclones were observed. Their specifics can be found inTtable F.1. In the same period, nine cyclonic eddies were identified. These can be found in Table F.2.

For overview, in Figure F.1 the location of where eddies were generated or dissipated is shown. In Figure F.2 the number of eddies that existed each year is shown. The steadily declining line of amount of large eddies per year could be related to the steadily decline in volume flux through the Grenada Passage, into the Caribbean Sea, but that cannot be concluded from only ten years of data.

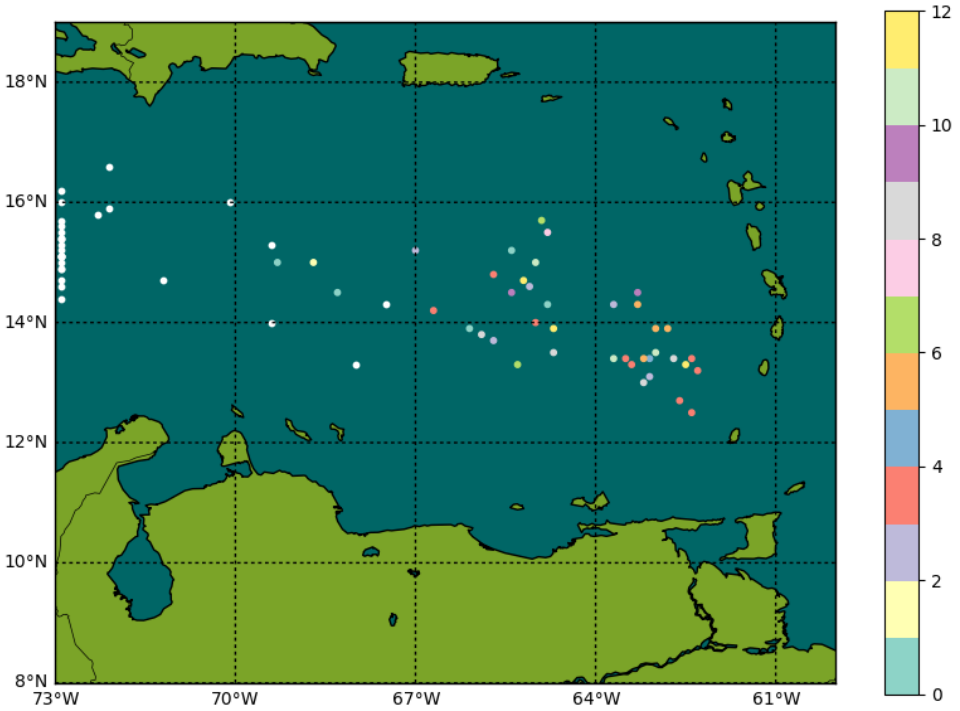

Figure F.1: Generation and dissipation location of the anticyclonic eddies identified. Dot identifies the center of the eddy. White dots are dissipation locations, colored dots are generation location per month. There is no clear correlation between generation month and generation location. The white dots that are on the 73° W line can also mean that the eddy dissappeared out of the region of interest, and not necessarily that the eddy dissipated.

Figure F.2: Eddies, cyclonic and anticyclonic, counted per year.

Table F.1: Anticyclonic eddies identified in the Venezuela Basin in the years 2007 to 2016.

Name	**Generation location**		**Dissipation location**		**Start date**	**End date**
	$^\circ E$	$^\circ N$	$^\circ E$	$^\circ N$	*yyyy-mm-dd*	*yyyy-mm-dd*
2007-01	-	-	-72.9	14.9	2007-01-01	2007-02-02
2007-02	-64.8	14.3	-72.9	16.2	2007-01-01	2007-03-22
2007-03	-63.1	13.1	-72.9	16	2007-03-04	2007-06-02
2007-04	-63.5	13.4	-72.9	15.1	2007-04-24	2007-08-24
2007-05	-62.7	13.4	-72.9	15.1	2007-09-17	2008-01-05
2007-06	-65	15	-72.9	15.1	2007-11-02	2008-01-05
2008-01	-66.1	13.9	-72.9	15.4	2008-01-01	2008-02-25
2008-02	-68.7	15	-72.9	15.1	2008-02-28	2008-04-07
2008-03	-62.4	13.4	-72.1	15.9	2008-04-12	2008-08-06
2008-05	-64.8	15.5	-69.4	15.3	2008-08-08	2008-10-12
2008-07	-62.5	13.3	-68	13.3	2008-12-13	2009-02-17
2009-01	-65.7	13.7	-69	14.8	2009-03-25	2009-05-06
2009-02	-62.8	13.9	-72.9	14.6	2009-06-28	2009-11-11
2009-03	-64.7	13.5	-66.4	14.7	2009-09-16	2009-11-15
2009-05	-63.7	13.4	-69.4	14	2009-11-13	2010-01-03
2010-01	-65.4	15.2	-72.9	15.4	2010-01-09	2010-03-31
2010-02	-65.1	14.6	-72.9	15.6	2010-03-27	2010-07-04
2010-03	-64.9	15.7	-72.9	15.1	2010-07-15	2010-11-11
2010-04	-63.3	14.5	-70.1	16	2010-10-17	2011-01-15
2011-01	-65	14	-72.9	15.5	2011-04-11	2011-07-18
2011-02	-62.4	12.5	-72.9	15.1	2011-04-25	2011-09-25
2011-03	-63.3	14.3	-72.9	15.1	2011-06-29	2011-09-25
2011-06	-64.7	13.9	-72.9	15.7	2011-12-03	2012-03-20
2012-01	-67	15.2	-72.9	15.4	2012-03-06	2012-05-24
2012-03	-63.1	13.4	-72.3	16.3	2012-05-07	2012-08-23
2012-05	-65.9	13.8	-72.9	15.4	2012-09-30	2012-12-03
2013-01	-69.3	15	-72.3	15.8	2013-01-11	2013-03-05
2013-02	-66.7	14.2	-72.9	14.4	2013-04-21	2013-07-24
2013-03	-62.6	12.7	-72.9	15	2013-04-29	2013-10-06
2013-04	-63.2	13	-69	17	2013-09-24	2013-12-21
2013-05	-63	13.5	-67.5	14.3	2013-11-11	2013-12-25
2014-02	-65.7	14.8	-72.9	14.9	2014-04-15	2014-07-02
2014-03	-63.2	13.4	-72.9	15	2014-06-03	2014-09-23
2014-06	-65.2	14.7	-71.2	14.7	2014-12-09	2015-03-07
2015-01	-63.4	13.3	-72.9	15.4	2015-05-01	2015-08-03
2015-02	-65.3	13.3	-72.9	15.3	2015-07-08	2015-09-30
2015-04	-65.4	14.5	-72.9	15.8	2015-10-09	2015-12-17
2016-01	-63.7	14.3	-72.9	14.7	2016-03-03	2016-06-20
2016-02	-62.3	13.2	-72.9	15.2	2016-04-17	2016-08-10
2016-03	-63	13.9	-72.1	16.6	2016-06-15	2016-09-22

Table F.2: Cyclonic eddies identified in the Venezuela Basin in the years 2007 to 2016.

Name	**Generation location**		**Dissipation location**		**Start date**	**End date**
	$^{\circ}E$	$^{\circ}N$	$^{\circ}E$	$^{\circ}N$	*yyyy-mm-dd*	*yyyy-mm-dd*
2008-04	-66.1	12.9	-72.9	15.4	2008-08-04	2008-10-29
2008-06	-67.6	14.7	-69.3	15.4	2008-10-14	2008-11-19
2009-04	-68.2	13.5	-71.9	13.2	2009-09-28	2009-11-22
2012-02	-65.6	13.5	-68.2	14.4	2012-05-06	2012-06-09
2012-04	-66	14.3	-72.9	16.1	2012-08-04	2012-10-26
2014-01	-65.7	13.3	-70.1	14.4	2014-04-03	2014-05-10
2014-04	-68.2	13.5	-71	13.7	2014-09-08	2014-10-30
2015-03	-66.3	15	-70.1	14.5	2015-08-31	2015-10-09
2016-04	-63.4	12.9	-66.4	13.2	2016-11-21	2016-12-21

Appendix: Surface velocity plots per year

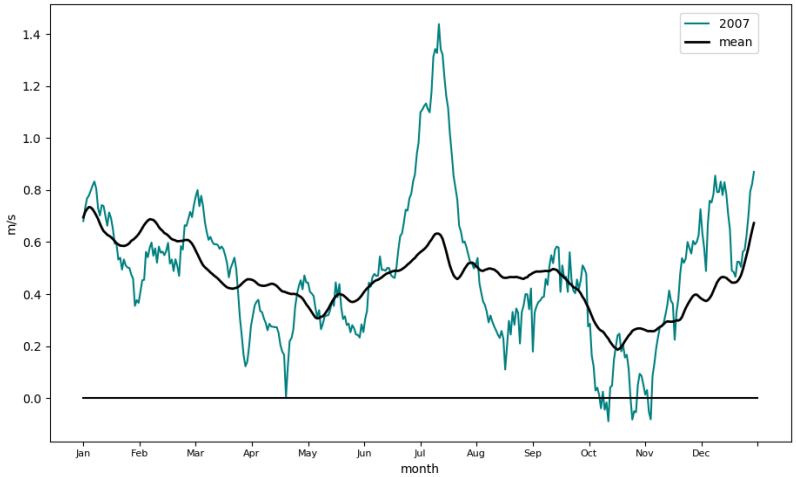

Figure G.1: Surface velocity in the channel region for the year 2007. The black line indicates the mean of all ten years.

Figure G.2: Surface velocity in the channel region for the year 2008. The black line indicates the mean of all ten years.

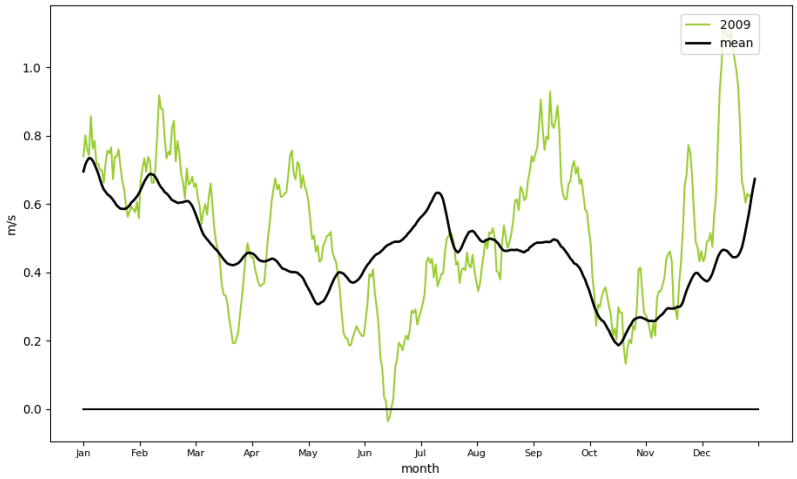

Figure G.3: Surface velocity in the channel region for the year 2009. The black line indicates the mean of all ten years.

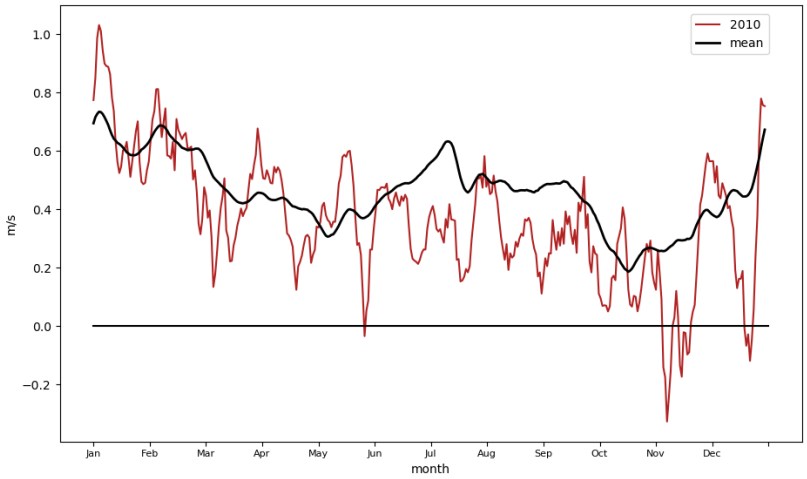

Figure G.4: Surface velocity in the channel region for the year 2010. The black line indicates the mean of all ten years.

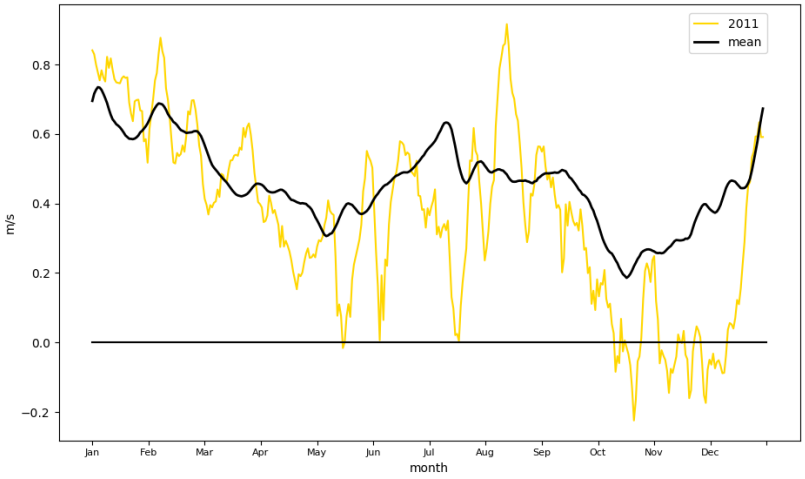

Figure G.5: Surface velocity in the channel region for the year 2011. The black line indicates the mean of all ten years.

Figure G.6: Surface velocity in the channel region for the year 2012. The black line indicates the mean of all ten years.

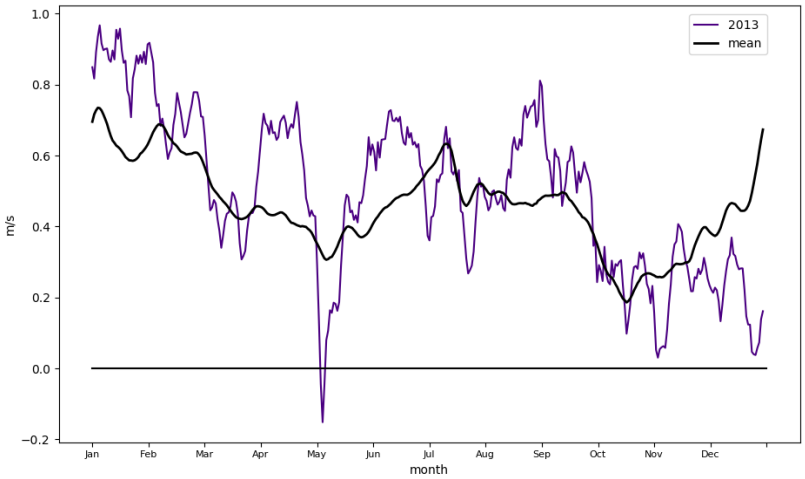

Figure G.7: Surface velocity in the channel region for the year 2013. The black line indicates the mean of all ten years.

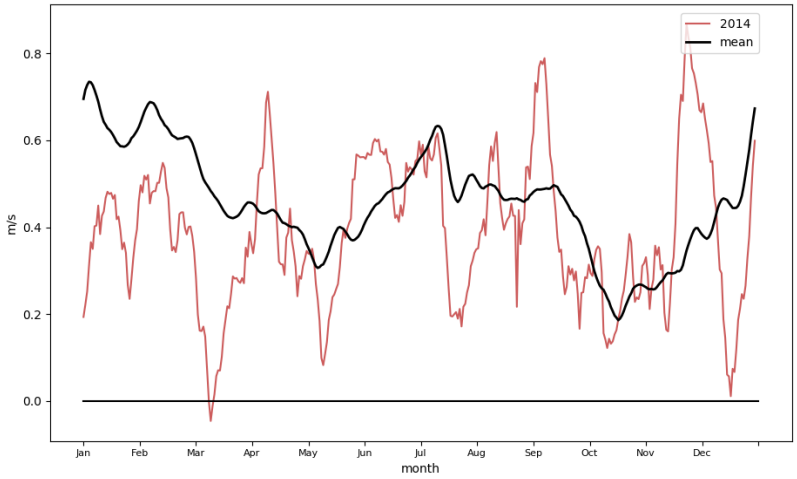

Figure G.8: Surface velocity in the channel region for the year 2014. The black line indicates the mean of all ten years.

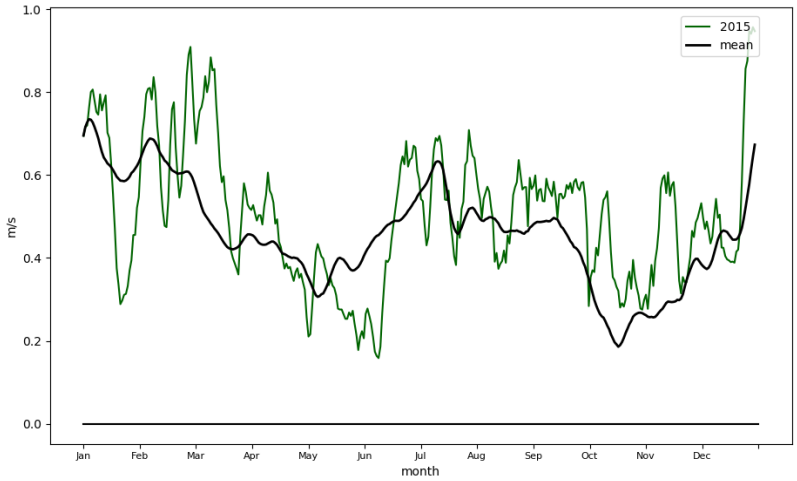

Figure G.9: Surface velocity in the channel region for the year 2015. The black line indicates the mean of all ten years.

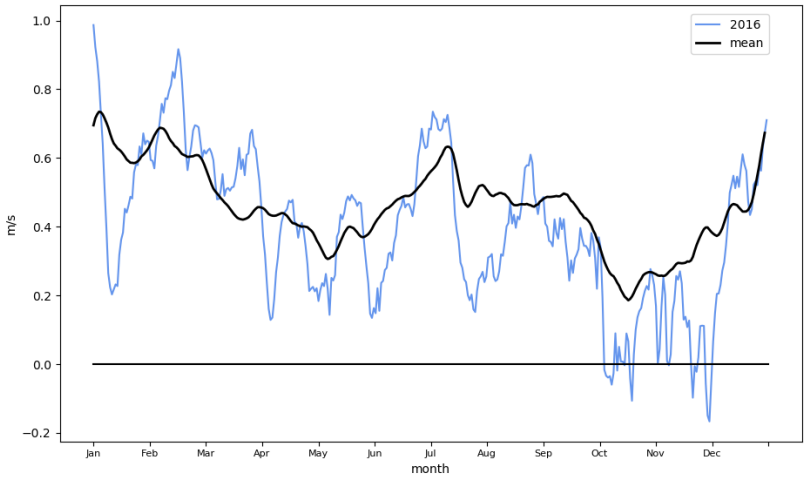

Figure G.10: Surface velocity in the channel region for the year 2016. The black line indicates the mean of all ten years.

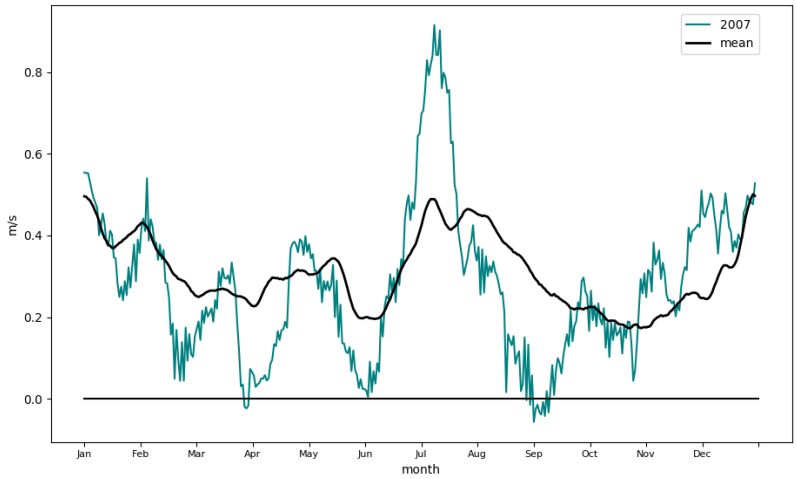

Figure G.11: Surface velocity in the unobstructed region for the year 2007. The black line indicates the mean of all ten years.

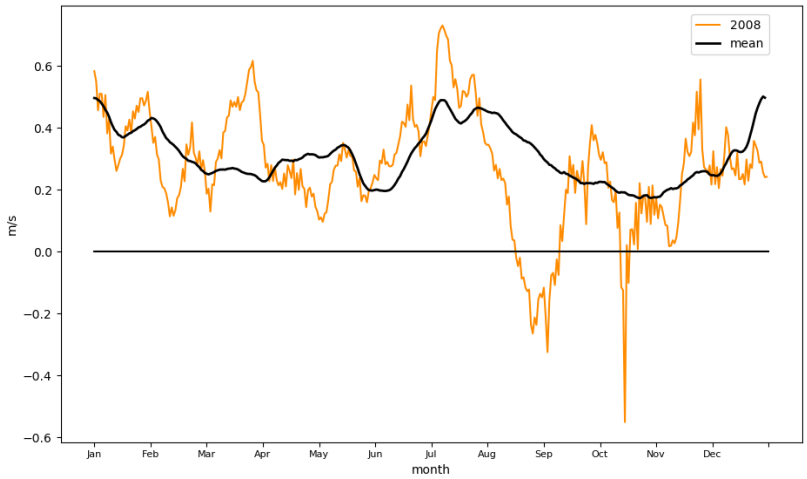

Figure G.12: Surface velocity in the unobstructed region for the year 2008. The black line indicates the mean of all ten years.

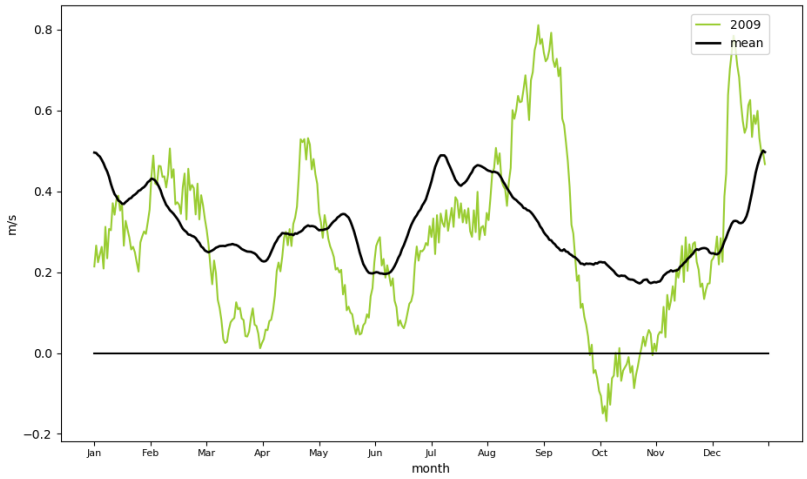

Figure G.13: Surface velocity in the unobstructed region for the year 2009. The black line indicates the mean of all ten years.

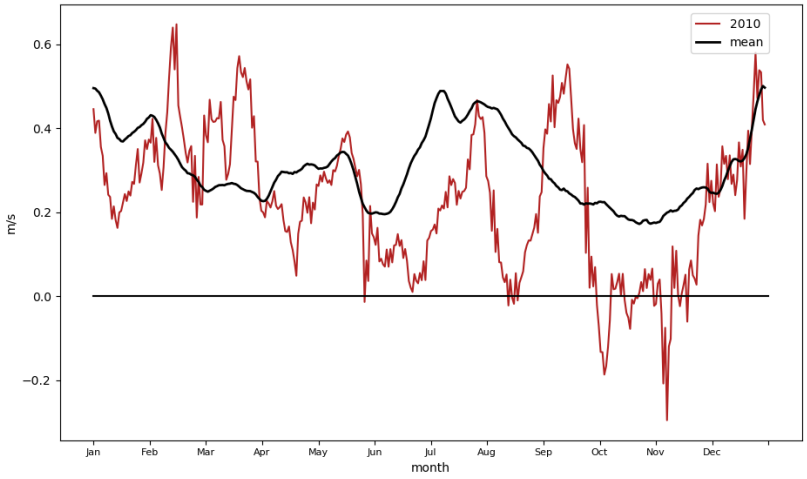

Figure G.14: Surface velocity in the unobstructed region for the year 2010. The black line indicates the mean of all ten years.

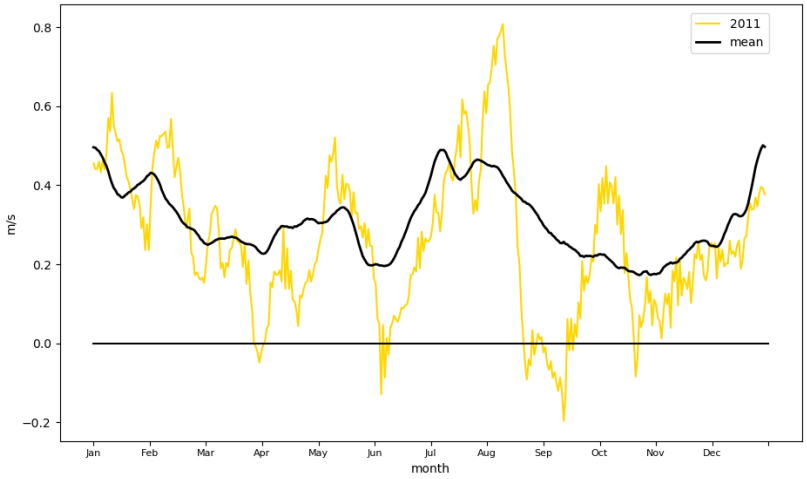

Figure G.15: Surface velocity in the unobstructed region for the year 2011. The black line indicates the mean of all ten years.

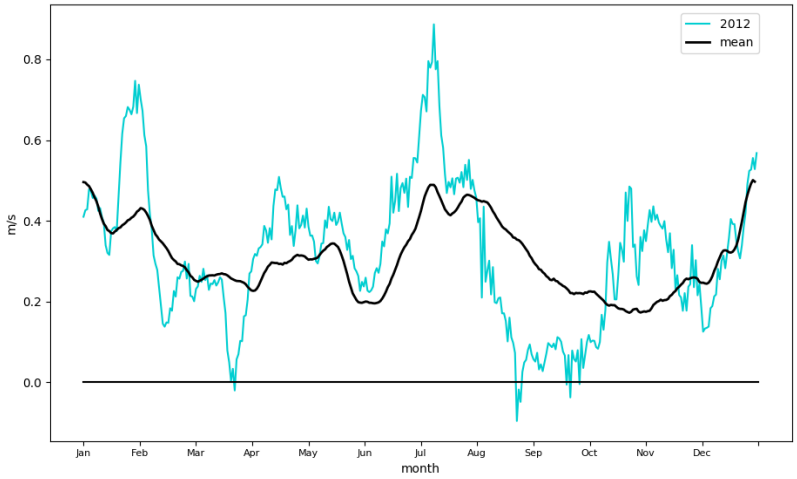

Figure G.16: Surface velocity in the unobstructed region for the year 2012. The black line indicates the mean of all ten years.

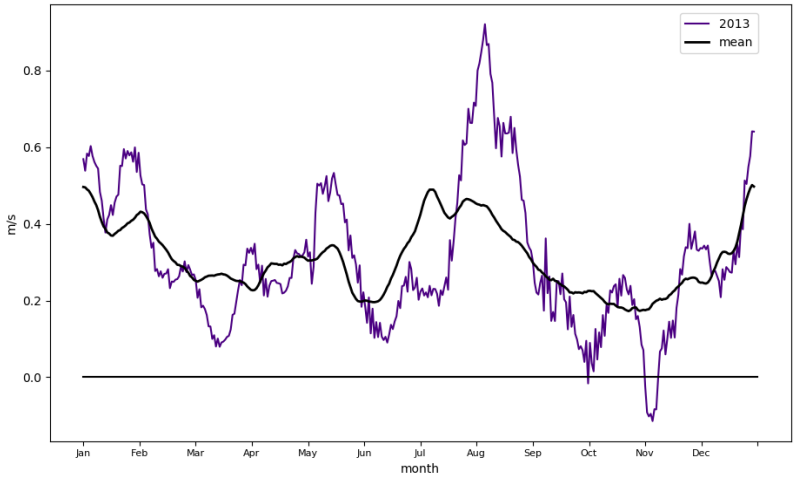

Figure G.17: Surface velocity in the unobstructed region for the year 2013. The black line indicates the mean of all ten years.

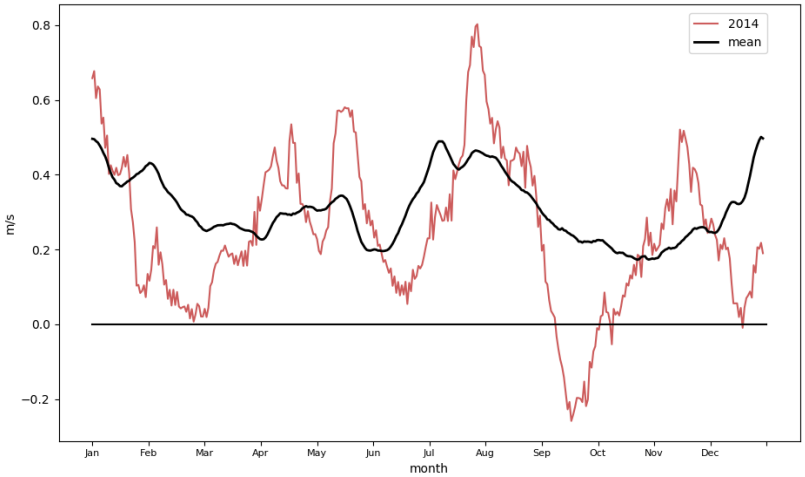

Figure G.18: Surface velocity in the unobstructed region for the year 2014. The black line indicates the mean of all ten years.

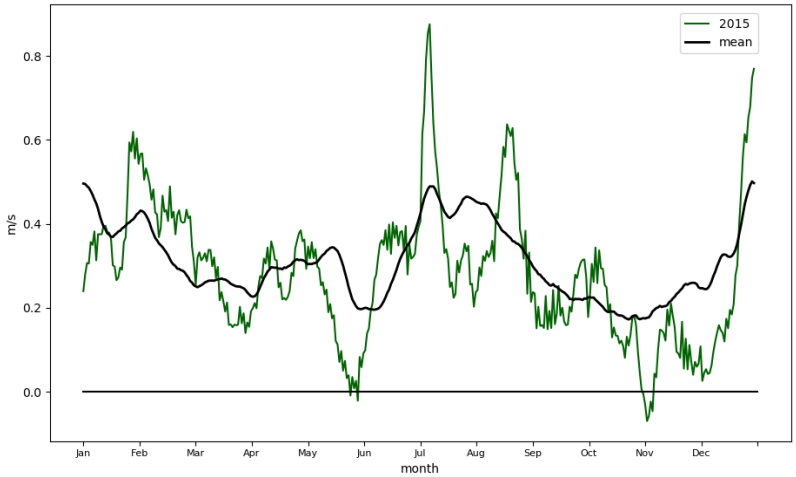

Figure G.19: Surface velocity in the unobstructed region for the year 2015. The black line indicates the mean of all ten years.

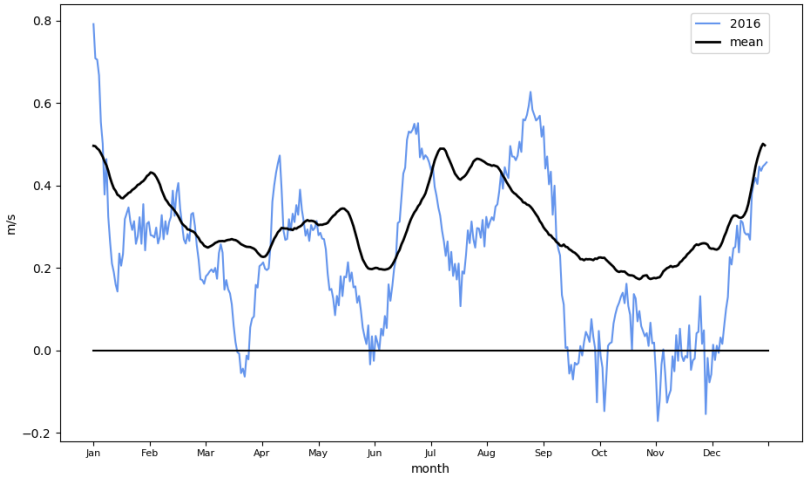

Figure G.20: Surface velocity in the unobstructed region for the year 2016. The black line indicates the mean of all ten years.

H

Appendix: Overview of identified backflow events from 2007 until 2016 in the channel between Venezuela and Curaçao

In the channel region, the number and duration of backflow events was analysed. To identify an event, the direction of the flow should be below 260°or above 340°, where 0°is pointing to the north with positive to the east. In Table H.1 an overview of all events is given. The overall mean velocity during backflow is 0.098 m/s and the maximum is 0.207 m/s.

The year is divided into two periods. The first period is from January 1st until September 30st. The second period starts at October 1st and runs to the end of the year. This division is made based on visual identification of these two periods with the first one having none to maximum two backflow events over nine months, and the second one having regularly occuring backflow events in the last three months. Graphical representation of the table is given in the Figures H.1 and H.2 that respectively show the amount of backflow events per period and the number of days on which backflow occurred per period.

Table H.1: Backflow events in the years 2007 until 2016.

Event	Start date	End date	Duration (days)	Mean velocity (m/s)
1	2007-04-21	2007-04-21	1	0.067
2	2007-10-06	2007-10-15	10	0.099
3	2007-10-25	2007-10-30	6	0.076
4	2007-10-31	2007-10-31	1	0.072
5	2007-11-01	2007-11-01	1	0.052
6	2007-11-02	2007-11-06	5	0.075
7	2008-08-27	2008-08-27	1	0.044

Event	Start date	End date	Duration (days)	Mean velocity (m/s)
8	2008-08-30	2008-09-06	8	0.110
9	2008-10-15	2008-10-15	1	0.093
10	2008-11-18	2008-11-22	5	0.072
11	2008-11-27	2008-11-29	3	0.059
12	2009-06-11	2009-06-12	2	0.139
13	2009-06-13	2009-06-13	1	0.068
14	2009-06-14	2009-06-18	5	0.108
15	2009-10-24	2009-10-24	1	0.201
16	2010-05-28	2010-05-28	1	0.137
17	2010-05-30	2010-05-30	1	0.181
18	2010-11-06	2010-11-12	7	0.201
19	2010-11-14	2010-11-22	9	0.107
20	2010-12-16	2010-12-17	2	0.181
21	2010-12-18	2010-12-18	1	0.147
22	2010-12-19	2010-12-19	1	0.162
23	2010-12-20	2010-12-20	1	0.010
24	2010-12-21	2010-12-26	6	0.132
25	2011-05-17	2011-05-18	2	0.051
26	2011-05-21	2011-05-21	1	0.072
27	2011-06-06	2011-06-06	1	0.153
28	2011-06-08	2011-06-08	1	0.116
29	2011-07-17	2011-07-19	3	0.063
30	2011-10-10	2011-10-14	5	0.097
31	2011-10-16	2011-10-26	11	0.126
32	2011-11-04	2011-11-05	2	0.107
33	2011-11-06	2011-12-16	41	0.088
34	2012-04-09	2012-04-15	7	0.060
35	2012-10-16	2012-10-17	2	0.085
36	2012-10-20	2012-10-20	1	0.044
37	2012-10-26	2012-10-28	3	0.130
38	2012-10-30	2012-10-30	1	0.109
39	2013-05-05	2013-05-09	5	0.090
40	2013-11-04	2013-11-04	1	0.069
41	2013-11-06	2013-11-06	1	0.043
42	2013-11-08	2013-11-08	1	0.059
43	2013-12-25	2013-12-28	4	0.023
44	2014-03-05	2014-03-05	1	0.207
45	2014-03-09	2014-03-16	8	0.096
46	2014-12-17	2014-12-20	4	0.051
47	2016-10-04	2016-10-15	12	0.078
48	2016-10-18	2016-10-20	3	0.071
49	2016-11-02	2016-11-02	1	0.040
50	2016-11-09	2016-11-09	1	0.094
51	2016-11-20	2016-11-24	5	0.051
52	2016-11-28	2016-12-02	5	0.129

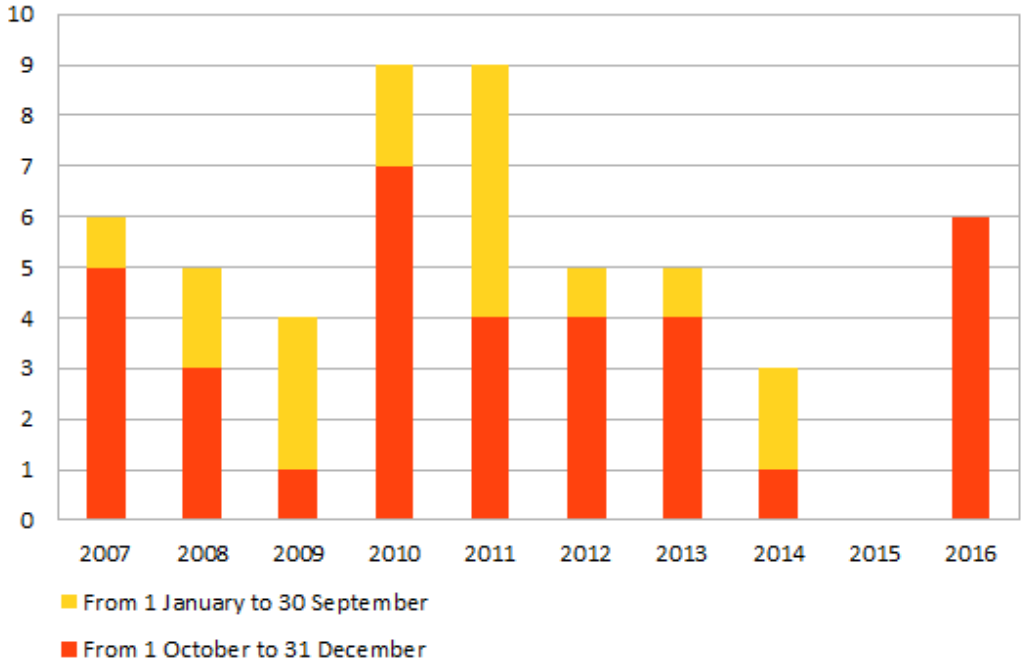

Figure H.1: Amount of backflow events per period over the years 2007 until 2016. In 2015 no backflow at all occurred.

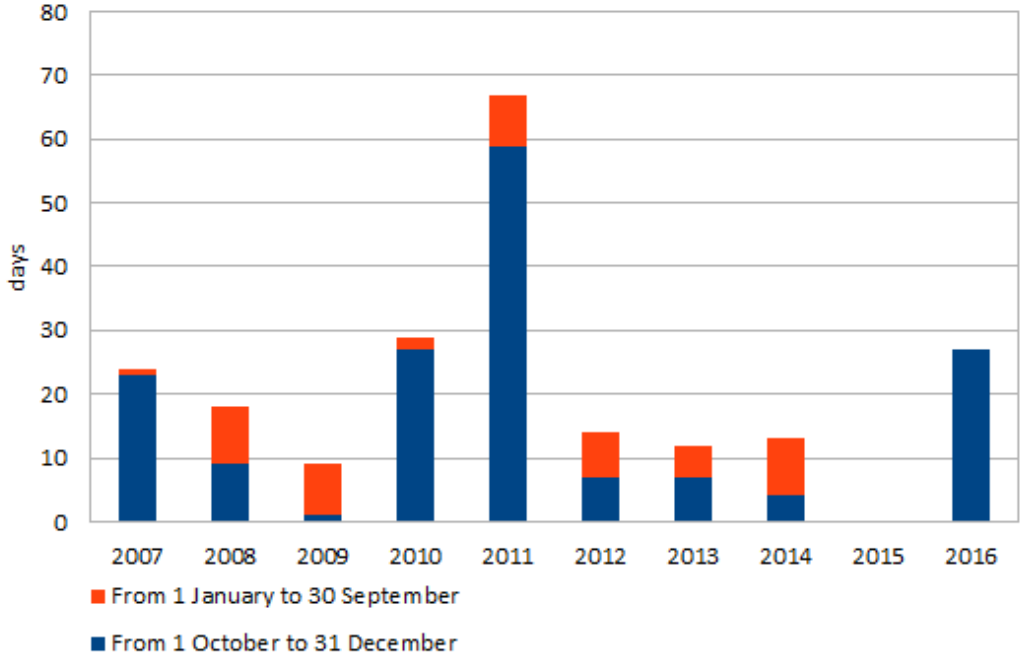

Figure H.2: Days with backflow per period over the years 2007 until 2016.

Appendix: Volume flux plots per year

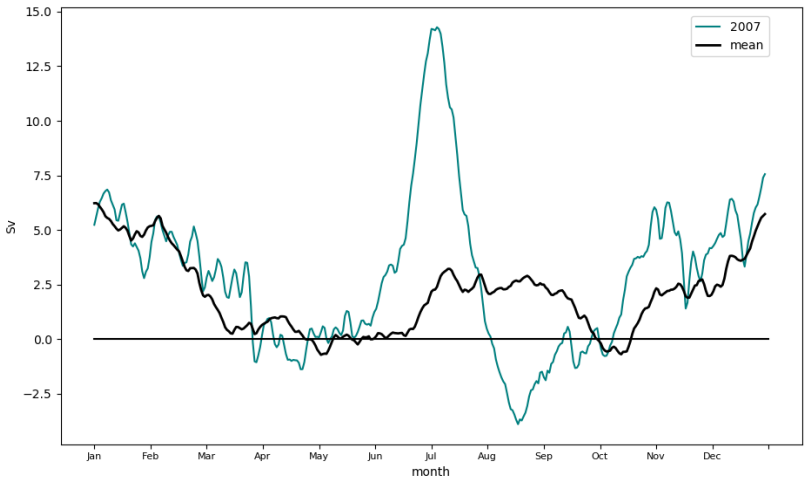

Figure I.1: Volume flux in the channel region for the year 2007. The black line indicates the mean of all ten years.

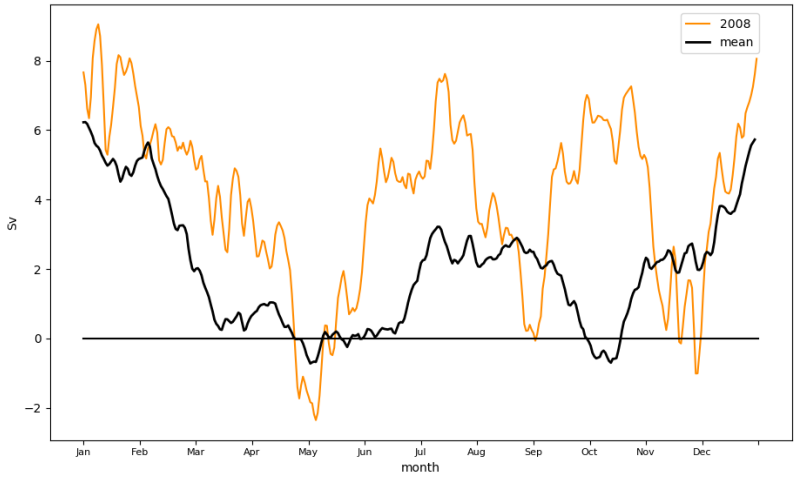

Figure I.2: Volume flux in the channel region for the year 2008. The black line indicates the mean of all ten years.

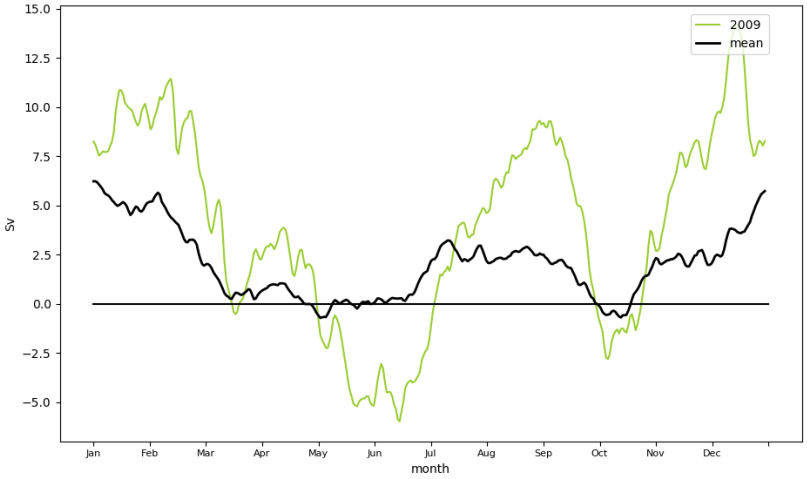

Figure I.3: Volume flux in the channel region for the year 2009. The black line indicates the mean of all ten years.

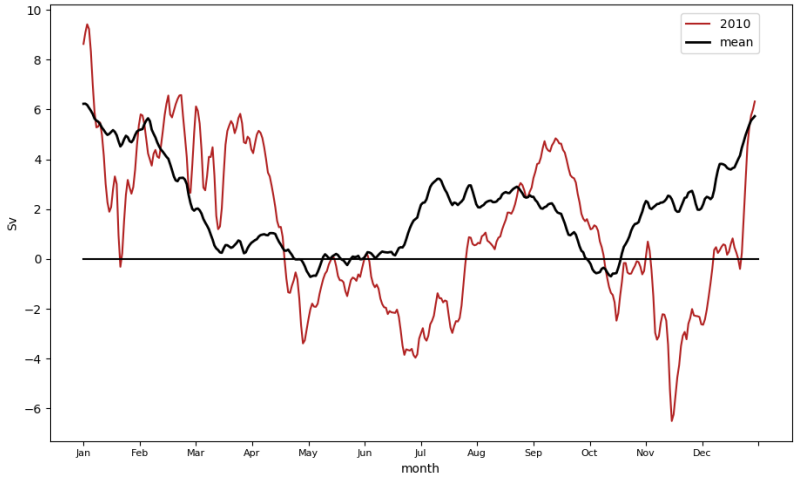

Figure I.4: Volume flux in the channel region for the year 2010. The black line indicates the mean of all ten years.

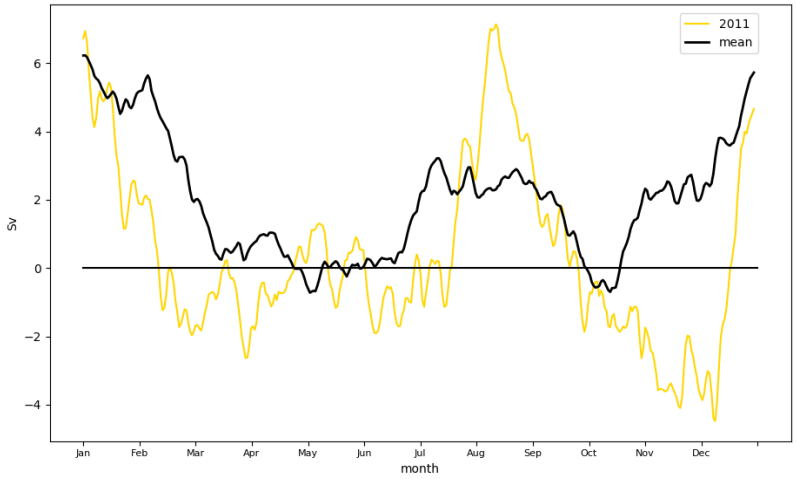

Figure I.5: Volume flux in the channel region for the year 2011. The black line indicates the mean of all ten years.

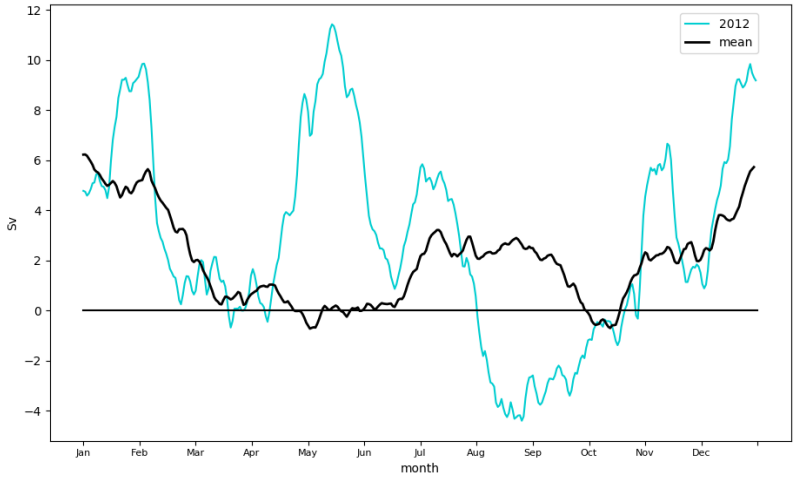

Figure I.6: Volume flux in the channel region for the year 2012. The black line indicates the mean of all ten years.

Figure I.7: Volume flux in the channel region for the year 2013. The black line indicates the mean of all ten years.

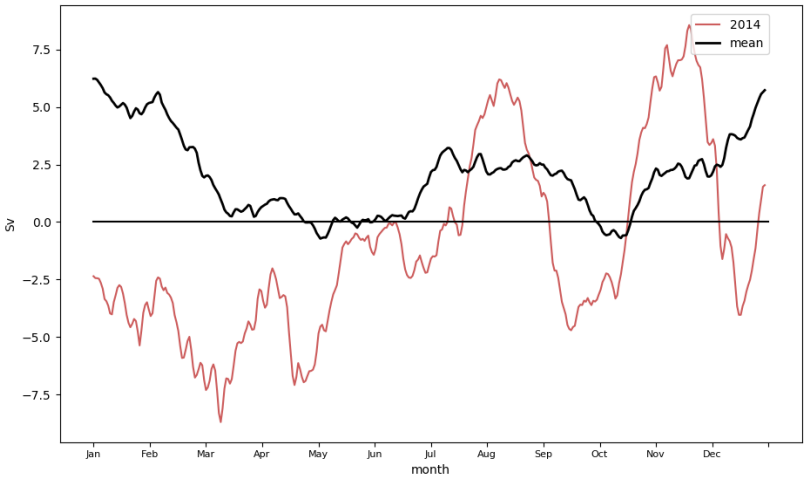

Figure I.8: Volume flux in the channel region for the year 2014. The black line indicates the mean of all ten years.

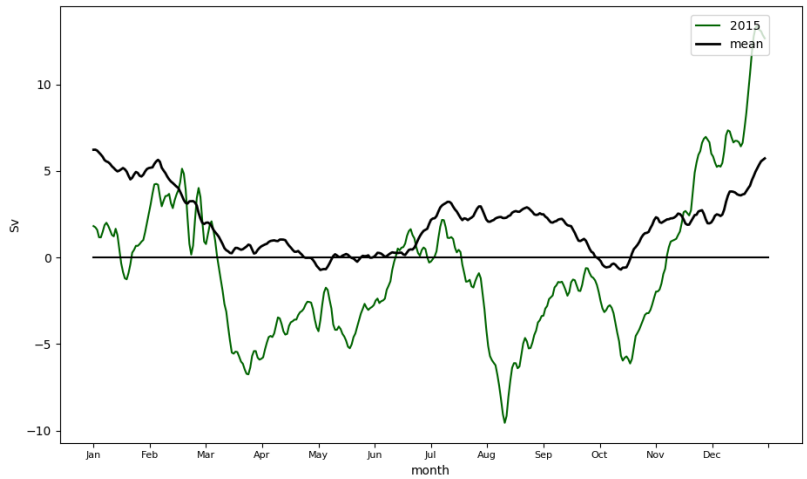

Figure I.9: Volume flux in the channel region for the year 2015. The black line indicates the mean of all ten years.

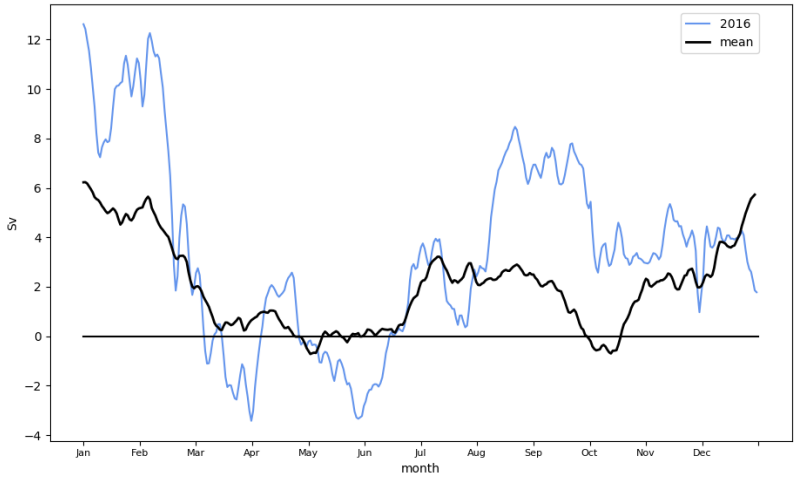

Figure I.10: Volume flux in the channel region for the year 2016. The black line indicates the mean of all ten years.

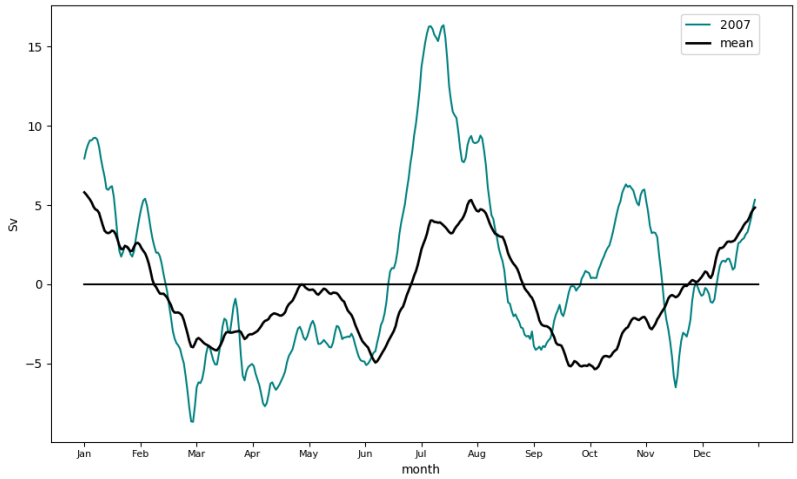

Figure I.11: Volume flux in the unobstructed region for the year 2007. The black line indicates the mean of all ten years.

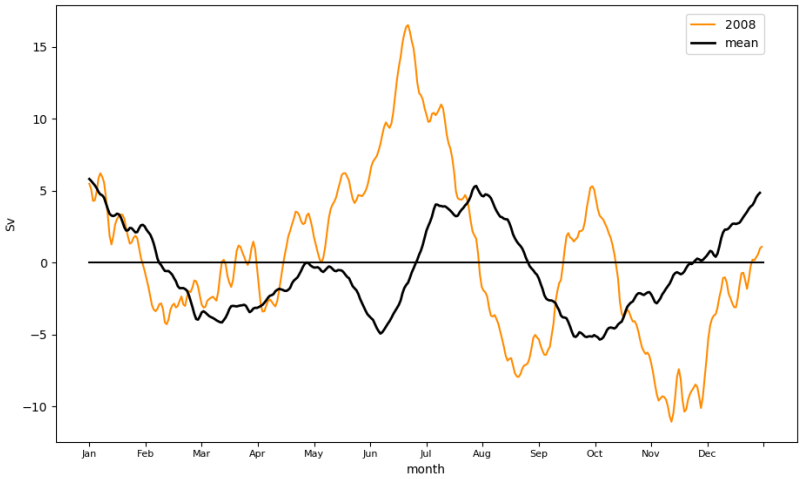

Figure I.12: Volume flux in the unobstructed region for the year 2008. The black line indicates the mean of all ten years.

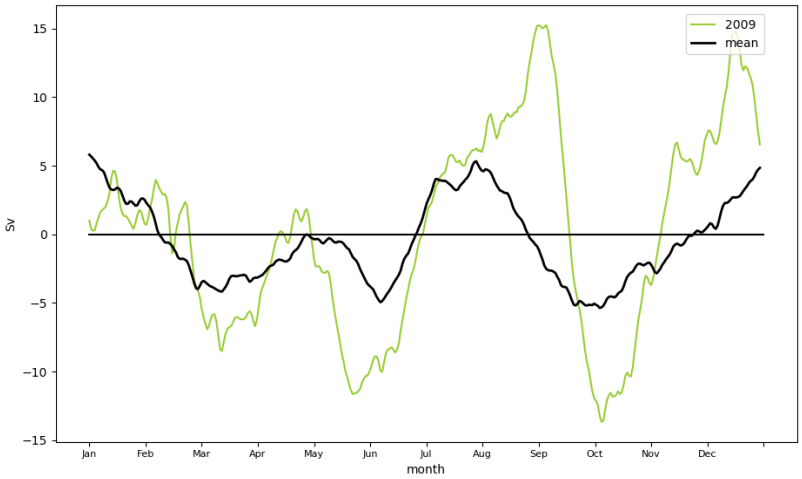

Figure I.13: Volume flux in the unobstructed region for the year 2009. The black line indicates the mean of all ten years.

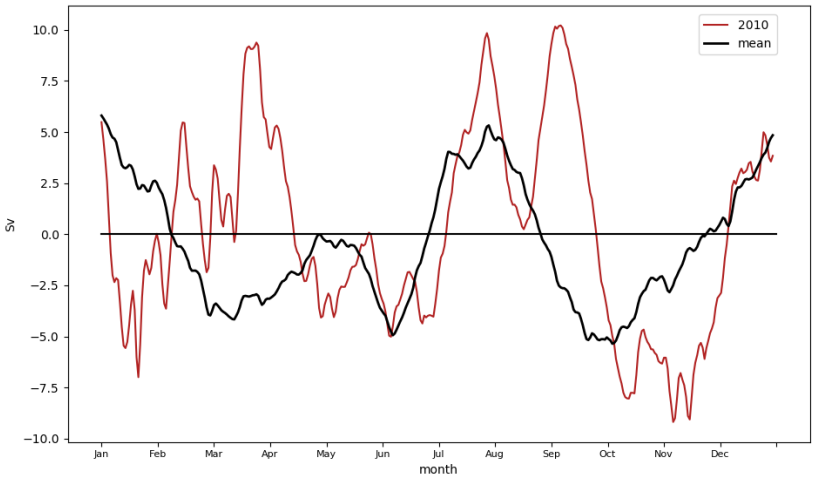

Figure I.14: Volume flux in the unobstructed region for the year 2010. The black line indicates the mean of all ten years.

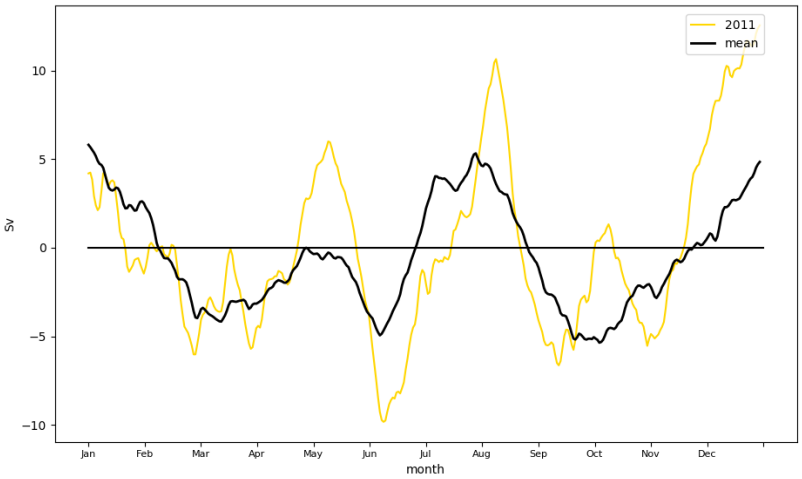

Figure I.15: Volume flux in the unobstructed region for the year 2011. The black line indicates the mean of all ten years.

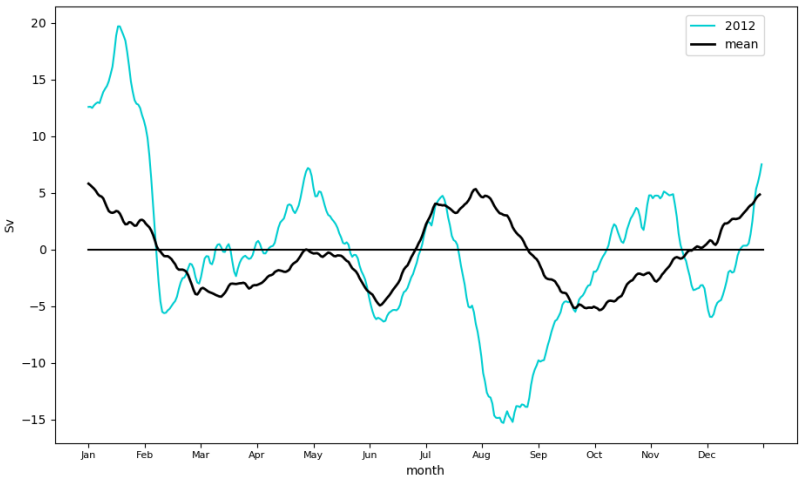

Figure I.16: Volume flux in the unobstructed region for the year 2012. The black line indicates the mean of all ten years.

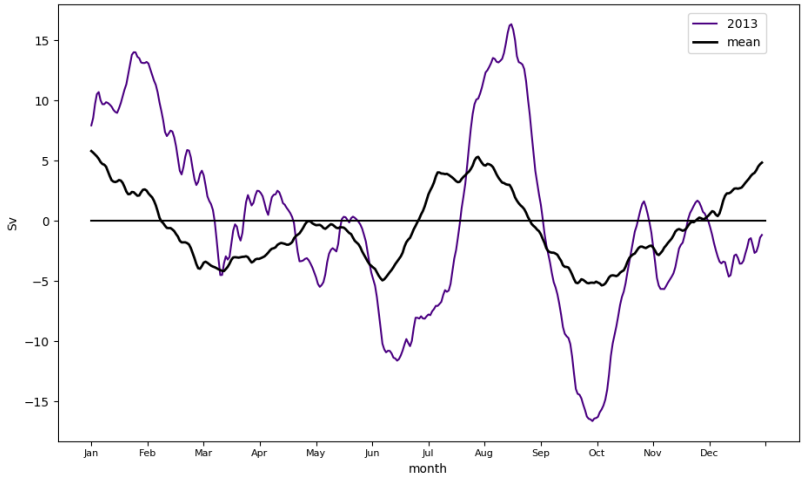

Figure I.17: Volume flux in the unobstructed region for the year 2013. The black line indicates the mean of all ten years.

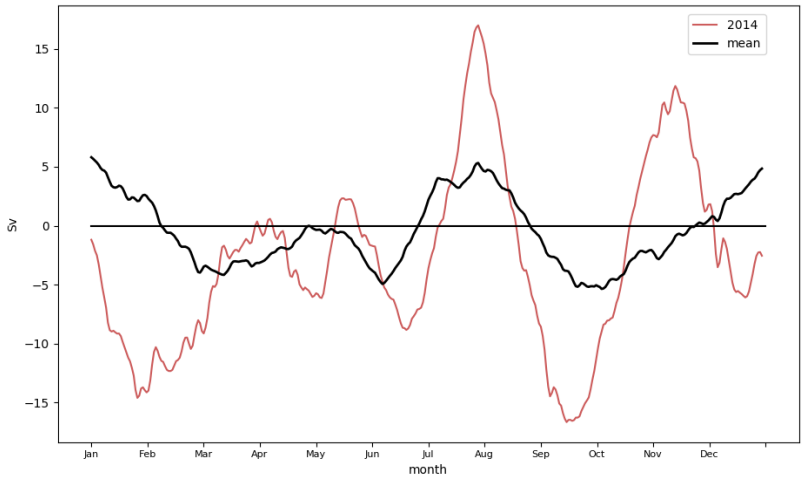

Figure I.18: Volume flux in the unobstructed region for the year 2014. The black line indicates the mean of all ten years.

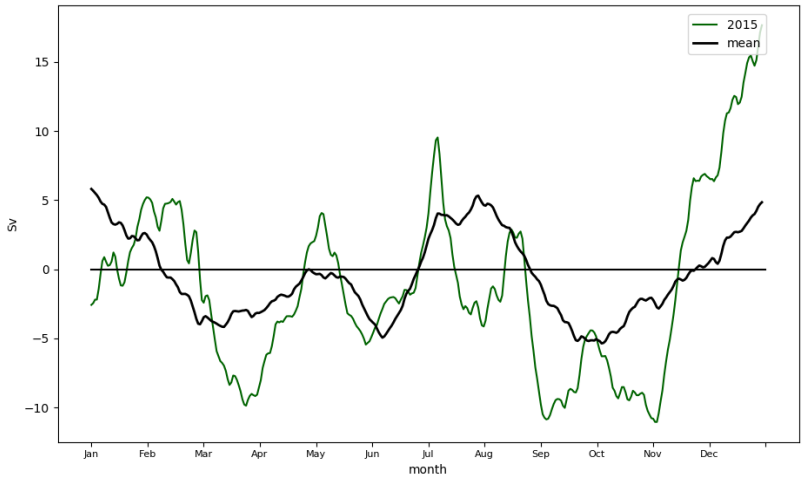

Figure I.19: Volume flux in the unobstructed region for the year 2015. The black line indicates the mean of all ten years.

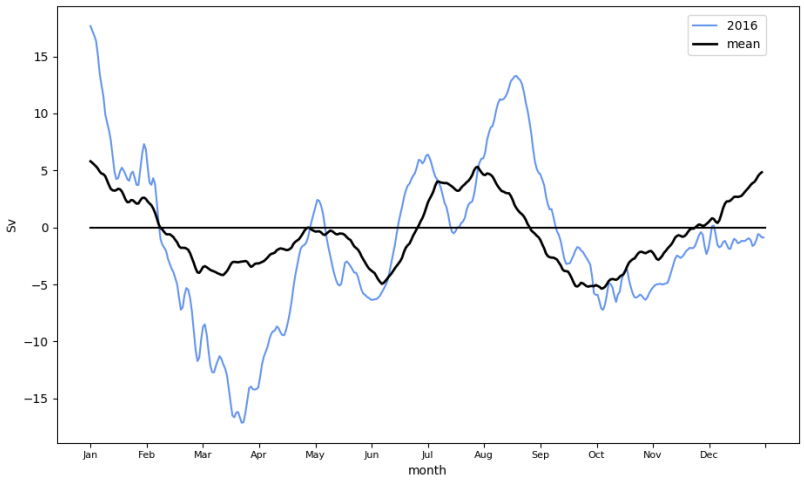

Figure I.20: Volume flux in the unobstructed region for the year 2016. The black line indicates the mean of all ten years.

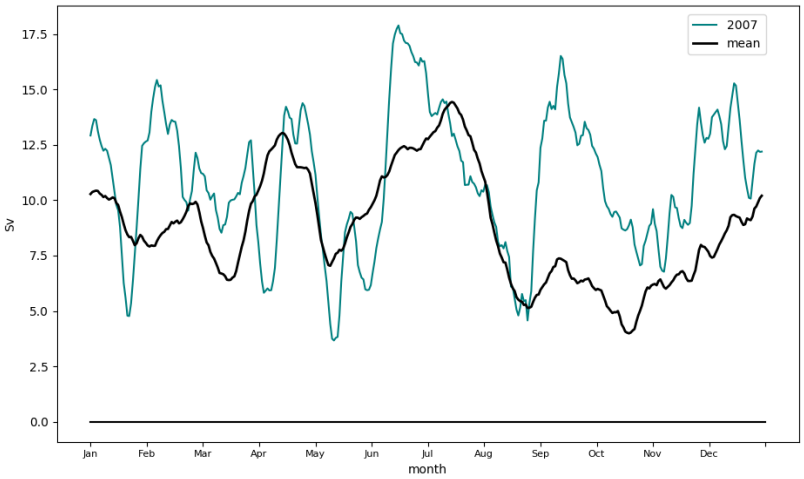

Figure I.21: Volume flux in the Grenada Passage for the year 2007. The black line indicates the mean of all ten years.

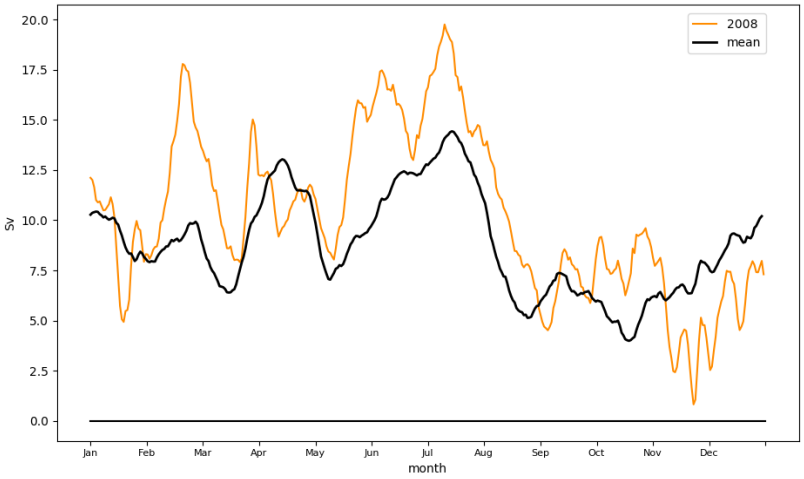

Figure I.22: Volume flux in the Grenada Passage for the year 2008. The black line indicates the mean of all ten years.

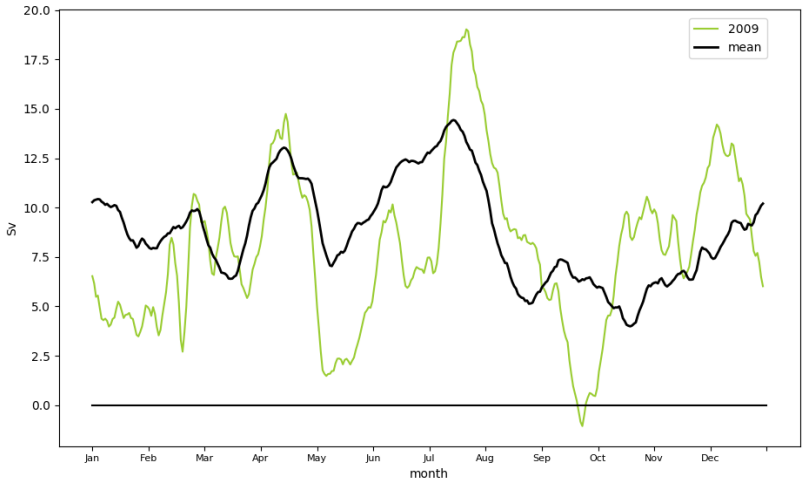

Figure I.23: Volume flux in the Grenada Passage for the year 2009. The black line indicates the mean of all ten years.

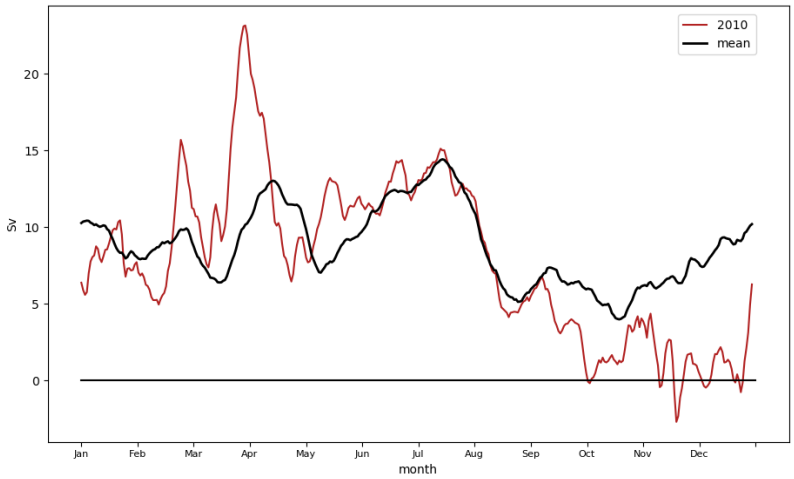

Figure I.24: Volume flux in the Grenada Passage for the year 2010. The black line indicates the mean of all ten years.

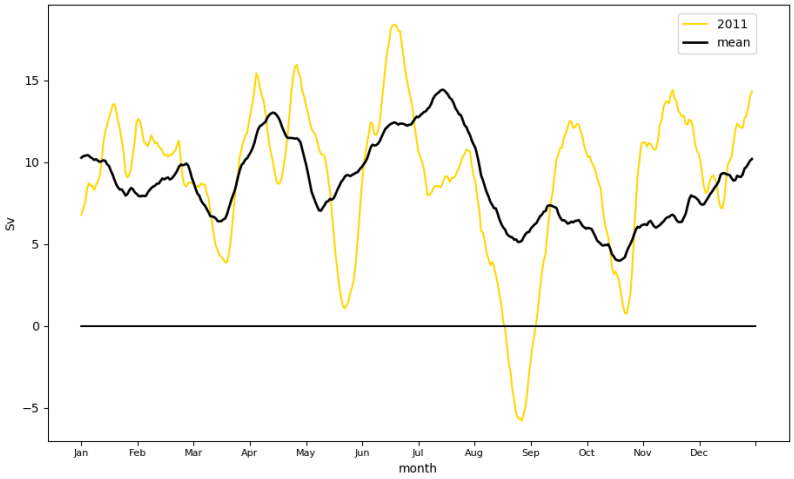

Figure I.25: Volume flux in the Grenada Passage for the year 2011. The black line indicates the mean of all ten years.

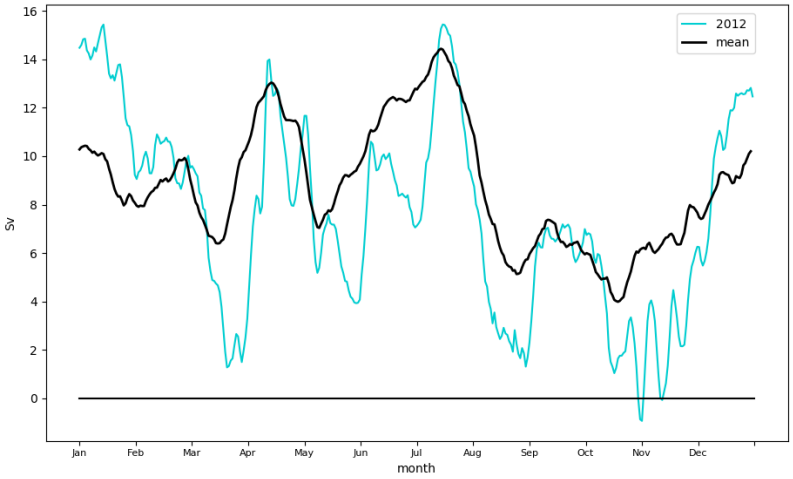

Figure I.26: Volume flux in the Grenada Passage for the year 2012. The black line indicates the mean of all ten years.

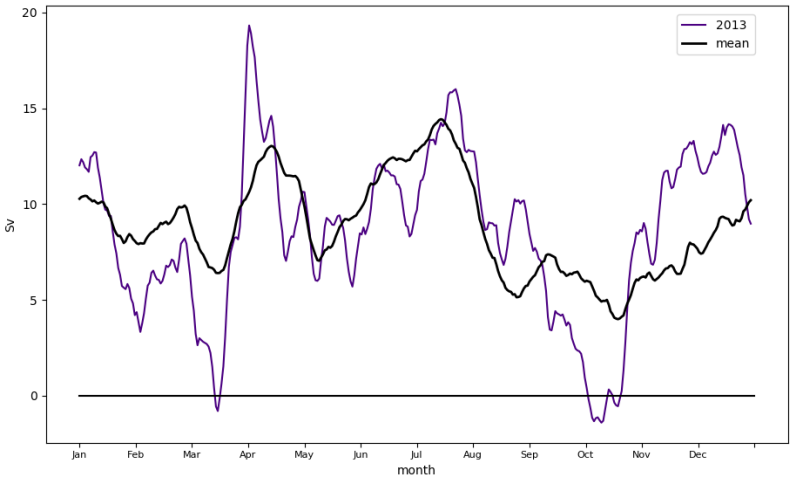

Figure I.27: Volume flux in the Grenada Passage for the year 2013. The black line indicates the mean of all ten years.

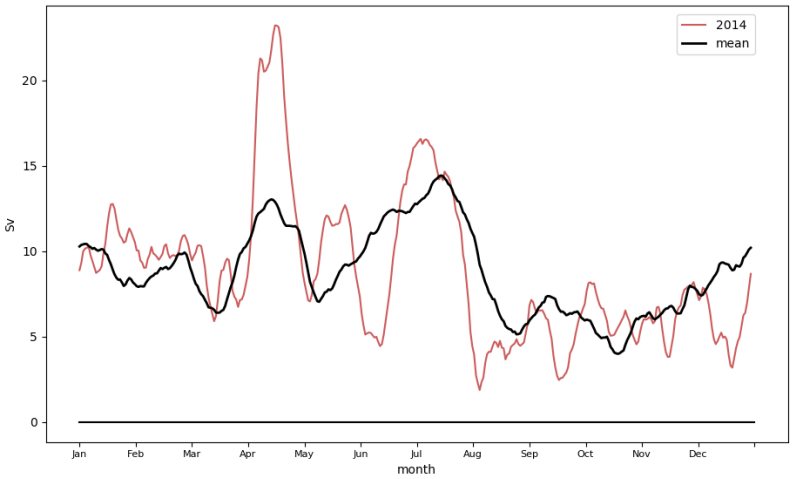

Figure I.28: Volume flux in the Grenada Passage for the year 2014. The black line indicates the mean of all ten years.

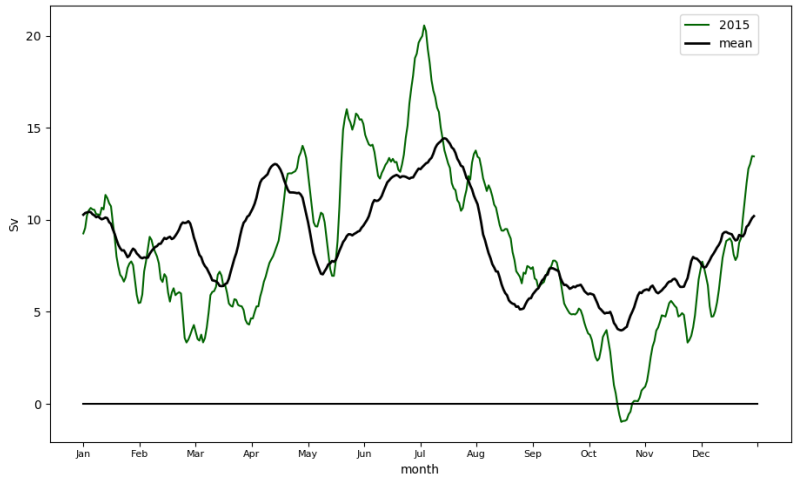

Figure I.29: Volume flux in the Grenada Passage for the year 2015. The black line indicates the mean of all ten years.

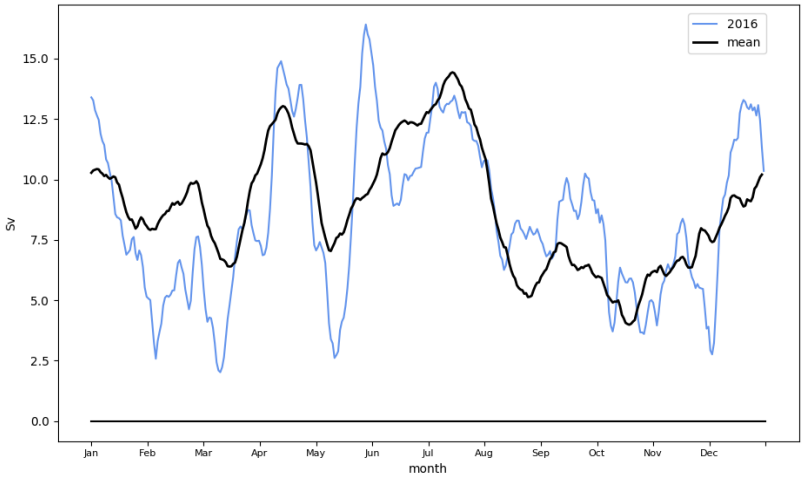

Figure I.30: Volume flux in the Grenada Passage for the year 2016. The black line indicates the mean of all ten years.

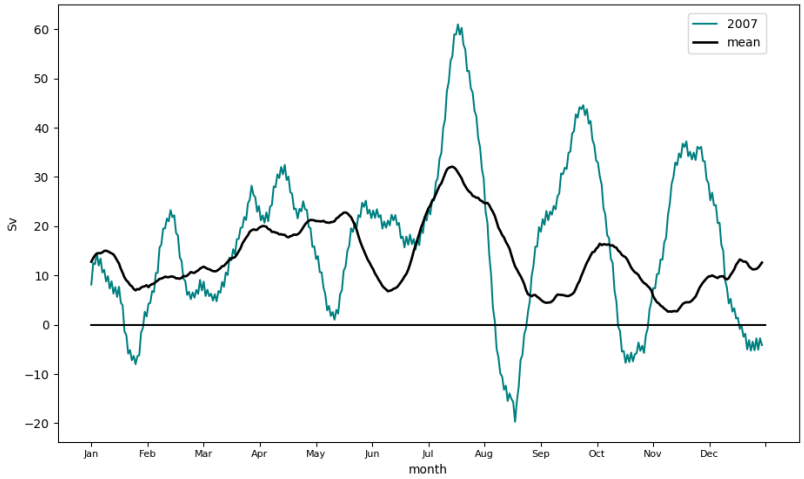

Figure I.31: Volume flux in the extended unobstructed region for the year 2007. The black line indicates the mean of all ten years.

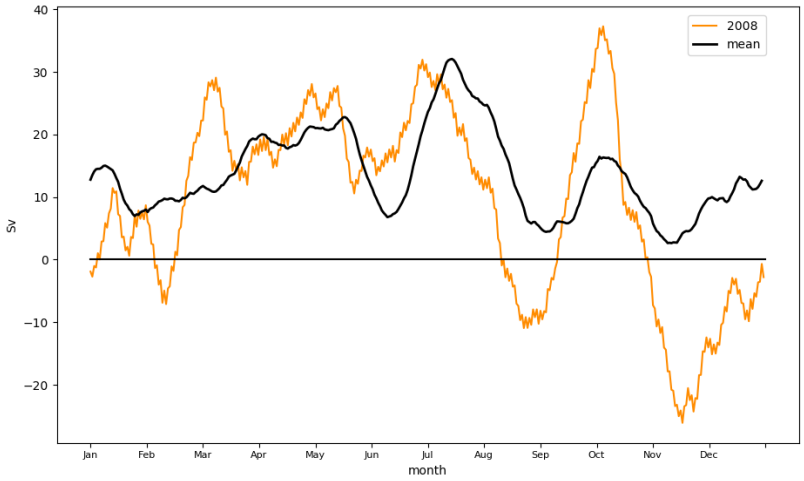

Figure I.32: Volume flux in the extended unobstructed region for the year 2008. The black line indicates the mean of all ten years.

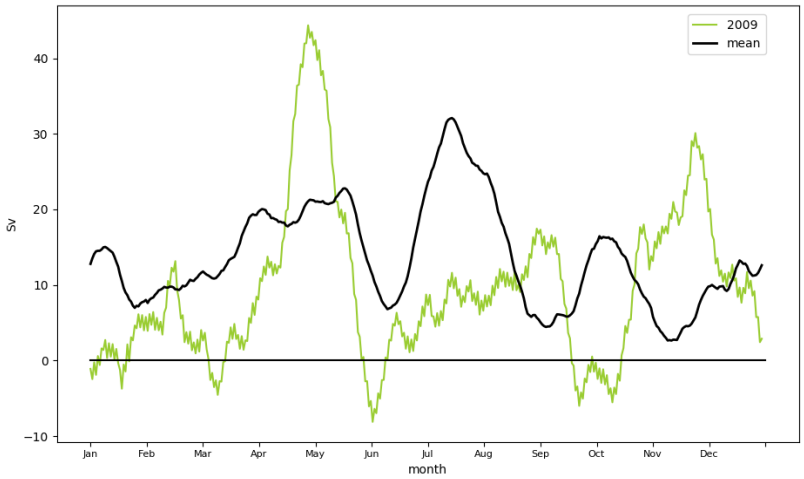

Figure I.33: Volume flux in the extended unobstructed region for the year 2009. The black line indicates the mean of all ten years.

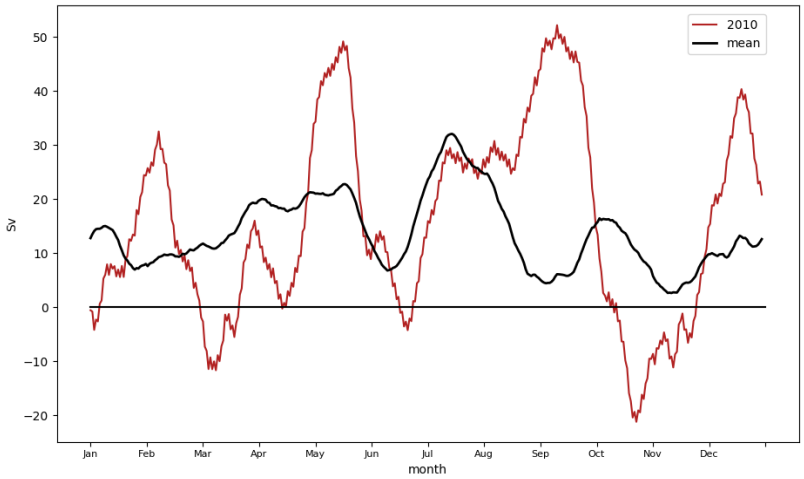

Figure I.34: Volume flux in the extended unobstructed region for the year 2010. The black line indicates the mean of all ten years.

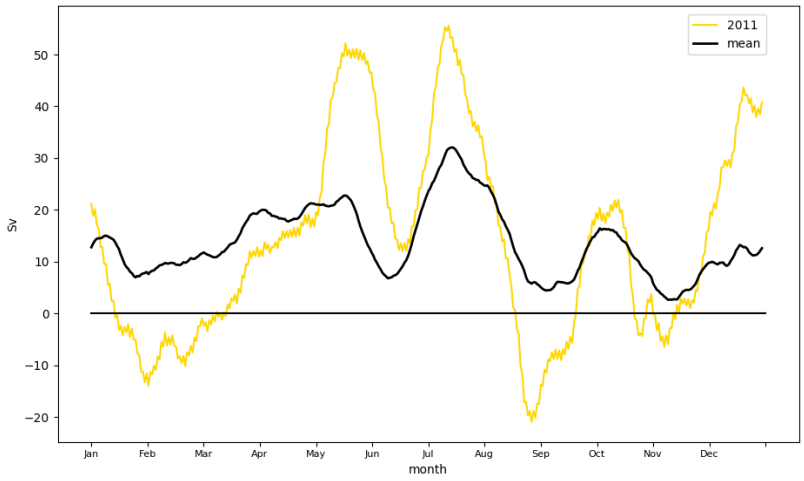

Figure I.35: Volume flux in the extended unobstructed region for the year 2011. The black line indicates the mean of all ten years.

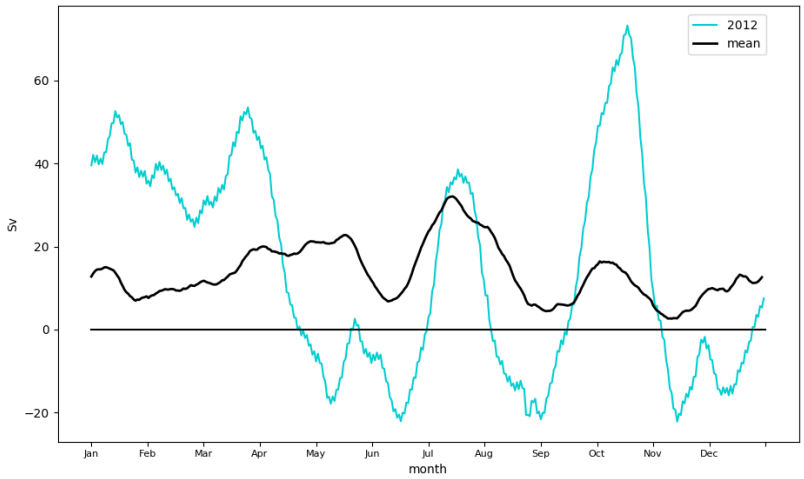

Figure I.36: Volume flux in the extended unobstructed region for the year 2012. The black line indicates the mean of all ten years.

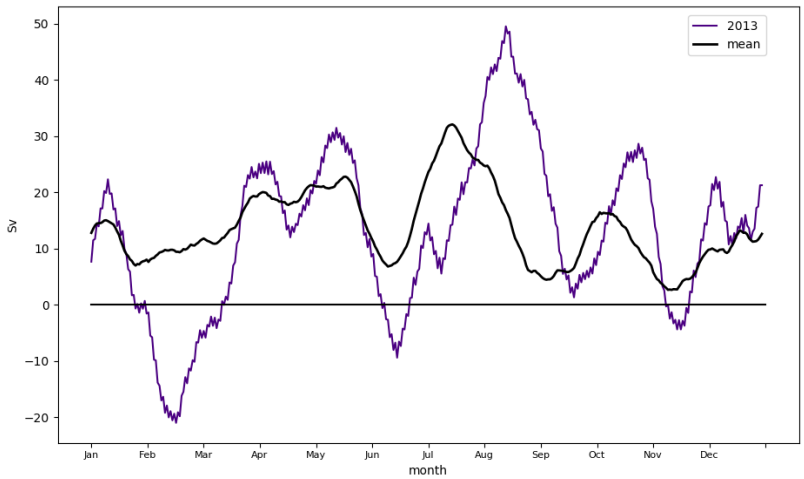

Figure I.37: Volume flux in the extended unobstructed region for the year 2013. The black line indicates the mean of all ten years.

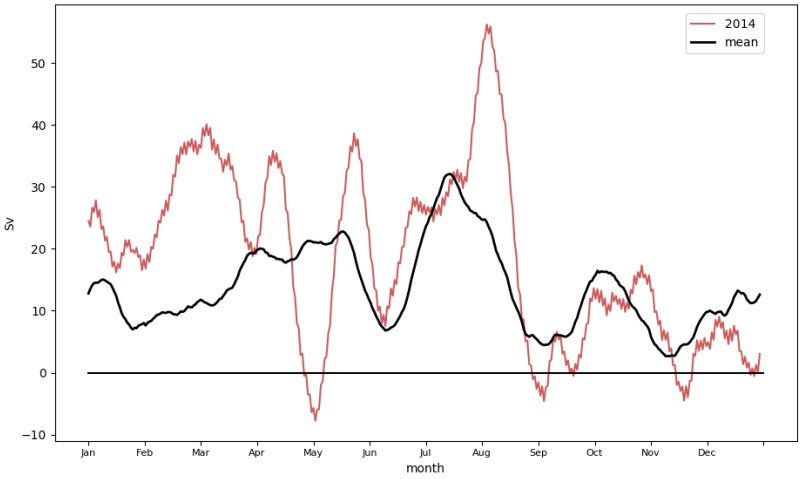

Figure I.38: Volume flux in the extended unobstructed region for the year 2014. The black line indicates the mean of all ten years.

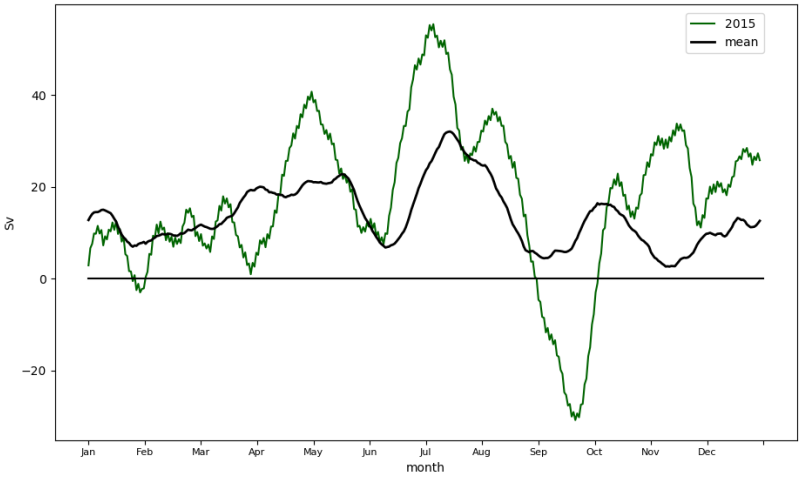

Figure I.39: Volume flux in the extended unobstructed region for the year 2015. The black line indicates the mean of all ten years.

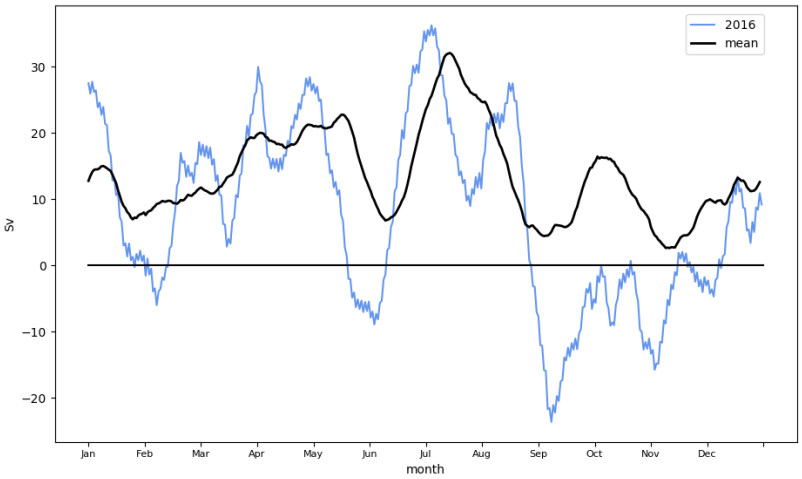

Figure I.40: Volume flux in the extended unobstructed region for the year 2016. The black line indicates the mean of all ten years.

J

Appendix: Miscellaneous figures

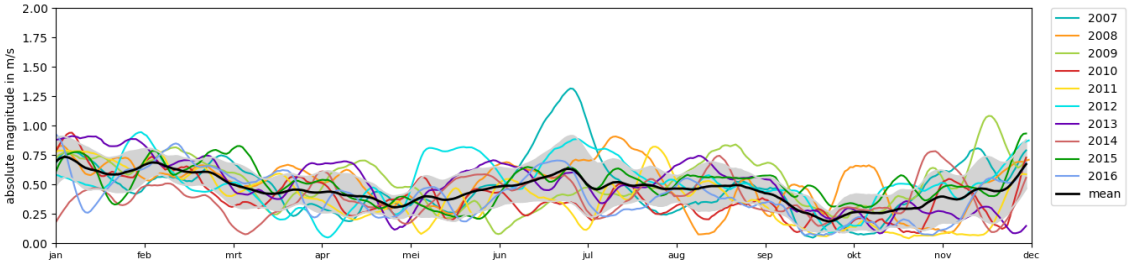

Figure J.1: Similar to Figure 5.2, surface currents in the channel region, except for the use of a rolling average over eight days to eliminate the spikes, smooth the graphs and make it more clear.

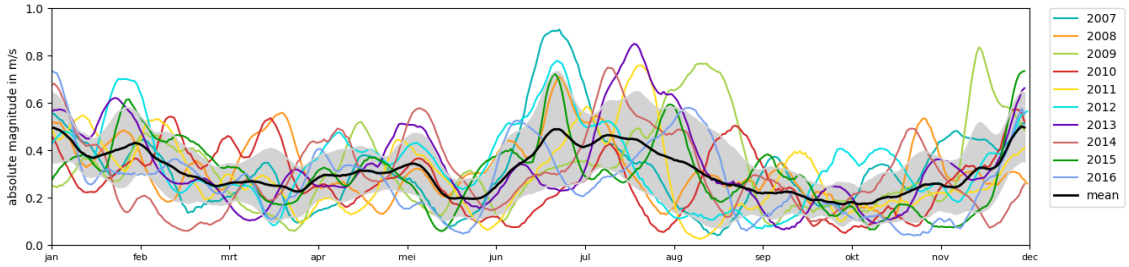

Figure J.2: Similar to upper pannel of Figure 5.3, except for the use of a rolling average over eight days to eliminate the spikes, smooth the graphs and make it more clear.

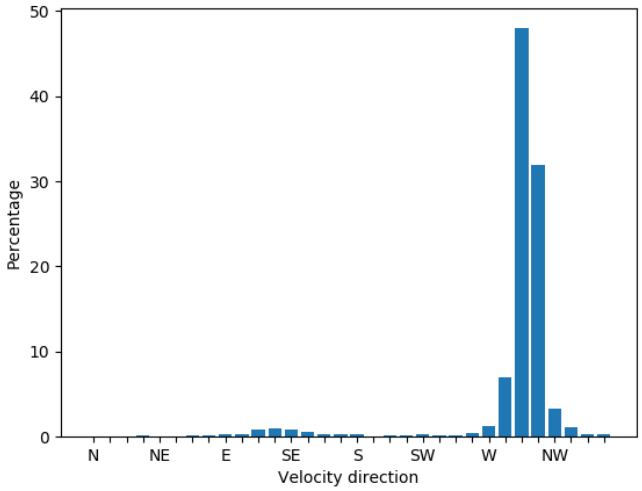

Figure J.3: Bar graph of surface current direction in the sheltered region for all data.

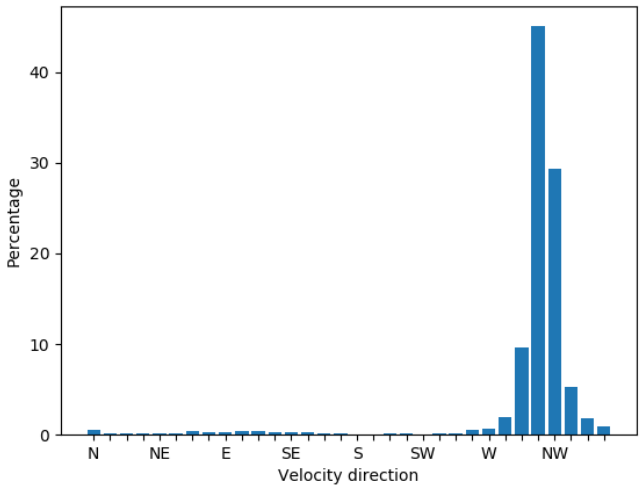

Figure J.4: Bar graph of surface current direction in the channel region for all data.

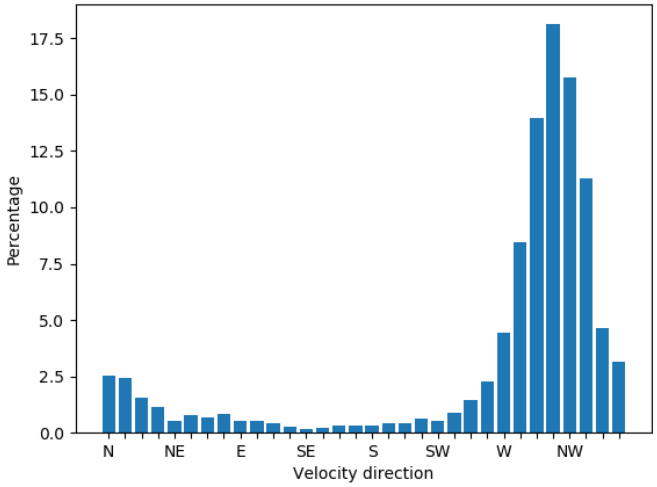

Figure J.5: Bar graph of surface current direction in the unobstructed region for all data.

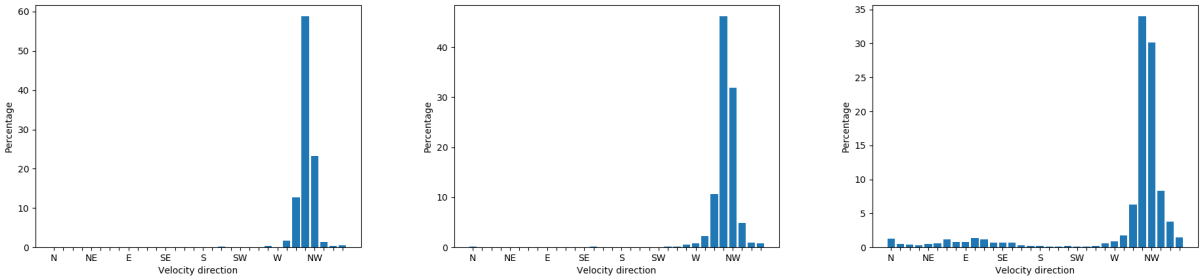

(a) January to March. *(b)* April to August. *(c)* September to December.

Figure J.6: Bar graphs of surface current direction in the channel region for all three periods. Channel region is southwest of Curaçao.

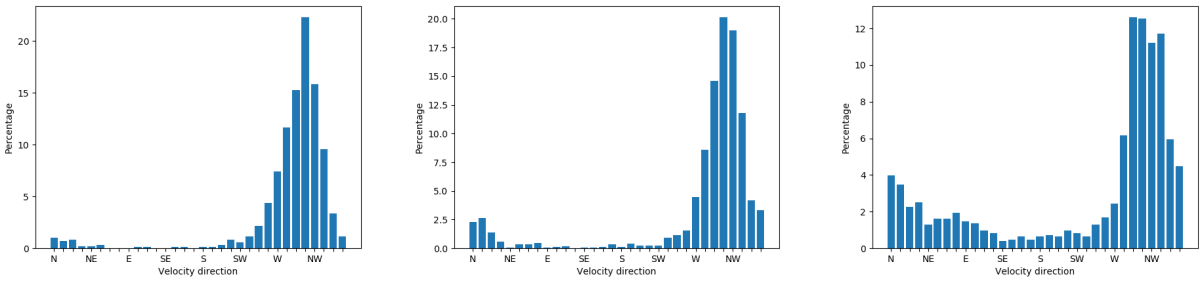

(a) January to March. *(b)* April to August. *(c)* September to December.

Figure J.7: Bar graphs of surface current direction in the unobstructed region for all three periods. Unobstructed region is northeast of Curaçao.

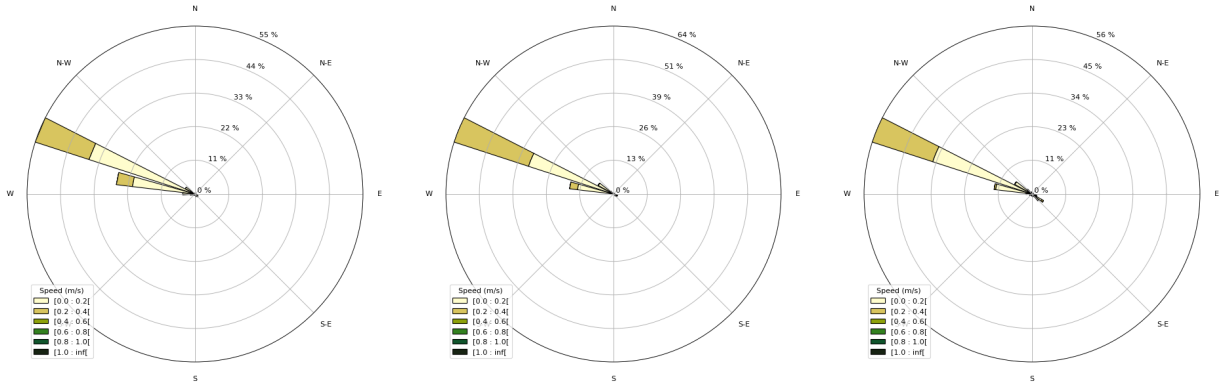

(a) January to March. *(b)* April to August. *(c)* September to December.

Figure J.8: Rose plots of surface current velocity in the sheltered region for all three periods. Sheltered region is defined as [69.5° W, 11.5° N] to [69.43° W, 11.6° N].

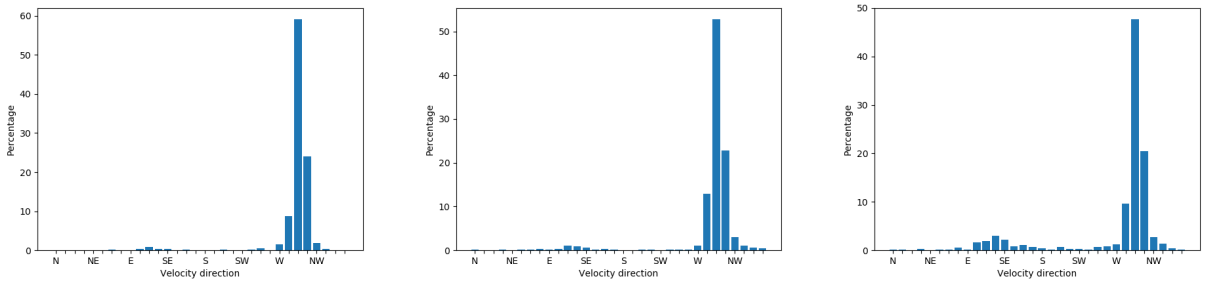

(a) January to March. *(b)* April to August. *(c)* September to December.

Figure J.9: Bar graphs of surface current direction in the sheltered region for all three periods. Sheltered region is southwest of Curaçao.

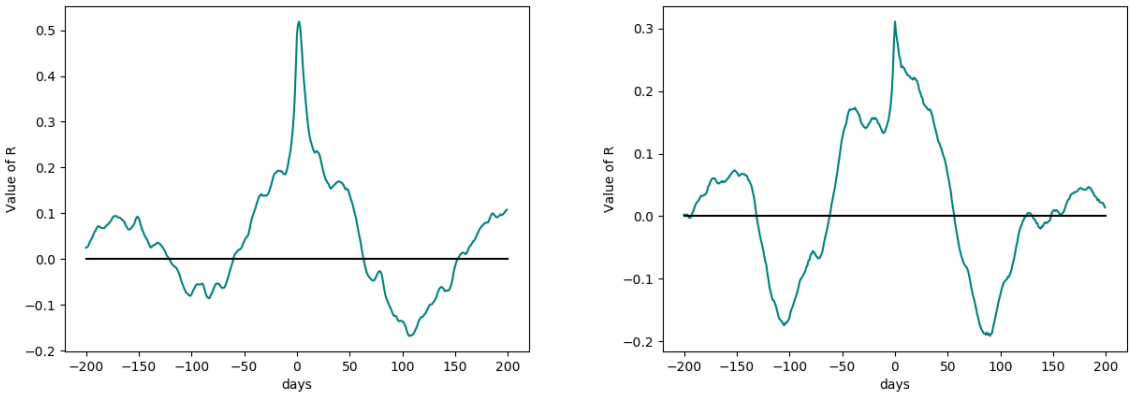

(a) Channel region. *(b) Unobstructed region.*

Figure J.10: Lag in days set out to correlation coefficient between the surface currents perpendicular to the transect for two different regions and the wind in western direction.

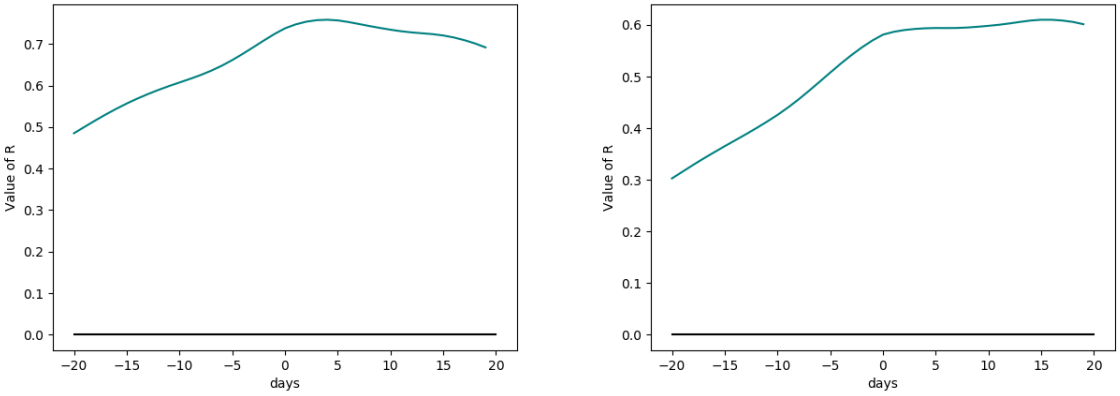

(a) Channel region. *(b) Unobstructed region.*

Figure J.11: Lag in days set out to correlation coefficient between the mean surface currents perpendicular to the transect for two different regions and the mean wind in western direction.

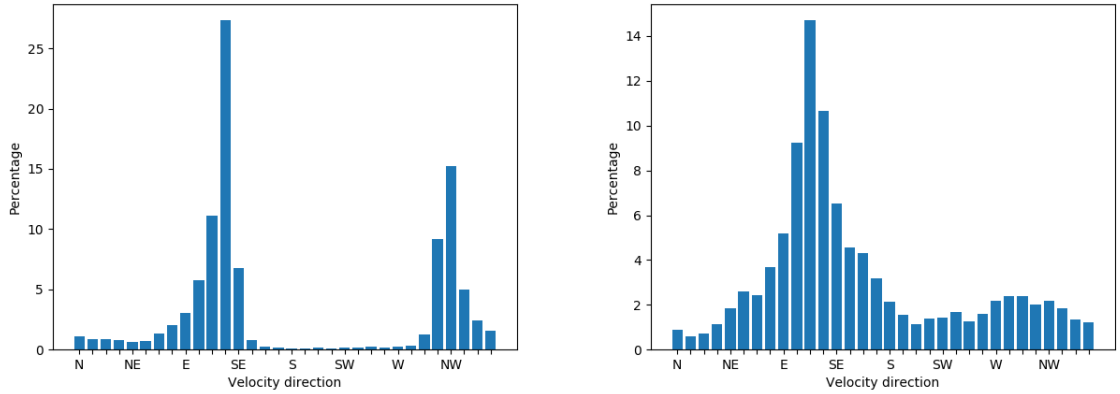

(a) Totalchannel region at 150 m depth. *(b) Unobstructed region at 800 m depth.*

Figure J.12: Bar graphs corresponding to Figure 6.4.

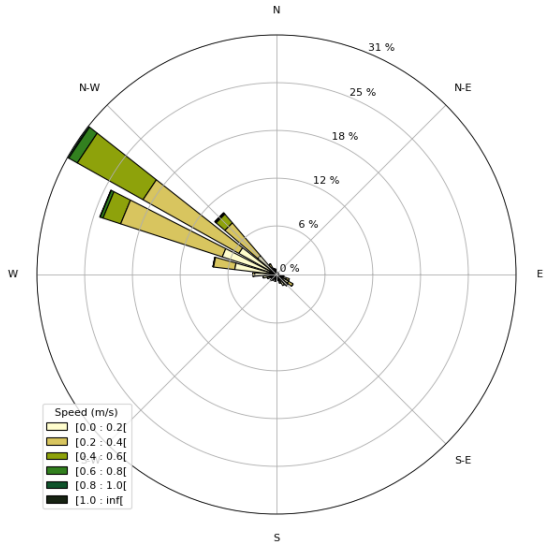

(a) Channel region at 50 m depth.

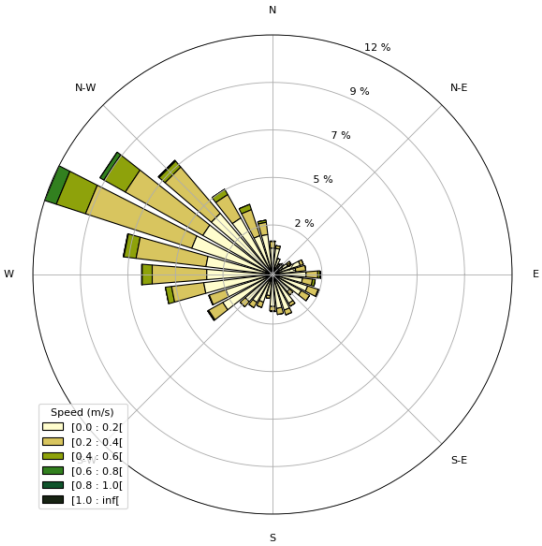

(b) Unobstructed region at 50 m depth.

Figure J.13: Rose plots at 50 m depth.

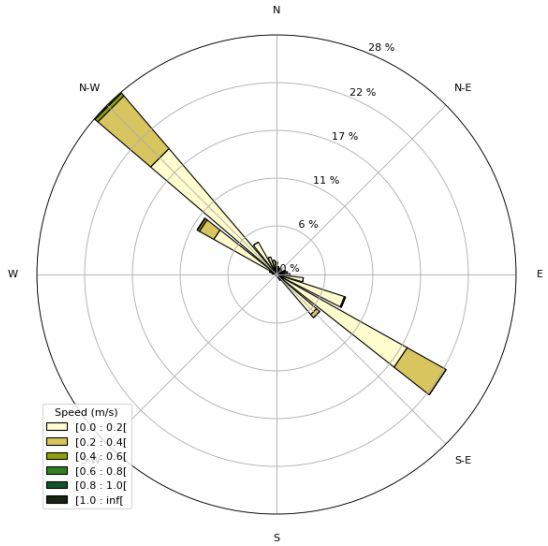

(a) Channel region at 200 m depth.

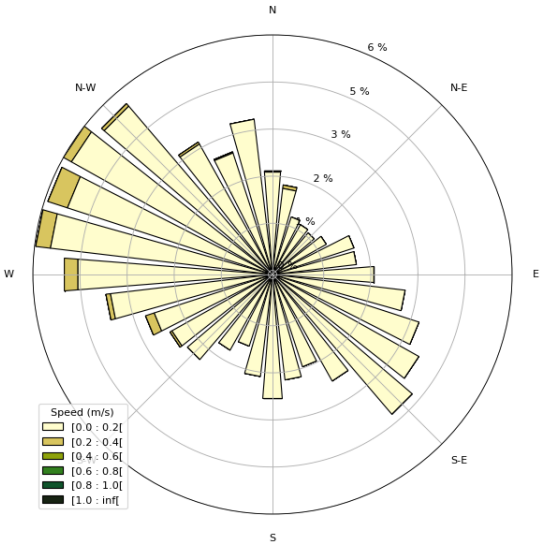

(b) Unobstructed region at 200 m depth.

Figure J.14: Rose plots at 200 m depth.

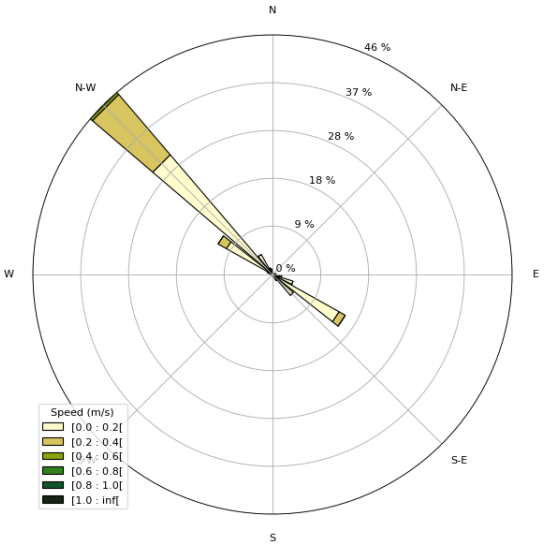

(a) Channel region at 400 m depth.

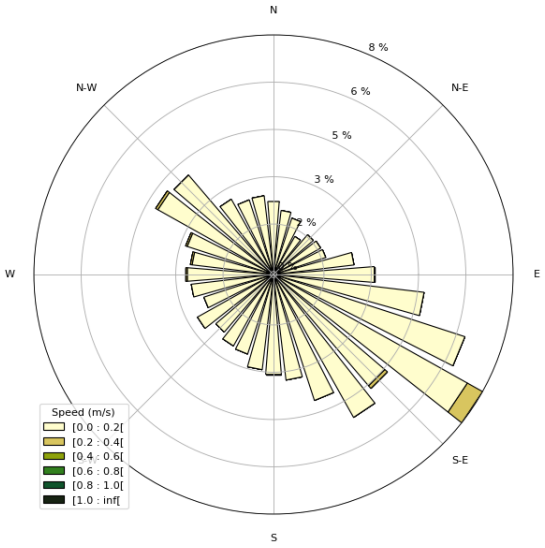

(b) Unobstructed region at 400 m depth.

Figure J.15: Rose plots at 400 m depth.

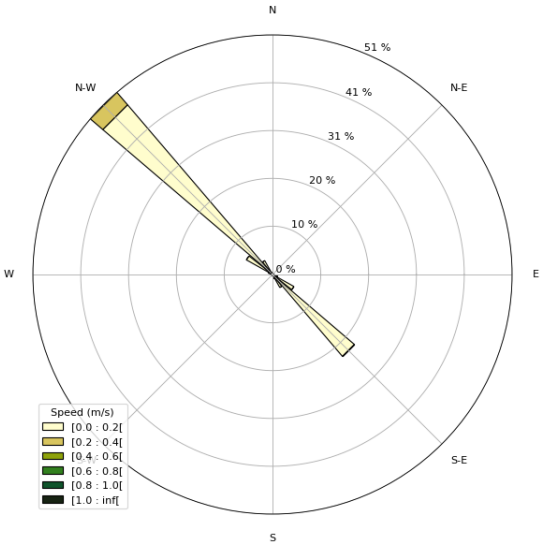

(a) Channel region at 800 m depth.

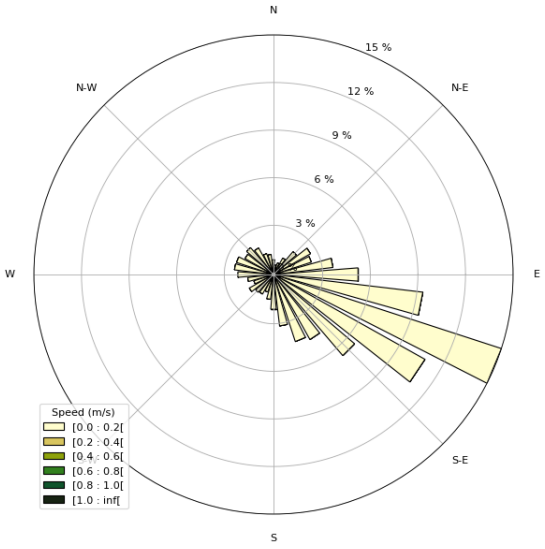

(b) Unobstructed region at 800 m depth.

Figure J.16: Rose plots at 800 m depth.

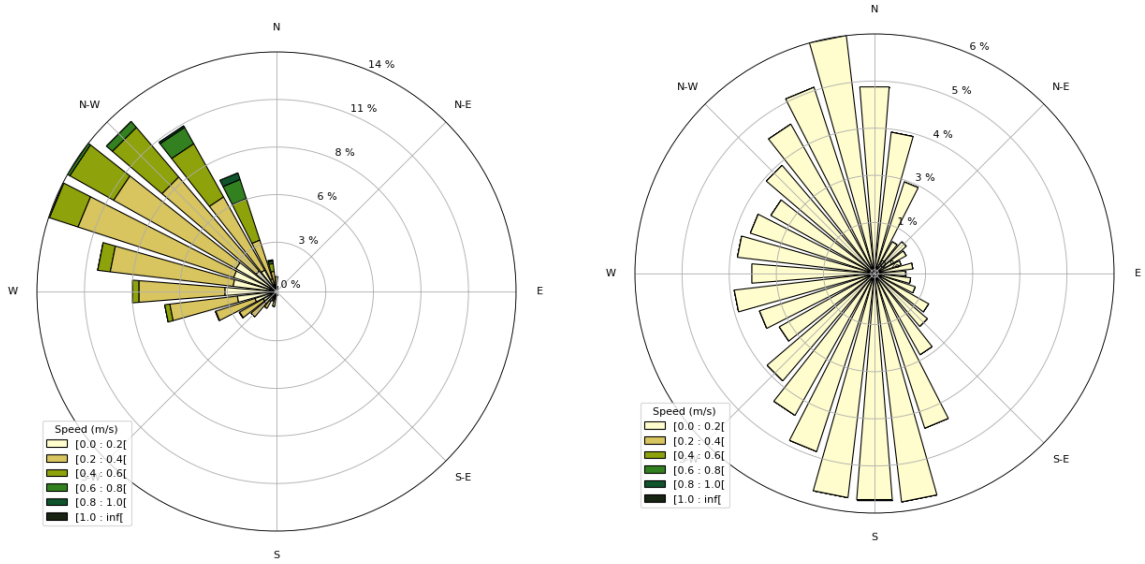

(a) Extended unobstructed region at the surface. *(b) Extended unobstructed region at 700 m depth.*

Figure J.17: Rose plots at the extended unobstructed region. Interesting is that at depth, velocities are no longer from east to west or opposed to it, but are generally from north to south or vice versa.

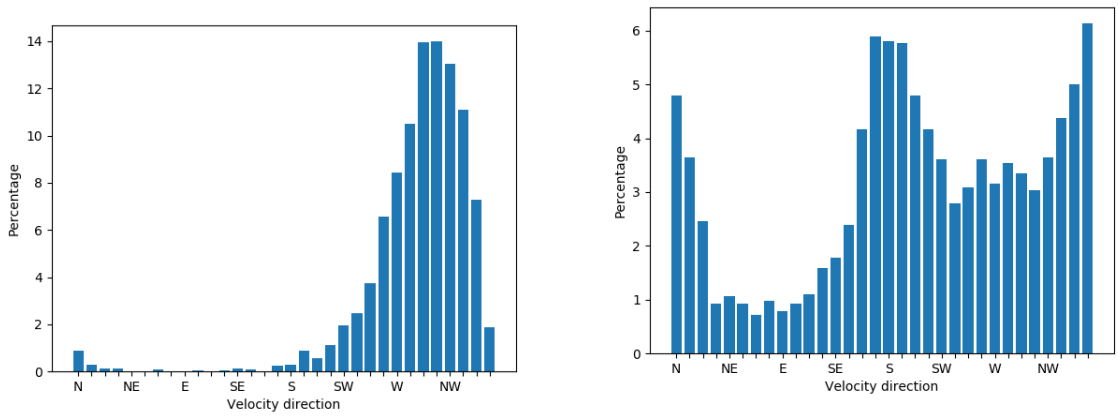

(a) Extended unobstructed region at the surface. *(b) Extended unobstructed region at 700 m depth.*

Figure J.18: Bar graphs corresponding to Figure J.17.

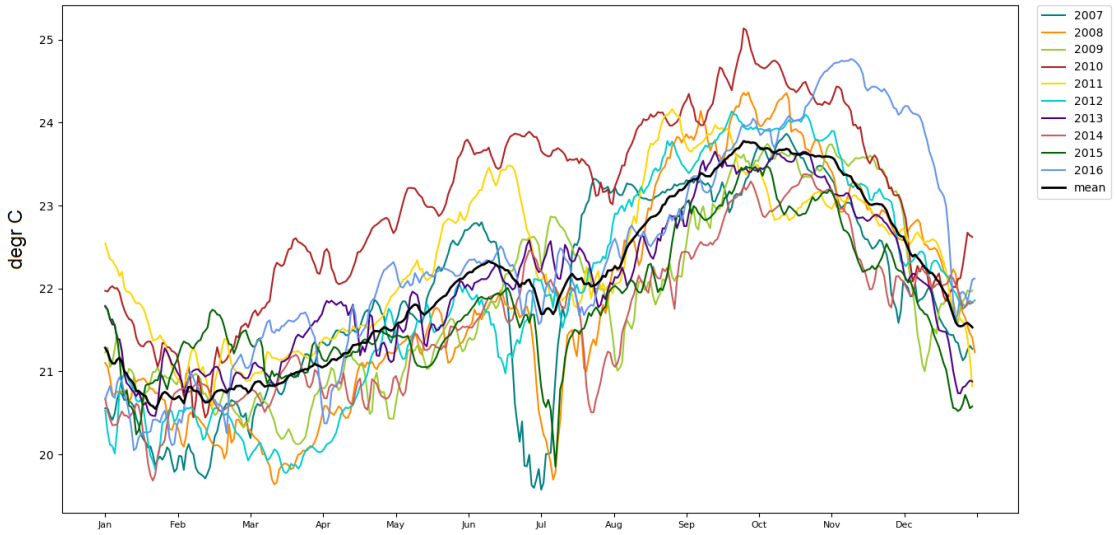

Figure J.19: Yearly values of temperature difference between the water temperature at the two inlet depths to the south of Curaçao. The mean is plotted in black.

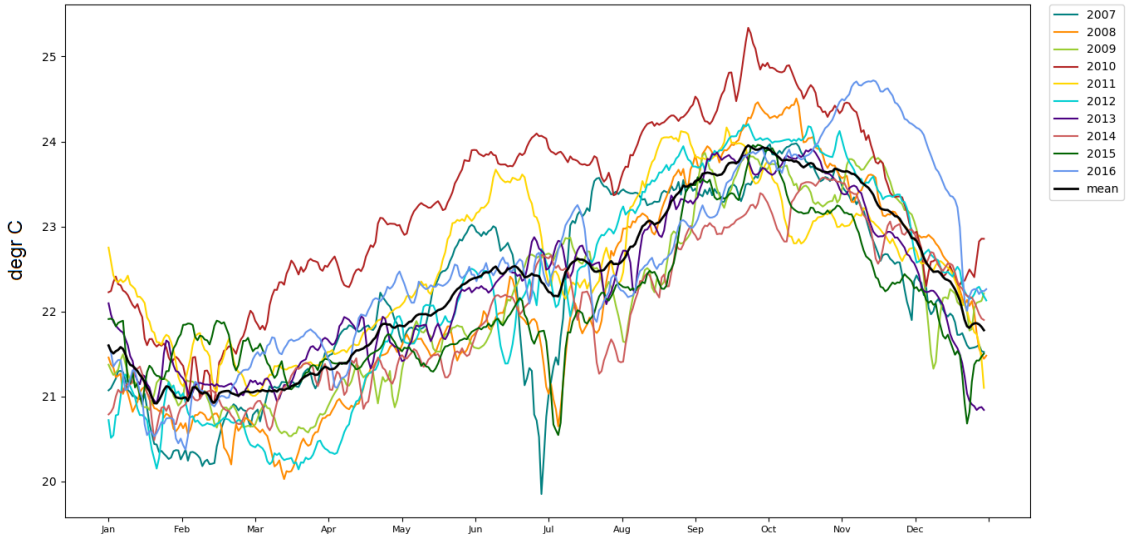

Figure J.20: Yearly values of temperature difference between the water temperature at the two inlet depths to the north of Curaçao. The mean is plotted in black.

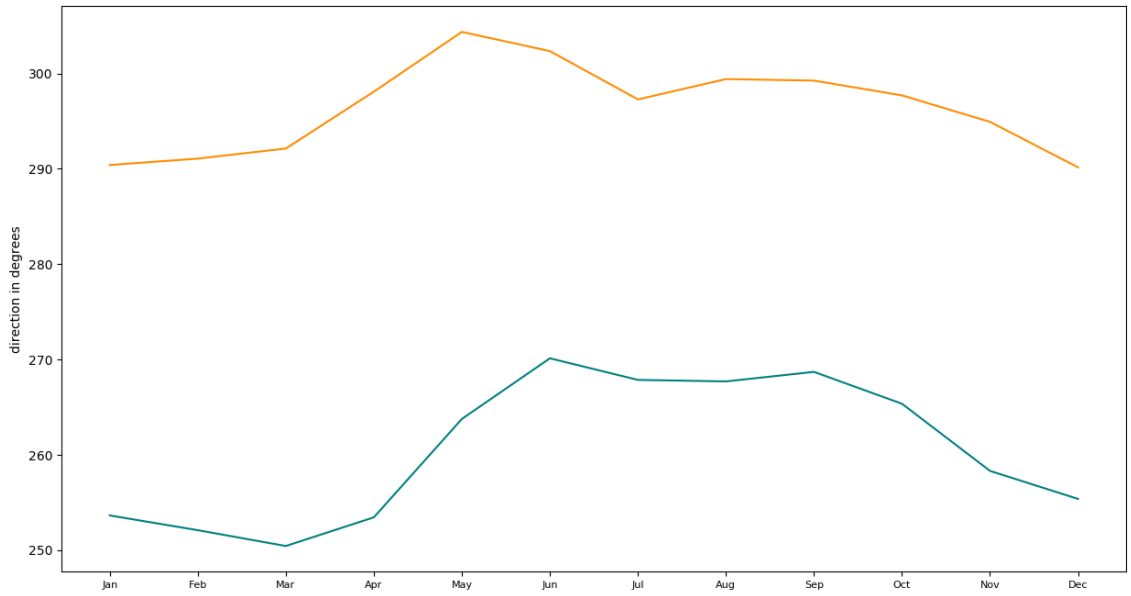

Figure J.21: Ten year mean year of wind direction and surface current direction in the channel region. Direction is in degrees and 0° is to the north with to the east as positive.

K

Appendix: Volume flux analysis

To be able to analyse the volume fluxes in the Caribbean Sea, more specific in the Venezuela Basin, the following procedure was followed. The velocity perpendicular to the line of interest was first calculated. This is done by first calculating the direction of the line α in radians, where δx is the distance between the starting point and the ending point of the line in longitudinal degrees, δy is in latitudinal degrees:

$$\alpha = \arcsin\left(\frac{1}{\sqrt{\delta x^2 + \delta y^2}} * \delta y\right)$$

The velocity perpendicular to the line can then be calculated by:

$$v_{perp} = -u * \sin\alpha + v * \cos\alpha$$

This perpendicular velocity is then multiplied by the area of the specific datapoint. So per depth:

$$area = (depth[i+1] - depth[i]) * \sqrt{x^2_{m/degr} + y^2_{m/degr}}$$

So the volume flux per location, depth and day can be calculated. For each line of interest, a yearly average was calculated. From that average, the positive part and the negative part were seperately calculated. The results can be found in the Tables K.1 to K.3.

Table K.1: Yearly volume fluxes in Sverdrups for the unobstructed region up to 15° N.

Year	Total volume flux	Positive volume flux	Negative volume flux
2007	13,32	20,14	-6,82
2008	8,62	13,92	-5,31
2009	7,62	13,41	-5,79
2010	14,20	18,67	-4,47
2011	13,02	16,71	-3,69
2012	12,36	18,92	-6,56
2013	11,03	14,37	-4,34
2014	15,38	23,34	-7,96
2015	14,79	21,08	-6,29
2016	5,91	15,37	-9,46
mean	*11,62*	*17,59*	*-6,07*
stdv	*2,69*	*3,47*	*1,37*

Table K.2: Yearly volume fluxes in Sverdrups for the channel region.

Year	Total volume flux	Positive volume flux	Negative volume flux
2007	4,21	4,64	-0,43
2008	5,14	5,44	-0,30
2009	5,73	6,54	-0,81
2010	1,86	2,72	-0,86
2011	0,80	2,09	-1,29
2012	4,14	4,73	-0,59
2013	4,41	4,95	-0,54
2014	-1,02	1,23	-2,24
2015	-0,48	1,90	-2,38
2016	4,76	5,20	-0,44
mean	*2,96*	*3,94*	*-0,99*
stdv	*2,46*	*1,80*	*0,75*

Table K.3: Yearly volume fluxes in Sverdrups for the Grenada Passage.

Year	Total volume flux	Positive volume flux	Negative volume flux
2007	11,01	11,39	-0,38
2008	10,38	10,73	-0,35
2009	8,01	8,54	-0,53
2010	7,97	8,42	-0,45
2011	9,15	9,47	-0,32
2012	7,69	8,04	-0,35
2013	8,68	9,09	-0,41
2014	8,93	9,44	-0,50
2015	8,49	9,07	-0,58
2016	8,57	9,02	-0,54
mean	*8,89*	*9,32*	*-0,44*
stdv	*1,06*	*1,03*	*0,09*

L

Appendix: Significant Ships of 2004 - PROTEFS

In this appendix, additional information on the ship that was used to calculate the hydridynamic forces is presented. This ship is called PROTEFS. Shown are page 101 and 102 from Lingwood and Knaggs [2004].

PROTEFS: fourth-generation Jiangnan Panamax bulker

Shipbuilder: ..... Jiangnan Shipyard (Group) Co Ltd, People's Republic of China
Vessel's name: ..... *Protefs*
Hull number: H2301
Owner/operator: ..... Cypres Enterprises Corp/Diana Shipping Agencies, Greece
Designer: .... Jiangnan Shipyard (Group) Co Ltd, People's Republic of China
Model test establishment used: ..... -
Flag: ..... Bahamas
Total number of sister ships already completed: 1
Total number of sister ships still on order: 3

JIANGNAN Shipyard is considered to be the oldest shipbuilder in China, however, its Shanghai city premises, which date back nearly 200 years, are now scheduled to be moved to a 'greenfield' site on an island in the River Yangtze where the company plans to set up two shipbuilding divisions. One of these will specialise in building bulk carriers up to Panamax size (the other will build larger vessels), thus continuing an involvement with this class of vessel begun in 1985, and which now totals over 30 units delivered or on order.

Protefs is an example of the fourth-generation (Mk IV) of the design, and is laid out in conventional style with a single-deck, forecastle, and seven cargo holds contained in a single-skin hull arranged with top and bottom wing ballast tanks, the latter being joined with double-bottom tanks centrally divided by a duct keel. Exceptions to this arrangement apply under Nos 5 and 6 holds where the port and starboard double-bottom tanks are separated from the wing tanks, and are designated as Nos 1 and 2 heavy fuel tanks. Additional fuel is carried in side tanks at the fore end of the engineroom, port and starboard. All ballast tanks, including No 4 hold which can be flooded, are coated with bleached tar epoxy. Basic tar epoxy coatings are used in the cargo holds.

Heavy cargoes can be loaded into alternate holds (Nos 1, 3, 5, and 7) in line with Lloyd's Register class notation 'strengthened for heavy cargoes: Nos 2, 4, and 6 holds may be empty', and tanktop, hopper side, and lower stool plating has been strengthened for grab discharge. Transverse bulkheads in the cargo space are of corrugated construction and built on stools at top and bottom of the holds. MacGregor side-rolling, chain-operated hatch covers are fitted, stowing each side of the opening whilst cargo is being worked.

The main propulsion machinery comprises a MAN B&W 5S60MC Mk6 low-speed diesel engine, manufactured under licence by Hudong Heavy Machinery (HHM) and developing 10,200kW at 105rev/min. This is directly coupled to a FP propeller running in an open-water stern frame and producing a service speed at 90% MCR (9198kW/102.80rev/min) and allowing a 15% sea margin of 14.40knots. With no shaft-driven alternator fitted, electrical supply is derived from three Yanmar/Taiyo diesel-driven sets each producing 600kW at 900rev/min. Steam requirements are satisfied from an Aalborg Mission boiler and an exhaust-gas economiser. A Lyngsø DMS-21001 engine remote control system is installed and provides bridge operation of the machinery installation.

Accommodation is arranged in the superstructure aft for eight officers, 15 crew and six 'spare' personnel, with the layout featuring an entire deck given over to the captain's quarters. Leisure facilities include a gymnasium. Traditional lifeboats are not provided, instead a free-fall craft with slipway and recovery davit operates over the stern. That section of the accommodation block housing the single-berth cabins and public rooms is separated from the funnel casing to reduce noise and vibration, but the intervening space is utilised by an athwartship gantry carrying a travelling spares and stores crane.

TECHNICAL PARTICULARS

Length, oa 225.00m
Length, bp 217.00m
Breadth, moulded 32.20m
Depth, moulded to main deck 19.20m
Gross 40,230gt
Displacement, at 14.05m draught 86,035tonnes
Deadweight
  design 63,395dwt
  scantling 73,630dwt
Draught
  design 12.50m
  scantling 14.05m
Speed, service at 90% MCR, 15% sea margin 14.40knots
Cargo capacity ..... 90,624m^3
Bunkers
  heavy oil ..... 2680m^3
  diesel oil ..... 137m^3
Water ballast ..... 32,480m^3
Fuel consumption
  main engine only 38.45tonnes/day
Classification ..... Lloyd's Register of Shipping +100A1, Bulk Carrier, 'Strengthened for Heavy Cargoes, Holds Number 2, 4, 6 may be Empty, ESN, LI, ESP, UMS, SCM
Percentage of high-tensile steel used in constuction ..... approx 45%
Main engine
  Design ..... MAN B&W
  Model 5S60MC-Mk6
  Manufacturer ..... Hudong Heavy Machinery
  Number 1
  Output 10,200kW/105rev/min
Propeller
  Material ..... Nickel-aluminium-bronze
  Manufacturer ..... Dalian Marine Propeller Works
  Number 1
  Diameter 6760mm
  Pitch ..... Fixed
  Speed 102.8rev/min
Diesel-driven alternators
  Number 3
  Engine make/type Yanmar/6N18AL-EV
  Alternator make/type Taiyo/FE547A-8
  Output 3
Boilers
  Number 1
  Type ..... Mission OS1600
  Make ..... Aalborg
  Output
    oil fired 1600kg/h
    exhaust gas 1300kg/h
Mooring equipment
  Number ..... 2 x mooring winch/windlass
    2 x mooring winch
  Make ..... Luzhou-Hatlapa
  Type ..... Hydraulic
Hatch covers
  Make ..... MacGregor
  Type ..... Side-rolling
Complement
  Officers 8
  Crew 15
  Spare 6
Ballast control system
  Make ..... SSSR
  Type ..... Remote air/electric control
Bridge control system
  Make ..... Lyngsø
  Type DMS-21001
Fire protection system
  Make ..... Salwico
  Type ..... C316 smoke detector
Fire extinguishing system
  Cargo holds ..... CO_2
  Engineroom ..... CO_2
  Make ..... Unitor
Radar
  Number 2
  Make ..... Japan Radio Co
  Models ..... 1 x JMA-9932-SA
    1 x JMA-9922-9XA
Satellite navigation system
  Make ..... Japan Radio Co
  Models ..... 2 x JLR-7700 MkII
Waste disposal system
  Incinerator
    Make ..... Luzhou
    Model OGS-200C
Contract date ..... 24 December 2002
Launch/float-out date ..... 28 March 2004
Delivery date ..... 31 August 2004

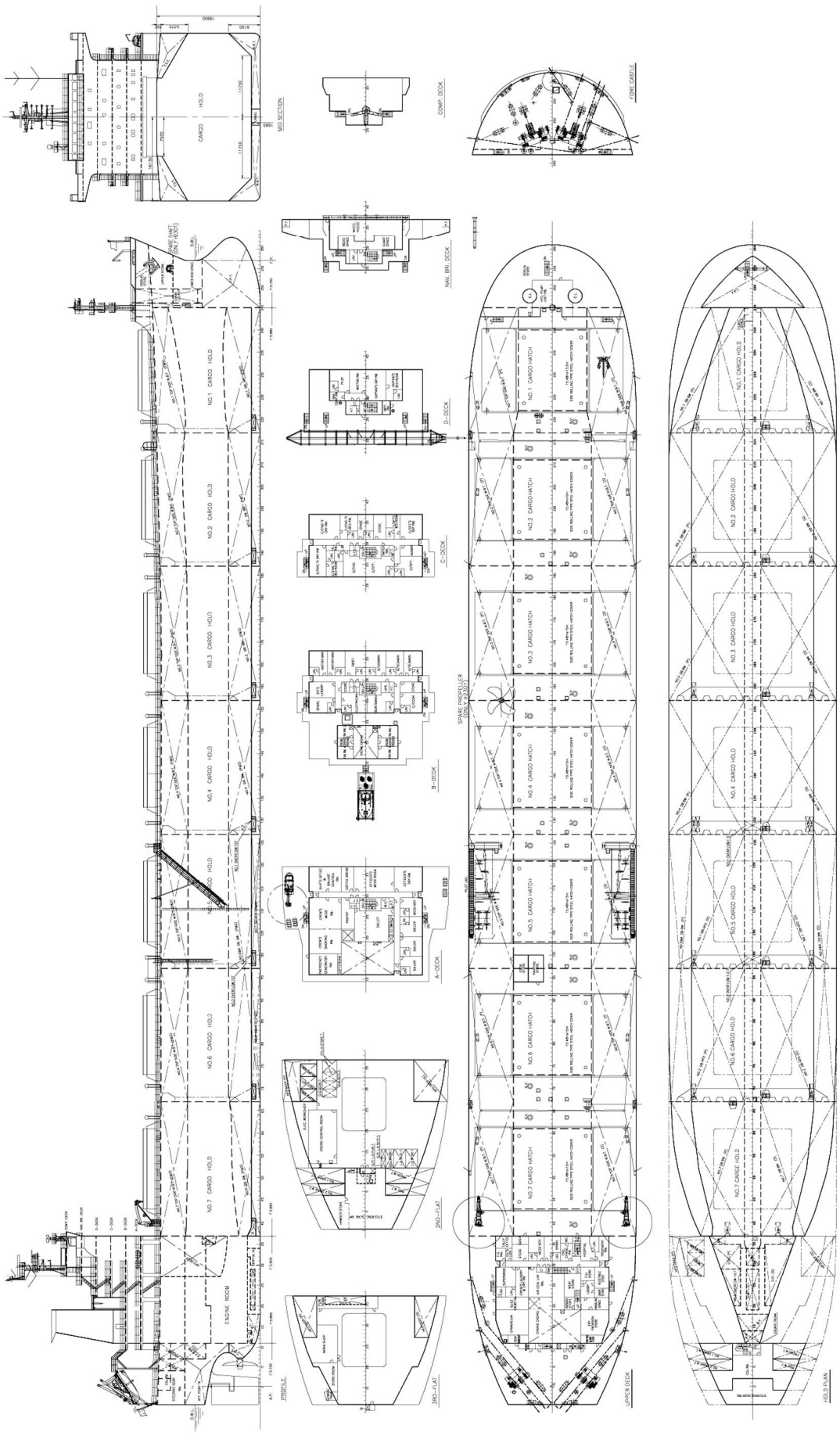
MID SECTION
CARGO HOLD
COMP. DECK
FORE CASTLE
NAV. BRI. DECK
D-DECK
C-DECK
B-DECK
A-DECK
2ND FLAT
3RD FLAT
UPPER DECK
PROFILE
NO.1 CARGO HOLD
NO.2 CARGO HOLD
NO.3 CARGO HOLD
NO.4 CARGO HOLD
NO.5 CARGO HOLD
NO.6 CARGO HOLD
NO.7 CARGO HOLD
ENGINE ROOM
NO.1 CARGO HATCH
NO.2 CARGO HATCH
NO.3 CARGO HATCH
NO.4 CARGO HATCH
NO.5 CARGO HATCH
NO.6 CARGO HATCH
NO.7 CARGO HATCH